Technische Universität München

Ingenieurfakultät Bau Geo Umwelt

Professur für Computational Mechanics

Explicit Isogeometric B-Rep Analysis for Nonlinear Dynamic Crash Simulations

Integrating Design and Analysis by Means of Trimmed Multi-Patch Shell Structures

Lukas F. Leidinger

Vollständiger Abdruck der von der Ingenieurfakultät Bau Geo Umwelt der Technischen Universität München zur Erlangung des akademischen Grades eines

Doktor-Ingenieurs

genehmigten Dissertation.

Vorsitzender:

Priv.-Doz. Dr.-Ing. habil. Roland Wüchner

Prüfer der Dissertation:

1. Prof. Dr.-Ing. habil. Fabian Duddeck
2. Prof. Dr.-Ing. Kai-Uwe Bletzinger
3. Prof. Dr.-Ing. habil. Manfred Bischoff

Die Dissertation wurde am 07.04.2020 bei der Technischen Universität München eingereicht und durch die Ingenieurfakultät Bau Geo Umwelt am 25.08.2020 angenommen.

Abstract

Current virtual (vehicle) development processes are characterized by time- and labor-intensive model conversions between the two strongly decoupled fields of Computer Aided Design (CAD) and Computer Aided Engineering (CAE). Isogeometric Analysis (IGA) aims at integrating these fields by using a unified geometry description, in particular the CAD description based on Non-Uniform Rational B-Splines (NURBS), and therefore has the potential to speed up the current development processes substantially. In order to enable direct analysis on trimmed multi-patch B-Rep models most widely used in industrial CAD, IGA was recently extended to Isogeometric B-Rep Analysis (IBRA). Via so-called B-Rep elements, IBRA allows enforcing coupling and boundary conditions along trimmed edges in a weak sense, for instance with a penalty approach. However, so far, IBRA has neither been systematically evaluated nor applied in the context of explicit dynamics, a crucial field for practical applications like crash simulations.

The aim of this thesis is to close this gap by developing Explicit IBRA, the extension of IBRA to explicit dynamic shell analysis. In particular, this thesis (i) introduces two novel types of penalty-based B-Rep element formulations for Reissner-Mindlin shells with rotational degrees of freedom, (ii) systematically studies the as yet unknown effects of trimming and weak penalty-based coupling and boundary conditions on the critical time step, (iii) presents a local selective mass scaling approach for B-Rep elements, and (iv) proposes a method to stabilize so-called light control points caused by small trimmed elements – all this with a focus on explicit dynamics and with regard to the required efficiency and conditional stability. Furthermore, this thesis demonstrates the technical feasibility of an integrated IBRA-based design-analysis process between a commercial CAD system and a commercial finite element solver. In fact, Explicit IBRA and the proposed methods were implemented into LS-DYNA via user-defined interfaces.

The validity and effectiveness of Explicit IBRA and the developed methods is demonstrated by means of various well-selected benchmark problems reaching from quasi-static linear elastic to highly dynamic nonlinear cases including plasticity, large deformations and contact. The practical applicability of Explicit IBRA is shown through explicit dynamic (impact) analyses on two BMW vehicle component models comprising up to 130 trimmed NURBS patches.

In conclusion, this thesis demonstrates the possibility to perform accurate, efficient and robust explicit dynamic analysis on trimmed multi-patch NURBS shell structures, thus opening the door towards a fully integrated CAD/CAE development process for vehicle safety.

Zusammenfassung

Virtuelle (Fahrzeug-)Entwicklungsprozesse sind aktuell gekennzeichnet durch zeit- und arbeitsintensive Modellumwandlungen zwischen den beiden stark entkoppelten Bereichen Computer Aided Design (CAD) und Computer Aided Engineering (CAE). Die Isogeometrische Analyse (IGA) zielt darauf ab, diese beiden Bereiche durch eine einheitliche Geometriebeschreibung, konkret durch die CAD-Beschreibung basierend auf Non-Uniform Rational B-Splines (NURBS), zusammenzuführen und hat somit das Potential, die heutigen Entwicklungsprozesse maßgeblich zu beschleunigen. Um Simulationen direkt auf, im industriellen CAD üblichen getrimmten mehrflächigen B-Rep Modellen zu ermöglichen, wurde IGA kürzlich auf die Isogeometrische B-Rep Analyse (IBRA) erweitert. Über sogenannte B-Rep Elemente erlaubt IBRA das Aufbringen von Kopplungs- und Randbedingungen entlang getrimmter Kanten in einer schwachen Form, etwa über einen Penalty-Ansatz. Bislang wurde IBRA jedoch im Kontext der expliziten Dynamik, einem wesentlichen Gebiet für praktische Anwendungen wie Crashsimulationen, weder systematisch untersucht noch eingesetzt.

Ziel der vorliegenden Dissertation ist es, diese Lücke durch die Entwicklung von Explicit IBRA, der Erweiterung von IBRA auf explizit dynamische Schalensimulationen, zu schließen. Konkret umfasst diese Arbeit (i) die Einführung zweier neuartiger B-Rep Elementformulierungen für Reissner-Mindlin Schalen mit Rotationsfreiheitsgraden, (ii) systematische Untersuchungen zum Einfluss von Trimmung und schwacher penalty-basierter Kopplungs- und Randbedingungen auf den kritischen Zeitschritt, (iii) eine Methode zur lokalen selektiven Massenskalierung von B-Rep Elementen und (iv) die Entwicklung einer Methodik zur Stabilisierung von, durch kleine getrimmte Elemente hervorgerufenen „leichten“ Kontrollpunkten (light control points) – all dies mit einem Fokus auf explizite Dynamik und hinsichtlich der geforderten Effizienz und bedingten Stabilität. Darüber hinaus demonstriert diese Arbeit die technische Umsetzbarkeit eines integrierten IBRA-basierten CAD/CAE-Entwicklungsprozess zwischen einem kommerziellen CAD-Programm und einem kommerziellen Finite-Elemente-Löser. Tatsächlich wurden Explicit IBRA und die entwickelten Methoden über benutzerdefinierte Schnittstellen in LS-DYNA implementiert.

Die Validität und Wirksamkeit von Explicit IBRA und der entwickelten Methoden werden anhand mehrerer wohl ausgewählter Benchmarkprobleme von quasi-statisch linear elastisch bis hin zu hochdynamisch nichtlinearen Beispielen inklusive Plastizität, großen Deformationen und Kontakt, demonstriert. Die praktische Anwendbarkeit von Explicit IBRA wird durch explizit dynamische (Aufprall-)Simulationen zweier, aus bis zu 130 getrimmten NURBS-Flächen bestehenden BMW Fahrzeugkomponentenmodelle gezeigt.

Insgesamt zeigt diese Dissertation, dass explizit dynamische Simulationen auf getrimmten mehrflächigen NURBS Schalenstrukturen mit der geforderten Genauigkeit, Effizienz und Robustheit praktisch durchführbar sind. Dies öffnet die Tür in Richtung eines voll integrierten CAD/CAE-Entwicklungsprozess für die Fahrzeugsicherheit.

Acknowledgments

This thesis was written from 2017 to 2020 during my time in the BMW Promotion scholarship program at the department for vehicle safety. I gratefully acknowledge this funding and the chance to conduct rather basic research with a clear vision of future applications in mind. I especially acknowledge the effort of Dr. Johannes Fender, Dr. Lailong Song, Franz Hoiss, Frank Bauer and Adam McNeill to initiate, enable and push Isogeometric Analysis at BMW.

I would like to express my sincere gratitude to my advisor Prof. Dr.-Ing. habil. Fabian Duddeck for the continuous support in all respects since my time as a scientific assistant at the Associate Professorship of Computational Mechanics, TU Munich in 2015, and especially for his constructive critical analysis of IGA in the field of explicit dynamics. His intentional, rather provocative claim that IGA won't work for explicit dynamic crash simulations has given me the immense motivation to prove the opposite.

Furthermore, I would like to thank Prof. Dr.-Ing. Kai-Uwe Bletzinger most sincerely for the prospering collaboration and the great opportunity to build upon the research achievements of the Chair of Structural Analysis, TU Munich, as well as for examining this dissertation. I also want to express my sincere thanks to PD Dr.-Ing. habil. Roland Wüchner for sharing his immense knowledge on IGA, which helped me a lot especially in the beginning of my work, for numerous scientific and strategic discussions, and for taking the examination chair. In that regard, I would also like to thank Prof. Dr.-Ing. habil. Manfred Bischoff for completing the board of examiners and his interest in my research.

I am also very pleased to thank my BMW supervisor Dr. Lailong Song, who has introduced me to industrial research and his professional network at BMW, provided ever-constructive "cold or hot showers", and managed to create a performance-oriented yet familiar working atmosphere in the office.

My special thanks goes to my mentor Dr. Michael Breitenberger. Besides the fact that I could not have imagined having a better mentor from a technical perspective, his solution-oriented, practical and clear way of thinking as well as his fascination for IGA have always left me full of enthusiasm and drive towards the next challenges. His guidance and his influence on this dissertation are greatly acknowledged.

Furthermore, I owe a debt of gratitude to Dr. Stefan Hartmann from DYNAmore, without whom it would not have been possible to conduct this research as he provided the user-defined LS-DYNA interface on which the implementations of this work are based. In addition, his continuous support in LS-DYNA related issues and his critical reviews are highly appreciated. I would also like to thank the IGA developer team at LSTC, in particular Prof. David J. Benson, Dr. Attila P. Nagy and Dr. Marco Pigazzini for their support and advice especially during my research stay at LSTC in Livermore, in which I developed and implemented the stabilization scheme presented in Chapter 5. I especially acknowledge that Prof. Benson made me aware of the shell normal coupling approach he and his coworkers developed for rotation-free Kirchhoff-Love shells, which I used and extended to increase the coupling accuracy of Reissner-Mindlin shells including rotational DOFs, as presented in Section 3.4. I also acknowledge the support of Pascal Weingärtner and Christian Balster from TWT in generating the guideline-conforming BMW component models.

I thank my fellow BMW colleagues for the great working atmosphere, critical inputs and technical support, especially Volker Lange, Christopher Bach, Dustin Draper, Johannes Stadler and Jonas Jehle. I also want to thank my PhD fellows from the Chair of Structural Analysis, in particular Anna Bauer for the support in setting up and maintaining the IBRA environment including TeDA and CARAT++, as well as Thomas Oberbichler, Andreas Apostolatos and Tobias Teschemacher for the inspiring projects and exchange on IGA. Furthermore, it is with pleasure to acknowledge the work of my students Ramesh K. Murugan, Jun-hyoung Kwon, Zeyu Lian and Theresa Pasch who have contributed significantly to this dissertation via their student projects and theses.

My special gratitude goes to Prof. Dr. Franz G. Rammerstorfer, former head of the Institute of Lightweight Design and Structural Biomechanics, and my teacher at the Vienna University of Technology. His fascinating lectures and exceptional knowledge in lightweight design and finite element analysis have encouraged me to discover the fields that gave me so much pleasure during the last years.

I also won't forget to thank my friends and football teammates for their company and the always well-appreciated diversion to my PhD life. Last, but by no means least, I am deeply grateful to my entire family, especially to my parents Regina and Gerhard for their strong support, encouragement and understanding.

Munich, March 2020 Lukas F. Leidinger

Contents

List of Symbols and Abbreviations

Indices, super- and subscripts

A, B, I, J	Upper case Latin indices denoting control points/nodes
α, β	Greek indices taking values from 1 to 2, if not defined otherwise
e	Element index
n	nth time step
t	$\boldsymbol{a}_{\mathrm{t}}$-direction
u	$\boldsymbol{a}_{\mathrm{u}}$-direction
3	$\boldsymbol{a}_3$-direction
(i)	Superscript indicating subdomain (i)
disp	Displacements
rot	Rotations
tan	Rotational coupling around curve tangent vector $\boldsymbol{a}_{\mathrm{t}}$
B-Rep	Contribution from B-Rep elements
m, s	Master resp. slave entities
C	Coupling
D	Dirichlet
N	Neumann
P	Penalty
S	Shell

Sets

$\mathbb{N}$	Set of natural numbers
$\mathbb{R}$	Set of real numbers
$\mathbb{C}$	Set of complex numbers
$\mathcal{M}$	Set of control points
$\mathcal{M}_{\mathrm{m}}$	Set of control points in master domain Ω^{m}
$\mathcal{M}_{\mathrm{s}}$	Set of control points in slave domain Ω^{s}
$\mathcal{M}_{\mathrm{t}}^{(i)}$	Set of trimmed control points in subdomain $\Omega^{(i)}$
$\mathcal{M}_{\mathrm{st}}^{(i)}$	Set of stable control points in subdomain $\Omega^{(i)}$

$\mathcal{M}_{\mathrm{li}}^{(i)}$	Set of light control points in subdomain $\Omega^{(i)}$
$\mathcal{M}_{\mathrm{in}}^{(i)}$	Set of inactive control points in subdomain $\Omega^{(i)}$
$\mathcal{M}_{\mathrm{i}}^{\mathrm{disp}}$	Set of translational matrix indices
$\mathcal{M}_{\mathrm{i}}^{\mathrm{rot}}$	Set of rotational matrix indices

Geometric quantities

b	Width
h	Shell or beam thickness
h_{p}, h_{t}	Heights indicating perturbations resp. trimming positions
l	Length, element length
l_{c}^{e}	Characteristic element length
l_{max}	Maximum element length
A	Cross-sectional area
H	Height
L	Length
W	Width
R, r	Radius
$L_{1,k}^{A}$	Initial distance btw. light control point A and its first reference control point $\mathrm{P}_{\mathrm{R1},k}^{A}$ in direction k
$L_{12,k}^{A}$	Initial distance btw. the reference control points $\mathrm{P}_{\mathrm{R1},k}^{A}$ and $\mathrm{P}_{\mathrm{R2},k}^{A}$ of light control point A in direction k

Material parameters

c	Material wave speed
E	Young's modulus
E_{H}	Tangent modulus
ν	Poisson's ratio
ρ	Mass density
σ_{y}	Yield strength

Parameters

x_i	Global spatial coordinates, $i \in \{1,2,3\}$
ζ	Out-of-plane shell coordinate
η	Parameter for NURBS or B-spline geometries
η_i	Knot value of knot vector $\mathcal{H}$
ξ	Parameter for NURBS or B-spline geometries
ξ_i	Knot value of knot vector Ξ
ξ_{t}	Trim position or distance
$\tilde{\xi}$	Trimming curve parameter or general curve parameter
$\mathcal{H}$	Knot vector in η-direction
Θ^i	Curvilinear, contravariant coordinates
$\tilde{\Theta}$	Curve parameter for curves on surfaces and surface boundaries
Ξ	Knot vector in ξ-direction

Basis functions

$N_{i,p}(\xi)$	Univariate B-spline basis function of degree p in ξ-direction
$N'_{i,p}(\xi)$	Basis function derivative w.r.t. ξ
$N_A(\xi,\eta)$	Bivariate B-spline/NURBS basis function
$M_{j,p}(\eta)$	Univariate B-spline basis function of degree q in η-direction
$R_{i,p}(\xi)$	Univariate NURBS basis function of degree p
$R_A(\xi,\eta)$	Bivariate NURBS basis function

Points, curves, surfaces, volumes and boundaries

P	Point on the shell midsurface in the initial (undeformed) configuration
P^*	Point in the shell body in the initial (undeformed) configuration
$\bar{\mathrm{P}}$	Point on the shell midsurface in the current (deformed) configuration
$\bar{\mathrm{P}}^*$	Point in the shell body in the current (deformed) configuration
$\mathrm{P}^A_{\mathrm{R1},k}$	First reference control point for light control point A in direction k
$\mathrm{P}^A_{\mathrm{R2},k}$	Second reference control point for light control point A in direction k
P'_A	Virtual reference point for light control point A
$\mathbf{P}_i, \mathbf{P}_{ij}, \mathbf{P}_A$	Control point in the geometry space
$\tilde{\mathbf{P}}_i$	Control point in the parameter space of a B-spline/NURBS surface
$\mathbf{C}(\xi)$	B-spline or NURBS curve
$\tilde{\mathbf{C}}(\tilde{\xi})$	Trimming curve in the parameter space of a B-spline/NURBS surface
$\mathbf{S}_{\text{visible}}$	Visible/material domain of a surface $\mathbf{S}$
$\mathbf{S}_{\text{void}}$	Void domain of a surface $\mathbf{S}$
$\mathbf{S}(\xi,\eta)$	B-spline/NURBS surface
Ω	Physical (shell) domain
$\tilde{\Omega}$	Shell domain in the parameter space of B-spline/NURBS surface
Γ_V	Surface boundary of a volume V
Γ	Boundary of a physical (shell) domain
$\tilde{\Gamma}$	Boundary of a shell domain in the parameter space of B-spline/NURBS surface
$\partial\,\mathbf{S}_{\text{visible}}$	Boundary of a trimmed B-spline/NURBS surface
Γ_e	Spatial extent of an isogeometric B-Rep edge element e in the geometry space
$\tilde{\Gamma}_e$	Spatial extent of an isogeometric B-Rep edge element e in the parameter space
V	Volume

Scalar values

e^{disp}	Error measure for light control point displacements
e^{rot}	Error measure for light control point rotations
f_A	Control point mass scaling factor
f^{s}	Stabilization mass scaling factor
k	Stiffness
m	Number of basis functions (in η-direction)

m_i	Multiplicity of the knot value ξ_i
m	Mass
m_{th}	Threshold mass for the determination of light control points
m_{max}	Maximum control point mass
Δm	Total mass increase through mass scaling
n	Number of basis functions (in ξ-direction)
n_{d}^A	Number of stable directions for light control point A
n_{DOF}	Number of DOFs
n_{el}	Number of elements
n_{lcp}	Number of light control points
n_{qp}	Number of quadrature points
p	Polynomial degree (in ξ-direction)
$\bar{p}$	Pressure load
q	Polynomial degree (in η-direction)
t	Time
Δt	Time step
Δt_0	Initial time step size
Δt_{crit}	Critical time step
$\Delta \bar{t}$	Prescribed time step
w_i	Control point weight for NURBS
w_l	Weights for numerical integration
$\tilde{w}_l$	Weights for numerical integration incl. J_2
C_{th}	Threshold constant for the determination of light control points
C^x	Parametric continuity of order x
G^x	Geometric continuity of order x
J_A	Rotational inertia of control point A
$\hat{J}_A$	Scaled rotational inertia of control point A
J_ε	Stabilization rotational inertia
M_A	Mass of control point A
$\hat{M}_A$	Scaled mass of control point A
M_ε	Stabilization mass
P	Point load or line load
δP	Virtual power
δP^{int}	Virtual internal power
δP^{ext}	Virtual external power
δP^{kin}	Virtual kinetic power
$\bar{V}$	Prescribed velocity
W	Work

δW	Virtual work
δW^{int}	Virtual internal work
δW^{ext}	Virtual external work
δW^{kin}	Virtual kinetic work
δW^{kin}	Virtual work from B-Rep elements
α	Penalty factor or fictitious domain factor
α_I, α_J	Modal decomposition coefficients
α_r	Relative penalty factor $\alpha_r = \alpha / E$
α'	Highest possible penalty factor without a time step reduction
α^{disp}	Penalty factor for the displacements
α^{rot}	Penalty factor for the rotations
β	Stabilization penalty factor
$\bar{\beta}$	Global stabilization penalty factor
$\tilde{\beta}_A$	Specific stabilization penalty factor for light control point A
δ	Trimmed length of one-dimensional bar elements
ε	Small perturbation, small scalar value close to zero
ε_1	Small stabilization mass scaling constant
κ	Scaling factor for rotational control point inertia
$\kappa(\mathbf{A})$	Condition number of a matrix $\mathbf{A}$
λ_I	Eigenvalue
λ_{max}	Maximum system eigenvalue
λ^E_{max}	Maximum of all element eigenvalues
ξ_I	Modal damping ratio associated with the eigenfrequency ω_I
ω_I	Eigenfrequency
ω_{max}	Maximum system eigenfrequency
ω^e_{max}	Maximum element eigenfrequency

Scalar fields and functions

g	Scalar-valued constraint
J_1	Jacobian of the mapping from the parameter to the geometry space
J_2	Jacobian of the mapping from the Gauss to the parameter space
$\tilde{J}_1$	Jacobian of the mapping from the trimming curve parameter space to the geometry space
$\tilde{J}_2$	Jacobian of the mapping from the Gauss to the trimming curve parameter space
$W(\xi)$	Weighting function for NURBS
γ	Shear angle
ϑ	Director rotation angle
$\hat{\vartheta}$	Shell unit normal rotation angle
ϕ, ϕ_0	Current resp. initial angle between master and slave unit normal shell vectors
ψ	Deviation angle $(\phi - \phi_0)$

Base vectors

$\boldsymbol{a}_i$	Covariant basis in the current (deformed) configuration, $i \in \{1,2,3\}$
$\boldsymbol{a}_\mathrm{u}$, $\boldsymbol{a}_\mathrm{t}$, $\boldsymbol{a}_3$	Basis vectors on a surface boundary $\partial\,\mathbf{S}_\mathrm{visible}$ in the current (deformed) configuration
$\boldsymbol{a}_3$	Shell unit normal vector on a surface boundary in the current configuration
$\boldsymbol{a}_\mathrm{t}$	Unit vector along a boundary curve tangent in the current configuration
$\boldsymbol{a}_\mathrm{u}$	Unit vector in the surface plane and perpendicular to the curve tangent vector $\boldsymbol{a}_\mathrm{t}$ in the current configuration
$\boldsymbol{e}_i$	Global orthonormal coordinate system, $i \in \{1,2,3\}$
$\boldsymbol{A}_i$	Covariant basis in the initial (undeformed) configuration, $i \in \{1,2,3\}$
$\boldsymbol{A}_\mathrm{u}$, $\boldsymbol{A}_\mathrm{t}$, $\boldsymbol{A}_3$	Basis vectors on a surface boundary $\partial\,\mathbf{S}_\mathrm{visible}$ in the initial (undeformed) configuration
$\boldsymbol{A}_3$	Shell unit normal vector on a surface boundary in the initial configuration
$\boldsymbol{A}_\mathrm{t}$	Unit vector along a boundary curve tangent in the initial configuration
$\boldsymbol{A}_\mathrm{u}$	Unit vector in the surface plane perpendicular to the boundary curve tangent vector $\boldsymbol{A}_\mathrm{t}$ in the initial configuration

Vector fields

$\boldsymbol{a}$	Acceleration
$\hat{\boldsymbol{a}}_3$	Shell normal vector not normalized
$\hat{\boldsymbol{a}}_\mathrm{t}$	Vector along a boundary curve tangent
$\boldsymbol{b}$	Body force
$\boldsymbol{d}_3$	Shell director in the current (deformed) configuration
$\boldsymbol{g}$	Vector-valued constraint
$\boldsymbol{n}$	Traction force
$\boldsymbol{m}$	Traction moment
$\boldsymbol{t}$	Traction force
$\tilde{\boldsymbol{t}}$	Trimming curve tangent vector in the parameter space of a B-spline/NURBS surface
$\boldsymbol{u}$	Displacement of a point on the shell midsurface
$\delta\boldsymbol{u}$	Virtual displacement
$\boldsymbol{u}^*$	Displacement of a point in the shell body
$\boldsymbol{v}$	Velocity
$\delta\boldsymbol{v}$	Virtual velocity
$\boldsymbol{w}$	Difference vector btw. the initial and the current shell directors $\boldsymbol{D}_3$ and $\boldsymbol{d}_3$
$\hat{\boldsymbol{w}}$	Difference vector btw. the initial and the current shell unit normal vectors $\boldsymbol{A}_3$ and $\boldsymbol{a}_3$
$\boldsymbol{x}(\Theta^1,\Theta^2)$	Position vector describing a point on the shell midsurface in the current (deformed) configuration
$\boldsymbol{x}^*(\Theta^1,\Theta^2,\Theta^3)$	Position vector describing a point in the shell body in the current (deformed) configuration
$\boldsymbol{D}_3$	Shell director in the initial (undeformed) configuration
$\boldsymbol{X}(\Theta^1,\Theta^2)$	Position vector describing a point on the shell midsurface in the initial (undeformed) configuration
$\boldsymbol{X}^*(\Theta^1,\Theta^2,\Theta^3)$	Position vector describing a point in the shell body in the initial (undeformed) configuration
$\boldsymbol{\gamma}$	Shear vector (difference vector btw. the shell unit normal $\boldsymbol{a}_3$ and the director $\boldsymbol{d}_3$)
$\boldsymbol{\vartheta}$	Director rotation vector
$\hat{\boldsymbol{\vartheta}}$	Shell unit normal rotation vector

$\boldsymbol{\theta}$	Rotation vector
$\delta\boldsymbol{\theta}$	Virtual rotation vector
$\boldsymbol{\omega}$	Angular velocity vector

Control point related vectors

$\mathbf{a}_A$	Acceleration of control point A
$\mathbf{e}_A$	Error vector of control point A
$\mathbf{f}_A$	Force vector of control point A
$\mathbf{f}_A^{\text{stab}}$	Stabilization force for light control point A
$\mathbf{u}_A$	Displacement of control point A
$\mathbf{u}_{\text{R1},k}^A$	Displacement of the first reference control point R1 for light control point A in direction k
$\mathbf{u}_{\text{R2},k}^A$	Displacement of the second reference control point R2 for light control point A in direction k
$\boldsymbol{u}'_A$	Reference displacement for light control point A
$\mathbf{v}_A$	Velocity of control point A
$\mathbf{x}_A$	Global spatial coordinates of control point A
$\mathbf{x}_{\text{R1},k}^A$	Position of the first reference control point R1 for light control point A in direction k in the current configuration
$\mathbf{x}_{\text{R2},k}^A$	Position of the second reference control point R2 for light control point A in direction k in the current configuration
$\boldsymbol{x}'_A$	Reference position for light control point A
$\boldsymbol{x}'_{A,k}$	Reference position for light control point A in direction k
$\hat{\mathbf{y}}_A$	Unit fiber vector or director associated with control point A
$\mathbf{X}_{\text{R1},k}^A$	Position of the first reference control point R1 for light control point A in direction k in the initial configuration
$\mathbf{X}_{\text{R2},k}^A$	Position of the second reference control point R2 for light control point A in direction k in the initial configuration
$\boldsymbol{\theta}_A$	Rotation of control point A
$\boldsymbol{\theta}_{\text{R1},k}^A$	Rotation of the first reference control point R1 for light control point A in direction k
$\boldsymbol{\theta}'_A$	Reference rotation for light control point A
$\boldsymbol{\theta}'_{A,k}$	Reference rotation for light control point A in direction k
$\boldsymbol{\omega}_A$	Angular velocity of control point A

Discrete vectors and matrices

$\mathbf{a}$	Vector of control point accelerations
$\mathbf{d}$	Vector of control point displacements
$\mathbf{f}$	Vector of control point forces
$\mathbf{f}^{\text{ext}}$	Vector of external control point forces
$\mathbf{f}^{\text{int}}$	Vector of internal control point forces
$\mathbf{f}^v$, $\mathbf{f}^\omega$	Vector of control point forces for translations resp. rotations
$\mathbf{m}$	Vector of control point moments
$\mathbf{v}$	Vector of control point velocities
$\mathbf{y}_I$	Eigenvector
$\mathbf{B}^v$, $\mathbf{B}^\omega$	Strain-displacement matrices for translations resp. rotations
$\mathbf{C}$	Damping matrix

$\mathbf{I}$	Identity matrix
$\mathbf{K}$	Stiffness matrix
$\tilde{\mathbf{K}}$	Lumped (diagonal) stiffness matrix
$\mathbf{K}^{vv}$	Translational stiffness matrix contribution
$\mathbf{K}^{\omega\omega}$	Rotational stiffness matrix contribution
$\mathbf{K}^{v\omega}$	Mixed translational and rotational stiffness matrix contributions
$\mathbf{M}$	Mass matrix
$\hat{\mathbf{M}}$	Scaled mass matrix
$\overline{\boldsymbol{\alpha}}$	Diagonal matrix of penalty factors
$\boldsymbol{\varphi}_A$	Diagonal matrix containing values of $\pm N_A$
$\boldsymbol{\Phi}$	Matrix of basis functions containing all $\boldsymbol{\varphi}_A$

Tensors

$\boldsymbol{C}$	Material tangent constitutive matrix
$\boldsymbol{D}$	Rate of deformation
$\delta\boldsymbol{D}$	Virtual rate of deformation
$\boldsymbol{L}$	Spatial velocity gradient
$\delta\boldsymbol{L}$	Virtual spatial velocity gradient
$\boldsymbol{\sigma}$	Cauchy stress tensor

Mathematical symbols and operators

$\otimes$	Dyadic or outer product
$\|\cdot\|$	Euclidean or L^2 norm
$[\boldsymbol{a}\times]\boldsymbol{b}$	Cross product $\boldsymbol{a}\times\boldsymbol{b}$ expressed as a matrix multiplication with the 3×3 skew symmetric matrix $[\boldsymbol{a}\times]$
$\mathrm{tr}(\mathbf{A})$	Trace of a matrix $\mathbf{A}$
δ_{IJ}	Kronecker delta
$\overline{(\cdot)}$	Generalized quantity comprising translational and rotational DOFs
$\check{(\cdot)}$	Penalty-related quantities with $\alpha = 1$
$\mathcal{G}$	Gauss space for numerical integration
$\mathcal{B}(x_0, R_0)$	Closed disc with center x_0 and radius R_0
$\mathcal{D}$	Gershgorin disc

Abbreviations

AGIP	Adaptive Gaussian Integration Procedure
AiCAD	Analysis in Computer Aided Design
API	Application Programming Interface
BEM	Boundary Element Method
BIW	Body-In-White
B-Rep	Boundary Representation
CAD	Computer Aided Design
CAE	Computer Aided Engineering

CDM	Central Difference Method
CFL	Courant Friedrichs Lewy (CFL condition)
CP	Control Point
CutFEM	Cut Finite Element Method
CutIGA	Cut Isogeometric Analysis
DG	Discontinuous Galerkin
DOF	Degree Of Freedom
E	Edge
F	Face
FCM	Finite Cell Method
FE	Finite Element
FEA	Finite Element Analysis
IBRA	Isogeometric B-Rep Analysis
IGA	Isogeometric Analysis
IP	Integration Point
JSON	JavaScript Object Notation
KL	Kirchhoff-Love
LCP	Light Control Point
LR	Locally Refined
NURBS	Non-Uniform Rational B-Spline
NVH	Noise Vibration Harshness
RM	Reissner-Mindlin
STEP	STandard for the Exchange of Product model data
TeDA	Tool to enhance Design by Analysis
THB	Truncated Hierarchical B-spline
V	Vertex
WEB	Weighted Extended B-spline

Chapter 1

Introduction

1.1 Motivation

Passenger cars specifically designed with respect to the highest crash safety requirements greatly reduce the risk of fatal and serious injuries [1], saving thousands of lives every day. Developing such safe vehicles able to protect occupants, pedestrians and other road users in various crash scenarios would not be possible without virtual design tools. Efficient virtual development processes with high predictive quality become ever more important because of (i) increasing passive safety requirements due to stricter legislation and more comprehensive consumer tests, (ii) a volatile and highly competitive market that requires ever faster development cycles, and (iii) the desire to consume less resources for actual hardware crash tests by validating vehicle concepts virtually. Future virtual development processes are therefore supposed to be both, more efficient and more accurate in their predictions. Pictures of a Euro NCAP [2] hardware crash test and of a virtual FEA side impact crash test are provided in Figure 1.1.

(a) Euro NCAP hardware crash test [3].

(b) Virtual side impact crash test.

Figure 1.1: Hardware (a) and virtual (b) crash tests. In (b) a part of the movable barrier is hidden for better visibility.

The main shortcoming of the current virtual development process is that it consists of two rather independent fields: (a) Geometrical design within a Computer Aided Design (CAD) system and (b) functional design by means of Finite Element Analysis (FEA) tools, also referred to as Computer Aided Engineering (CAE). Because these two fields are based on different model descriptions, the duration of the current development process, depicted in Figure 1.2, is dominated by time- and labor-intensive model conversions and synchronization problems. Starting point of this process is a geometrically precise *design model* in the CAD system, based on a Non-Uniform Rational B-Spline (NURBS) boundary representation (B-Rep). This design model is then converted into an *analysis model* (FEA), described by an approximate geometry based on (linear) Lagrange polynomials. This conversion is usually performed in a separate preprocessing program and includes only partially automated model cleaning and meshing steps. The change of the geometry description in the meshing step is indicated by a change of color from light blue to light orange in Figure 1.2. After attributes like material properties, boundary conditions and connections between components are assigned, the analysis can be performed in the FEA solver. Generating a full vehicle FEA model

through all these steps currently takes several weeks (in each design cycle). After the analysis, results are visualized and interpreted in a postprocessor. Based on the simulated model behavior, design modifications are made, in fact, directly on the FEA model within the preprocessor, and simulations of the updated model are run again. The higher the number of iterations and applied model modifications, the more the FEA geometry will deviate from the original CAD geometry, which may also have changed in the meantime, yielding significantly different versions of the same object. At some determined synchronization point in the project timeline, however, the performed modifications need to be incorporated into the CAD model – a second time- and labor-intensive model conversion characterized by error-prone data transfer and manual surface reconstruction performed by the design engineer. This issue is aggravated by the fact that a vehicle needs to be analyzed with respect to several different disciplines like crashworthiness, stiffness, strength, durability and NVH (noise, vibration, harshness). The focus of this thesis, however, is on explicit dynamic analysis for crashworthiness design.

The procedure described so far represents only the first of multiple design cycles within a vehicle development project. For the next design cycle(s), most FEA model components are generated from scratch again including cleaning and meshing steps as well as the assignment of analysis attributes. Performing all these preprocessing steps for the same (but updated) components again is necessary because the relation between the FEA model and the parametric feature-based CAD model was lost. In fact, the FEA model is a “dead” and independent model with a completely different geometry description, modeling paradigm and data structure. That is, while features like holes, cut-outs or beadings are actually described as features in the CAD model, they are just a set of nodes and elements in the FEA model. Geometry modifications require remeshing of the FEA model. Therefore, features in the updated FEA model will be described by completely different nodes and elements, and corresponding analysis attributes need to be assigned from scratch again.

In conclusion, the time- and labor-intensive model conversions, the lost connection between the design and the analysis model and the approximated geometry are the main shortcomings of the current virtual development process based on FEA.

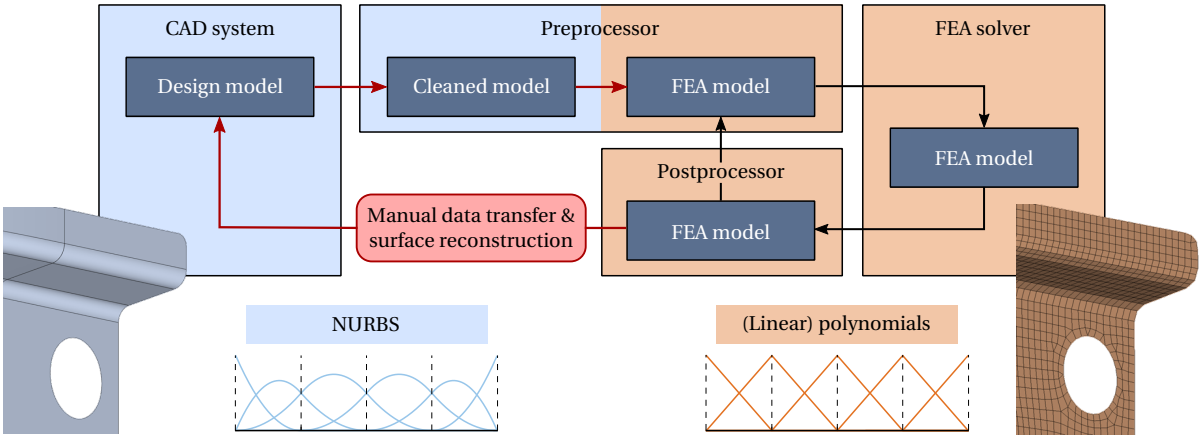

Figure 1.2: Current virtual development process comprising geometrical design in a CAD system and functional design via FEA tools including a preprocessor, a solver and a postprocessor. The CAD geometry description based on NURBS is indicated in light blue, while the FEA geometry description based on (linear) Lagrange polynomials is indicated in light orange. All steps indicated by red arrows require significant manual effort and prevent a direct connection between the design and the analysis model.

Attempts to overcome the issue of cumbersome analysis model generation and decoupling between design and analysis have been made in the past, some of which resulted in commercially available tools. Two approaches that aim at incorporating finite element analysis tools into an existing CAD environment are the 3DEXPERIENCE platform from Dassault Systèmes [4, 5] and Simcenter 3D from Siemens [6]. Both approaches allow pre- and postprocessing within the CAD environment and promise an association between the design model and the mesh, carry-over of analysis-related attributes from the design model and faster FEA model generation. Still, an FEA model based on an approximated geometry description with an inherently different modeling paradigm and data structure is used. Thus, the association between the design and the analysis model needs to be established artificially in the background software. Although extensively promoted by software vendors, these approaches have not yet achieved broad usage in (automotive) industry. Other, more designer oriented tools are for instance SimSolid from Altair [7] and Discovery Live from Ansys [8]. These tools promise to not require any defeaturing or mesh generation steps and to provide

fast analysis results. However, both approaches are designer oriented with a focus on quick results and are not able to replace detailed high-quality FEA [9]. In particular, they do not cover highly dynamic nonlinear explicit analysis required for different vehicle crash scenarios. Also worth mentioning in this context are immersed methods, for example the Finite Cell Method (FCM) [10], and meshfree methods [11]. Both methods have in common that they do not use boundary-fitted meshes and therefore avoid the cumbersome mesh generation process often encountered within standard FEA.

The focus of this thesis, however, is on Isogeometric Analysis (IGA), introduced by Hughes et al. [12] in 2005. The main idea behind IGA is to use the accurate NURBS-based geometry description from CAD also for the analysis, thus avoiding cumbersome geometry conversions within the development process. By adhering to the same geometry description, IGA has the great potential to unite the as yet separated fields of design and analysis. Because NURBS basis functions exhibit properties like partition of unity, linear independence and affine covariance, NURBS can be also used to describe the solution field in an isoparametric sense. Thus, IGA can, broadly speaking, be seen as FEA with NURBS basis functions or FEA on accurate CAD geometries. Referring to the overall goal for the development process stated above, IGA has not only the potential to increase its efficiency, but also its predictive accuracy, due to a more accurate geometry description and the superior approximation properties of the higher-order and higher-continuity NURBS basis; see for instance Cottrell et al. [13] for structural eigenvalue problems, and Hartmann and Benson [14] for sheet metal forming problems.

A possible IGA-based development process is depicted in Figure 1.3. Due to the consistent NURBS-based geometry description throughout the entire process all design, pre- and postprocessing steps can be performed within the CAD environment. Furthermore, using the same geometry description, the same modeling paradigm and the same data structure allows maintaining an active parametric relation between the design and the analysis model. In fact, the so-called *analysis-suitable* model is intended to be a direct result of the actual CAD process – ideally, if the design model is changed, the analysis model is updated automatically. For the analysis, the NURBS basis may be appropriately refined by an algorithm. After the analysis, results can be visualized in the CAD environment and design changes are directly performed on the design model, yielding an updated analysis model as an output. In this way, design and analysis remain synchronized throughout the entire process comprising multiple design cycles. Consequently, multiple redundant model generations and definitions of analysis-related attributes, boundary conditions or connections between components can be avoided.

Despite its numerous benefits, IGA has not yet achieved a major breakthrough in productive industrial applications. One reason for this may be the fact that industrial CAD models usually consist of multiple trimmed NURBS surfaces and that IGA, in its original form, is not directly applicable to such models. However, different approaches to perform isogeometric analysis on industrial models exist. This thesis addresses this issue with a special focus on explicit dynamic (crash) analysis. The following section provides a review of the state of the art regarding explicit isogeometric analysis on industrial models, motivating the research conducted within this work.

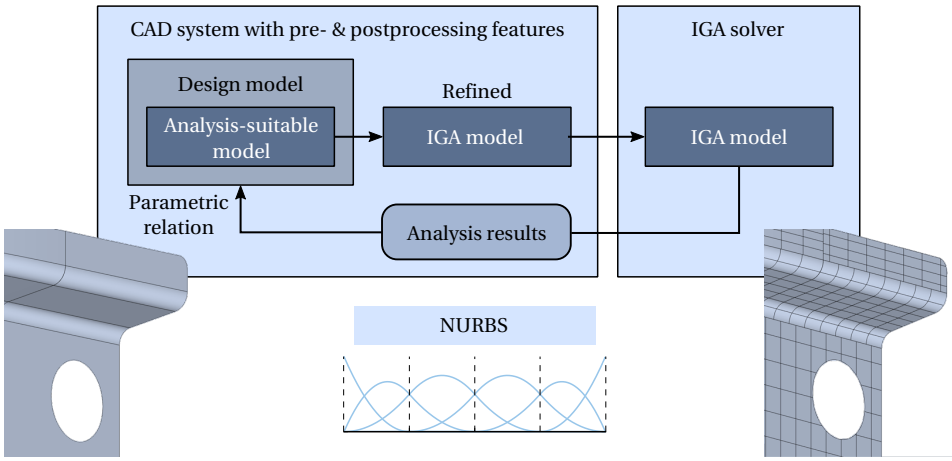

Figure 1.3: A possible virtual development process using NURBS-based IGA. All design, pre- and postprocessing steps are performed in the CAD environment. A consistent geometry description, modeling paradigm and data structure is used within the entire process. The analysis-suitable model is a direct result of the design model connected via parametric relations. Refinement is performed automatically via an algorithm. Design and analysis are synchronized.

1.2 State of the art – Explicit isogeometric analysis on industrial models

This section outlines existing approaches, methods and findings relevant for explicit isogeometric analysis on industrial models and motivates the research conducted within this thesis.

1.2.1 Handling of industrial CAD models within isogeometric analysis

To date, CAD models in (automotive) industry are mainly constructed using the boundary representation (B-Rep) modeling approach based on Non-Uniform Rational B-Splines (NURBS), in which a three-dimensional physical object is represented only by its skin, i.e. its bounding surfaces [15, 16]. If the bounding surfaces of a B-Rep model are topologically connected and thus represent a closed body, such models are referred to as *solid* models in the CAD community [17]. In finite element analysis, on the contrary, the term *solid* model indicates that a physical object is represented by a full volume discretization and not by a dimensionally reduced midsurface shell model.

In industrial (automotive) CAD, even thin sheet metal components are constructed as solid models (solid in the CAD sense, i.e. as hollow B-Rep models), to allow accurate packaging space analysis and to provide the precise geometry for manufacturing. In fact, a vast majority of the body-in-white (BIW) components are such sheet metal components, which are modeled as shells in FEA[1] and therefore require a midsurface representation of the physical component. For most sheet metal components, the midsurface can be extracted automatically in CAD or preprocessing programs, for other components this step may not be trivial[2]. In the following, midsurface B-Rep models are considered as an output of the design process.

The fact that industrial B-Rep models generally consist of multiple trimmed NURBS surfaces with non-matching discretizations prevents direct isogeometric analysis on complex CAD geometries with analysis capabilities known from standard FEA. The main issues are the handling and coupling of trimmed patches during analysis. To enable isogeometric analysis on complex CAD geometries, various attempts have been made, which may be classified into *global* and *local* approaches according to Marussig and Hughes [16].

Global approaches aim at solving this issue on the geometry side by reconstructing the model, for instance by remodeling trimmed with untrimmed NURBS surfaces (see [16] and the references therein) or by using different (untrimmed, unstructured) spline technologies like subdivision surfaces [18–21] and T-splines [22–24]. *Local* approaches, on the contrary, aim at solving this issue on the analysis side by enhancing the analysis technology with features like numerical integration of trimmed NURBS elements, the application of weak coupling and boundary conditions along trimmed edges/faces, processing of topology information and probably numerical stabilization of small trimmed elements[3].

Global approaches may not require additional analysis capabilities, but again imply a kind of meshing step, which is not in the initial sense of IGA, and (at least small) deviations from the original geometry. And as in FEA, a "dead" analysis model, without a relation to the original CAD model and with a different data structure may be created, leading to the same synchronization problems. Nevertheless, compared to conventional FEA, a more accurate geometry, a basis of higher order and continuity, and thus higher solution accuracy can be achieved. The main drawback of using alternative unstructured spline technologies like T-splines for the reconstruction is expected to be the lacking support within standard CAD systems and exchange formats.

As mentioned above, *local* approaches require additional analysis capabilities not presented in conventional FEA, but ideally do not require model modifications. Adhering to the trimmed multi-patch NURBS model furthermore allows maintaining a consistent feature-based data structure throughout the design process. Still, for accurate and efficient analysis, the model has to follow certain guidelines, which need to be considered in the construction process and ideally also within the algorithms of CAD systems. All in all, trimmed NURBS-based B-Rep models are the quasi-standard in industrial CAD and there is no prospect of change any time soon. Thus, local approaches are expected to be the most promising way for achieving a full integration of design and analysis in the near future. Accordingly, the following section provides a more detailed review on isogeometric analysis of trimmed multi-patch NURBS models and, due to their prevalence, with a particular focus on shells.

[1] Only shell elements allow vehicle crash simulations with reasonable computing time.

[2] In Section 6.4 of this thesis, more details on a possible modeling approach including a parametrically connected midsurface as a result of the geometric design process are provided.

[3] Due to the fact that local approaches use trimmed geometries for which only a part of the discretized domain is considered as material, local approaches may be considered as closely related to immersed or fictitious domain methods.

1.2.2 Isogeometric shell analysis on trimmed multi-patch NURBS models

Numerical integration of trimmed elements

The numerical integration of trimmed NURBS elements is extensively studied in the literature, and various approaches more or less suitable for certain applications exist, see [16] and the references therein. An ideal integration approach for trimmed elements is robust (can handle any type of trimmed element), sufficiently accurate and efficient (requires a minimum number of integration points per trimmed element).

Most approaches aim at integrating the various types of trimmed elements exactly by introducing different forms of mappings to simple Gauss spaces, see [25–35]. Schmidt et al. [36] proposed a local reconstruction technique in which each trimmed element is remodeled by a single patch and then accordingly integrated. In [37, 38] resp. [39–41], quadtree- resp. octree-based sub-cell integration schemes originally developed for FCM [10, 42] are used to integrate trimmed NURBS shell and solid elements. A potential drawback of the sub-cell integration schemes with regard to large-scale explicit analysis is the high number of integration points around trimming curves, required for a good approximation of the integration domain, see [16, 42].

The approaches employed within this thesis are the point elimination algorithm proposed by Nagy and Benson [43] and the adaptive Gaussian integration procedure (AGIP) proposed by Breitenberger [32]. The former approach approximates trimming curves via polygons and generates a specific integration rule, optimized for efficiency, for each trimmed element. The latter uses the exact trimming curves, introduces additional mappings from the trimmed Gauss space to an untrimmed Gauss space and can thus handle all elements in an equal manner. More detailed descriptions of these two approaches are provided in Section 2.7. A broad overview on numerical integration schemes for trimmed elements can be found in [16].

Application of boundary and coupling conditions

The application of boundary and coupling conditions along trimmed edges is crucial for the analysis of trimmed multi-patch NURBS models. The difficulty lies in the fact that control points are in general not located on trimmed boundaries and that adjacent patches have non-matching discretizations. This prevents a direct node-by-node coupling and boundary conditions directly applied on individual control points. Potential alternatives are:

1. Enforcing (linear) coupling constraints analytically by expressing slave degrees of freedom (DOFs) as function of master DOFs, thus eliminating the constrained DOFs [44–46]. This approach is difficult, if not impossible, to apply in case of nonlinear constraints along trimmed edges.
2. Enforcing constraints in a strong sense (exactly) only at specified points along the boundary [28, 47]. Benson et al. [47] used a penalty approach to apply coupling conditions at specific points along arbitrary curves on surfaces and reported excellent accuracy. Wang et al. [28] used a Lagrange multiplier approach to couple trimmed patches at specified points along the coupling edge.
3. Applying boundary and coupling conditions in a weak integral sense, i.e. to enforce the constraint approximately over a certain domain. This is probably the most popular approach in the literature for trimmed and non-matching NURBS discretizations.

While the first approach can be considered as infeasible for nonlinear analysis of trimmed multi-patch shell structures, the second approach of enforcing constraints exactly at predefined points seems to be a viable pathway. However, enforcing constraints exactly at specific points between the generally non-congruent trimming curves of two intersecting NURBS surfaces, is again only an approximation and may introduce artificial stresses already in the initial undeformed state. Weak coupling approaches, on the other hand, are more tolerant with respect to geometrical deviations and are expected to yield smoother and more accurate solutions across coupling edges. The successful applications of weak coupling approaches to trimmed NURBS patches stated below may confirm this perception. The following discussion is therefore restricted to weak constraint enforcement approaches.

Weak coupling and boundary conditions

Within IGA, weak coupling and boundary conditions are commonly enforced via: (a) the Lagrange multiplier method, (b) the penalty method, (c) Nitsche's method [48] and (d) hybrid approaches of the former methods such as the augmented Lagrange multiplier method [49]. A lot of research regarding isogeometric analysis on multiple *non-matching* NURBS patches was conducted using penalty methods [30–32, 50–54], Lagrange multiplier or mortar-type methods [50, 52, 55–62] and Nitsche-type methods [37, 40, 41, 50, 63–70], and this list is not even complete.

Only a few of these approaches, however, also cover *trimming*. Trimmed multi-patch shell and membrane problems were successfully solved with Isogeometric B-Rep Analysis based on the penalty method [30–32, 52, 54] and the

Lagrange multiplier method [52]. Nitsche-type methods were used to couple trimmed NURBS patches in [37, 41, 66–68, 70] and to apply boundary conditions on trimmed edges in [40, 71, 72]. Especially relevant in the context of this thesis are the contributions by Guo et al. [37, 68, 70], in which Nitsche methods are used to couple trimmed NURBS-based rotation-free Kirchhoff-Love (KL) shells. The applicability of the developed Nitsche-type coupling approach to nonlinear problems and large multi-patch models (engine bonnet model) is shown in [68].

The focus of this thesis is on explicit isogeometric (crash) analysis. The question is, therefore, how well particular (domain decomposition) methods are applicable to explicit time integration schemes.

a. The Lagrange multiplier method in its original form introduces additional DOFs and equations to be solved. Moreover, the resulting system is no longer positive definite. According to Benson et al. [44], "The cost of enforcing constraints with Lagrange multipliers is prohibitive in explicit calculations due to the cost of solving linear systems of equations. Constraints are usually imposed approximately with penalty methods or they are eliminated analytically".

b. Penalty methods benefit from their simple formulation and efficiency, do not introduce additional DOFs, but require the definition of a sufficiently high penalty factor in order to obtain accurate results. In fact, excessively high penalty factors may lead to ill-conditioned stiffness matrices and, more relevant for this thesis, to a reduction in time step size within explicit schemes. Still, in explicit FEA, penalty methods prevail, mainly due to their simplicity and efficiency [44, 45].

c. Nitsche-type methods do not introduce additional DOFs or equations, the equation system remains positive definite, but require the determination of a penalty-like stabilization parameter which may vary during nonlinear analysis [68]. Moreover, the extension of Nitsche coupling to nonlinear analysis is reported to be not straightforward [68]. Also the computational cost per time step compared to penalty methods is a relevant aspect to be considered.

To the best of the author's knowledge, in the literature, none of these approaches has been assessed in explicit dynamic analysis of trimmed multi-patch NURBS models, especially not with respect to critical time step size and computational cost per time step.

Constraint formulations for shell coupling

Different types of constraint formulations for enforcing displacement continuity (C^0) and especially rotational continuity (G^1 continuity as a special case for smoothly joined shells)[4] between shells shall be discussed here, since the latter was found to be a crucial aspect for large deformation scenarios. For (vehicle) crash simulations of complex shell structures undergoing large deformations, in particular, rotational coupling constraints need to be able to handle (i) smooth and non-smooth shell interfaces, and (ii) arbitrarily large rotations. Enforcing displacement continuity is straightforward for all shell formulations, since the displacements on both edges can be simply enforced to be equal. For rotational continuity, several approaches for different shell formulations have been proposed.

For Reissner-Mindlin (RM) shells with rotational DOFs, the rotations on both edges can be directly enforced to be equal, which is especially straightforward for rotational DOFs in global coordinates [73]. However, this requires accurately computed control point rotations in the vicinity of (trimmed) edges. In explicit analysis in which rotational inertias are scaled such that their modes do not control the critical time step [73], this is not always guaranteed. For rotation-free Kirchhoff-Love shells, on the other hand, the rotational continuity between patches needs to be enforced via translational DOFs. Within Isogeometric B-Rep Analysis (IBRA) on rotation-free KL shells [30, 32], a local coordinate system is introduced along boundary edges. Based on a difference vector between the current and the initial shell normals at the boundary, the rotation around the edge tangent is computed and enforced to be equal on both edges. Due to the appearance of the *arcsin* function with a singularity at $\pi/2$, the edge tangent rotation is restricted to values smaller than $\pi/2$. This limitation is unfavorable for crash simulations including large deformations and accordion buckling modes. For Nitsche-type approaches, Guo and coworkers [37, 65, 68] enforced rotational continuity via constraints on the shell normals of both patches. As reported in [68], these rotational constraints are restricted to cases with G^1 continuity between patches and can therefore not deal with non-smooth patch interfaces.

In order to avoid such restrictions and singularities, Benson et al. [47] and more recently Herrema et al. [53] proposed rotational constraints, which are here referred to as *blended* constraint formulations. The main idea behind these blended formulations is to define the constraint as a sum of two sub-constraints, of which at least one is always non-singular. That is, singularities also appear in the sub-constraints at 0, $\pi/2$, etc., but never for both at the same angle. In case both sub-constraints are active, the overall constraint blends between both, hence the name *blended*

[4] The terms displacement and rotational continuity are adopted from [53].

constraint. In [47] also the angle φ between the unit normal vectors of both shells is considered, but the actual constraint is in fact on the sine of the difference between the initial and the current value of this angle $(\varphi - \varphi_0)$. By applying trigonometric addition theorems, this constraint is divided into two sub-constraints. In [53] the two sub-constraints are on the difference between initial and current scalar products of (i) unit shell normals and (ii) one unit shell normal and one in-plane unit vector normal to the boundary, respectively. Both formulations [47, 53] also hold for arbitrarily large absolute rotations, which makes these blended constraint formulations well-suited for crash-type problems with large deformations and non-smooth patch interfaces.

Analysis frameworks for trimmed multi-patch shell models

In order to achieve a fully integrated design-analysis workflow based on trimmed NURBS B-Rep models, all of the aforementioned analysis capabilities need to be covered. Additionally, all necessary information need to be consistently transferred between the CAD environment and the solver, which requires a suitable data exchange format that includes geometry, topology and analysis related data. In order to perform the analysis based on this data, the solver must be able to process topology information and to automatically establish connections between surface patches. There are basically two analysis frameworks that cover these capabilities and therefore allow direct analysis on trimmed multi-patch NURBS shell structures.

The first approach, developed by Breitenberger et al., is here referred to as the IBRA approach [30–32, 52]. Within IBRA, the available geometry and topology information from the B-Rep model are directly used to setup the analysis model. More precisely, so-called isogeometric B-Rep elements are introduced to couple topologically connected (trimmed non-matching) patches in a weak sense during analysis, or to apply weak Dirichlet boundary conditions. The dedicated IBRA exchange format proposed by Teschemacher et al. [52] allows for a consistent data transfer between the CAD system and the solver, see Section 6.2. The pre- and postprocessing tool TeDA (Tool to enhance Design by Analysis) [74] furthermore enables performing all steps of the development process within the CAD environment, see Section 6.1. The related publications [30, 32, 52] mainly used the penalty method to couple rotation-free Kirchhoff-Love shells. It should be noted, though, that the IBRA framework is not restricted to certain constraint enforcement methods or shell formulations.

The second approach proposed by Guo et al. [68] is similar, but uses the more common STEP (STandard for the Exchange of Product model data) format [75] for data transfer between CAD and solver. This approach is based on a rotation-free Kirchhoff-Love shell formulation and coupling of trimmed non-matching patches is achieved in a weak sense via a Nitsche-type method.

Both approaches have been successfully applied to nonlinear static shell problems and complex industry-type NURBS models in [30, 32] and [68]. However, none of them has been applied to explicit dynamic (crash-type) problems or problems including material plasticity and contact. Their accuracy, efficiency and robustness in such analysis scenarios is therefore still unknown.

1.2.3 Isogeometric analysis for explicit dynamics

Highly dynamic finite element analyses of large problems with strong nonlinearities like vehicle crash scenarios are primarily solved with explicit time integration schemes [45, 76]. Due to the conditionally stable nature of explicit schemes, the time step size is limited by a critical value. Also isogeometric analyses have already been performed with explicit time integration schemes, but several aspects remain to be answered.

Benson and coworkers [44, 73, 77] developed various NURBS-based shell formulations with and without rotational DOFs with a focus on explicit dynamics. Successful sheet metal forming and dynamic buckling simulations demonstrated the applicability of these shell formulations with higher order elements to large deformation explicit dynamic analysis. For explicit NURBS-based IGA, Hartmann and Benson [14] developed a suitable mass scaling approach as well a heuristic time step estimate accounting for polynomial degree and type of integration (reduced vs. full), see also Section 2.9.4. In [14], the authors performed an explicit sheet metal forming simulation with the NURBS-based Reissner-Mindlin shell developed in [73] and obtained a similar accuracy as with FEA, but with a two times larger element size and in only 40% of the FEA simulation time. These developments [14, 44, 73, 77] are only a few among many (also implicit) IGA features [43, 78–80] now firmly implemented and available in the commercial FEA/IGA solver LS-DYNA [45].

Adam et al. [81] developed a similar heuristic time step estimate for 1D rod and 2D plate problems in explicit IGA accounting for polynomial degree *and* continuity of the basis. In fact, the latter was found to have a significant influence on the critical time step size. They furthermore distinguished between different types of elements based on the varying shape of basis functions in open knot vector patches. This distinction is based on their finding that elements near the boundary of open knot vector patches possess a larger eigenfrequency and thus require smaller time steps. Besides mass scaling, the authors in [81] proposed two remedies to eliminate the time step

restricting effect of such boundary elements: (i) Increasing the size of elements near patch boundaries and (ii) using unclamped (non-open) knot vectors. However, the practical applicability of these remedies, especially in standard CAD programs is unclear. Moreover, the authors evaluated different time step estimates commonly used in explicit FEA and confirmed their applicability to explicit NURBS-based IGA.

Chan and Evans [82] studied discontinuous Galerkin (DG) isogeometric analysis with explicit time integration for wave propagation problems. The authors found that NURBS basis of higher continuity allow for larger time steps than C^0 NURBS and DG finite element discretizations. They furthermore studied the influence of knot positions within initially uniform open knot vector patches and found that a non-uniform distribution can increase the critical time step for explicit time integration schemes; in particular, larger knot spans at the patch boundaries. This finding and the suggestion to increase the size of elements at the patch boundaries by increasing knot spans is similar to what is reported in [81], where the element size is increased by moving control points.

Limbert et al. [83] used explicit time integration and rotation-free NURBS-based Kirchhoff–Love shells to solve dynamic membrane problems such as airbag inflation. They reported a similar accuracy, but with a lower number of DOFs compared to conventional finite element analysis. In his PhD thesis [84], Occelli described the implementation of LR (locally refined) B-spline *solid* elements including contact and stable time step estimates for explicit analysis into the commercial solver Radioss [85]. With this implementation, nonlinear dynamic benchmark problems including plasticity, large deformations and contact were successfully solved.

Several publications dealt with the development of novel mass matrix formulations and the aim to improve the accuracy or efficiency of explicit dynamic isogeometric analysis [86–88]. However, only the mass matrix suggested in [88] has diagonal form and therefore allows decoupling the equation system which only makes explicit analysis efficient for large problems.

Auricchio et al. [89] and more recently Evans et al. [90] and Marino et al. [91] solved explicit dynamic isogeometric problems with collocation methods, which require a minimum number of integration points and could therefore be an efficient alternative to Galerkin methods, especially for explicit analysis. The work from Schillinger et al. [92] provides a cost comparison between isogeometric collocation, isogeometric Galerkin and finite element Galerkin methods for an explicit Newmark predictor-multicorrector scheme with two corrector steps. It is worth noting that the aforementioned approaches use consistent [91], or a combination of consistent and lumped mass matrices in predictor multi-corrector schemes [89, 90, 92]. Overall, it seems that there is still much work left to do until collocation methods are applicable to large scale industrial problems including plasticity, large deformations and contact, such as vehicle crash simulations.

Finally, it should be noted that none of the aforementioned publications on explicit IGA considered trimming and that the author is not aware of any literature describing the influence of trimming on the critical time step in explicit isogeometric analysis.

1.2.4 Stabilization techniques for small trimmed elements

Trimming of regular tensor product NURBS patches generally yields small trimmed elements and consequently basis functions with only small support in the material/physical domain. Concomitant effects are small entries in the system matrices causing large condition numbers, control points with small mass and stiffness, as well as unstable solutions, whereby the term (in)stability is left undefined at this point. Similar issues are encountered whenever a domain discretization is not boundary-conforming, e.g. in meshfree methods, immersed boundary methods, fictitious domain methods, embedded domain methods, finite cell methods or however named. To overcome these issues, several stabilization techniques have been developed – some even specifically for IGA and B-spline bases. This section discusses relevant approaches in the context of IGA and FEA and especially with respect to their applicability to complex multi-patch NURBS models in explicit dynamic analysis. In the following, the problematic basis functions with small support[5] are referred to as unstable or degenerated basis functions.

Neglecting the contribution of small trimmed elements or basis functions with small support

The probably most straightforward approach to deal with small trimmed elements and basis functions with small support in the material domain is to simply neglect them during analysis, as done, for example in [71, 72, 93–95]. If the eliminated elements are small, the impact on the solution is negligible. In fact, there is always a trade-off between solution accuracy and stability/conditioning of the system and it will depend on the intention of the analysis whether certain elements or basis functions can be eliminated or not. Furthermore, the effect of element and DOF elimination on the accuracy of weak coupling and boundary conditions has to be considered. Embar et al. [71]

[5] The definition of *small* support is often problem dependent and linked to different criteria such as the location of basis function anchors or threshold values.

eliminated trimmed elements smaller than an area-fraction of 10^{-6}. In the context of CutIGA, Elfverson et al. [95] recently proposed an element selection procedure based on the energy norm of basis functions approximated via the diagonal elements in the stiffness matrix. Its simplicity and efficiency makes the elimination approach attractive for explicit analysis. It is, however, also worth noting that eliminating elements and basis functions requires full access to the corresponding solver routines and consistent bookkeeping.

Fictitious domain stiffness

Another common approach, especially within (isogeometric) FCM, is the application of a small stiffness in the fictitious (void) domain [42]. For this purpose, numerical integration is performed over the entire domain, while a factor commonly denoted as α differentiates between the material ($\alpha = 1$) and the fictitious domain ($\alpha = \varepsilon \ll 1$). The value ε is commonly chosen in the range of 10^{-4} to 10^{-14} [40–42] or estimated via material parameters [40]. The additional contributions from the fictitious domain increase the (arbitrarily) small matrix entries of basis functions with (arbitrarily) small support in the material domain and thus the conditioning. A detailed study on the convergence properties of FCM using such an extension into the fictitious domain is provided in [96]. In the context of trimmed NURBS patches with weakly enforced coupling and boundary conditions, this fictitious domain stiffness approach was successfully applied to linear elastic (thin) solid problems [40, 41] and (nonlinear) elastic shell problems [37, 68]. Potential drawbacks of this approach with regard to existing solver frameworks and explicit analysis are (i) the necessary ability to perform numerical integration over the fictitious domain and (ii) the increased computational cost (per time step) due to a higher number of integration points.

Scaling of basis functions / Preconditioning

With a focus on the (isogeometric) finite cell method, De Prenter et al. [97] developed a preconditioner to improve the condition number of system matrices. In order to eliminate the effect of trimmed basis functions with small support, the affected basis functions are scaled by the inverse of the square root of the diagonal system matrix entries. After solving the preconditioned system, the solution is projected back to the original system. In [98], De Prenter et al. generalized this preconditioning approach to systems which are not symmetric positive definite.

Already in 2008, Mößner and Reif [99] suggested a "skip-and-scale" strategy to stabilize a B-spline basis including B-splines with only small support in the physical domain. That is, depending on certain criteria, elements are either neglected (skipped) or appropriately normalized (scaled).

Recently, Buffa et al. [100] investigated the small support issue for Poisson problems solved with IGA on trimmed geometries and Nitsche's method. It is worth noting that they differentiated between (i) stability, in the sense of boundedness and coercivity of a bilinear form, and (ii) bad matrix conditioning. For the former, they suggested a stabilization technique that approximates the normal derivatives along trimmed boundaries. For the latter the authors applied a simple diagonal scaling as a kind of preconditioning. However, within explicit analysis, the term *stability* is defined differently and the applicability of the proposed approach to explicit IGA is unknown.

Basis function extension / Extended B-splines

A mathematically sound and elegant approach is the use of extended B-spline basis functions. Within this approach, unstable B-spline basis functions are substituted by extended B-splines, which are a subtle linear combination of adjacent stable B-spline basis functions. Extended B-splines were originally proposed by Höllig et al. in the context of the Weighted Extended B-spline (WEB) method [101–103], which uses weight functions (multiplied with the basis) to define the analysis domain within a non-boundary-conforming discretization. Also in this case, the basis was found to be unstable and extended B-splines were developed to solve this issue.

In the context of IGA, Höllig et al. [104] proposed a combination of the WEB method with IGA and Marussig et al. [34] demonstrated the effectiveness of extended B-splines within a collocated isogeometric Boundary Element Method (BEM). Rüberg and Cirak used extended B-splines to stabilize small cut elements for flow problems with moving boundaries [105] and fluid-structure interaction problems [106], in combination with Nitsche's method.

It is important to note that, as the name implies, extended B-splines are limited to B-spline basis functions and that NURBS-based models require special treatment [16, 34, 107]: One can either convert the NURBS-based model into a full B-spline-based model or use an independent field approximation, i.e. using a B-spline basis for the solution field and a NURBS basis for the geometry, which is not in accordance with the isoparametric concept [16, 34, 107]. Furthermore, extending B-splines requires a certain number of stable adjacent basis functions, e.g. in 2D $(p+1)(q+1)$ basis functions [16]. This can cause problems in case of very narrow and tapered patches, which are unavoidable in practical applications. Another aspect reported in the literature is that the length of the extrapolation should not be too high for accurate results [107]. Recently, Marussig et al. [107] used local refinement via THB-splines (Truncated Hierarchical B-splines) to overcome the two aforementioned issues. Finally, it should be noted that the modified

B-spline basis along trimmed boundaries also has to be considered when applying (weak) boundary and coupling conditions, which may require special attention.

A, to some extent, related approach for unfitted Lagrangian finite element methods are aggregation techniques, for example the one proposed by Badia et al. [108]. Herein, cut elements are appropriately merged with adjacent interior elements, forming so-called aggregates. Based on that, problematic DOFs are replaced by an extrapolation of DOFs from interior elements, yielding a new aggregated finite element space with improved conditioning properties. In [108], the applicability of this approach was demonstrated by solving the Poisson equation on 2D and 3D geometries.

Ghost penalty term

Within CutFEM, a fictitious domain finite element method, the issue of poorly conditioned system matrices due small cut elements, was solved by adding a ghost penalty term [109, 110]. This additional penalty term is reported to increase robustness, ensure optimal convergence properties and coercivity. In [110], Poisson, Laplace–Beltrami and Stoke's problems were solved with CutFEM in combination with Nitsche's method and the ghost penalty stabilization. However, later for CutIGA, the issue of small cut elements and ill-conditioned matrices was solved by eliminating problematic elements [72, 95], as already mentioned above.

Applicability of stabilization schemes to explicit dynamic analysis

To conclude, many attempts to stabilize basis functions with small support in the material domain have been made within IGA and FEA. But none of the aforementioned approaches was designed for the use in explicit methods in which (i) all DOFs can be decoupled (when using a lumped mass matrix), (ii) the system matrices are not assembled and (iii) no equation systems are solved. Thus, bad matrix conditioning is not the actual reason for stability problems in explicit analysis of trimmed models. Also the term *stability* is defined differently in explicit dynamics. Furthermore, none of the presented attempts has been applied to (a) *highly dynamic nonlinear* explicit isogeometric analysis and (b) *penalty-coupled* trimmed NURBS shell structures including material plasticity and contact. Therefore, their effectiveness in this context is unknown.

1.2.5 Practical considerations for an integrated IGA-based development process

This section is intended to close the state of the art review regarding explicit isogeometric analysis on industrial models with a brief overview on crucial practical aspects for an integrated IGA-based development process. This comprises attempts for an integrated IGA-based design-analysis workflow, a concise review on the (still limited) IGA activities within commercial software products and guidelines for IGA-suitable CAD modeling.

Attempts for an integrated IGA-based design-analysis workflow

In the literature, several attempts towards a fully integrated design and analysis workflow were made considering shells [30, 32, 52, 68, 111–113], membranes [31] and solids [84, 112, 114, 115]. Some attempts are based on NURBS [30–32, 52, 68, 111, 112, 114], others on LR (locally refined) B-splines [84] or T-splines [112, 115]. Most of these attempts used the CAD system Rhinoceros [116] together with dedicated pre- and postprocessing plug-ins for IGA [30–32, 52, 84, 111–115]. In [30, 32] an *analysis in computer aided design* (AiCAD) workflow was also realized using the CAD system Siemens NX [117]. These attempts are just prototypical implementations and not ready for productive usage in industry. Nevertheless, they demonstrate that it is technically feasible to perform pre- and postprocessing steps for IGA within the CAD environment, to first extract analysis-related data and to later import analysis results.

IGA implementations in commercial software

IGA capabilities have also been implemented into commercial solvers. Already in 2010, Benson et al. [73] implemented the first NURBS-based shell formulation via user-defined elements into LS-DYNA. Other shell formulations [44, 77], mass scaling approaches, time step estimates [14], and trimmed elements [43] followed. LS-DYNA therefore became the first commercial solver with firmly implemented IGA capabilities including the aforementioned features, various isogeometric shell and solid elements, unstructured spline technologies supported via the Bézier extraction format [118], different types of contact and basically all LS-DYNA material models [78–80]. Besides that, Elguedj et al. [114] and Lai et al. [115] implemented NURBS- and T-spline-based solid elements, respectively, via a user-defined element interface into Abaqus [119], while Occelli [84] implemented solid LR B-spline elements and isogeometric contact into Radioss [85].

From this overview one might get the impression that all necessary ingredients for an integrated IGA-based design-analysis process are in place, and that it is just a matter of time until such a process is realized in industry. But in fact, little effort has been made from CAD vendors to develop and provide appropriate design, pre-, and postprocessing

tools for commercial use. One reason may be the fact that the analysis industry is relatively small compared to the CAD industry. This is also a reason why separate preprocessor programs for FEA exist today at all. Nevertheless, the developers of the preprocessor ANSA recognized the potential of IGA and already implemented first IGA features [120], particularly aligned with the IGA features in LS-DYNA.

IGA-suitable CAD modeling

Another crucial aspect for an efficient, accurate and robust usage of IGA in industry are guidelines for IGA-suitable CAD modeling, similar to the FEA modeling guidelines successively developed over the last decades. In the literature, first attempts and IGA modeling recommendations can be found. In 2010, Cohen et al. [17] already emphasized that model quality criteria for IGA similar to mesh quality criteria for FEA are required and that such criteria may be even considered in CAD systems. They referred to this modeling philosophy as *analysis-aware* modeling for IGA. Cohen et al. [17] furthermore demonstrated the impact of different model parameterizations and knot vector definitions on the accuracy of analysis results. Similar considerations regarding analysis-aware modeling can be found in [111]. A few recommendations regarding NURBS-based models for explicit analysis are provided in [81], as already mentioned in the previous section. However, the author is not aware of more comprehensive and more practical investigations on isogeometric analysis model quality criteria for complex models. What is especially lacking are practical guidelines for trimming and patch coupling (e.g. trimming and coupling locations, shape of trimmed patches), as well as for explicit analysis (influencing factors on the critical time step size), which still need to be discovered.

1.3 Aims & Objectives

As described in the state of the art section above, several questions remain to be answered on the way towards a fully integrated design-analysis process for explicit isogeometric (crash) analysis on industrial models. This thesis aims at contributing to this overall goal by focusing on

- Shell structures, most widely used in vehicle crash and sheet metal forming simulations.
- Trimmed NURBS-based multi-patch models, the most common geometry description in industrial CAD.
- Weak penalty-based coupling and boundary conditions in the framework of Isogeometric B-Rep Analysis (IBRA).

This thesis therefore pursues a *local* approach for handling industrial CAD models within IGA. Having stated the focus of the thesis, the fundamental research question to be answered is:

How to achieve accurate, efficient and robust explicit dynamic isogeometric analyses on penalty-coupled trimmed NURBS shell structures in order to enable an integrated design-analysis process for vehicular crashworthiness?

This broad research question can be subdivided into four main aspects. In particular, the aims of this thesis are to

1. Extend the IBRA framework for trimmed NURBS-based multi-patch shell structures to explicit dynamics and Reissner-Mindlin shells with rotational DOFs.

   So far, IBRA including penalty-based B-Rep elements has only been applied to implicit static analysis of rotation-free Kirchhoff-Love shells. To enable crash-type simulations, IBRA shall be extended to explicit dynamic analysis within the commercial solver LS-DYNA. In order to capture the significant shear deformations appearing within vehicle crash simulations, IBRA shall also be extended to the Reissner-Mindlin (RM) shell theory; in particular to an RM shell formulation with six DOFs (three translations and three rotations) described in global coordinates as proposed by Benson et al. [73]. This requires the development of an accurate and robust B-Rep element formulation including rotational DOFs, applicable to large deformation and large rotation scenarios as well as non-smooth patch interfaces. Furthermore, it shall be investigated if, and under which conditions, explicit analyses of penalty-coupled trimmed NURBS shells are numerically stable. The final objective is to compute or at least estimate the corresponding critical time step size considering trimming and penalty-based B-Rep elements.

2. Identify and study factors influencing the critical time step size within explicit analysis of penalty-coupled trimmed NURBS shells and develop methods to increase the time step size.

   As mentioned in the state of the art section, elements at the boundaries of open knot vector patches restrict the critical time step. In this context, the first objective is to investigate whether trimming is a suitable mean

to eliminate this time step restriction. The second objective is to study the effect of trimming and especially the effect of small trimmed elements on the critical time step size, with a particular focus on the influence of varying polynomial degree and inter-element continuity of the underlying patch. Another crucial aspect within explicit analysis is the influence of weak penalty-based coupling and boundary conditions on the time step. Mass scaling is a common approach to increase the time step size in explicit analysis. Thus, it shall be studied whether mass scaling can be locally applied to specifically eliminate a possible time step reduction caused by weak penalty-based coupling and boundary conditions.

3. Stabilize trimmed control points with low mass and stiffness in explicit dynamic IBRA effectively and without a deterioration in accuracy and time step size.

   Small trimmed elements lead to basis functions with small support in the material domain and consequently to control points with small mass and stiffness. When solving equation systems, the main problem is the high condition number of the system matrices. Within explicit methods, the system matrices are not assembled and no equation systems are solved. Still, stability issues were observed. The first objective in the context of stabilization is therefore to identify the actual reason for instabilities in explicit analysis and to classify the type of instability. Stabilizing problematic control points first requires a suitable criterion to identify these control points prior to analysis. Finding such a criterion is the second objective. The third objective is to develop an effective stabilization scheme for highly dynamic explicit analysis that (i) can handle control points with masses and stiffnesses differing by orders of magnitudes, (ii) is compatible with weak penalty-based coupling and boundary conditions, (iii) does neither affect the critical time step size nor the solution accuracy, (iv) is applicable to complex industrial multi-patch NURBS models and (v) can be implemented into an existing solver environment. Finally, a suitable error measure for assessing the effectiveness of the proposed stabilization approach shall be developed.

4. Set up an integrated IBRA-based design and analysis process between commercial software programs.

   The integration of design and analysis with a focus on vehicular crashworthiness is the main motivation for this thesis. Accordingly, the possibility to set up an integrated design and analysis process between a commercial CAD and a commercial (explicit crash) solver shall be demonstrated. Using the IBRA framework comprising pre- and postprocessing tools for Rhinoceros as well as an appropriate data exchange format, the objective is to (i) extract the necessary geometry, topology and analysis information from the exchange format, (ii) convert the data into a solver-compatible format, (iii) implement B-Rep elements into the (explicit crash) solver LS-DYNA and (iv) convert analysis results into a suitable format for postprocessing in the CAD environment.

1.4 Overview

The remainder of this thesis closely follows the structure defined by the above aims & objectives. Chapter 2 provides the essential fundamentals, comprising the basic concepts of trimmed NURBS-based B-Rep CAD, differential geometry of trimmed surfaces, continuity and refinement within IGA. It furthermore gives a brief overview on shell theories required to appropriately extend the B-Rep element formulation from Kirchhoff-Love to Reissner-Mindlin shells, and describes the RM shell used within this thesis in more detail. It also provides information on the employed numerical integration procedures for trimmed elements, Isogeometric B-Rep Analysis (IBRA) – the basic idea this thesis builds upon – as well as on the corresponding penalty-based isogeometric B-Rep elements. Finally, this chapter introduces explicit dynamic analysis including the central difference scheme, stability conditions and common stable time step estimates.

Chapter 3 presents Explicit IBRA, the extension of IBRA to explicit dynamics and RM shells. This includes the required adaptations towards explicit dynamics as well as considerations on suitable B-Rep element formulations accounting for shear deformations and rotational DOFs. Basically two types of B-Rep edge element formulations are proposed in this chapter: The *standard* and the *enhanced* B-Rep edge element formulation for coupling, Dirichlet and Neumann conditions. The *enhanced* formulation enforces additional constraints on the shell normals, providing higher accuracy and extra robustness in highly dynamic large deformation scenarios. Control point forces and stiffness matrices are derived for all B-Rep edge element formulations. Finally, this chapter demonstrates under which conditions penalty-coupled trimmed NURBS shells yield stable explicit analyses and how to determine the critical time step size.

Chapter 4 deals with the stable time step size within Explicit IBRA, in particular with (i) trimming as a mean to eliminate the negative effect of elements at the boundary of open knot vector patches, (ii) the influence of trimming for varying polynomial degree and inter-element continuity and (iii) the effect of weak penalty-based coupling and boundary conditions. Theoretical considerations are supplemented with minimal numerical examples in one and

two dimensions. Furthermore, this chapter proposes a local selective mass scaling approach for penalty-based B-Rep elements.

Chapter 5 addresses stability issues encountered in highly dynamic analysis of models with small trimmed elements and proposes a suitable stabilization scheme. First, the actual reasons for the occurring instabilities in explicit dynamic analysis are studied, followed by the negative consequences on the analysis and a rough classification of the appearing instability. A detailed explanation of the proposed penalty-based stabilization scheme forms the core of this chapter. Subsequently, it is shown that the stabilization scheme does not affect the numerical stability of the overall analysis and that time step estimates are further on applicable. Finally, a suitable error measure is introduced and the effectiveness of the proposed stabilization scheme is demonstrated via minimal numerical examples.

Chapter 6 presents a prototypical implementation of an integrated CAD/CAE process based on IBRA and the corresponding exchange format, between the commercial CAD program Rhinoceros and the commercial (explicit crash) solver LS-DYNA. This chapter aims at highlighting the benefits compared to conventional CAD/CAE processes, namely a CAD environment for design, pre- and postprocessing, a uniform geometry description and a consistent feature-based data structure. It furthermore presents a brief overview on the employed IBRA exchange format with its various data extraction levels and aspects regarding the implementations via a user-defined interface into LS-DYNA. Finally, suggestions for analysis-aware CAD modeling are made.

In Chapter 7, the validity and effectiveness of Explicit IBRA and the corresponding developments is assessed by means of various well-selected benchmark examples, reaching from quasi-static linear elastic to highly dynamic nonlinear elasto-plastic shell problems including contact. These benchmark examples are solved on penalty-coupled trimmed multi-patch NURBS models and compared to results obtained from untrimmed NURBS or FEA models. Finally, the practical applicability of the Explicit IBRA framework is shown through dynamic analysis on two industrial models: the exterior skin and the reinforcement structure of a BMW engine bonnet, comprising up to 130 trimmed NURBS patches.

If considered useful, these chapters are closed with a brief summary. Chapter 8 summarizes the most important findings, developments and practical implications of this thesis, and finally provides suggestions for improvement and further research.

Chapter 2

Preliminaries

The aim of this chapter is to review fundamental concepts on which this thesis builds upon and to introduce the corresponding notation. This comprises the basics of Non-Uniform Rational B-Splines (Section 2.1), trimmed NURBS-based B-Rep CAD modeling (Section 2.2), differential geometry (Section 2.3), geometric continuity (Section 2.4) and specifically refinement within IGA (Section 2.5). In order to comprehend the developments proposed in subsequent chapters, Section 2.6 reviews shell analysis in general and the underlying Reissner-Mindlin shell formulation in particular. Furthermore, Section 2.7 describes the procedures deployed for the numerical integration of (trimmed) elements. Section 2.8 provides an overview on Isogeometric B-Rep Analysis (IBRA) and the concept of isogeometric B-Rep elements. Finally, Section 2.9 reviews explicit dynamic analysis, the central difference method, stability conditions, and common time step estimates – aspects that are all vital for this thesis.

2.1 Non-Uniform Rational B-Splines (NURBS)

Non-Uniform Rational B-Splines (NURBS) are the common technology to describe geometries in industrial CAD. NURBS are also the original basis for IGA [12] and the basis for the IBRA framework [30, 32], in which NURBS are used to describe both, geometry and displacement fields. In this section, only the basic concept of NURBS, required for the notation and subsequent definitions, is provided. More details on B-splines and NURBS can be found in [121–123]. Since NURBS are a generalization of B-splines, the concept of B-splines is described first and then extended to NURBS.

B-spline basis functions $N_{i,p}(\xi)$ are piecewise polynomial functions, uniquely defined through the knot vector Ξ and the polynomial degree p. The knot vector Ξ is defined as a set of non-decreasing parametric coordinates

$$\Xi = \{\xi_1, \xi_2, \dots, \xi_{n+p+1}\}, \tag{2.1}$$

where n is the number of B-spline basis functions associated with this knot vector. The so-called knots $\xi_i \leq \xi_{i+1}$ divide the parameter space into knot spans. In case of equidistant knot spans, a knot vector is called *uniform*, otherwise *non-uniform*. Non-zero knot spans $[\xi_i, \xi_{i+1}]$ define the elements for isogeometric analysis. A knot vector may also have multiple knot values, which has an effect on the shape and continuity of basis functions. That is, a knot value with multiplicity m_i reduces the continuity between elements to C^{p-m_i}. The continuity of the basis within an element, however, remains to be C^∞. For more information on the concept of continuity the reader is referred to Section 2.4. If the first and the last knot value have multiplicity of $p+1$, the knot vector is denoted as an *open* knot vector. With the Cox-de Boor recursion formula, B-spline basis functions are computed as

$$N_{i,0}(\xi) = \begin{cases} 1 & \text{if } \xi_i \leq \xi < \xi_{i+1} \\ 0 & \text{otherwise} \end{cases} \tag{2.2}$$

$$N_{i,p}(\xi) = \frac{\xi - \xi_i}{\xi_{i+p} - \xi_i} N_{i,p-1}(\xi) + \frac{\xi_{i+p+1} - \xi}{\xi_{i+p+1} - \xi_{i+1}} N_{i+1,p-1}(\xi). \tag{2.3}$$

By assigning a control point $\mathbf{P}_i$ to each basis function $N_{i,p}$, a B-spline curve $\mathbf{C}(\xi)$ of degree p is defined as

$$\mathbf{C}(\xi) = \sum_{i=1}^{n} N_{i,p}(\xi) \mathbf{P}_i. \tag{2.4}$$

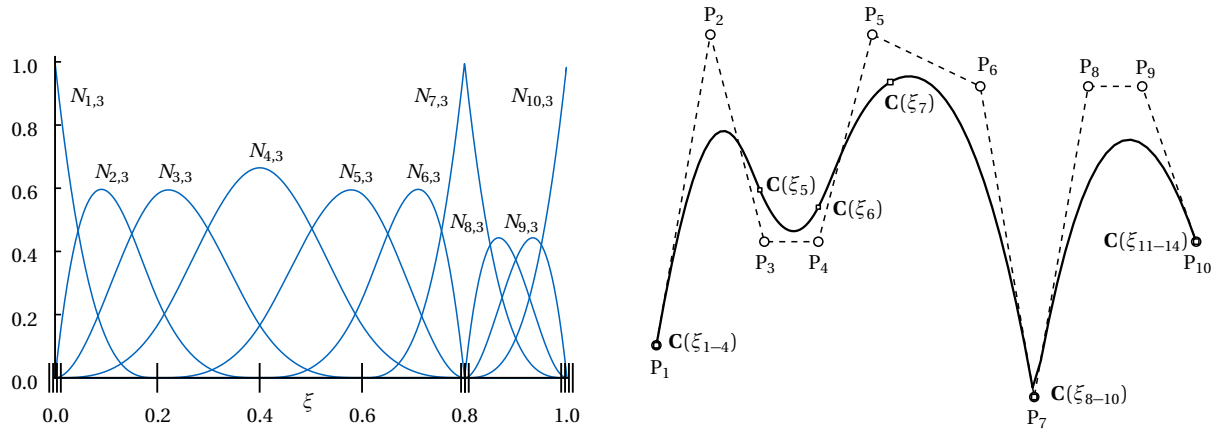

(a) Cubic B-spline basis functions: Knot values are indicated by vertical lines on the ξ-axis, also showing the multiplicity of a knot.

(b) Cubic B-spline curve with its control points (circles), control polygon (dashed lines) and knot values (squares).

Figure 2.1: Cubic B-spline curve in (a) and corresponding basis functions in (b) generated from the open knot vector $\Xi = \{0,0,0,0,0.2,0.4,0.6,0.8,0.8,0.8,1,1,1,1\}$.

An example of a cubic B-spline curve with the corresponding $n = 10$ basis functions is provided in Figure 2.1. This B-spline curve is generated from an open knot vector $\Xi = \{0,0,0,0,0.2,0.4,0.6,0.8,0.8,0.8,1,1,1,1\}$. Due to the fact that the knot value 0.8 has multiplicity $m_8 = 3$, the basis function $N_{7,3}$ is only C^0 continuous with a maximum value of one (see Figure 2.1a) and the B-spline curve is interpolatory at control point P_7. The piecewise linear connection of control points as shown with dashed lines in Figure 2.1b is denoted as the *control polygon*.

In order to allow for the exact description of a larger set of geometrical entities including conic sections, the concept of B-splines is generalized to NURBS. Introducing a weighting factor w_i for each control point $\mathbf{P}_i$ and normalizing the B-spline basis functions with a weighting function $W(\xi)$ yields the NURBS basis functions $R_{i,p}(\xi)$. A NURBS curve $\mathbf{C}(\xi)$ is then defined similarly to Eq. (2.4) as

$$\mathbf{C}(\xi) = \sum_{i=1}^{n} \frac{N_{i,p}(\xi) w_i \mathbf{P}_i}{W(\xi)} = \sum_{i=1}^{n} \frac{N_{i,p}(\xi) w_i \mathbf{P}_i}{\sum_{k=1}^{n} N_{k,p}(\xi) w_k} = \sum_{i=1}^{n} R_{i,p}(\xi) \mathbf{P}_i. \tag{2.5}$$

Extending B-spline and NURBS curves to surfaces is straightforward, as a surface is basically the tensor product extension in two parametric dimensions ξ and η with two knot vectors Ξ and $\mathcal{H}$. A B-spline surface $\mathbf{S}(\xi,\eta)$ is then given as

$$\mathbf{S}(\xi,\eta) = \sum_{i=1}^{n} \sum_{j=1}^{m} N_{i,p}(\xi) M_{j,q}(\eta) \mathbf{P}_{ij} = \sum_{A=1}^{nm} N_A(\xi,\eta) \mathbf{P}_A \tag{2.6}$$

with n basis functions $N_{i,p}$ of degree p in ξ-direction, m basis functions $M_{j,q}$ of degree q in η-direction and $n \times m$ control points $\mathbf{P}_{ij}$. For a more concise notation, the univariate basis functions $N_{i,p}$ and $M_{j,q}$ can be expressed as bivariate functions $N_A(\xi,\eta)$ associated with the control points $\mathbf{P}_A$. A NURBS surface $\mathbf{S}(\xi,\eta)$ can then be similarly described as

$$\mathbf{S}(\xi,\eta) = \sum_{A=1}^{nm} \frac{N_A(\xi,\eta) w_A \mathbf{P}_A}{\sum_{B=1}^{nm} N_B(\xi,\eta) w_B} = \sum_{A=1}^{nm} R_A(\xi,\eta) \mathbf{P}_A. \tag{2.7}$$

In the following, both B-spline and NURBS basis functions are denoted as N_A in order to conform with the familiar finite element notation.

2.2 Trimmed NURBS-based B-Rep CAD

As the name implies, *Isogeometric B-Rep Analysis (IBRA)* bases on the *B-Rep* modeling approach, the quasi-standard in industrial CAD. This section therefore provides a brief overview on the basics of trimmed NURBS-based B-Rep

CAD models. The term *B-Rep* stands for *boundary representation* and indicates the fact that a three-dimensional physical model is only represented by its outer boundary (skin) rather than by its complete volume. That is, the boundary representation separates the inside of an object from its outside.

The data structure of B-Rep models consists of two parts, namely (i) geometry data and (ii) topology data, which allows for a clear and definite model description [15, 16, 30]. While the geometry part describes (the shape of) surfaces (S), curves (C) and points (P), the topology part defines how the corresponding topological entities faces (F), edges (E), and vertices (V) are related to each other [15, 16, 30]. In a simplified manner, one can imagine faces as portions of surfaces, surrounded by sets of ordered edges, the so-called loops, and edges as segments of curves limited by two vertices [15]. In Figure 2.2 for instance, the two adjacent faces F_1 and F_2 are connected by their common edge E_2.

As described in the previous section, B-spline and NURBS surfaces (patches) rely on a tensor product structure, which limits the topology to rectilinear surfaces. To overcome this limitation in topological complexity, B-Rep surfaces are often trimmed [124]. The concept of trimming can be described as dividing a NURBS patch into visible $\mathbf{S}_{\text{visible}}$ and void domains $\mathbf{S}_{\text{void}}$ by means of trimming curves, see Figure 2.2a. To clearly define which part of the model is intended to be visible and which one to be void, connected trimming curves form a trimming loop with a specified orientation: a clockwise orientation indicates an inner loop, while a counter-clockwise orientation indicates an outer loop [125]. The trimming curves are usually defined in the parameter space (ξ,η) of the underlying surface patch, and often as B-spline or NURBS curves, see Eq. (2.8). A number of M trimming curves $\tilde{\mathbf{C}}_k(\tilde{\xi})$, as shown in Figure 2.2c, can be described as

$$\tilde{\mathbf{C}}_k(\tilde{\xi}) = \begin{Bmatrix} \xi_k(\tilde{\xi}) \\ \eta_k(\tilde{\xi}) \end{Bmatrix} = \sum_{i=1}^{n_k} N_{i,l}^k(\tilde{\xi})\, \tilde{\mathbf{P}}_i^k, \quad k = 1,2,\ldots,M, \tag{2.8}$$

with the trimming curve parameter $\tilde{\xi}$, the trimming curve parameters ξ_k and η_k in the parametric space of the patch, the polynomial degree l and the n_k control points $\tilde{\mathbf{P}}_i^k$ defined in the parametric space of the patch. The actual curves $\mathbf{C}_k(\tilde{\xi})$ in the physical space, which bound the visible surface domain $\mathbf{S}_{\text{visible}}$ as shown in Figure 2.2a, are then obtained by applying the surface mapping $\mathbf{S}(\xi,\eta)$ to the curves $\tilde{\mathbf{C}}_k(\tilde{\xi})$ as

$$\mathbf{C}_k(\tilde{\xi}) = \mathbf{S}(\xi_k(\tilde{\xi}),\eta_k(\tilde{\xi})) = \sum_{A=1}^{nm} N_A(\xi_k(\tilde{\xi}),\eta_k(\tilde{\xi}))\, \mathbf{P}_A, \quad k = 1,2,\ldots,M. \tag{2.9}$$

It is worth noting that trimming does not change the mathematical description of the underlying patch, it just considers certain domains in- or outside of trimming loops as void. This also applies to trimmed curves, limited by points.

Industrial B-Rep models generally consist of multiple intersecting surfaces, trimmed along intersection curves. Due to the fact that the resulting intersection curves can have excessively high polynomial degrees [126], an exact representation is, in general, practically infeasible. For this reason, both the intersection curve in the physical space and the two trimming curves in the corresponding patch parameter spaces are approximated by simplified curves, leading to small gaps and overlaps between intersecting patches [15, 16, 30]. A direct downstream analysis must therefore be able to deal with such non-watertight B-Rep models; as will be shown in Chapter 7, Isogeometric B-Rep Analysis is able to do so. More information on B-Rep modeling and trimming can be found in [15] and [16, 124, 125], respectively, and the references provided therein.

The focus of this thesis is on shell structures, which are characterized by the fact that one body dimension (shell thickness) is much smaller than the other two. The actual shell continuum is therefore reduced to a surface representation with an assigned wall thickness. In such case the B-Rep surface model describes the whole object rather than only its boundary, enabling a direct application of isogeometric B-Rep analysis. The IBRA framework including trimming and weakly enforced boundary conditions is, however, not restricted to shell structures and can be also extended to solids. This would then result in a methodology similar to the isogeometric Finite Cell Method (FCM), see for instance [42]. Compared to shell structures, though, some additional effort is required to generate a trivariate volume parametrization from the model boundary.

In the following, a trimmed B-Rep model shall be considered as the domain Ω composed of multiple subdomains $\Omega^{(a)}$ such that

$$\Omega = \bigcup_a \Omega^{(a)} \in \mathbb{R}^3. \tag{2.10}$$

Each of these subdomains $\Omega^{(a)}$ shall be described by a trimmed surface $\mathbf{S}_{\text{visible}}^{(a)}$ and its boundary $\Gamma^{(a)}$. This boundary described by $\partial\, \mathbf{S}_{\text{visible}}^{(a)}$ shall again consist of multiple curves such that

$$\partial\, \mathbf{S}_{\text{visible}}^{(a)} = \bigcup_k \mathbf{C}_k^{(a)} = \bigcup_k \partial\, \mathbf{S}_k^{(a)}. \tag{2.11}$$

The corresponding descriptions of $\Omega^{(a)}$ and $\Gamma^{(a)}$ in the surface parameter space are denoted as $\tilde{\Omega}^{(a)}$ and $\tilde{\Gamma}^{(a)}$, respectively.

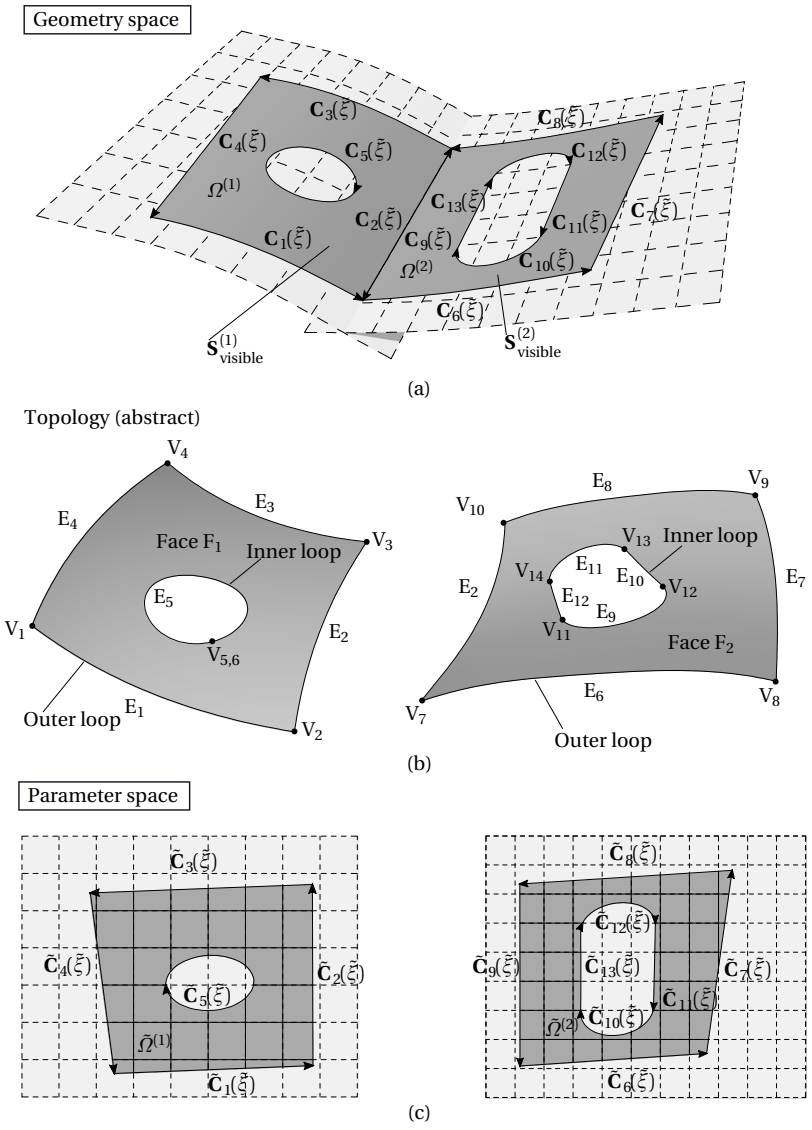

Figure 2.2: Trimmed surface B-Rep model represented in geometry space (a), as an abstract topology (b), and in parameter space (c). Figure taken from [54] in a slightly modified form.

2.3 Differential geometry of trimmed surfaces

To allow for a discussion on shell kinematics and mechanics, the basic concepts of differential geometry for surfaces, surface boundaries and trimming curves are provided in this section.

2.3.1 Surfaces

As stated in Eq. (2.7), a point on a surface $\mathbf{S}_{\text{visible}}$ in a 3D Euclidean space can be described by two parameters, see Figure 2.3. In particular, a point on a shell midsurface in the initial (undeformed) configuration shall be described by its position vector $\boldsymbol{X}(\Theta^1,\Theta^2)$ as a function of the parameters Θ^1 and Θ^2; the same applies to the position vector $\boldsymbol{x}(\Theta^1,\Theta^2)$ in the current (deformed) configuration. These parameters are defined as curvilinear, contravariant coordinates with the common notation Θ^1 and Θ^2 [30, 127]. The corresponding covariant bases $\boldsymbol{A}_1,\boldsymbol{A}_2$ in the initial and $\boldsymbol{a}_1,\boldsymbol{a}_2$ in the current configuration are defined as the tangent vectors along the Θ^α curves and obtained as the partial derivatives

with respect to the coordinates Θ^α:

$$\boldsymbol{A}_\alpha = \frac{\partial \boldsymbol{X}}{\partial \Theta^\alpha}, \quad \boldsymbol{a}_\alpha = \frac{\partial \boldsymbol{x}}{\partial \Theta^\alpha}, \tag{2.12}$$

where $\alpha \in \{1,2\}$. Based on the midsurface description, a material point in the shell body is described via a position vector $\boldsymbol{X}^*$ resp. $\boldsymbol{x}^*$ in the initial resp. current configuration as

$$\boldsymbol{X}^*(\Theta^1,\Theta^2,\Theta^3) = \boldsymbol{X}(\Theta^1,\Theta^2) + \Theta^3 \boldsymbol{D}_3, \qquad \boldsymbol{x}^*(\Theta^1,\Theta^2,\Theta^3) = \boldsymbol{x}(\Theta^1,\Theta^2) + \Theta^3 \boldsymbol{d}_3, \tag{2.13}$$

where Θ^3 is a contravariant coordinate in thickness direction along the shell director $\boldsymbol{d}_3$, that is, a line of constant Θ^1 and Θ^2. In the initial configuration and in case the deformed director $\boldsymbol{d}_3$ remains normal to the midsurface, the director coincides with the third basis vector ($\boldsymbol{D}_3 = \boldsymbol{A}_3$ and $\boldsymbol{d}_3 = \boldsymbol{a}_3$) defined as

$$\boldsymbol{A}_3 = \frac{\boldsymbol{A}_1 \times \boldsymbol{A}_2}{\|\boldsymbol{A}_1 \times \boldsymbol{A}_2\|}, \quad \boldsymbol{a}_3 = \frac{\boldsymbol{a}_1 \times \boldsymbol{a}_2}{\|\boldsymbol{a}_1 \times \boldsymbol{a}_2\|}. \tag{2.14}$$

The displacement vectors on the midsurface and in the shell body are then computed as

$$\boldsymbol{u}(\Theta^1,\Theta^2) = \boldsymbol{X}(\Theta^1,\Theta^2) - \boldsymbol{x}(\Theta^1,\Theta^2), \qquad \boldsymbol{u}^*(\Theta^1,\Theta^2,\Theta^3) = \boldsymbol{X}^*(\Theta^1,\Theta^2,\Theta^3) - \boldsymbol{x}^*(\Theta^1,\Theta^2,\Theta^3) \tag{2.15}$$

2.3.2 Surface boundaries

For subsequent discussions on coupling and boundary conditions, the differential geometry of surface boundaries and a corresponding orthonormal coordinate system are introduced, closely following the notation in [127]. As shown in Eqs. (2.8) and (2.9), a curve $\mathbf{C}(\tilde{\Theta})$ on a surface $\mathbf{S}$ may be described by a curve $\tilde{\mathbf{C}}(\tilde{\Theta})$ in the parameter space (Θ^1,Θ^2) of the surface[1]. This gives an implicit curve description $\mathbf{C}(\tilde{\Theta}) = \mathbf{S}(\Theta^1(\tilde{\Theta}),\Theta^2(\tilde{\Theta}))$ controlled by the curve parameter $\tilde{\Theta}$. By describing the surface boundary $\partial\,\mathbf{S}_{\text{visible}}$ in this way, a point on the surface boundary is obtained as $\boldsymbol{x}(\Theta^1(\tilde{\Theta}),\Theta^2(\tilde{\Theta}))$. An orthonormal coordinate system $(\boldsymbol{a}_\text{t}, \boldsymbol{a}_3, \boldsymbol{a}_\text{u})$ aligned with the surface boundary as depicted in Figure 2.3 can then be defined as follows. The first basis vector $\boldsymbol{a}_\text{t}$ pointing along the curve tangent is obtained by partially differentiating the implicit curve description with respect to $\tilde{\Theta}$, applying the chain rule and normalizing as

$$\boldsymbol{a}_\text{t} = \frac{\hat{\boldsymbol{a}}_\text{t}}{\|\hat{\boldsymbol{a}}_\text{t}\|}, \quad \hat{\boldsymbol{a}}_\text{t} = \frac{\partial \boldsymbol{x}}{\partial \tilde{\Theta}} = \frac{\partial \boldsymbol{x}}{\partial \Theta^1}\frac{\partial \Theta^1}{\partial \tilde{\Theta}} + \frac{\partial \boldsymbol{x}}{\partial \Theta^2}\frac{\partial \Theta^2}{\partial \tilde{\Theta}}. \tag{2.16}$$

The second basis vector is identified as the surface normal vector $\boldsymbol{a}_3$ already introduced in Eq. (2.14) as

$$\boldsymbol{a}_3 = \frac{\boldsymbol{a}_1 \times \boldsymbol{a}_2}{\|\boldsymbol{a}_1 \times \boldsymbol{a}_2\|}. \tag{2.17}$$

Based on that, the third basis vector, pointing away from the surface, is computed as the cross product of the previous two:

$$\boldsymbol{a}_\text{u} = \boldsymbol{a}_\text{t} \times \boldsymbol{a}_3. \tag{2.18}$$

The same of course applies to the initial configuration with $\boldsymbol{A}_\text{t}$, $\boldsymbol{A}_\text{u}$ and $\boldsymbol{A}_3$

2.3.3 Trimming curves in parameter space

Applying weak coupling and boundary conditions requires numerical integration along trimmed surface boundaries and hence trimming curve tangent vectors, see Section 2.8.3, Eqs. (2.39) and (2.37). The trimming curve definition $\tilde{\mathbf{C}}(\tilde{\xi})$ in Eq. (2.8) establishes the link between the trimming curve parameter $\tilde{\xi}$ and the surface parameters $(\xi,\,\eta)$ of a spatial point on a surface boundary $\partial\,\mathbf{S}_{\text{visible}}$. Differentiating $\tilde{\mathbf{C}}(\tilde{\xi})$ partially with respect to the trimming curve parameter $\tilde{\xi}$, the tangent vector in the parameter space is obtained as

$$\tilde{\boldsymbol{t}} = \begin{Bmatrix} \tilde{t}_1 \\ \tilde{t}_2 \end{Bmatrix} = \frac{\partial\,\tilde{\mathbf{C}}(\tilde{\xi})}{\partial\,\tilde{\xi}} = \begin{Bmatrix} \frac{\partial \xi}{\partial \tilde{\xi}} \\ \frac{\partial \eta}{\partial \tilde{\xi}} \end{Bmatrix}. \tag{2.19}$$

[1] There is no particular need to differentiate between the curve parameters $\tilde{\Theta}$ and $\tilde{\xi}$. However, here $\tilde{\Theta}$ is used to describe curves on surfaces and surface boundaries in the familiar differential geometry notation, while $\tilde{\xi}$ indicates trimming curves and general curve parametrizations.

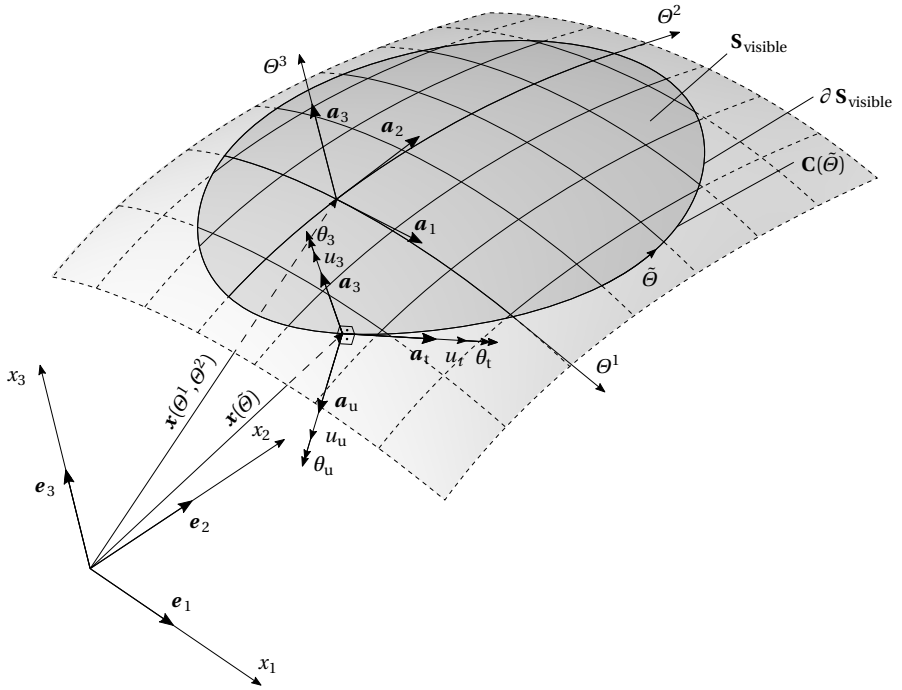

Figure 2.3: Differential geometry of trimmed surfaces, following [32, 127].

2.4 Geometric and parametric continuity

Since continuity plays a significant role in this thesis – be it the continuity between coupled NURBS patches or the continuity of the underlying basis functions – the concept of continuity shall be briefly explained here, see also [32, 123, 128]. In general one must differentiate between geometric and parametric continuity, which are also commonly interpreted as physical and mathematical continuity, respectively [123].

2.4.1 Geometric continuity

Geometric continuity can be easily explained by considering two curve segments $\mathbf{C}_1(\tilde{\xi})$ and $\mathbf{C}_2(\tilde{\xi})$ with $\tilde{\xi} \in [0,1]$. If the two curve segments are joined, i.e. if the end point of one curve ($\tilde{\xi}=1$) is equal to the starting point of the other curve ($\tilde{\xi}=0$), the resulting curve is G^0 continuous at the join:

$$\mathbf{C}_1(1) = \mathbf{C}_2(0). \tag{2.20}$$

If the curve tangent vectors at the join point into the same direction

$$\frac{\partial\,\mathbf{C}_1(1)}{\partial\,\tilde{\xi}} = c\,\frac{\partial\,\mathbf{C}_2(0)}{\partial\,\tilde{\xi}}, \tag{2.21}$$

the resulting curve is said to be G^1 continuous where the curve segments join. Please note that the constant $c>0$ indicates that the tangent vectors do not necessarily have the same magnitude.

2.4.2 Parametric continuity

Parametric continuity is indeed similar to geometric continuity, but more restrictive, i.e. parametric continuity implies geometric continuity, but not vice versa [123]. The only exception is C^0 continuity which is identical to G^1 continuity, see Eq. (2.20). For C^1 continuity, the curve tangent vectors do not only need to point into the same direction, they also need to have the same magnitude [123], leading to the condition

$$\frac{\partial\,\mathbf{C}_1(1)}{\partial\,\tilde{\xi}} = \frac{\partial\,\mathbf{C}_2(0)}{\partial\,\tilde{\xi}}. \tag{2.22}$$

More generally, a curve generated from two curve segments is regarded as C^n continuous if the nth derivatives of two curve segments at the join have the same direction and magnitude [123], yielding the condition

$$\frac{\partial^n \mathbf{C}_1(1)}{\partial \tilde{\xi}^n} = \frac{\partial^n \mathbf{C}_2(0)}{\partial \tilde{\xi}^n}. \tag{2.23}$$

2.4.3 Applications

The extension of geometric and parametric continuity from curves to surfaces is straightforward and requires the consideration of two parametric directions (ξ, η). The actual conditions for G^1 continuity of B-spline and NURBS surface imposed on control points can be found in [128].

In Chapter 3, G^0 and G^1 continuity between trimmed NURBS patches shall be enforced by means of penalty-based B-Rep edge elements. In Chapter 4, the effect of continuity of the underlying NURBS basis functions on the critical time step is studied.

2.5 Refinement in isogeometric analysis

Because of the variable order *and* continuity of the NURBS basis, IGA allows for a larger variety of refinement schemes than known from standard FEA. That is, instead of only varying the element size via h-refinement and varying the polynomial degree via p-refinement, IGA also allows for a variation in the continuity of the basis [12, 121]. Furthermore, the regular tensor product nature of NURBS patches in IGA, allows for (i) automatic refinement by relatively simple algorithms and (ii) refinement that neither alters geometry nor parametrization, see for instance [12, 121, 122]. This is a clear advantage over standard FEA on unstructured meshes.

Since Chapter 4 contains a detailed study on the influence of continuity on the critical time step size of trimmed NURBS models, the corresponding refinement schemes to create models of varying continuity shall be briefly reviewed here.

- Knot insertion: Inserting a knot at a new knot value, partitions an existing element into two elements. If this new knot is only inserted once, the continuity of the basis at this knot is C^{p-1}. Because of a possibly higher continuity, knot insertion is not identical to h-refinement known from FEA, which always leads to C^0 continuity. To reproduce h-refinement exactly, the new knot needs to be inserted p times.
- Order elevation: Order elevation allows increasing the polynomial order of a basis with an arbitrary degree of continuity. Order elevation is indeed similar to the known p-refinement from FEA, but without the restriction of an initial basis with C^0 continuity. Thus, p-refinement can be considered as a special case of order elevation in which the continuity is always C^0.
- k-refinement: This new type of refinement allows increasing the order *and* continuity of a basis, which is not possible in standard FEA.

The simple example in Figure 2.4 demonstrates the difference between p- and k-refinement. Starting point for both types of refinement is the single-element knot vector $\Xi = \{0, 0, 4, 4\}$ for $p = 1$, in which knots at three distinct positions 1, 2 and 3 are inserted with a multiplicity depending on the type of refinement. Within p-refinement in Figure 2.4a, each knot value is inserted p times, where p is the desired polynomial degree, followed by order elevation. In that way a four element patch with C^0 continuity across element boundaries is achieved for all p. Within k-refinement in Figure 2.4b, on the other hand, order elevation is performed on the single-element knot vector. Only afterwards, new knots with multiplicity $m_i = 1$ are inserted, leading to a four element patch with C^{p-1} continuity across element boundaries. One can furthermore see that for p-refinement the number of basis functions per each element, and thus also the number of control points per each element, increases by one as the degree is increased by one. Within k-refinement, on the contrary, only the total number of basis functions and control points increases as the degree is increased by one. This shows that p-refinement leads to a much denser control point distribution and a much higher number of DOFs than k-refinement. More detailed information on the different refinement schemes for NURBS can be found in [12, 121, 122].

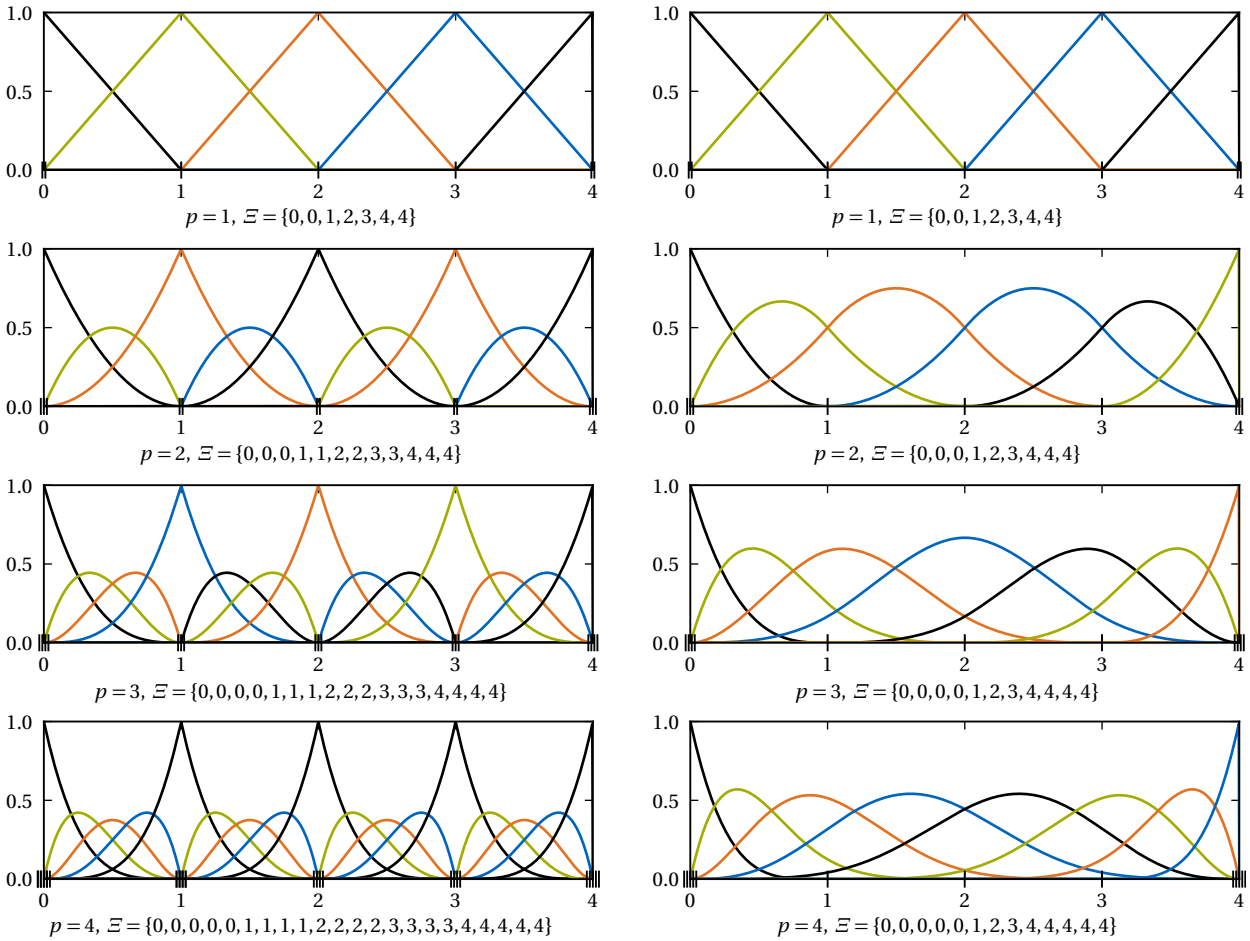

(a) p-refinement. (b) k-refinement.

Figure 2.4: Comparison between p-refinement (a) and k-refinement (b) for p=1 to 4.

2.6 Shell analysis

Since extending IBRA from Kirchhoff-Love (KL) to shear deformable Reissner-Mindlin (RM) shells is a core aspect of this thesis, the fundamental assumptions, kinematics and differences of both shell theories are briefly discussed in Section 2.6.1. More detailed descriptions can be found in [49, 127, 129]. Section 2.6.2 furthermore provides a concise overview on the formulation and implementation of the NURBS-based RM shell from Benson et al. [73] used within this thesis.

2.6.1 Shell theories

For beam and shell structures, kinematic and kinetic assumptions are made. Among a vast number of specific theories, the two most common theories are referred to as the Euler-Bernoulli theory and the Timoshenko theory for beams, and the Kirchhoff-Love theory and the Reissner-Mindlin theory for shells.

The main assumptions for the Euler-Bernoulli beam theory and the Kirchhoff-Love shell theory are: (i) straight cross-sections remain straight and (ii) normals remain normal to the midsurface. Thus, transverse shear strains are neglected. This is regarded as a good assumption for relatively thin beams and shells.

The main assumptions for the Timoshenko beam theory and the Reissner-Mindlin shell theory are: (i) straight cross-sections remain straight, but (ii) normals do not necessarily remain normal to the midsurface. Thus, transverse shear strains are accounted for, which is vital for rather thick beams and shells.

In Section 2.3, a material point $\boldsymbol{x}^*(\Theta^1,\Theta^2,\Theta^3)$ in the shell body is described by a midsurface position vector $\boldsymbol{x}(\Theta^1,\Theta^2)$ and the coordinate Θ^3 in thickness direction along the director $\boldsymbol{d}_3$. The director is crucial for the shell kinematics and a distinguishing characteristic between the Kirchhoff-Love and Reissner-Mindlin shell theories. A direc-

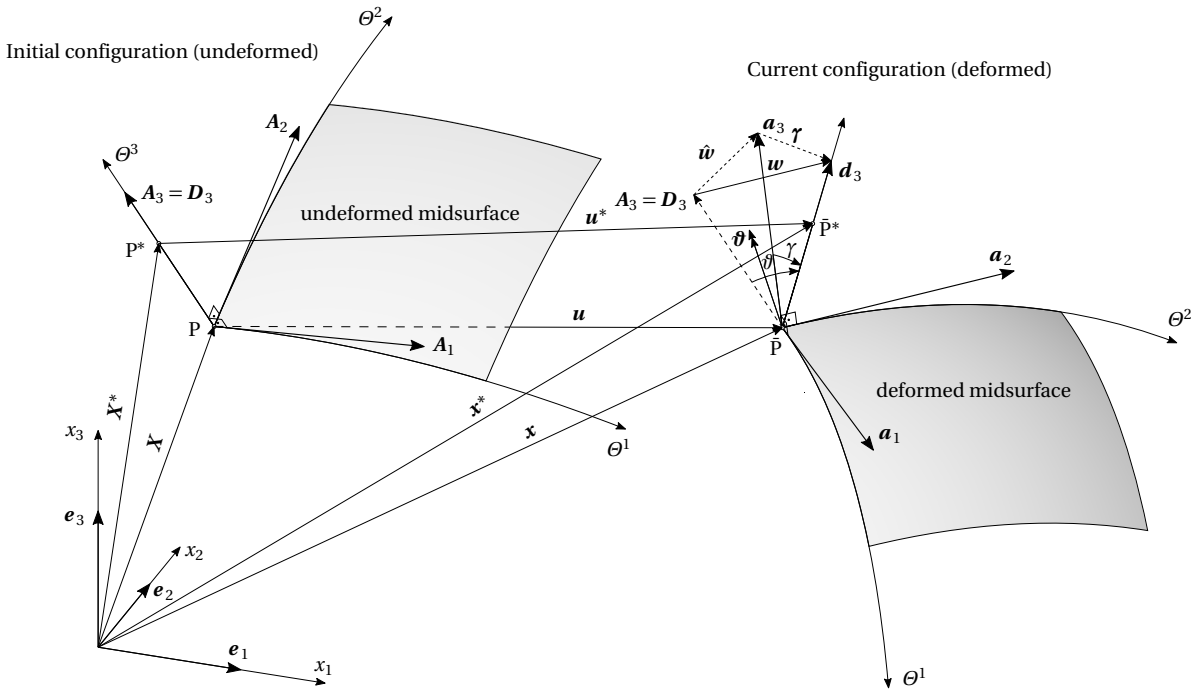

Figure 2.5: Kinematics of a shear deformable Reissner-Mindlin shell, following [127].

tor $\boldsymbol{d}_3(\Theta^1,\Theta^2)$ is defined as a unit vector pointing into the direction of material points initially normal to the midsurface at point $\boldsymbol{x}(\Theta^1,\Theta^2)$. Thus, the initial director $\boldsymbol{D}_3$ coincides with the initial unit normal vector $\boldsymbol{A}_3$, independent of the underlying shell theory. As stated above, for KL shells shear deformations are neglected and normals are assumed to remain normal to the midsurface; therefore $\boldsymbol{d}_3 = \boldsymbol{a}_3$ always holds. The kinematics of an RM shell are different as depicted in Figure 2.5: Due to shear deformations, the director $\boldsymbol{d}_3$ deviates from $\boldsymbol{a}_3$ by the shear angle γ. Since both $\boldsymbol{d}_3$ and $\boldsymbol{a}_3$ are of unit length, γ can, for small values, be determined as

$$\gamma = \|\boldsymbol{\gamma}\| = \|\boldsymbol{d}_3 - \boldsymbol{a}_3\|, \tag{2.24}$$

where $\boldsymbol{\gamma}$ (in bold) is the difference vector between $\boldsymbol{a}_3$ and $\boldsymbol{d}_3$, see also Figure 2.5. The difference vector $\hat{\boldsymbol{w}}$ and the corresponding rotation vector $\hat{\boldsymbol{\vartheta}}$ and rotation angle $\hat{\vartheta}$ (not depicted in Figure 2.5) between the unit normal vectors $\boldsymbol{a}_3$ and $\boldsymbol{A}_3$, uniquely defined by the midsurface displacement $\boldsymbol{u}(\Theta^1,\Theta^2)$, can be determined via

$$\hat{\boldsymbol{w}} = \boldsymbol{a}_3 - \boldsymbol{A}_3 = \hat{\boldsymbol{\vartheta}} \times \boldsymbol{a}_3. \tag{2.25}$$

Based on this, the director displacement vector $\boldsymbol{w}$ and the director rotation vector $\boldsymbol{\vartheta}$ are defined as

$$\boldsymbol{w} = \boldsymbol{d}_3 - \boldsymbol{A}_3 = (\boldsymbol{d}_3 - \boldsymbol{a}_3) + (\boldsymbol{a}_3 - \boldsymbol{A}_3) = \boldsymbol{\gamma} + \hat{\boldsymbol{w}} = \boldsymbol{\vartheta} \times \boldsymbol{a}_3. \tag{2.26}$$

To distinguish translational from rotational motion, the displacement of a material point in the shell body can be described as

$$\boldsymbol{u}^* = \boldsymbol{u} + \Theta^3 \boldsymbol{w} = \boldsymbol{u} + \Theta^3(\boldsymbol{\vartheta} \times \boldsymbol{a}_3). \tag{2.27}$$

From this decomposition one can see that the translational part $\boldsymbol{u}$ requires the three midsurface displacements u_i as free variables, while the rotational part $\boldsymbol{\vartheta}$ is uniquely defined by two independent parameters in case the drilling rotation around the director is neglected [129]. Thus, *five* independent parameters are required to describe RM shell kinematics. For KL shells Eq. (2.27) also holds, when neglecting the shear contribution $\boldsymbol{\gamma}$ in $\boldsymbol{w}$. However, the rotational part then only consists of the unit normal rotation given in (2.25), which is uniquely defined by the midsurface displacement $\boldsymbol{u}(\Theta^1,\Theta^2)$, leading to only *three* independent variables for KL shells [129].

This difference can also be seen in the number of boundary conditions to be prescribed for a shell, which is crucial for the derivation of patch coupling conditions within this thesis. Considering the surface boundary coordinate system

described by $\boldsymbol{a}_\mathrm{t}, \boldsymbol{a}_3$ and $\boldsymbol{a}_\mathrm{u}$ as depicted in Figure 2.3, RM shells require in total *five* boundary conditions[2] for the three translations of the shell midsurface and the two rotations around $\boldsymbol{a}_\mathrm{t}$ (bending) and $\boldsymbol{a}_\mathrm{u}$ (twisting), respectively (see Basar and Krätzig [127], pages 122–123). The drilling rotation around $\boldsymbol{a}_3$ is usually neglected. For KL shells, on the contrary, the twisting rotation around $\boldsymbol{a}_\mathrm{u}$ is not a free, prescribable variable, due to the absence of shear deformations. For this reason, only *four* boundary conditions may be prescribed for KL shells [127].

2.6.2 A Reissner-Mindlin shell formulation with rotational DOFs

In this thesis, IBRA is extended from KL to RM shells and from implicit static to explicit dynamic analysis. To achieve this, the Explicit IBRA framework [54] relies on the explicit dynamic isogeometric (crash) features of LS-DYNA [78, 79]. Therefore the isogeometric Reissner-Mindlin shell with rotational DOFs developed by Benson et al. [73], now available in LS-DYNA, is used for Explicit IBRA. Although Explicit IBRA can also be applied to other shell formulations, the shell formulation from [73] is exclusively considered within this thesis and described next.

This shear deformable NURBS-based shell formulation relies on the degenerated solid approach by Hughes and Liu [130], see also [45]. It is based on an updated Lagrangian formulation and uses corotational coordinate systems defined at the integration points. The principle of virtual power[3] with internal, external and kinetic terms for the three-dimensional degenerated solid is given as

$$\delta P = \delta P^{\mathrm{int}} - \delta P^{\mathrm{ext}} + \delta P^{\mathrm{kin}} = \int_V (\boldsymbol{\sigma} : \delta \boldsymbol{D}) \,\mathrm{d}V - \left(\int_{\Gamma_V} \boldsymbol{t} \cdot \delta \boldsymbol{v} \,\mathrm{d}\Gamma_V + \int_V \boldsymbol{b} \cdot \delta \boldsymbol{v} \,\mathrm{d}V \right) + \int_V \rho \boldsymbol{a} \cdot \delta \boldsymbol{v} \,\mathrm{d}V = 0, \tag{2.28}$$

with the Cauchy stress $\boldsymbol{\sigma}$, the traction $\boldsymbol{t}$, the body force $\boldsymbol{b}$, the mass density ρ, the velocity $\boldsymbol{v}$, the acceleration $\boldsymbol{a}$, the volume V, the surface area Γ_V and the virtual velocity $\delta \boldsymbol{v}$. The virtual rate of deformation $\delta \boldsymbol{D}$ is computed as

$$\delta \boldsymbol{D} = \frac{1}{2}(\delta \boldsymbol{L} + \delta \boldsymbol{L}^T), \quad \boldsymbol{L} = \frac{\partial \boldsymbol{v}}{\partial \boldsymbol{x}}, \tag{2.29}$$

with the spatial velocity gradient $\boldsymbol{L}$. By using a linear through-thickness interpolation, a spatial point $\boldsymbol{x}(\xi)$ of the shell body in the current (deformed) configuration is defined in a discretized way equivalent to Eq. (2.13) as

$$\boldsymbol{x}(\xi) = \sum_A N_A(\xi, \eta) \left(\mathbf{x}_A + \frac{h_A}{2} \zeta \hat{\mathbf{y}}_A \right). \tag{2.30}$$

The parametric coordinates $\boldsymbol{\xi} = \{\xi, \eta, \zeta\}^T$ comprise the in-plane coordinates ξ and η, and the out-of-plane coordinate $\zeta \in [-1, 1]$. The control point coordinates are denoted as $\mathbf{x}_A$, the shell thickness as h_A, and the director (or unit fiber vector) as $\hat{\mathbf{y}}_A$. Similar to Eq. (2.27), where the overall motion is divided into a translational and a rotational part, the velocity $\boldsymbol{v}$ is described as a function of the translational velocity $\mathbf{v}_A$ and the angular velocity $\boldsymbol{\omega}_A$ at the control points,

$$\boldsymbol{v}(\xi) = \sum_A N_A(\xi, \eta) \left(\mathbf{v}_A + \frac{h_A}{2} \zeta \boldsymbol{\omega}_A \times \hat{\mathbf{y}}_A \right). \tag{2.31}$$

In the following, the control point force vector and the stiffness matrix are given in a generalized form, including translational and rotational parts, identified by the superscripts υ and ω, respectively. Please note that the stiffness matrix is actually not required for the explicit analysis, but for the considerations on time step size based on the maximum eigenfrequency in Chapter 4, as well as for the stabilization approach presented in Chapter 5. The generalized residual force $\bar{\mathbf{f}}$ computed from the stresses can then be given as

$$\bar{\mathbf{f}} = \begin{Bmatrix} \mathbf{f}^\upsilon \\ \mathbf{f}^\omega \end{Bmatrix} = - \int_V \begin{bmatrix} (\mathbf{B}^\upsilon)^T \\ (\mathbf{B}^\omega)^T \end{bmatrix} \boldsymbol{\sigma} \,\mathrm{d}V, \tag{2.32}$$

where the Cauchy stress tensor is represented as a vector in Voigt form, $\boldsymbol{\sigma} = \{\sigma_{11}, \sigma_{22}, \sigma_{33}, \sigma_{12}, \sigma_{23}, \sigma_{31}\}^T$, and the strain-displacement matrices $\mathbf{B}^\upsilon$ and $\mathbf{B}^\omega$, see [73].

[2] It should be noted that for each condition either traction forces (moments) or displacements (rotations) can be described, not both.

[3] Despite the fact that the derivations in Chapter 3 are based on the principle of virtual work, the principle of virtual power is used in this section in order maintain the notation from [73]. Nonetheless, by substituting the virtual velocity $\delta \boldsymbol{v}$ with a virtual displacement $\delta \boldsymbol{u}$, the virtual power terms can be easily transformed into virtual work terms.

The generalized material tangent stiffness matrix is then defined as

$$\overline{\mathbf{K}} = \begin{bmatrix} \mathbf{K}^{\nu\nu} & \mathbf{K}^{\nu\omega} \\ \mathbf{K}^{\omega\nu} & \mathbf{K}^{\omega\omega} \end{bmatrix} = \int_V \begin{bmatrix} (\mathbf{B}^{\nu})^T \\ (\mathbf{B}^{\omega})^T \end{bmatrix} \boldsymbol{C} \begin{bmatrix} \mathbf{B}^{\nu} & \mathbf{B}^{\omega} \end{bmatrix} \mathrm{d}V, \tag{2.33}$$

where $\mathbf{K}^{\nu\nu}$, $\mathbf{K}^{\omega\omega}$, and $\mathbf{K}^{\nu\omega}$ denote the translational, rotational, and mixed contributions, respectively, and where $\boldsymbol{C}$ is the material tangent constitutive matrix. To allow for efficient explicit analysis through decoupled equations of motion, the mass matrix is lumped through row summing, which gives the control point mass as

$$\mathrm{M}_A = \int_V \rho N_A \,\mathrm{d}V = h \int_\Omega \rho N_A \,\mathrm{d}\Omega, \tag{2.34}$$

with $\mathrm{d}V = h\mathrm{d}\Omega$, where h and $\mathrm{d}\Omega$ are the shell thickness and the differential surface area, respectively. The rotational control point inertia is computed as a function of the control point mass

$$\mathrm{J}_A = \kappa \frac{h^3}{12} \int_\Omega \rho N_A \,\mathrm{d}\Omega = \kappa \frac{h^2}{12} \mathrm{M}_A. \tag{2.35}$$

The scaling factor κ is chosen such that the rotational modes do not restrict the critical time step size [73]. Finally, some remarks on the shell implementation, relevant for the coupling formulations in Chapter 3 shall be mentioned.
Remark 2.1: Although, as stated in the previous section, five DOFs are sufficient to describe the kinematics of RM shells, this shell formulation is based on a six DOF implementation with three translational and three rotational DOFs. According to [73] this choice is motivated by a computationally simpler usage of angular velocities in global coordinates. Moreover, for practical non-smooth models, finite element shell formulations with six DOFs and element-wise directors are commonly used, since this facilitates the treatment of kinks and intersections [129]. However, on smooth surfaces the three rotational DOFs cause singularities in the drilling stiffness (rotation around director $\hat{\mathbf{y}}_A$). To eliminate this singularity, a small amount of drilling stiffness is introduced, see [73].
Remark 2.2: For explicit analysis, the rotational inertias are scaled with κ such that the rotational modes do not restrict the critical time step size, see also [14, 45, 73, 131, 132]. This may lead to significantly higher rotational inertias, directors significantly deviating from the shell normal and thus artificial thinning [73]. To avoid this, the director (fiber vector) $\hat{\mathbf{y}}_A$ is not updated via angular velocities, but instead identified as the unit normal vector computed from translational DOFs [73]. Angular velocities are only used to evaluate the strain rate in Eq. (2.29) via the velocities in Eq. (2.31).
Remark 2.3: In LS-DYNA currently two variants of this shell formulation are available, which differ in the way the shell normals are defined. The first variant is the one described in [73], where the shell normals are associated with control points. The second variant evaluates the normals at integration points and computes the director $\hat{\mathbf{y}}_A$ via the so-called *lifting operator* method as described in [77]. This ensures exact normals at the integration points and superior results.

More details on this shell formulation can be found in the related publications [45, 73, 77, 130].

2.7 Numerical integration of trimmed elements

As described in [12], untrimmed elements can be numerically integrated with standard Gaussian quadrature rules. The numerical integration of trimmed elements, on the contrary, requires more sophisticated methods. At present, numerous different approaches can be found in the literature, thoroughly summarized in the review paper by Marussig and Hughes [16], see also Section 1.2.2. The integration method primarily used within this thesis is the so-called *Adaptive Gaussian Integration Procedure (AGIP)* developed by Breitenberger [32], see also [52], which allows for a uniform treatment of trimmed and untrimmed elements. Considering surface elements defined by non-zero knot spans $\xi \in [\xi_s, \xi_e]$ and $\eta \in [\eta_s, \eta_e]$, the corresponding surface area $|\Omega_\mathrm{e}|$ is computed as

$$|\Omega_\mathrm{e}| = \int_{\Omega_\mathrm{e}} \mathrm{d}\Omega = \int_{\xi_\mathrm{s}}^{\xi_\mathrm{e}} \int_{\eta_\mathrm{s}}^{\eta_\mathrm{e}} J_1 \,\mathrm{d}\xi \mathrm{d}\eta = \int_{\mathcal{G}} J_1 J_2 \,\mathrm{d}\mathcal{G} = \sum_{l=1}^{n_\mathrm{qp}} J_1 J_2 w_l^A = \sum_{l=1}^{n_\mathrm{qp}} J_1 \tilde{w}_l, \tag{2.36}$$

where w_l^A denotes the quadrature weight, $\tilde{w}_l = J_2 w_l^A$ the quadrature weight including the deformation-independent Jacobian J_2 and n_qp the number of quadrature points. The Jacobians J_2 and J_1 and the corresponding mappings from the Gauss to the parameter space and from the parameter to the geometry space are depicted in Figure 2.6. The Jacobian J_1 is defined as

$$J_1 = \left\| \frac{\partial \boldsymbol{x}}{\partial \xi} \times \frac{\partial \boldsymbol{x}}{\partial \eta} \right\| = \left\| \boldsymbol{a}_1 \times \boldsymbol{a}_2 \right\|, \tag{2.37}$$

and the Jacobian J_2 as

$$J_2 = \left| \frac{\partial \xi}{\partial \xi_\mathcal{G}} \frac{\partial \eta}{\partial \eta_\mathcal{G}} \right| \quad \text{or} \quad J_2 = \left| \frac{\partial \xi}{\partial \eta_\mathcal{G}} \frac{\partial \eta}{\partial \xi_\mathcal{G}} \right| \quad \text{(depending on the rotation)}, \tag{2.38}$$

where $\xi_\mathcal{G}$ and $\eta_\mathcal{G}$ are the coordinates in the Gauss space. With Eq. (2.36), both untrimmed and trimmed elements can be integrated. While untrimmed elements employ the standard Gaussian quadrature point locations and weights, trimmed elements require some additional treatment, described as follows. First, the relevant trimming curve segments and trimming curve control points of a trimmed element are appropriately mapped from the parameter space to the Gauss space. This mapping may involve shifting, scaling and rotating and is defined such that the trimming curve segment can be described by the parameter $\xi_\mathcal{G}$ in the Gauss space, see the highlighted element in Figure 2.6. This kind of mapping is only feasible if the trimmed element fulfills the following requirements: (i) not more than one assigned decoupled and not closed trimming curve segment, and (ii) the trimming curve segment must not have undercuts in at least one of the two parametric directions [32]. If this is not the case, the integration domain is bisected accordingly, until both requirements are fulfilled. Based on this, an auxiliary NURBS surface $\hat{\mathbf{S}}$ is generated in the Gauss space. This auxiliary surface $\hat{\mathbf{S}}$ in the Gauss space is then treated as an untrimmed element in the geometry space. That is, $\hat{\mathbf{S}}$ is mapped into a pseudo parameter space and then into an untrimmed Gauss space, where $(p+1)\times(q+1)$ standard Gaussian quadrature points (ξ_l, η_l) with weights w_l are generated. The two additional mappings represented by $\hat{J}_1$ and $\hat{J}_2$ are equivalent to (2.37) and (2.38). Applying the inverse mappings to these Gauss points finally yields the desired quadrature point locations (ξ_l^A, η_l^A) and the weights $w_l^A = \hat{J}_1 \hat{J}_2 w_l$ in the original trimmed Gauss space. For more details on AGIP the reader is referred to [32], pages 87–95, and [52].

As previously stated, many different numerical integration approaches for trimmed elements are available in the literature; the AGIP described above is one of them. It gives exact results, but can lead to a rather high number of quadrature points in case the integration domain needs to be bisected multiple times. In comparison to that, the standard in explicit finite element crash simulations is using one integration point per linear element. Even if IGA permitted a significantly lower number of elements in total, the numerical efficiency of current finite element analyses would be hard to reach. Another approach, developed with a focus on efficiency, is the point elimination algorithm proposed by Nagy and Benson [43]. This algorithm is based on a polygonal trimming curve approximation and optimizes the number, location and weight of integration points specifically for each trimmed element, while fulfilling the moment-fitting equation up to a prescribed tolerance. That is, an optimization problem is solved for each trimmed element in a preprocessing step. Compared to AGIP, the point elimination algorithm can be considered as more efficient, but its accuracy depends on the quality of the trimming curve approximation and the predefined tolerance for the moment-fitting equation. The numerical examples in Chapter 7 are solved with AGIP, except for the energy absorbing tube and the industrial examples, which use the point elimination algorithm.

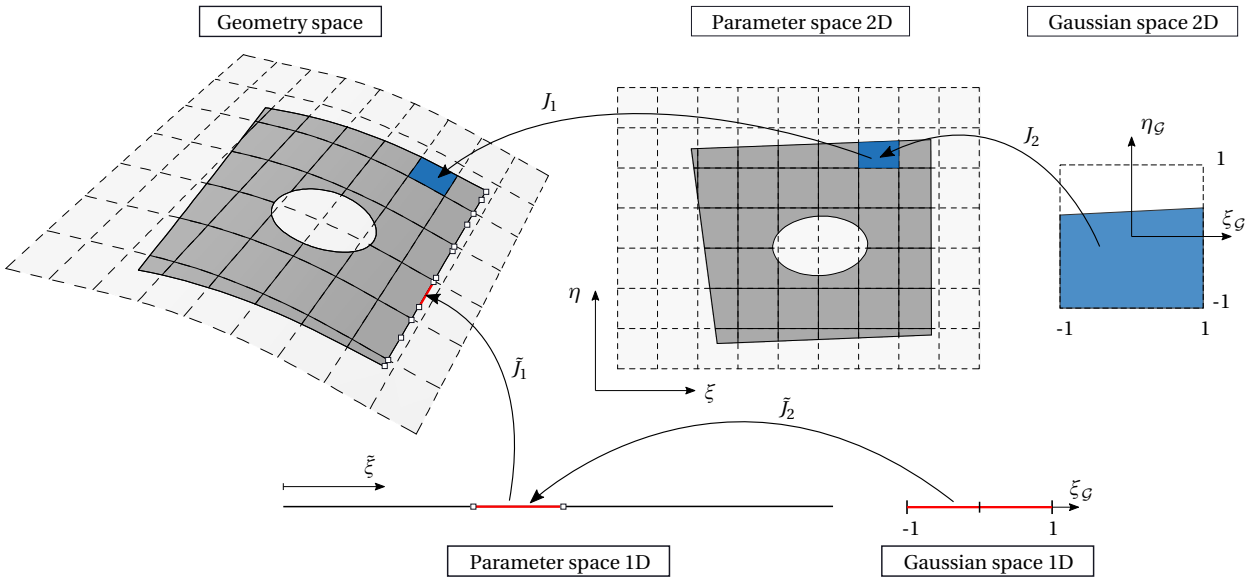

Figure 2.6: Mappings involved in the numerical integration of 2D surface and 1D B-Rep edge elements, taken from [54] in a slightly modified form.

2.8 Isogeometric B-Rep Analysis (IBRA)

Isogeometric B-Rep Analysis developed by Breitenberger et al. at the Chair of Structural Analysis of the Technical University of Munich [30, 32], is the essential basis of this thesis. This section therefore provides the most important concepts of IBRA including (i) the numerical integration of trimmed elements, (ii) the definition of isogeometric B-Rep elements for the weak enforcement of coupling and boundary conditions, and (iii) penalty-based B-Rep element formulations for Kirchhoff-Love shells as described in the original work on IBRA [30, 32].

2.8.1 Overview

Isogeometric B-Rep Analysis was the first methodology that allowed performing structural shell analysis directly on trimmed NURBS-based multi-patch models used in industrial CAD. To achieve a full integration of design and analysis, IBRA uses both geometry and topology information directly from B-Rep CAD models, i.e.

- NURBS basis functions (possibly refined) to describe both the geometry and the displacement field of the simulation model,
- trimming curves to separate a patch into material and void domains, and to define the integration domains,
- topology information including faces, (common) edges and vertices, to establish coupling and boundary conditions.

Another characteristic of IBRA is that coupling and boundary conditions along trimmed edges are enforced in a weak, integral sense via so-called B-Rep elements, for instance with a penalty approach. In addition to that, the IBRA framework also includes

- pre- and postprocessing plug-ins (TeDA) [74] for the CAD programs Rhino [116] and Siemens NX [117],
- a sophisticated data exchange format to transfer all required information including material and simulation-specific parameters, between CAD and analysis [52].

This actually allows setting up a closed design-analysis workflow between the CAD program and the solver, without the need for manual user interaction outside the CAD environment. More detailed information on TeDA and the IBRA exchange format is provided in Chapter 6.

2.8.2 Numerical integration of trimmed elements

A robust, accurate and reasonably efficient numerical integration procedure is an essential building block for IBRA. Among other integration methods like the *Nested Jacobian Approach* [30], the Adaptive Gaussian Integration Procedure (AGIP) [32] presented in Section 2.7 is the current method of choice within IBRA. For Explicit IBRA [54], however, also the Point Elimination Algorithm from Nagy et al. [43] was shown to be a well-suited integration procedure for trimmed NURBS elements. More information on numerical integration is provided in Section 2.7.

2.8.3 Isogeometric B-Rep elements

When dealing with the analysis of trimmed multi-patch models, the challenging task is to enforce continuity between and boundary conditions on trimmed patches. The difficulty lies in the fact that (i) adjoining patches generally have non-matching discretizations and that (ii) control points are not directly located on trimming curves, so a direct DOF-wise enforcement is not possible. Alternative ways to enforce constraints are described in Section 1.2.2.

Within IBRA, coupling and boundary conditions are enforced in a weak integral sense. This involves the numerical solution of integral terms along the coupling or boundary domains (in general topological B-Rep entities) for instance with standard quadrature rules. In order to achieve accurate results, the numerical integration is not performed over the entire boundary domain, but over finite domains. That is, the B-Rep entity is subdivided into finite elements, the so-called isogeometric B-Rep elements or just B-Rep elements for short. Depending on the dimension of the boundary domain and the type of boundary condition to be enforced (point, curve or surface), isogeometric B-Rep elements can take the form of zero-dimensional vertex, one-dimensional edge or two-dimensional face elements. A favorable aspect of B-Rep elements is that no additional control points or basis functions are introduced. Instead, a B-Rep element acts upon the existing control points and basis functions with non-zero support on the B-Rep element domain, see Figure 2.7.

The different types of B-Rep elements are very similar and basically only differ by the dimension of their integration domain. In the following, the focus is on B-Rep *edge* elements, since enforcing one-dimensional curve boundary

conditions along edges is the most important case for shell analysis. In accordance with the description given above, a B-Rep edge element is then defined as a subdomain Γ_e of a trimming curve $\mathbf{C}_k(\tilde{\xi})$ in the geometry space or equivalently as a subdomain $\tilde{\Gamma}_e$ of a trimming curve $\tilde{\mathbf{C}}_k(\tilde{\xi})$ in the parameter space of the underlying patch, as depicted in Figure 2.7.

A well-suited definition of the spatial extent of B-Rep elements is the following: Start ($\tilde{\xi}_\mathrm{s}$) and end points ($\tilde{\xi}_\mathrm{e}$) of a B-Rep edge element are defined at (i) intersections of the trimming curve $\tilde{\mathbf{C}}_k(\tilde{\xi})$ with master and slave knot lines and (ii) knot values of the underlying trimming curve. In case of boundary conditions, the slave side is omitted and the identification of start and end points is straightforward. For coupling conditions, on the other hand, mappings from the slave to the master patch parameter space are required, realized via a closest point projection in the geometry space. Figure 2.8 depicts this process of subdividing a coupling edge into B-Rep elements, denoted as *clipping* in [32]. The start and end points $\tilde{\xi}_\mathrm{s}$ and $\tilde{\xi}_\mathrm{e}$, respectively, are then given as parameters of the master curve. A more detailed description of this operation can be found in [32].

One can compute the length of a B-Rep edge element as

$$|\Gamma_\mathrm{e}| = \int_{\tilde{\xi}_s}^{\tilde{\xi}_e} \tilde{J}_1 \,\mathrm{d}\tilde{\xi} = \int_{-1}^{1} \tilde{J}_1 \tilde{J}_2 \,\mathrm{d}\xi_{\mathcal{G}}, \tag{2.39}$$

where $\tilde{J}_2$ and $\tilde{J}_1$ are the Jacobians of the mappings from the Gaussian space $\mathcal{G}$ to the trimming curve parameter space and from the trimming curve parameter space to the geometry space, respectively, as shown in Figure 2.6. The Jacobian $\tilde{J}_1$ is defined as

$$\tilde{J}_1 = \left\| \frac{\partial \boldsymbol{x}}{\partial \tilde{\xi}} \right\| = \left\| \frac{\partial \boldsymbol{x}}{\partial \xi} \frac{\partial \xi}{\partial \tilde{\xi}} + \frac{\partial \boldsymbol{x}}{\partial \eta} \frac{\partial \eta}{\partial \tilde{\xi}} \right\| = \left\| \boldsymbol{a}_1 \tilde{t}_1 + \boldsymbol{a}_2 \tilde{t}_2 \right\| \tag{2.40}$$

and the Jacobian $\tilde{J}_2$ as

$$\tilde{J}_2 = \frac{\partial \tilde{\xi}}{\partial \xi_{\mathcal{G}}}. \tag{2.41}$$

Due to the required approximations described in Section 2.2, the master and slave curves ($\mathbf{C}_k^\mathrm{m}(\tilde{\xi})$ resp. $\mathbf{C}_l^\mathrm{s}(\tilde{\xi})$) in the geometry space, which are described by the curves $\tilde{\mathbf{C}}_k^\mathrm{m}(\tilde{\xi})$ and $\tilde{\mathbf{C}}_l^\mathrm{s}(\tilde{\xi})$ in the corresponding parameter spaces, do not necessarily coincide. The numerical integration is therefore always performed along the master side, which implies the determination of quadrature points on the master curve. The default choice in this thesis is $p_\mathrm{max}+1$ Gauss points per B-Rep edge element, where $p_\mathrm{max} = \max\{p^\mathrm{m}, q^\mathrm{m}, p^\mathrm{s}, q^\mathrm{s}\}$ with the polynomial degrees p resp. q in ξ- resp. η-direction of the master and slave patches. The evaluation of slave basis function values and derivatives, however, still requires integration points on the slave patch. These integration points are determined from the integration points of the master patch, again via mappings and closest point projections in geometry space.

For a clear distinction between different domains and boundary conditions, the boundary domain is in the following assumed to consist of the subsets $\Gamma_\mathrm{C}^{(a)}$, $\Gamma_\mathrm{D}^{(a)}$, and $\Gamma_\mathrm{N}^{(a)}$ for coupling, Dirichlet, and Neumann conditions, respectively. The same applies to $\tilde{\Gamma}^{(a)}$ with the subsets $\tilde{\Gamma}_\mathrm{C}^{(a)}$, $\tilde{\Gamma}_\mathrm{D}^{(a)}$, and $\tilde{\Gamma}_\mathrm{N}^{(a)}$.

2.8.4 Penalty-based B-Rep element formulation

This section describes the penalty-based B-Rep element formulation for rotation-free KL shells proposed in the original work on IBRA [30, 32]. This will later on in Chapter 3 help pointing out the distinct features and main novelties of the B-Rep element formulation for RM shells with rotational DOFs proposed in this thesis and [54]. The B-Rep edge element formulation is based on the boundary terms of the weak form for KL shells, see for instance [32] and[127], given as

$$\delta W = \int_\Gamma \left(\boldsymbol{n} \cdot \delta \boldsymbol{u} + \boldsymbol{m}_\mathrm{t} \cdot \delta \boldsymbol{\theta}_\mathrm{t} \right) \mathrm{d}\Gamma \tag{2.42}$$

$$= \int_\Gamma \left(n_\mathrm{t} \delta u_\mathrm{t} + n_\mathrm{u} \delta u_\mathrm{u} + n_3 \delta u_3 + m_\mathrm{t} \delta \theta_\mathrm{t} \right) \mathrm{d}\Gamma, \tag{2.43}$$

where $\boldsymbol{n}$ and $\boldsymbol{m}$ denote traction forces and moments, respectively, and where the indices t, u and 3 indicate the directions of a local coordinate system along a (trimming) curve $\mathbf{C}_k(\tilde{\xi})$ as shown in Figure 2.3. From Eq. (2.42) one can identify three translational terms in all three directions (t, u, 3), and one rotational term around the t-direction. This means that for KL shells three translational and one rotational boundary conditions may be described. As will be shown in Section 3.2, this is different for shear deformable RM shells. In order to only enforce rotational coupling

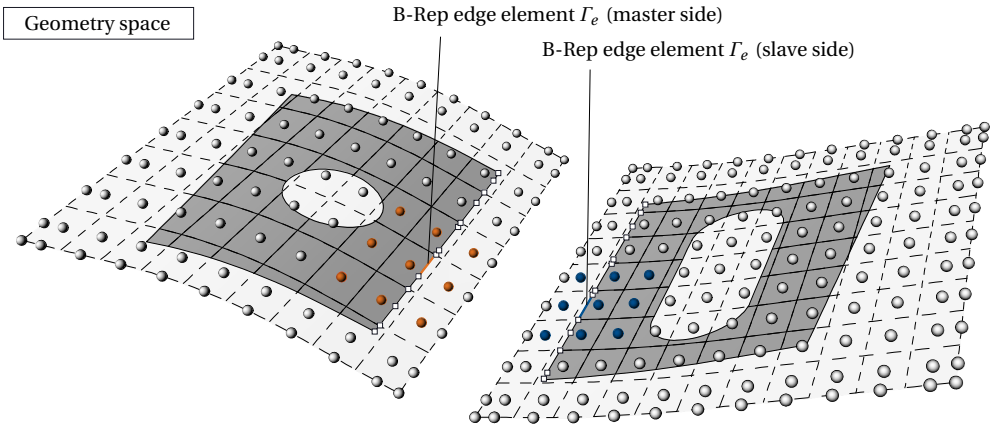

(a) B-Rep edge elements on master and slave side of two coupled trimmed patches in geometry space. One B-Rep edge element together with the involved master and slave control points are highlighted in orange and blue, respectively.

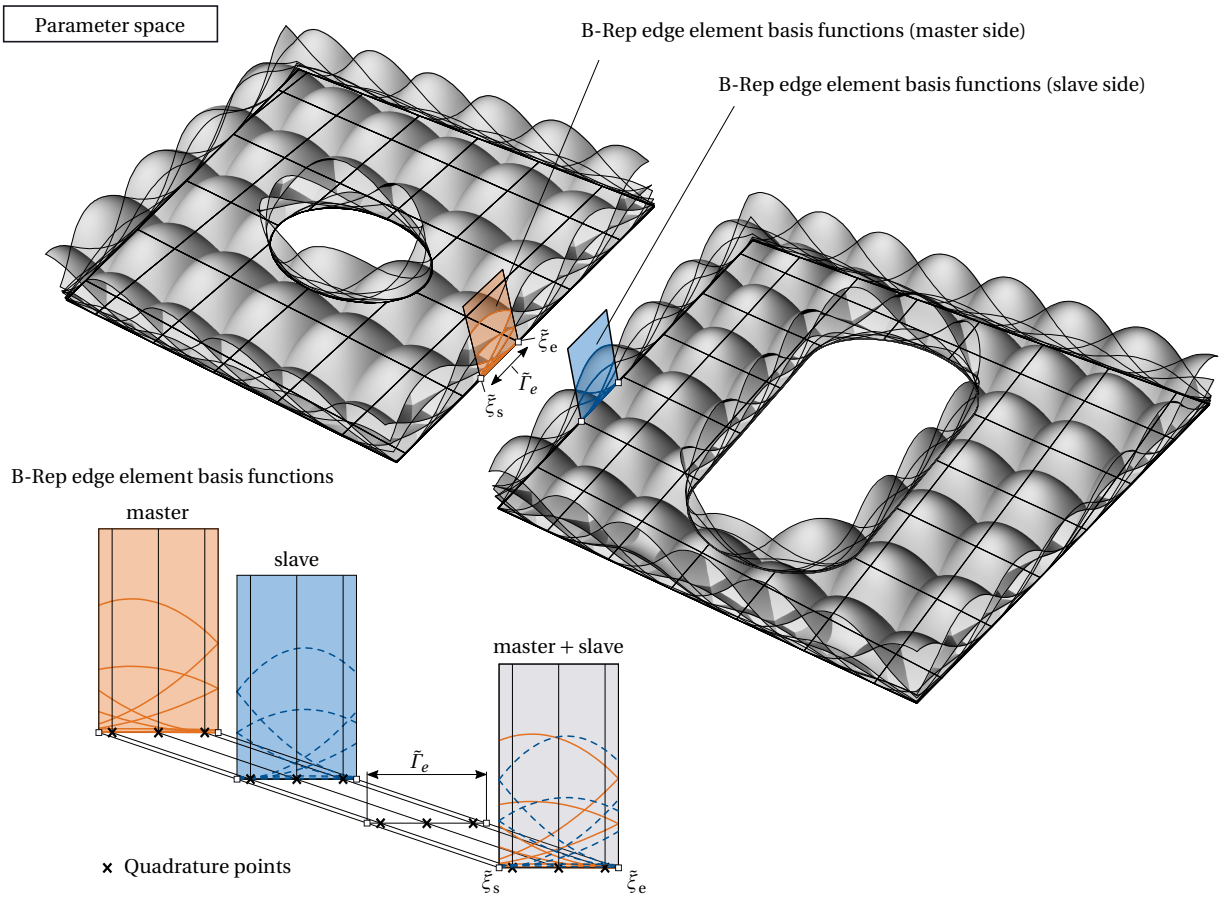

(b) Basis functions of the two trimmed patches in parameter space. The basis functions corresponding to the highlighted B-Rep edge element master and slave control points in (a) are displayed in orange and blue, respectively.

Figure 2.7: Definition of B-Rep edge elements [54].

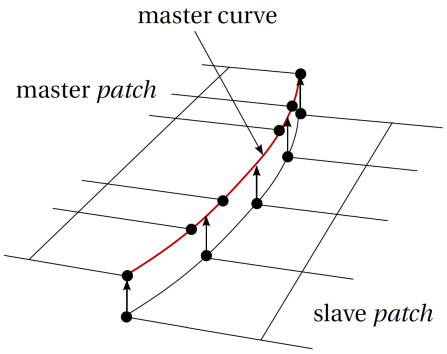

(a) Closest point projection of slave curve parameters onto the master curve.

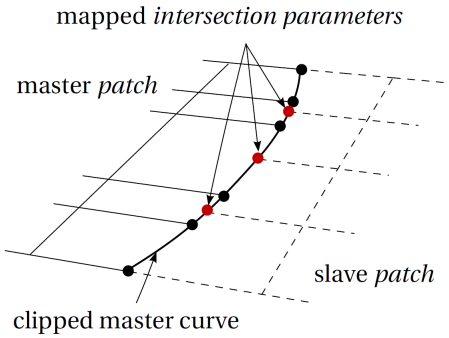

(b) Clipped master curve: all intersections are defined by parameter values of the master curve.

Figure 2.8: Clipping operation including closest point projections, taken from [32].

conditions around the t-direction, a corresponding local coordinate system along edges is required, see Figure 2.3. Moreover, the Kirchhoff-Love shell [133] employed in the original version of IBRA [30, 32] has no rotational DOFs. The rotation θ_t around $\boldsymbol{a}_\mathrm{t}$ is, for each patch, therefore computed via the displacement vector $\boldsymbol{w}$ between the initial and current unit normal vector $\boldsymbol{A}_3$ and $\boldsymbol{a}_3$ as described in Eqs. (2.25) and (2.26).

Internal coupling conditions

For the case of internal coupling conditions between two (trimmed) patches, the traction forces must fulfill the equilibrium

$$\boldsymbol{n} = \boldsymbol{n}^\mathrm{m} = -\boldsymbol{n}^\mathrm{s}, \quad \text{with} \quad \boldsymbol{n} = n_\mathrm{t}\boldsymbol{a}_\mathrm{t} + n_\mathrm{u}\boldsymbol{a}_\mathrm{u} + n_3\boldsymbol{a}_3, \tag{2.44}$$

where the superscripts m and s indicate the master and slave subdomains Ω^m and Ω^s, respectively. The same holds for the moment along an internal boundary:

$$\boldsymbol{m} = \boldsymbol{m}^\mathrm{m} = -\boldsymbol{m}^\mathrm{s}, \quad \text{with} \quad \boldsymbol{m} = m_\mathrm{t}\boldsymbol{a}_\mathrm{t}. \tag{2.45}$$

Considering the boundary terms on both master and slave side in Eq. (2.42), gives the virtual work for internal KL shell boundaries as

$$\delta W = \int_{\Gamma_\mathrm{C}^\mathrm{m}} \left[\boldsymbol{n}\cdot(\delta\boldsymbol{u}^\mathrm{m} - \delta\boldsymbol{u}^\mathrm{s}) + \boldsymbol{m}\cdot(\delta\boldsymbol{\theta}^\mathrm{m} - \delta\boldsymbol{\theta}^\mathrm{s})\right] \mathrm{d}\Gamma \tag{2.46}$$

$$= \int_{\Gamma_\mathrm{C}^\mathrm{m}} \left[n_\mathrm{t}(\delta u_\mathrm{t}^\mathrm{m} - \delta u_\mathrm{t}^\mathrm{s}) + n_\mathrm{u}(\delta u_\mathrm{u}^\mathrm{m} - \delta u_\mathrm{u}^\mathrm{s}) + n_3(\delta u_3^\mathrm{m} - \delta u_3^\mathrm{s}) + m_\mathrm{t}(\delta\theta_\mathrm{t}^\mathrm{m} - \delta\theta_\mathrm{t}^\mathrm{s})\right] \mathrm{d}\Gamma. \tag{2.47}$$

Within IBRA, the traction force $\boldsymbol{n}$ between the master and the slave boundary is defined as a function of the boundary displacement difference

$$\boldsymbol{n} = -\alpha^\mathrm{disp}(\boldsymbol{u}^\mathrm{m} - \boldsymbol{u}^\mathrm{s}), \tag{2.48}$$

where α^disp is a penalty factor, representing the stiffness of the coupling condition. Please note the slightly different notation compared to [30, 32]. The moment $\boldsymbol{m}_\mathrm{t}$ acting around the trimming curve tangent vector $\boldsymbol{a}_\mathrm{t}$ between two patches, see Figure 2.3, is similarly defined as

$$m_\mathrm{t} = -\alpha^\mathrm{rot}(\theta_\mathrm{t}^\mathrm{m} - \theta_\mathrm{t}^\mathrm{s}), \tag{2.49}$$

where α^rot is now the rotation penalty factor. Inserting conditions (2.48) and (2.49) into Eq. (2.46) then gives the virtual work of B-Rep edge elements for internal boundary conditions, split into displacement and rotation parts, as

$$\delta W^\mathrm{B\text{-}Rep,disp} = -\alpha^\mathrm{disp} \int_{\Gamma_\mathrm{C}^\mathrm{m}} (\boldsymbol{u}^\mathrm{m} - \boldsymbol{u}^\mathrm{s})\cdot(\delta\boldsymbol{u}^\mathrm{m} - \delta\boldsymbol{u}^\mathrm{s}) \mathrm{d}\Gamma, \tag{2.50}$$

$$\delta W^\mathrm{B\text{-}Rep,rot} = -\alpha^\mathrm{rot} \int_{\Gamma_\mathrm{C}^\mathrm{m}} (\theta_\mathrm{t}^\mathrm{m} - \theta_\mathrm{t}^\mathrm{s})\cdot(\delta\theta_\mathrm{t}^\mathrm{m} - \delta\theta_\mathrm{t}^\mathrm{s}) \mathrm{d}\Gamma. \tag{2.51}$$

Dirichlet boundary conditions

For Dirichlet boundary conditions, the traction force and moment are defined similarly to (2.48) and (2.49), with the difference that the displacements and rotation are prescribed on one domain as $\boldsymbol{u}^{\mathrm{D}}$ and $\theta_{\mathrm{t}}^{\mathrm{D}}$, respectively. Since the variations $\delta\boldsymbol{u}^{\mathrm{D}}$ and $\delta\theta_{\mathrm{t}}^{\mathrm{D}}$ vanish, the virtual work of B-Rep edge elements for Dirichlet boundary conditions can be written as

$$\delta W^{\text{B-Rep,disp}} = -\alpha^{\text{disp}} \int_{\Gamma_{\mathrm{D}}} (\boldsymbol{u} - \boldsymbol{u}^{\mathrm{D}}) \cdot \delta\boldsymbol{u} \, \mathrm{d}\Gamma, \tag{2.52}$$

$$\delta W^{\text{B-Rep,rot}} = -\alpha^{\text{rot}} \int_{\Gamma_{\mathrm{D}}} (\theta_{\mathrm{t}} - \theta_{\mathrm{t}}^{\mathrm{D}}) \cdot \delta\theta_{\mathrm{t}} \, \mathrm{d}\Gamma. \tag{2.53}$$

Neumann boundary conditions

Also Neumann boundary conditions may be applied via B-Rep edge elements. In that case, the traction forces resp. moment in the virtual work expression for KL shell boundaries (2.42) are prescribed directly as $\boldsymbol{n}^{\mathrm{N}}$ resp. $m_{\mathrm{t}}^{\mathrm{N}}$, without the need for a penalty formulation. This leads to the B-Rep edge element formulation

$$\delta W^{\text{B-Rep,disp}} = \int_{\Gamma_{\mathrm{N}}} \boldsymbol{n}^{\mathrm{N}} \cdot \delta\boldsymbol{u} \, \mathrm{d}\Gamma, \tag{2.54}$$

$$\delta W^{\text{B-Rep,rot}} = \int_{\Gamma_{\mathrm{N}}} m_{\mathrm{t}}^{\mathrm{N}} \cdot \delta\theta_{\mathrm{t}} \, \mathrm{d}\Gamma. \tag{2.55}$$

The B-Rep edge element formulations for coupling and Dirichlet boundary conditions presented in this section are, as in the original work on IBRA [30, 32], based on weakly enforced penalty constraints. Besides that, also other constraint enforcement approaches such as the Lagrange multiplier method or Nitsche's method may be utilized for B-Rep elements, see [50, 52].

2.9 Explicit dynamic analysis

In accordance with the main focus of this thesis, namely explicit isogeometric (crash) simulations, this section explains the essential aspects of explicit dynamic analysis. After a brief motivation of why to use explicit time integration (for crash simulations), the central difference method (CDM) is specifically discussed. Finally, the well-known stability condition and different stable time step estimates for the CDM are introduced, in order to assess Explicit IBRA with respect to explicit time integration in subsequent chapters. This particularly involves the influence of trimming, weak penalty-based coupling and boundary conditions, and the proposed stabilization scheme.

2.9.1 Time integration of dynamic problems

In the following, the semi-discrete (only spatial discretization) second order equations of motion without damping in the form

$$\mathbf{M}\mathbf{a}^n = \mathbf{f}^{\text{ext},n}(\mathbf{d}^n, t^n) - \mathbf{f}^{\text{int},n}(\mathbf{d}^n, t^n), \tag{2.56}$$

at time t^n shall be considered, with the vector of control point accelerations $\mathbf{a}^n = \ddot{\mathbf{d}}^n$ and the external and internal control point forces as a function of control point displacements and time. Progressing the solution in time requires suitable time integration methods, which may be classified into implicit and explicit methods. Without going into details regarding construction and properties of distinct time integration methods (see for instance [49, 76, 134]), only aspects relevant for automotive crash simulations shall be discussed here.

One distinctive characteristic of explicit time integration methods is that advancing the solution to time t^{n+1} (or updating displacements and velocities at time step $n+1$) only requires information from previous time steps. Additionally using a diagonal lumped mass matrix allows to decouple the equation system and to perform all operations on an element level. Thus, in fact, no equations are solved. This makes explicit methods very attractive and efficient for large problems like automotive crash simulations, because both the inversion and storage of huge matrices can be avoided. Because no system of equations is solved, explicit procedures are also more robust in strongly nonlinear problems for which implicit solution procedures tend to have convergence problems. Automotive crash simulations with strong nonlinearities of all kind including large deformations, plasticity, contact and buckling is again a perfect example. However, explicit methods are, in contrast to implicit methods, only conditionally stable. That is, for a stable solution the time step size needs to be smaller than a critical value, see the derivation of the critical time step for the central difference method in Section 2.9.3 below. Explicit methods therefore require significantly

smaller time steps, in general. This disadvantage fades though for highly dynamic problems for which the accuracy of the solution requires relatively small time steps anyway, regardless of the applied method.

2.9.2 Central difference method

Within this thesis, the practically well-established explicit central difference method (CDM) [45, 49] is used for Explicit Isogeometric B-Rep Analysis in LS-DYNA; however, also other explicit time integration methods could be used. To eliminate the time derivatives in the equations of motion (2.56), the velocity $\dot{\mathbf{d}} = \mathbf{v}$ and the acceleration $\ddot{\mathbf{d}} = \mathbf{a}$, are expressed by central differences as

$$\dot{\mathbf{d}}^{n+1/2} = \mathbf{v}^{n+1/2} = \frac{\mathbf{d}^{n+1} - \mathbf{d}^{n}}{\Delta t}, \tag{2.57}$$

$$\ddot{\mathbf{d}}^{n} = \mathbf{a}^{n} = \frac{\mathbf{v}^{n+1/2} - \mathbf{v}^{n-1/2}}{\Delta t}, \tag{2.58}$$

for which constant time increments Δt are assumed here. By rearranging the terms, one can transform these difference formulas into integration formulas, used to update displacements and velocities, thereby progressing the solution in time:

$$\mathbf{d}^{n+1} = \mathbf{d}^{n} + \Delta t\, \mathbf{v}^{n+1/2}, \quad \mathbf{v}^{n+1/2} = \mathbf{v}^{n-1/2} + \Delta t\, \mathbf{a}^{n} \tag{2.59}$$

By inserting (2.57) into (2.58), the acceleration can be expressed solely in terms of displacements, yielding the finite difference approximation for the second derivative of a function as

$$\mathbf{a}^{n} = \frac{\mathbf{d}^{n+1} - 2\mathbf{d}^{n} + \mathbf{d}^{n-1}}{(\Delta t)^2}. \tag{2.60}$$

The error made through this finite difference approximation is of order $(\Delta t)^2$ in the displacements [49, 76]. Inserting (2.60) into the semi-discrete equations of motion (2.56) gives

$$\frac{1}{(\Delta t)^2}\, \mathbf{M}\left(\mathbf{d}^{n+1} - 2\mathbf{d}^{n} + \mathbf{d}^{n-1}\right) = \mathbf{f}^{\mathrm{ext},n} - \mathbf{f}^{\mathrm{int},n}, \tag{2.61}$$

clearly showing that the calculation of $\mathbf{d}^{n+1}$ only requires information from previous time steps – a characteristic of explicit time integration schemes. One can furthermore see that the only matrix to invert for computing $\mathbf{d}^{n+1}$ is the mass matrix $\mathbf{M}$. As already mentioned above, using a diagonal lumped mass matrix renders the inversion of $\mathbf{M}$ trivial, decouples the equation system and (only) makes explicit methods very efficient.

For explicit analysis of shells with rotational DOFs, the equations of motion for a control point A may be expressed in generalized coordinates as

$$\overline{\mathbf{M}}_A \bar{\mathbf{a}}_A^n = \bar{\mathbf{f}}_A^{\mathrm{ext},n} - \bar{\mathbf{f}}_A^{\mathrm{int},n}, \tag{2.62}$$

with the generalized control point mass $\overline{\mathbf{M}}_A$, the generalized accelerations $\bar{\mathbf{a}}_A^n = \{(\mathbf{a}_A^n)^T, (\dot{\boldsymbol{\omega}}_A^n)^T\}^T$. The rotations and angular velocities of a control point A are then updated similarly as their translational counterparts:

$$\boldsymbol{\theta}_A^{n+1} = \boldsymbol{\theta}_A^{n} + \Delta t\, \boldsymbol{\omega}_A^{n+1/2}, \quad \boldsymbol{\omega}_A^{n+1/2} = \boldsymbol{\omega}_A^{n-1/2} + \Delta t\, \dot{\boldsymbol{\omega}}_A^{n}. \tag{2.63}$$

2.9.3 Stability of the central difference method

The focus in this section is on the stability of the CDM. As mentioned above, explicit time integration schemes are only conditionally stable, that is, only numerically stable under the condition that the time step size does not exceed a critical value. Determining this critical value is therefore essential. Within this thesis, numerical stability shall be defined in the sense of Liapunov as follows, see also [49], p. 391, Eq. (6.6.1).

Definition 2.1: Numerical stability. A numerical procedure is considered as numerically stable if the difference between two solutions $\boldsymbol{u}_{\mathrm{A}}^n$ and $\boldsymbol{u}_{\mathrm{B}}^n$ with slightly different initial conditions $\boldsymbol{u}_{\mathrm{A}}^0$ and $\boldsymbol{u}_{\mathrm{B}}^0$ remains small and bounded. To be more precise, a numerical solution $\boldsymbol{u}_{\mathrm{A}}^n$ is stable if

$$\left\|\boldsymbol{u}_{\mathrm{A}}^n - \boldsymbol{u}_{\mathrm{B}}^n\right\|_2 \leq C\varepsilon \quad \forall n > 0 \quad \text{for all } \boldsymbol{u}_{\mathrm{A}}^0 \quad \text{such that } \left\|\boldsymbol{u}_{\mathrm{A}}^0 - \boldsymbol{u}_{\mathrm{B}}^0\right\|_2 \leq \varepsilon, \tag{2.64}$$

with a small initial perturbation $\varepsilon > 0$ and an arbitrary constant $C > 0$.

Due to difficulties in assessing numerical stability for nonlinear systems, one commonly assesses the stability of the linearized system and then transfers the result to the nonlinear case [49]. For explicit analysis this means that the critical time step is computed for the linearized system and then, together with a suitable safety factor, used for solving the nonlinear system. This entails frequent linearizations of the system equations during analysis. For linear stability analysis, the linearized equations of motion including damping shall be considered as

$$\mathbf{M}\ddot{\mathbf{d}} + \mathbf{C}\dot{\mathbf{d}} + \mathbf{K}\mathbf{d} = \mathbf{f}^{\text{ext}}, \tag{2.65}$$

where the overline indicating generalized coordinates is omitted for brevity; still, both translational and rotational DOFs are considered. For convenience, the linear equations of motion are commonly diagonalized and decoupled by means of a modal decomposition. This decomposition exploits the orthogonality of the eigenvectors $\mathbf{y}_I$ of the undamped eigenproblem

$$\mathbf{K}\mathbf{y}_I = \lambda_I \mathbf{M}\mathbf{y}_I, \tag{2.66}$$

with the eigenvalues λ_I. To enable the diagonalization of the damped system (2.65), $\mathbf{C}$ can be expressed as a linear combination of $\mathbf{M}$ and $\mathbf{K}$, that is, as a Rayleigh damping matrix. Based on that, linear stability analysis yields the critical time step size of the central difference method as a function of the eigenfrequency ω_I ($\lambda_I = \omega_I^2$) of the undamped system and the associated modal damping ratio ξ_I

$$\Delta t_{\text{crit}} = \min_I \frac{2}{\omega_I}\left(\sqrt{\xi_I^2+1} - \xi_I\right) = \min_I \frac{2}{\sqrt{\lambda_I}}\left(\sqrt{\xi_I^2+1} - \xi_I\right). \tag{2.67}$$

The full linear stability analysis, closely following [49], is provided in Appendix A. As this derivation shows, the stability condition (2.67) holds for any system in the form of (2.65) that fulfills the following two premises: (i) symmetry and positive semidefiniteness of $\mathbf{M}$ and $\mathbf{K}$ and (ii) describing $\mathbf{C}$ as a Rayleigh damping matrix. Within this thesis, damping shall be neglected, so the second premise becomes irrelevant. The crucial requirement for the developments in subsequent chapters (B-Rep element formulations, stabilization scheme, etc.) will therefore be that the mass and stiffness matrices remain symmetric and positive semidefinite. Otherwise condition (2.67) can no longer be used to determine the critical time step of the central difference method.

2.9.4 Stable time step estimation

For determining the critical time step size through (2.67), only the maximum system eigenvalue needs to be computed instead of all. Still, for large systems even computing only the maximum eigenvalue yields significant computational costs. Moreover it should be noted that the eigenvalues alter during nonlinear analysis and since condition (2.67) is determined for linearized equations, it only provides a decent time step estimation around the linearization point. That is, an accurate time step estimation requires multiple linearizations and eigenvalue evaluations. For these reasons, computationally more efficient time step estimates are desired for practical applications. In order to assess the applicability of time step estimates to explicit analysis on penalty-coupled trimmed NURBS shells in subsequent chapters, a brief overview on the most common estimates in FEA and IGA is provided next.

Heuristic element estimate

The simplest and most common time step estimate in practical FEA is based on a characteristic element length l_c^e (which may be updated during the simulation) and the material wave speed c. This heuristic approach estimates the critical time step in the absence of damping by

$$\Delta t_{\text{crit}} \leq \min_e \frac{l_\text{c}^e}{c}. \tag{2.68}$$

This approach involves two approximations on the maximum system eigenfrequency in the stability condition (2.67). The first one uses the element eigenvalue inequality [49, 135, 136], i.e. the fact that the maximum system eigenvalue λ_max is bounded from above by the maximum of all element eigenvalues λ_max^E:

$$|\lambda_\text{max}| \leq |\lambda_\text{max}^E| \quad \text{where} \quad \lambda_\text{max}^E = \max_{I,e} \lambda_I^e. \tag{2.69}$$

With this upper bound, the problem of determining the maximum system eigenvalue can be replaced by the numerically less expensive problem of finding the maximum of all element eigenvalues. More details about the eigenvalue inequality are given in [49, 135, 136]. For the case of a one-dimensional rod with lumped masses, the maximum element eigenvalue λ_max can be determined as a function of element length l and wave speed c as $\lambda_\text{max} = 4c^2/l^2$.

Inserting this relation into Eq. (2.67) and neglecting damping then yields Eq. (2.68). This estimation is closely related to the popular CFL condition [137] originally developed for the finite difference method. However, this relation can, together with a heuristically determined characteristic element length l_c^e, also be applied to multi-dimensional meshes [45], which is the second approximation. Hartmann and Benson [14] recently developed a heuristic estimation for the characteristic length of NURBS-based elements in IGA as

$$l_c = S \min(\|\boldsymbol{l}_1\|, \|\boldsymbol{l}_2\|) \quad \text{with} \quad \boldsymbol{l}_1 = \frac{\partial \boldsymbol{x}}{\partial \xi_{\mathcal{G}}} \min_i(w_i), \quad \boldsymbol{l}_2 = \frac{\partial \boldsymbol{x}}{\partial \eta_{\mathcal{G}}} \min_i(w_i). \tag{2.70}$$

Herein, $\boldsymbol{l}_1$ and $\boldsymbol{l}_2$ are computed as the partial derivatives of the spatial coordinate with respect to the Gauss parameters $\xi_{\mathcal{G}}$ and $\eta_{\mathcal{G}}$, respectively, times the minimum of the standard quadrature weights for one-dimensional integration w_i in the respective direction. The empirically determined scale factor S depends on the polynomial degree and the integration rule; see [14] for more details. This is the currently used stable time step estimate for IGA in LS-DYNA. Adam et al. [81] proposed a similar heuristic time step estimation based on the element length and on a scalar value accounting for polynomial degree and also regularity of the B-spline basis functions. Such heuristic element estimates are attractive, since they only require element lengths and the material wave speed, and avoid solving any eigenvalue problem.

Nodal estimate based on the Gershgorin circle theorem

The nodal time step estimate for explicit IGA suggested by Adam et al. [81] and inspired by the work of Flanagan and Belytschko [138] is another possible approach. It bounds the maximum system eigenfrequency $\lambda_{\max}$ required in (2.67) by means of the Gershgorin circle theorem [139, 140]. This theorem states that all eigenvalues of a matrix lie within circles around the diagonal values with radii equal to the sum of the absolute off-diagonal entries of the corresponding row.

Definition 2.2: Gershgorin disc. Consider a complex square matrix $\mathbf{A} = [a_{ij}] \in \mathbb{C}^{n\times n}$, $n \in \mathbb{N}$ and a closed disc $\mathcal{B}(x_0, R_0) \subseteq \mathbb{C}$, with a center $x_0 \in \mathbb{C}$ and a radius $R_0 \in \mathbb{R}^+$. A Gershgorin disc is then defined as

$$\mathcal{D}_i\big(a_{ii}, R_i\big) = \mathcal{D}_i\big(a_{ii}, \sum_{j\neq i} |a_{ij}|\big) = \{x \in \mathbb{C} \,\big|\, |a_{ii} - x| \leq \sum_{j\neq i} |a_{ij}|\}, \tag{2.71}$$

with a center of a_{ii} and a radius of $R_i = \sum_{j\neq i} |a_{ij}|$.

Definition 2.3: Gershgorin circle theorem. Each eigenvalue $\lambda \in \mathbb{C}$ of $\mathbf{A} = [a_{ij}] \in \mathbb{C}^{n\times n}$, $n \in \mathbb{N}$, lies within at least one of the Gershgorin discs $\mathcal{D}_i\big(a_{ii}, R_i\big)$, which means that

$$\lambda \in \bigcup_i \mathcal{D}_i. \tag{2.72}$$

In the explicit dynamic setting the real matrix $\mathbf{A} = \mathbf{M}^{-1}\mathbf{K} = [a_{ij}] \in \mathbb{R}^{n\times n}$, $n \in \mathbb{N}$ with only real positive eigenvalues is considered. Thus, for each eigenvalue λ, the following holds:

$$\lambda \leq \max_i \big(a_{ii} + R_i\big). \tag{2.73}$$

In that sense, the stiffness matrix $\mathbf{K}$ can be diagonalized (lumped) by row summing of absolute values as

$$\tilde{K}_{ii} = K_{ii} + \sum_{j\neq i} |K_{ij}|, \tag{2.74}$$

for which the following holds:

$$\lambda_{\max}^{\mathbf{M}^{-1}\mathbf{K}} \leq \lambda_{\max}^{\mathbf{M}^{-1}\tilde{\mathbf{K}}}. \tag{2.75}$$

That is, the maximum eigenvalue of the lumped system $\mathbf{M}^{-1}\tilde{\mathbf{K}}$ provides an upper bound for the eigenvalues of the original system $\mathbf{M}^{-1}\mathbf{K}$. Due to the fact that the eigenvalues of a diagonal matrix are equal to its entries, the maximum eigenvalue of $\mathbf{M}^{-1}\tilde{\mathbf{K}}$ can be computed as

$$\lambda_{\max}^{\mathbf{M}^{-1}\tilde{\mathbf{K}}} = \max_i \left(\frac{\tilde{K}_{ii}}{M_{ii}} \right). \tag{2.76}$$

By combining this with Eq. (2.67) without damping, one obtains a conservative and computationally cheap estimation for the critical time step of the original system $\mathbf{M}^{-1}\mathbf{K}$ as

$$\Delta t_{\text{crit}}^{\mathbf{M}^{-1}\tilde{\mathbf{K}}} = \frac{2}{\sqrt{\max_i\left(\frac{\tilde{K}_{ii}}{M_{ii}}\right)}} \leq \Delta t_{\text{crit}}^{\mathbf{M}^{-1}\mathbf{K}}. \tag{2.77}$$

This conservative estimate is reported to be an accurate approximation and outperforms the element estimate in case of non-uniform meshes [81]. In Section 4.5, this estimate will be employed to achieve a local selective mass scaling of control points involved in penalty-based B-Rep elements. Please note that damping may be considered in Eq. (2.67) when inserting Eq. (2.76).

Power iteration method

With the power iteration method [140], the maximum system eigenvalue in (2.67) can be accurately estimated by an iterative scheme. It is a common alternative for cases in which the element time step estimate is not sufficiently accurate or characteristic element lengths are not expedient, e.g. in [14, 73, 77, 81, 141]. It is therefore briefly explained here. An $n \times n$ matrix $\mathbf{A}$ with real elements, n linearly independent eigenvectors $\mathbf{y}_J$, and a unique maximum eigenvalue $\lambda_{\max}$ shall be assumed, together with an arbitrary n-dimensional vector $\mathbf{x}_0$. The power iteration method exploits the fact that the directions of the vector $\mathbf{x}_\nu = \mathbf{A}^\nu \mathbf{x}_0$ converge towards the ones of the eigenvector $\mathbf{y}_{\max}$ associated with $\lambda_{\max}$ for $\nu \to \infty$. Together with a proper normalization, the corresponding iterative scheme can be written as

$$\mathbf{x}_{\nu+1} = \frac{\mathbf{A}^\nu \mathbf{x}_\nu}{\|\mathbf{A}^\nu \mathbf{x}_\nu\|}. \tag{2.78}$$

The maximum eigenvalue $\lambda_{\max}$ can then be obtained by means of the Rayleigh quotient

$$R = \frac{\mathbf{x}_\nu^* \mathbf{A} \mathbf{x}_\nu}{\mathbf{x}_\nu^* \mathbf{x}_\nu} \to \lambda_{\max} \quad \text{for} \quad \nu \to \infty, \tag{2.79}$$

where $\mathbf{x}^*$ denotes the conjugate transpose of $\mathbf{x}$. A number of twelve iterations is reported to be sufficient for the stable time step estimation in explicit isogeometric shell analysis in [73]. In conclusion, the power iteration method provides a highly accurate time step estimation, but also higher computational costs compared to the heuristic element estimate and the nodal estimate.

In the following chapters, the applicability of these three time step estimates to Explicit IBRA including trimming, weak penalty-based coupling and boundary conditions, and the proposed stabilization scheme will be assessed.

Chapter 3

Explicit Isogeometric B-Rep Analysis

This chapter on Explicit IBRA forms the core of this thesis as it presents the extension of IBRA to (i) explicit dynamic analysis and (ii) Reissner-Mindlin shells. For the extension to RM shells with rotational DOFs [73], two novel penalty-based B-Rep edge element formulations are proposed: The *standard* B-Rep element formulation, presented in Section 3.3 and previously in [54], introduces forces and moments along boundaries solely via constraints on the respective translational and rotational DOFs. The *enhanced* B-Rep element formulation presented in Section 3.4 aims at increasing the numerical robustness and accuracy of B-Rep edge elements by additionally enforcing rotational continuity between (trimmed) patches via a constraint on the shell normals, uniquely defined by translational DOFs. For both B-Rep edge element formulations, the corresponding control point forces and stiffness matrices are derived from the boundary terms of the weak forms for internal (coupling) and Dirichlet boundary conditions; for the standard element formulation also the control point forces for Neumann boundary conditions are derived. By means of the derived stiffness matrices, Section 3.5.1 investigates the effect of both B-Rep edge element formulations on the stability of the explicit central difference scheme. Finally, Section 3.5.2 discusses the applicability of common time step estimates to problems with penalty-based B-Rep elements.

3.1 Extension of IBRA to explicit dynamics

For the extension of IBRA to explicit dynamic analysis, the principle of virtual work (equivalent to the principle of virtual power in Eq. (2.28)) is formally extended with a B-Rep term $\delta W^{\text{B-Rep}}$:

$$\delta W = \delta W^{\text{int}} - \delta W^{\text{ext}} + \delta W^{\text{kin}} + \delta W^{\text{B-Rep}} = 0. \tag{3.1}$$

Within the explicit analysis procedure, one furthermore needs to consider the control point forces and moments from B-Rep elements in Eq. (2.62) when computing the accelerations:

$$\overline{\mathbf{M}}_A \bar{\mathbf{a}}_A^n = \bar{\mathbf{f}}_A^{\text{ext},n} - \bar{\mathbf{f}}_A^{\text{int},n} - \bar{\mathbf{f}}_A^{\text{B-Rep},n}. \tag{3.2}$$

In the two subsequent sections, the corresponding virtual work terms, control point forces and moments, and stiffness matrices are derived for different types of B-Rep element formulations and boundary conditions. It should be noted that the stiffness matrices are not used within the explicit analysis, but only for the investigations on numerical stability and time step size in Section 3.5.

3.2 Extension of IBRA to shear deformable Reissner-Mindlin shell theory

Isogeometric B-Rep Analysis (IBRA) in its original form was developed for and applied to thin shells according to the Kirchhoff-Love shell theory. In this section, IBRA is extended to thick shells described by the shear deformable Reissner-Mindlin shell theory.

3.2.1 Boundary conditions

Kirchhoff-Love shells

The basic assumptions for the KL and RM shell theories are provided in Section 2.6.1. As stated in [32] and [127], the boundary terms of the weak form (virtual work) for KL shells are given as

$$\delta W = \int_\Gamma \left(\boldsymbol{n} \cdot \delta \boldsymbol{u} + \boldsymbol{m}_\mathrm{t} \cdot \delta \boldsymbol{\theta}_\mathrm{t} \right) \mathrm{d}\Gamma \tag{3.3}$$

$$= \int_\Gamma \left(n_\mathrm{t} \delta u_\mathrm{t} + n_\mathrm{u} \delta u_\mathrm{u} + n_3 \delta u_3 + m_\mathrm{t} \delta \theta_\mathrm{t} \right) \mathrm{d}\Gamma, \tag{3.4}$$

where the indices t, u, and 3 are the directions of a local coordinate system introduced along a (trimming) curve $\mathbf{C}$, see Figure 2.3. As can be seen, the moment $\boldsymbol{m}_\mathrm{t}$ only has *one* contribution in t-direction, since the contributions in u- and 3-direction are dependent variables in the KL theory, which may only be prescribed implicitly via $\boldsymbol{n}$, see [127], p. 172. This is in accordance with the fact that in the KL theory, the kinematics of the shell continuum are uniquely described by the kinematics of the shell midsurface [127], p. 163. For IBRA with KL shells in [30, 32], rotational boundary constraints were therefore only enforced around the t-direction, i.e. around the (trimming) curve tangent.

Reissner-Mindlin shells

For the RM shell theory, due to the considered shear deformations, *two* rotational boundary conditions around the u- and t-direction may be prescribed in addition to the three translational boundary conditions in u-, t- and 3-direction [127], p. 122. The corresponding weak form for the boundary terms (see [127], p. 122, Eq. (3.3.51)) is thus given as

$$\delta W = \int_\Gamma \left(\boldsymbol{n} \cdot \delta \boldsymbol{u} + \boldsymbol{m} \cdot \delta \boldsymbol{\theta} \right) \mathrm{d}\Gamma \tag{3.5}$$

$$= \int_\Gamma \left(n_\mathrm{t} \delta u_\mathrm{t} + n_\mathrm{u} \delta u_\mathrm{u} + n_3 \delta u_3 + m_\mathrm{t} \delta \theta_\mathrm{t} + m_\mathrm{u} \delta \theta_\mathrm{u} \right) \mathrm{d}\Gamma. \tag{3.6}$$

For IBRA with RM shells, rotational constraints may therefore be enforced around the t- and u-direction, i.e. a bending constraint around the trimming curve tangent $\boldsymbol{a}_\mathrm{t}$, and a twisting constraint around the vector perpendicular to the surface normal $\boldsymbol{a}_3$ and the curve tangent $\boldsymbol{a}_\mathrm{t}$.

3.2.2 Internal boundary conditions for Reissner-Mindlin shells

Now, internal boundary conditions as shown in Figure 3.1 are considered. In order to fulfill the equilibrium along internal boundaries, the following must hold for traction forces:

$$\boldsymbol{n} = \boldsymbol{n}^\mathrm{m} = -\boldsymbol{n}^\mathrm{s}, \quad \text{with} \quad \boldsymbol{n} = n_\mathrm{t} \boldsymbol{a}_\mathrm{t} + n_\mathrm{u} \boldsymbol{a}_\mathrm{u} + n_3 \boldsymbol{a}_3, \tag{3.7}$$

where the superscripts indicate master and slave sides, although no distinction between the two sides is required at this point. Similarly, the following must hold for the traction moments:

$$\boldsymbol{m} = \boldsymbol{m}^\mathrm{m} = -\boldsymbol{m}^\mathrm{s}, \quad \text{with} \quad \boldsymbol{m} = m_\mathrm{t} \boldsymbol{a}_\mathrm{t} + m_\mathrm{u} \boldsymbol{a}_\mathrm{u}. \tag{3.8}$$

With Eq. (3.5) the virtual work term for internal RM shell boundaries can then be written as

$$\delta W = \int_{\Gamma_\mathrm{C}^\mathrm{m}} \left[\boldsymbol{n} \cdot (\delta \boldsymbol{u}^\mathrm{m} - \delta \boldsymbol{u}^\mathrm{s}) + \boldsymbol{m} \cdot (\delta \boldsymbol{\theta}^\mathrm{m} - \delta \boldsymbol{\theta}^\mathrm{s}) \right] \mathrm{d}\Gamma \tag{3.9}$$

$$= \int_{\Gamma_\mathrm{C}^\mathrm{m}} \left[n_\mathrm{t} (\delta u_\mathrm{t}^\mathrm{m} - \delta u_\mathrm{t}^\mathrm{s}) + n_\mathrm{u} (\delta u_\mathrm{u}^\mathrm{m} - \delta u_\mathrm{u}^\mathrm{s}) + n_3 (\delta u_3^\mathrm{m} - \delta u_3^\mathrm{s}) + m_\mathrm{t} (\delta \theta_\mathrm{t}^\mathrm{m} - \delta \theta_\mathrm{t}^\mathrm{s}) + m_\mathrm{u} (\delta \theta_\mathrm{u}^\mathrm{m} - \delta \theta_\mathrm{u}^\mathrm{s}) \right] \mathrm{d}\Gamma, \tag{3.10}$$

where the integration is performed along the master boundary $\Gamma_\mathrm{C}^\mathrm{m}$. Based on the (internal) boundary terms of the virtual work for RM shells provided in Eqs. (3.5) and (3.9), a B-Rep edge element formulation including translational and rotational DOFs is presented in the following section.

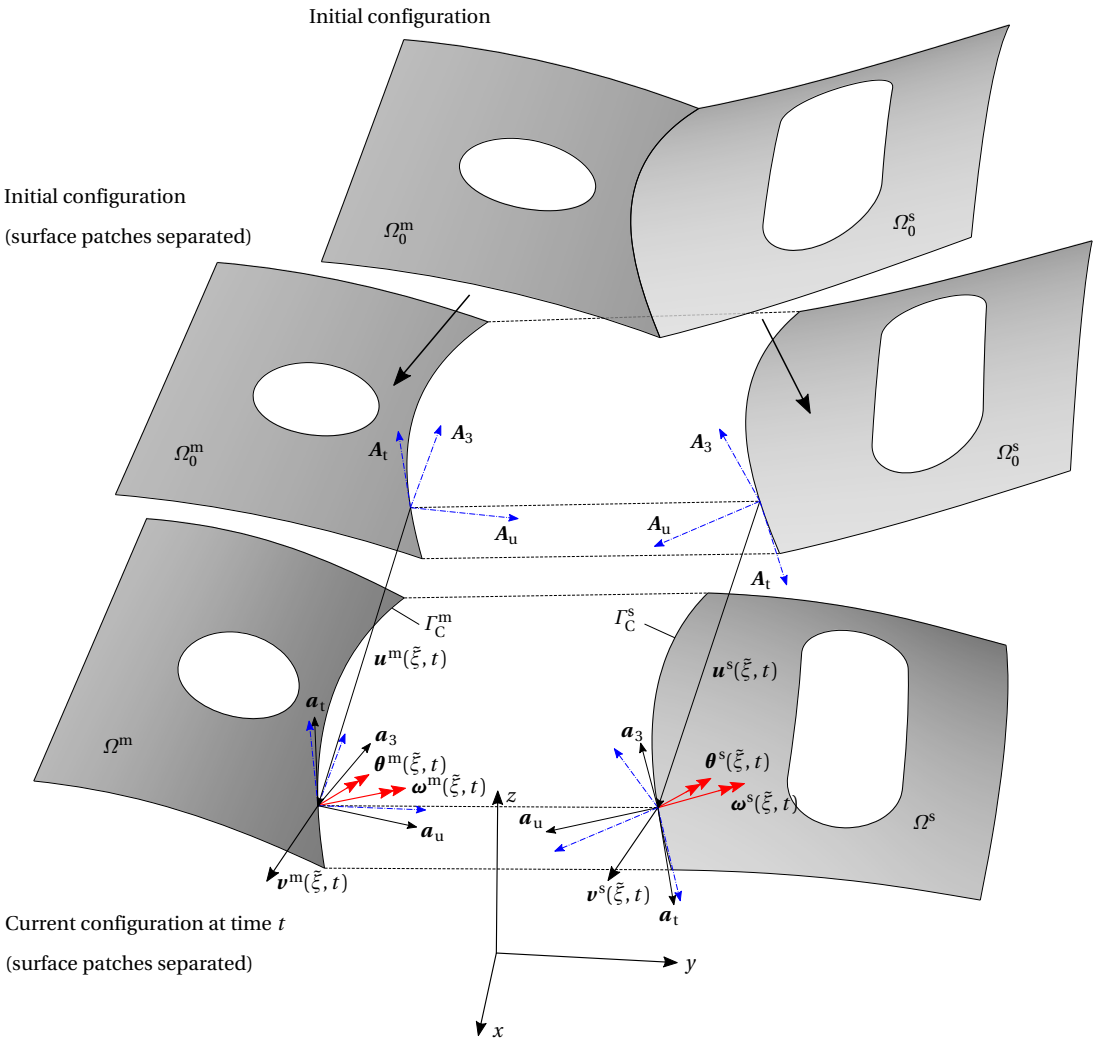

Figure 3.1: Kinematics for a B-Rep edge element formulation between trimmed master and slave patches (Ω^{m} and Ω^{s}). The coupled master and slave patch are separated for clarity as indicated by dashed lines.

3.3 The standard B-Rep edge element formulation – Translational and rotational DOFs

In this section, the standard B-Rep edge element formulation first proposed by Leidinger et al. [54] is presented. In contrast to [54], the following derivations use the mechanically motivated (internal) shell boundary formulations from [127] (see Eqs. (3.5) and (3.9)) as a starting point. Therefore, the principle of virtual work instead of the principle of virtual power is used throughout this thesis. However, the two principles are equivalent and interchangeable (as mentioned in [49], p. 55). This choice allows for a proper interpretation of the involved variables and a consistent derivation for all formulations including the enhanced B-Rep edge element formulation presented in Section 3.4.

3.3.1 Element formulation for coupling conditions

The starting point for the B-Rep edge element formulation for internal boundaries is the corresponding virtual work term from Eq. (3.9), split into a translational and a rotational part

$$\delta W^{\text{B-Rep,disp}} = \int_{\Gamma_{\mathrm{C}}^{\mathrm{m}}} \boldsymbol{n} \cdot (\delta \boldsymbol{u}^{\mathrm{m}} - \delta \boldsymbol{u}^{\mathrm{s}}) \, \mathrm{d}\Gamma = \int_{\Gamma_{\mathrm{C}}^{\mathrm{m}}} \left[n_{\mathrm{t}} (\delta u_{\mathrm{t}}^{\mathrm{m}} - \delta u_{\mathrm{t}}^{\mathrm{s}}) + n_{\mathrm{u}} (\delta u_{\mathrm{u}}^{\mathrm{m}} - \delta u_{\mathrm{u}}^{\mathrm{s}}) + n_3 (\delta u_3^{\mathrm{m}} - \delta u_3^{\mathrm{s}}) \right] \mathrm{d}\Gamma, \tag{3.11}$$

$$\delta W^{\text{B-Rep,rot}} = \int_{\Gamma_{\mathrm{C}}^{\mathrm{m}}} \boldsymbol{m} \cdot (\delta \boldsymbol{\theta}^{\mathrm{m}} - \delta \boldsymbol{\theta}^{\mathrm{s}}) \, \mathrm{d}\Gamma = \int_{\Gamma_{\mathrm{C}}^{\mathrm{m}}} \left[m_{\mathrm{t}} (\delta \theta_{\mathrm{t}}^{\mathrm{m}} - \delta \theta_{\mathrm{t}}^{\mathrm{s}}) + m_{\mathrm{u}} (\delta \theta_{\mathrm{u}}^{\mathrm{m}} - \delta \theta_{\mathrm{u}}^{\mathrm{s}}) \right] \mathrm{d}\Gamma. \tag{3.12}$$

In Eqs. (3.11) and (3.12), the traction force $\boldsymbol{n}$ and the moment $\boldsymbol{m}$ need to be prescribed, respectively. By employing a penalty approach, $\boldsymbol{n}$ can be expressed in the form

$$\boldsymbol{n} = \alpha^{\text{disp}}\, \boldsymbol{g}^{\text{disp}}(\boldsymbol{u}, \boldsymbol{v}, t), \tag{3.13}$$

where α^{disp} is a constant penalty factor. The actual constraint is denoted as $\boldsymbol{g}(\boldsymbol{u}, \boldsymbol{v}, t) = 0$, potentially depending on interface displacements, velocities and time. For Explicit IBRA a pure displacement-based, rate-independent constraint

$$\boldsymbol{g}^{\text{disp}}(\boldsymbol{u}, t) = \boldsymbol{u}^{\text{m}} - \boldsymbol{u}^{\text{s}}, \tag{3.14}$$

is found to be satisfactory, although also other formulations may be justifiable. This constraint may also be interpreted as a kind of gap function. With this constraint the interface traction vector is defined as

$$\boldsymbol{n} = \alpha^{\text{disp}}(\boldsymbol{u}^{\text{m}} - \boldsymbol{u}^{\text{s}}). \tag{3.15}$$

At this point, the importance of specifying the constraint $\boldsymbol{g}^{\text{disp}}$ in terms of displacements instead of absolute coordinates $\boldsymbol{x}$ should be emphasized. Although this might be indifferent for simple plane geometries, it is crucial for curved geometries, for which NURBS-based B-Rep models are generally not watertight, i.e. small gaps and overlaps appear between patch boundaries. Defining $\boldsymbol{g}^{\text{disp}}$ in terms of absolute coordinates could already lead to stresses in the initial state and consequently distorted results.

Inserting Eq. (3.15) into (3.11) then yields the translational virtual work contribution of penalty-based B-Rep edge elements along internal boundaries

$$\delta W^{\text{B-Rep,disp}} = \alpha^{\text{disp}} \int_{\Gamma_{\text{C}}^{\text{m}}} (\boldsymbol{u}^{\text{m}} - \boldsymbol{u}^{\text{s}}) \cdot (\delta \boldsymbol{u}^{\text{m}} - \delta \boldsymbol{u}^{\text{s}}) \, \mathrm{d}\Gamma. \tag{3.16}$$

With a similar penalty approach, the moment in Eq. (3.12) can be expressed in the form

$$\boldsymbol{m} = \alpha^{\text{rot}}\, \boldsymbol{g}^{\text{rot}}(\boldsymbol{\theta}, \boldsymbol{\omega}, t), \tag{3.17}$$

again with a constant penalty factor α^{rot}, and the rotational constraint $\boldsymbol{g}^{\text{rot}}(\boldsymbol{\theta}, \boldsymbol{\omega}, t) = 0$, potentially depending on interface rotations, angular velocities and time.

As can be seen from Eq. (3.12), the moment vector $\boldsymbol{m}$ is assumed to act in the surface tangent plane spanned by $\boldsymbol{a}_{\text{t}}$ and $\boldsymbol{a}_{\text{u}}$, see Figure 2.3. The component m_3 is not present. It would therefore be sufficient to only consider m_{t} and m_{u} in the constraints. This is usually done in the classical shell theory and in five-DOF shell implementations [49]. The Reissner-Mindlin shell to be coupled [73] is, however, based on a six DOF implementation with three translational and three rotational DOFs. The reason for this choice is reported to be a computationally simpler usage of angular velocities in global coordinates [73]. In such cases all three components of the moment need to be prescribed, as also stated in [49]. Therefore, and to avoid the introduction of a local coordinate system, the rotational constraint is formulated in global coordinates including moments in all three spatial directions.

As for the translations, the constraint is defined as rate-independent

$$\boldsymbol{g}^{\text{rot}}(\boldsymbol{\theta}, t) = \boldsymbol{\theta}^{\text{m}} - \boldsymbol{\theta}^{\text{s}}, \tag{3.18}$$

leading to the penalty-based interface moment vector

$$\boldsymbol{m} = \alpha^{\text{rot}}(\boldsymbol{\theta}^{\text{m}} - \boldsymbol{\theta}^{\text{s}}). \tag{3.19}$$

Inserting Eq. (3.19) into Eq. (3.12) gives the rotational virtual work contribution of penalty-based B-Rep edge elements along internal boundaries as

$$\delta W^{\text{B-Rep,rot}} = \alpha^{\text{rot}} \int_{\Gamma_{\text{C}}^{\text{m}}} (\boldsymbol{\theta}^{\text{m}} - \boldsymbol{\theta}^{\text{s}}) \cdot (\delta \boldsymbol{\theta}^{\text{m}} - \delta \boldsymbol{\theta}^{\text{s}}) \, \mathrm{d}\Gamma. \tag{3.20}$$

3.3.2 Element formulation for Dirichlet boundary conditions

The B-Rep edge element formulation for Dirichlet boundary conditions can be derived from the case of internal boundary conditions in a straightforward manner. For this purpose, the kinematic quantities along the boundary $\Gamma_{\text{C}}^{\text{s}}$ of the slave domain Ω^{s} in Eqs. (3.16) and (3.20) are formally replaced by prescribed kinematic quantities. That is, the

slave displacement vector $\boldsymbol{u}^{\mathrm{s}}(\tilde{\xi},t)$ and the slave rotation vector $\boldsymbol{\theta}^{\mathrm{s}}(\tilde{\xi},t)$ are replaced by a prescribed displacement $\boldsymbol{u}^{\mathrm{D}}(\tilde{\xi},t)$ and a prescribed rotation $\boldsymbol{\theta}^{\mathrm{D}}(\tilde{\xi},t)$, yielding

$$\boldsymbol{g}^{\mathrm{disp}}(\boldsymbol{u},t)=\boldsymbol{u}-\boldsymbol{u}^{\mathrm{D}}, \tag{3.21}$$

$$\boldsymbol{g}^{\mathrm{rot}}(\boldsymbol{\theta},t)=\boldsymbol{\theta}-\boldsymbol{\theta}^{\mathrm{D}}. \tag{3.22}$$

Integrating along the Dirichlet boundary Γ_{D} and using the fact that the virtual displacement $\delta\boldsymbol{u}^{\mathrm{D}}=0$ and the virtual rotation $\delta\boldsymbol{\theta}^{\mathrm{D}}=0$, the virtual work terms for Dirichlet boundary conditions are obtained as

$$\delta W^{\text{B-Rep,disp}}=\alpha^{\mathrm{disp}}\int_{\Gamma_{\mathrm{D}}}(\boldsymbol{u}-\boldsymbol{u}^{\mathrm{D}})\cdot\delta\boldsymbol{u}\,\mathrm{d}\Gamma, \tag{3.23}$$

$$\delta W^{\text{B-Rep,rot}}=\alpha^{\mathrm{rot}}\int_{\Gamma_{\mathrm{D}}}(\boldsymbol{\theta}-\boldsymbol{\theta}^{\mathrm{D}})\cdot\delta\boldsymbol{\theta}\,\mathrm{d}\Gamma. \tag{3.24}$$

The redundant superscript m is skipped, because only one domain Ω^{m} is considered.

3.3.3 Element formulation for Neumann boundary conditions

For the B-Rep edge element formulation for Neumann boundary conditions, Eq. (3.5) is used as a starting point. Prescribing the traction force as $\boldsymbol{n}=\boldsymbol{n}^{\mathrm{N}}(\tilde{\xi},t)$ and the moment as $\boldsymbol{m}=\boldsymbol{m}^{\mathrm{N}}(\tilde{\xi},t)$, and integrating along the Neumann boundary Γ_{N}, the virtual work terms for translations and rotations can be computed as

$$\delta W^{\text{B-Rep,disp}}=\int_{\Gamma_{\mathrm{N}}}\boldsymbol{n}^{\mathrm{N}}\cdot\delta\boldsymbol{u}\,\mathrm{d}\Gamma, \tag{3.25}$$

$$\delta W^{\text{B-Rep,rot}}=\int_{\Gamma_{\mathrm{N}}}\boldsymbol{m}^{\mathrm{N}}\cdot\delta\boldsymbol{\theta}\,\mathrm{d}\Gamma. \tag{3.26}$$

3.3.4 Control point forces and stiffness matrices for coupling conditions

In this section the discrete control point force and stiffness matrix expressions for B-Rep edge elements along internal boundaries are derived from the virtual work terms presented in Section 3.3.1 above. In the two subsequent sections, this is done in a very similar manner also for B-Rep edge elements of Dirichlet respectively Neumann type.

Following the isoparametric concept, the displacements are discretized with the same NURBS basis functions as the geometry, see Eq. (2.7), yielding

$$\boldsymbol{u}(\xi,\eta)=\sum_{A=1}^{nm}N_A(\xi,\eta)\mathbf{u}_A. \tag{3.27}$$

In the virtual work terms presented above, displacements at the patch boundaries appear. Such displacements along a physical boundary curve $\mathbf{C}_k(\tilde{\xi})$, see Eq. (2.9), are obtained by evaluating the surface mapping in Eq. (3.27) along a curve in the surface parameter space $\tilde{\mathbf{C}}_k(\tilde{\xi})$, see Eq. (2.8), as

$$\boldsymbol{u}_k(\tilde{\xi})=\boldsymbol{u}_k(\xi_k(\tilde{\xi}),\eta_k(\tilde{\xi}))=\sum_{A=1}^{nm}N_A(\xi_k(\tilde{\xi}),\eta_k(\tilde{\xi}))\mathbf{u}_A. \tag{3.28}$$

This means that the displacements along patch boundaries are computed from control point displacements $\mathbf{u}_A$ as a function of the curve parameter $\tilde{\xi}$. The same discretization and evaluation, of course, also applies to velocities $\boldsymbol{v}$, rotations $\boldsymbol{\theta}$ and angular velocities $\boldsymbol{\omega}$. Introducing the control point sets $\mathcal{M}_{\mathrm{m}}$ resp. $\mathcal{M}_{\mathrm{s}}$ for the subdomains Ω^{m} resp. Ω^{s}, and their union $\mathcal{M}=\mathcal{M}_{\mathrm{m}}\cup\mathcal{M}_{\mathrm{s}}$, the displacement constraint $\boldsymbol{g}^{\mathrm{disp}}$ can be written as

$$\boldsymbol{g}^{\mathrm{disp}}(\tilde{\xi})=\boldsymbol{u}^{\mathrm{m}}(\tilde{\xi})-\boldsymbol{u}^{\mathrm{s}}(\tilde{\xi})=\sum_{I\in\mathcal{M}_m}N_I\mathbf{u}_I-\sum_{J\in\mathcal{M}_s}N_J\mathbf{u}_J=\sum_{A\in\mathcal{M}}\pm N_A\mathbf{u}_A=\sum_{A\in\mathcal{M}}\boldsymbol{\varphi}_A\mathbf{u}_A, \tag{3.29}$$

with

$$\boldsymbol{\varphi}_A=\pm\begin{bmatrix}N_A & & \\ & N_A & \\ & & N_A\end{bmatrix}. \tag{3.30}$$

For $A \in \mathcal{M}_\mathrm{m}$ the sign in φ_A is positive, for $A \in \mathcal{M}_\mathrm{s}$ negative. Introducing the matrix of basis functions $\mathbf{\Phi} = [\ldots, \varphi_A, \ldots]$, $A \in \mathcal{M}$ and the vector of control point displacements $\mathbf{d}^\mathrm{disp} = \{\ldots, \mathbf{u}_A^T, \ldots\}^T$, $A \in \mathcal{M}$, the sum in Eq. (3.29) can be replaced by a matrix multiplication. The displacement constraint can then be written as

$$\boldsymbol{g}^\mathrm{disp} = \mathbf{\Phi}\,\mathbf{d}^\mathrm{disp}. \tag{3.31}$$

For the rotational case, the vector of control point rotations $\mathbf{d}^\mathrm{rot} = \{\ldots, \boldsymbol{\theta}_A^T, \ldots\}^T$ with $A \in \mathcal{M}$ is introduced, which allows expressing the rotational constraint similarly as

$$\boldsymbol{g}^\mathrm{rot} = \mathbf{\Phi}\,\mathbf{d}^\mathrm{rot}. \tag{3.32}$$

To facilitate a consistent derivation for translations, rotations and different element formulations, a generally applicable approach for penalty-based constraints is desired. From Eqs. (3.16) and (3.20), one can recognize the general form of the virtual work for a weakly enforced penalty constraint along a domain Γ as

$$\delta W^\mathrm{p} = \alpha \int_\Gamma \boldsymbol{g} \cdot \delta \boldsymbol{g}\, \mathrm{d}\Gamma. \tag{3.33}$$

Exploiting the fact that

$$\delta W^\mathrm{p} = \frac{\partial W^\mathrm{p}}{\partial \boldsymbol{g}} \delta \boldsymbol{g}, \tag{3.34}$$

the potential of a weakly enforced penalty constraint can, in a general form, be identified as

$$W^\mathrm{p} = \frac{1}{2} \alpha \int_\Gamma \boldsymbol{g}^2\, \mathrm{d}\Gamma. \tag{3.35}$$

One can verify this by inserting Eq. (3.35) into (3.34). Based on W^p the general form of a penalty force vector is defined as the partial derivative of the potential with respect to the vector of displacements $\mathbf{d}$ as

$$(\mathbf{f}^\mathrm{p})^T = \frac{\partial W}{\partial \mathbf{d}} = \alpha \int_\Gamma \boldsymbol{g}^T \frac{\partial \boldsymbol{g}}{\partial \mathbf{d}}\, \mathrm{d}\Gamma. \tag{3.36}$$

The general form of a penalty stiffness matrix is then defined as

$$\mathbf{K}^\mathrm{p} = \frac{\partial^2 W}{\partial \mathbf{d} \partial \mathbf{d}} = \alpha \int_\Gamma \left[\left(\frac{\partial \boldsymbol{g}}{\partial \mathbf{d}} \right)^T \frac{\partial \boldsymbol{g}}{\partial \mathbf{d}} + \boldsymbol{g}^T \frac{\partial^2 \boldsymbol{g}}{\partial \mathbf{d} \partial \mathbf{d}} \right] \mathrm{d}\Gamma. \tag{3.37}$$

For a linear constraint $\boldsymbol{g}$ the second term containing the second derivative of the constraint vanishes. By inserting the different types of constraints $\boldsymbol{g}$ into (3.35), (3.36) and (3.37), the potential, the vector of control point forces and the stiffness matrix can be obtained, respectively. The same is valid for the rotational contributions. Thus, by inserting the displacement constraint $\boldsymbol{g}^\mathrm{disp}$ (3.31) and the rotation constraint $\boldsymbol{g}^\mathrm{rot}$ (3.32), respectively, into Eq. (3.35), one obtains the translational and rotational contributions to the potential

$$W_\mathrm{C}^\mathrm{B\text{-}Rep,disp} = \frac{1}{2} \alpha^\mathrm{disp} \int_{\Gamma_\mathrm{C}^\mathrm{m}} (\mathbf{d}^\mathrm{disp})^T \mathbf{\Phi}^T \mathbf{\Phi}\, \mathbf{d}^\mathrm{disp}\, \mathrm{d}\Gamma, \tag{3.38}$$

$$W_\mathrm{C}^\mathrm{B\text{-}Rep,rot} = \frac{1}{2} \alpha^\mathrm{rot} \int_{\Gamma_\mathrm{C}^\mathrm{m}} (\mathbf{d}^\mathrm{rot})^T \mathbf{\Phi}^T \mathbf{\Phi}\, \mathbf{d}^\mathrm{rot}\, \mathrm{d}\Gamma. \tag{3.39}$$

Inserting (3.31) into Eq. (3.36) gives the vector of control point forces for penalty-based B-Rep edge elements along internal boundaries as

$$\mathbf{f}_\mathrm{C}^\mathrm{B\text{-}Rep} = \alpha^\mathrm{disp} \int_{\Gamma_\mathrm{C}^\mathrm{m}} \mathbf{\Phi}^T \mathbf{\Phi}\, \mathrm{d}\Gamma\, \mathbf{d}^\mathrm{disp}, \quad \mathbf{f}_{A,\mathrm{C}}^\mathrm{B\text{-}Rep} = \alpha^\mathrm{disp} \int_{\Gamma_\mathrm{C}^\mathrm{m}} \varphi_A \varphi_B\, \mathrm{d}\Gamma\, \mathbf{u}_B, \tag{3.40}$$

where $A, B \in \mathcal{M}$ and where the summation over repeated indices applies. Equivalently, the vector of control point moments is obtained by inserting (3.32) into the general form (3.36) as

$$\mathbf{m}_\mathrm{C}^\mathrm{B\text{-}Rep} = \alpha^\mathrm{rot} \int_{\Gamma_\mathrm{C}^\mathrm{m}} \mathbf{\Phi}^T \mathbf{\Phi}\, \mathrm{d}\Gamma\, \mathbf{d}^\mathrm{rot}, \quad \mathbf{m}_{A,\mathrm{C}}^\mathrm{B\text{-}Rep} = \alpha^\mathrm{rot} \int_{\Gamma_\mathrm{C}^\mathrm{m}} \varphi_A \varphi_B\, \mathrm{d}\Gamma\, \boldsymbol{\theta}_B. \tag{3.41}$$

The translational resp. rotational stiffness matrix contributions are obtained by inserting (3.31) resp. (3.32) into Eq. (3.37)

$$\mathbf{K}_{\mathrm{C}}^{\text{B-Rep,disp}} = \alpha^{\text{disp}} \int_{\Gamma_{\mathrm{C}}^{\mathrm{m}}} \mathbf{\Phi}^T \mathbf{\Phi} \, \mathrm{d}\Gamma, \quad \mathbf{K}_{AB,\mathrm{C}}^{\text{B-Rep,disp}} = \alpha^{\text{disp}} \int_{\Gamma_{\mathrm{C}}^{\mathrm{m}}} \varphi_A \varphi_B \, \mathrm{d}\Gamma, \tag{3.42}$$

$$\mathbf{K}_{\mathrm{C}}^{\text{B-Rep,rot}} = \alpha^{\text{rot}} \int_{\Gamma_{\mathrm{C}}^{\mathrm{m}}} \mathbf{\Phi}^T \mathbf{\Phi} \, \mathrm{d}\Gamma, \quad \mathbf{K}_{AB,\mathrm{C}}^{\text{B-Rep,rot}} = \alpha^{\text{rot}} \int_{\Gamma_{\mathrm{C}}^{\mathrm{m}}} \varphi_A \varphi_B \, \mathrm{d}\Gamma, \tag{3.43}$$

Since the translational and rotational contributions are formally identical, a more concise notation is achieved by using generalized quantities, identified by an overline as $\overline{(\cdot)}$: the generalized control point displacements $\overline{\mathbf{u}}_A = \{\mathbf{u}_A^T, \boldsymbol{\theta}_A^T\}^T$, the generalized force vector $\bar{\mathbf{f}}_A = \{\mathbf{f}_A^T, \mathbf{m}_A^T\}^T$, the extended diagonal matrix of basis functions $\overline{\boldsymbol{\varphi}}_A = \pm\mathrm{diag}\{N_A, N_A, N_A, N_A, N_A, N_A\}$, and the diagonal matrix of penalty factors $\overline{\boldsymbol{\alpha}} = \mathrm{diag}\{\alpha^{\text{disp}}, \alpha^{\text{disp}}, \alpha^{\text{disp}}, \alpha^{\text{rot}}, \alpha^{\text{rot}}, \alpha^{\text{rot}}\}$. Equations (3.40) and (3.41) can then be summarized as

$$\bar{\mathbf{f}}_{A,\mathrm{C}}^{\text{B-Rep}} = \overline{\boldsymbol{\alpha}} \int_{\Gamma_{\mathrm{C}}^{m}} \overline{\boldsymbol{\varphi}}_A \overline{\boldsymbol{\varphi}}_B \, \mathrm{d}\Gamma \, \overline{\mathbf{u}}_B. \tag{3.44}$$

Furthermore, the generalized penalty stiffness matrix can be written as

$$\overline{\mathbf{K}}_{AB,\mathrm{C}}^{\text{B-Rep}} = \overline{\boldsymbol{\alpha}} \int_{\Gamma_{\mathrm{C}}^{\mathrm{m}}} \overline{\boldsymbol{\varphi}}_A \overline{\boldsymbol{\varphi}}_B \, \mathrm{d}\Gamma. \tag{3.45}$$

3.3.5 Control point forces and stiffness matrices for Dirichlet boundary conditions

Similar to the coupling conditions above, the control point force and stiffness matrix expressions are derived for Dirichlet boundary conditions in this section. Here, the displacements and rotations are discretized as

$$\boldsymbol{u} = \sum_{A \in \mathcal{M}} \varphi_A \mathbf{u}_A = \mathbf{\Phi} \mathbf{d}^{\text{disp}} \quad \text{and} \quad \boldsymbol{\theta} = \sum_{A \in \mathcal{M}} \varphi_A \boldsymbol{\theta}_A = \mathbf{\Phi} \mathbf{d}^{\text{disp}}, \tag{3.46}$$

with $\mathbf{\Phi} = [\ldots, \varphi_A, \ldots]$, $A \in \mathcal{M}$, where $\mathcal{M}$ is the set of all control points in the considered domain and with φ_A from Eq. (3.30) with only positive signs. The translational and rotational constraints from (3.21) and (3.22) can be consequently expressed as

$$\boldsymbol{g}^{\text{disp}} = \mathbf{\Phi} \mathbf{d}^{\text{disp}} - \boldsymbol{u}^{\mathrm{D}}, \tag{3.47}$$

$$\boldsymbol{g}^{\text{rot}} = \mathbf{\Phi} \mathbf{d}^{\text{disp}} - \boldsymbol{\theta}^{\mathrm{D}}. \tag{3.48}$$

To obtain the translational and rotational contributions of the potential, these Dirichlet constraints are inserted into the general form (3.35), respectively, leading to

$$W_{\mathrm{D}}^{\text{B-Rep,disp}} = \frac{1}{2} \alpha^{\text{disp}} \int_{\Gamma_{\mathrm{D}}} \left[(\mathbf{d}^{\text{disp}})^T \mathbf{\Phi}^T \mathbf{\Phi} \mathbf{d}^{\text{disp}} - 2 (\mathbf{d}^{\text{disp}})^T \mathbf{\Phi}^T \boldsymbol{u}^{\mathrm{D}} + \left(\boldsymbol{u}^{\mathrm{D}}\right)^T \boldsymbol{u}^{\mathrm{D}} \right] \mathrm{d}\Gamma, \tag{3.49}$$

$$W_{\mathrm{D}}^{\text{B-Rep,rot}} = \frac{1}{2} \alpha^{\text{rot}} \int_{\Gamma_{\mathrm{D}}} \left[(\mathbf{d}^{\text{rot}})^T \mathbf{\Phi}^T \mathbf{\Phi} \mathbf{d}^{\text{rot}} - 2 (\mathbf{d}^{\text{rot}})^T \mathbf{\Phi}^T \boldsymbol{\theta}^{\mathrm{D}} + \left(\boldsymbol{\theta}^{\mathrm{D}}\right)^T \boldsymbol{\theta}^{\mathrm{D}} \right] \mathrm{d}\Gamma. \tag{3.50}$$

By either computing the partial derivative of $W_{\mathrm{D}}^{\text{B-Rep,disp}}$ and $W_{\mathrm{D}}^{\text{B-Rep,rot}}$ with respect to $\mathbf{d}^{\text{disp}}$ and $\mathbf{d}^{\text{rot}}$, or by inserting the Dirichlet constraints (3.47) and (3.48) into Eq. (3.36), the control point forces and moments, respectively, are obtained as

$$\mathbf{f}_{\mathrm{D}}^{\text{B-Rep}} = \alpha^{\text{disp}} \int_{\Gamma_{\mathrm{D}}} \left(\mathbf{\Phi}^T \mathbf{\Phi} \mathbf{d}^{\text{disp}} - \mathbf{\Phi}^T \boldsymbol{u}^{\mathrm{D}} \right) \mathrm{d}\Gamma, \quad \mathbf{f}_{A,\mathrm{D}}^{\text{B-Rep}} = \alpha^{\text{disp}} \int_{\Gamma_{\mathrm{D}}} \left(\varphi_A \varphi_B \mathbf{u}_B - \varphi_A \boldsymbol{u}^{\mathrm{D}} \right) \mathrm{d}\Gamma, \tag{3.51}$$

$$\mathbf{m}_{\mathrm{D}}^{\text{B-Rep}} = \alpha^{\text{rot}} \int_{\Gamma_{\mathrm{D}}} \left(\mathbf{\Phi}^T \mathbf{\Phi} \mathbf{d}^{\text{rot}} - \mathbf{\Phi}^T \boldsymbol{\theta}^{\mathrm{D}} \right) \mathrm{d}\Gamma, \quad \mathbf{f}_{A,\mathrm{D}}^{\text{B-Rep}} = \alpha^{\text{rot}} \int_{\Gamma_{\mathrm{D}}} \left(\varphi_A \varphi_B \boldsymbol{\theta}_B - \varphi_A \boldsymbol{\theta}^{\mathrm{D}} \right) \mathrm{d}\Gamma. \tag{3.52}$$

The stiffness matrices can again be obtained by either differentiating (3.51) and (3.52) with respect to the $\mathbf{d}^{\text{disp}}$ and $\mathbf{d}^{\text{rot}}$, or by inserting (3.47) and (3.48) into Eq. (3.37). As can be seen from Eqs. (3.51) and (3.52), only the first terms are dependent on control point displacements and rotations, while the second terms depend on prescribed displacements and rotations, respectively. That is, only the first terms provide a contribution to the stiffness matrices for Dirichlet boundary conditions, which are obtained as

$$\mathbf{K}_{\mathrm{D}}^{\text{B-Rep,disp}} = \alpha^{\text{disp}} \int_{\Gamma_{\mathrm{D}}} \mathbf{\Phi}^T \mathbf{\Phi} \, \mathrm{d}\Gamma, \quad \mathbf{K}_{AB,\mathrm{D}}^{\text{B-Rep,disp}} = \alpha^{\text{disp}} \int_{\Gamma_{\mathrm{D}}} \varphi_A \varphi_B \, \mathrm{d}\Gamma, \tag{3.53}$$

$$\mathbf{K}_{\mathrm{D}}^{\text{B-Rep,rot}} = \alpha^{\text{rot}} \int_{\Gamma_{\mathrm{D}}} \mathbf{\Phi}^T \mathbf{\Phi} \, \mathrm{d}\Gamma, \quad \mathbf{K}_{AB,\mathrm{D}}^{\text{B-Rep,rot}} = \alpha^{\text{rot}} \int_{\Gamma_{\mathrm{D}}} \varphi_A \varphi_B \, \mathrm{d}\Gamma. \tag{3.54}$$

Although this seems formally identical to the case of coupling conditions, it should be noted that $\boldsymbol{\Phi}$ and φ_A differ slightly since only basis functions of one domain instead of two are involved for Dirichlet boundary conditions. Employing the generalized quantities introduced in the previous section and the generalized displacement vector $\overline{\boldsymbol{u}} = \{\boldsymbol{u}^T, \boldsymbol{\theta}^T\}^T$, Eqs. (3.51) and (3.52) can be summarized by

$$\overline{\mathbf{f}}_{A,\mathrm{D}}^{\text{B-Rep}} = \overline{\boldsymbol{\alpha}} \int_{\Gamma_\mathrm{D}} \left(\overline{\varphi}_A \overline{\varphi}_B \, \overline{\mathbf{u}}_B - \overline{\varphi}_A \overline{\boldsymbol{u}}^\mathrm{D} \right) \mathrm{d}\Gamma. \tag{3.55}$$

In the same way Equations (3.53) and (3.54) can be concisely expressed as

$$\overline{\mathbf{K}}_{AB,\mathrm{D}}^{\text{B-Rep}} = \overline{\boldsymbol{\alpha}} \int_{\Gamma_\mathrm{D}} \overline{\varphi}_A \overline{\varphi}_B \, \mathrm{d}\Gamma, \tag{3.56}$$

which is again similar, but not identical to the case of coupling conditions.

3.3.6 Control point forces for Neumann boundary conditions

For Neumann boundary conditions the translational potential corresponding to Eq. (3.25) is computed as the integral of the scalar product of a prescribed traction force $\boldsymbol{n}^\mathrm{N}(\tilde{\xi}, t)$ and boundary displacement $\boldsymbol{u}(\tilde{\xi})$ over the Neumann boundary Γ_N:

$$W^{\text{B-Rep,disp}} = \int_{\Gamma_\mathrm{N}} \boldsymbol{n}^\mathrm{N} \cdot \boldsymbol{u} \, \mathrm{d}\Gamma. \tag{3.57}$$

Similarly the rotational potential corresponding to Eq. (3.26) is computed as

$$W^{\text{B-Rep,rot}} = \int_{\Gamma_\mathrm{N}} \boldsymbol{m}^\mathrm{N} \cdot \boldsymbol{\theta} \, \mathrm{d}\Gamma, \tag{3.58}$$

with the prescribed moment $\boldsymbol{m}^\mathrm{N}(\tilde{\xi}, t)$ and the boundary rotation $\boldsymbol{\theta}(\tilde{\xi})$. With the same discretization for displacements and rotations as in the case of Dirichlet boundary conditions, see Eq. (3.46), the potentials can be written as

$$W^{\text{B-Rep,disp}} = \int_{\Gamma_\mathrm{N}} \left(\boldsymbol{n}^\mathrm{N}\right)^T \boldsymbol{\Phi} \, \mathbf{d}^{\text{disp}} \, \mathrm{d}\Gamma, \tag{3.59}$$

$$W^{\text{B-Rep,rot}} = \int_{\Gamma_\mathrm{N}} \left(\boldsymbol{m}^\mathrm{N}\right)^T \boldsymbol{\Phi} \, \mathbf{d}^{\text{rot}} \, \mathrm{d}\Gamma. \tag{3.60}$$

Differentiating the translational and rotational potentials with respect to $\mathbf{d}^{\text{disp}}$ and $\mathbf{d}^{\text{rot}}$, respectively, the control point forces and moments are obtained as

$$\mathbf{f}^{\text{B-Rep}} = \int_{\Gamma_\mathrm{N}} \boldsymbol{\Phi}^T \boldsymbol{n}^\mathrm{N} \, \mathrm{d}\Gamma, \quad \mathbf{f}_A^{\text{B-Rep}} = \int_{\Gamma_\mathrm{N}} \varphi_A \boldsymbol{n}^\mathrm{N} \, \mathrm{d}\Gamma, \tag{3.61}$$

$$\mathbf{m}^{\text{B-Rep}} = \int_{\Gamma_\mathrm{N}} \boldsymbol{\Phi}^T \boldsymbol{m}^\mathrm{N} \, \mathrm{d}\Gamma, \quad \mathbf{m}_A^{\text{B-Rep}} = \int_{\Gamma_\mathrm{N}} \varphi_A \boldsymbol{m}^\mathrm{N} \, \mathrm{d}\Gamma. \tag{3.62}$$

As can be seen, these force and moment expressions do not contain control point displacements $\mathbf{d}^{\text{disp}}$ or rotations $\mathbf{d}^{\text{rot}}$. Computing the corresponding stiffness matrices would require another partial differentiation with respect to $\mathbf{d}^{\text{disp}}$ and $\mathbf{d}^{\text{rot}}$, respectively. Thus, the stiffness vanishes. This makes clear that no additional stiffness is introduced by B-Rep edge elements for Neumann boundary conditions. Since traction forces and moments are prescribed directly, it can be furthermore seen that Neumann boundary conditions do not require a penalty approach. The obtained control point forces and moments from B-Rep edge elements for Neumann boundary conditions can therefore be interpreted as consistently computed forces and moments. With generalized displacements and the generalized traction $\overline{\boldsymbol{t}} = \{\boldsymbol{n}^T, \boldsymbol{m}^T\}^T$ the control point forces and moments can be summarized as

$$\overline{\mathbf{f}}_{A,\mathrm{N}}^{\text{B-Rep}} = \int_{\Gamma_\mathrm{N}} \overline{\varphi}_A \overline{\boldsymbol{t}}^\mathrm{N} \, \mathrm{d}\Gamma. \tag{3.63}$$

3.4 The enhanced B-Rep edge element formulation – Constraints on shell normals

3.4.1 Introduction

The standard B-Rep edge element formulation imposing direct constraints on the respective translational and rotational DOFs as presented above and in [54], enforces all mechanically required boundary conditions for Reissner-Mindlin shells, see Eq. (3.6). This is confirmed by the accurate results obtained for several benchmark problems

in [54]. In particular, the standard B-Rep edge element formulation, enforces rotational continuity (G^1 continuity or a consistent angle) between patches solely based on rotational DOFs. Obviously, the quality of coupling and boundary conditions strongly depends on the quality of the involved control point DOFs. That is, even the best coupling approach cannot work as intended, if the underlying control point rotations are inaccurate. In fact, it turned out that the rotational DOFs of the Reissner-Mindlin shell tend to show large, unrealistic rotations, especially for trimmed elements in dynamic large deformation problems. The reasons for this effect are manifold. First of all, for critical time step reasons, the rotational inertias are scaled up substantially [73]. Even if this scaling does not affect the overall results, the actual control point rotations may differ significantly from the case without scaling. Second, as described in Chapter 5, control points of very low mass and stiffness caused by small trimmed elements show, in many cases, unstable behavior, particularly in the rotations. Although this unstable behavior can be avoided by the approach proposed in Chapter 5, the accuracy of the control point rotations may still be affected. However, it should again be noted that these inaccuracies in the rotational DOFs have very little influence on the actual results as long as no patch coupling is involved.

The large deformation cantilever beam example [142] depicted in Figure 3.2 shall demonstrate the possible coupling deficiencies of the standard B-Rep element formulation. This beam consists of two cubic NURBS patches, trimmed such that no small trimmed elements appear and thus no stabilization is required, see Chapter 5. A line load P linearly increasing over the simulation time of $t = 0.01\,\mathrm{s}$ is applied at the tip of the beam. Since the load and the deformation of the beam increase during the analysis, the standard B-Rep element formulation achieves accurate coupling results until a certain point, see the deformed shape at $t = 0.0085\,\mathrm{s}$ in Figure 3.2. Shortly before reaching the maximum load, however, the rotational coupling condition "fails", leading to a sudden and distinct kink along the coupling edge between the two patches, clearly shown by the deformed shape at $t = 0.0090\,\mathrm{s}$ in Figure 3.2. The depicted control points furthermore show the expected behavior without large displacements, which would be an indicator for instabilities, see Chapter 5. The reason for the failing rotational coupling are inaccuracies in the rotational DOFs, evolving over simulation time.

It is worth noting that, although the rotational coupling does not work as intended, the weakly formulated coupling constraint in Eq. (3.20) itself may still be fulfilled. One can, for example, imagine a solution in which the effective rotations on both patch edges are identical (the constraint is therefore fulfilled), although the individual control point rotations may have completely different values, canceling each other on each edge. Figure 3.3 depicts the y-rotations of control points of patch 1 and 2 (marked in blue and black in Figure 3.2, respectively), which are involved in the same B-Rep element formulation (marked in red in Figure 3.2). This plot shows reasonable y-rotations until shortly before $t = 0.009\,\mathrm{s}$, followed by large rotations quite evenly distributed in both, the positive and negative direction. This indicates that the weak constraint is, in total, still fulfilled, but with meaningless control point rotations and therefore bad results. Such effects are, in the literature, commonly denoted as *spurious checkerboard modes*, see for instance [134], and a general drawback of weak constraint enforcement methods. The fact that the control points can perform such large rotations is facilitated by trimming and the thereby loosened connection between control points and the material domain. Indeed, the largest rotations are observed for the outermost control points with low mass and stiffness. To increase the accuracy and numerical robustness of the coupling condition along trimmed boundaries, an additional constraint on the rotation around the boundary curve tangent based on translational DOFs only is introduced here.

This additional constraint is based on a Total Lagrangian normal coupling approach for thin rotation-free KL shells proposed by Benson et al. [47]. In contrast to [47], the constraint is (i) not enforced point-wise, but in a weak integral sense via B-Rep edge elements, and (ii) applied to RM shells. A B-Rep edge element formulation entirely based on translational DOFs for (i) C^0 continuity as in the standard formulation and (ii) a consistent angle between patches with this novel approach would be universally applicable and, of course, well-suited for rotation-free Kirchhoff-Love shell elements, see [143]. However, the focus of this thesis is on shear deformable Reissner-Mindlin shells.

In the following, the translational DOF-based constraint on the rotation around the boundary (trimming) curve is presented for coupling and Dirichlet boundary conditions. It should be noted that this constraint is intended to be applied in addition to the displacement and rotation constraint presented in Section 3.3 above.

3.4.2 Element formulation for coupling conditions

The goal of this constraint is to preserve the angle around the boundary curved tangent $\boldsymbol{a}_\mathrm{t}$ between two (trimmed) patches throughout the simulation, only via translational DOFs. Recalling Eq. (3.6), the virtual work expression for Reissner-Mindlin shells, it can be seen that this constraint only entails a moment m_t around the curve tangent vector $\boldsymbol{a}_\mathrm{t}$, but *not* a moment m_u around $\boldsymbol{a}_\mathrm{u}$. The latter still needs to be enforced via rotational DOFs as described in Section 3.3 above.

In the following, the local orthonormal coordinate systems ($\boldsymbol{a}_\mathrm{t}$, $\boldsymbol{a}_\mathrm{u}$, $\boldsymbol{a}_3$) resp. ($\boldsymbol{A}_\mathrm{t}$, $\boldsymbol{A}_\mathrm{u}$, $\boldsymbol{A}_3$) in the current resp. initial configuration as introduced in Section 2.3.1 are used. The arbitrary curvilinear surface coordinates Θ^1 and Θ^2 are

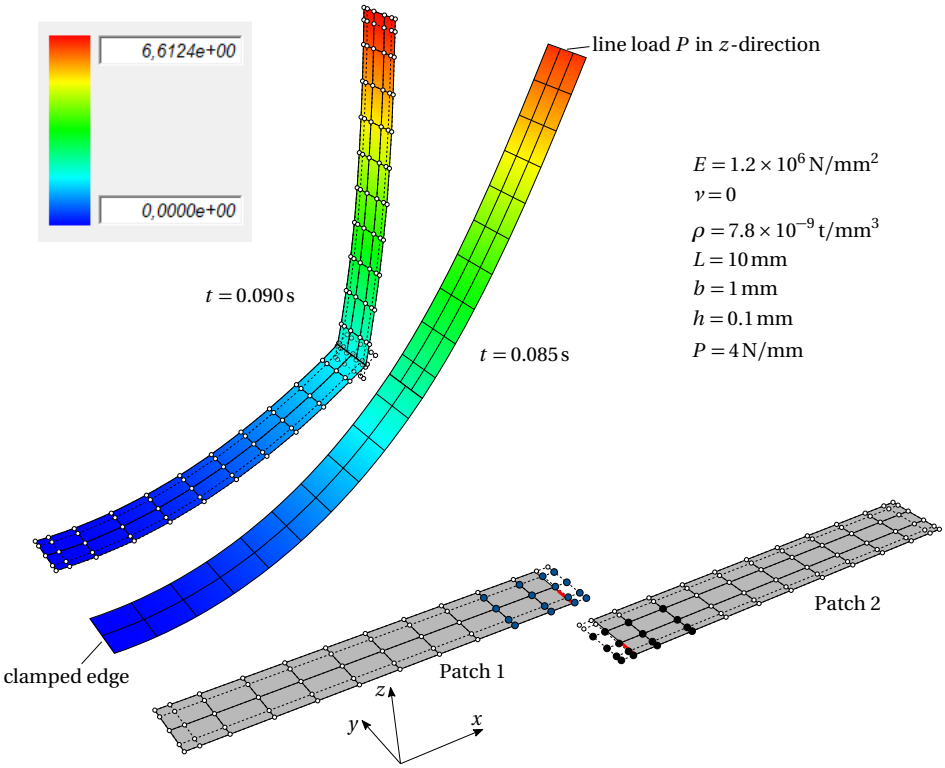

Figure 3.2: Trimmed NURBS-based multi-patch cantilever beam ($p = q = 3$) loaded by a linearly increasing end shear force in z-direction [142]: The two trimmed patches are coupled by standard B-Rep elements enforcing the rotational constraints only via rotational DOFs. No small trimmed elements appear. The deformed shape at $t = 0.009\,\mathrm{s}$, obtained by an explicit dynamic analysis, shows a distinct kink between the patches. The color plot indicates z-displacements in mm.

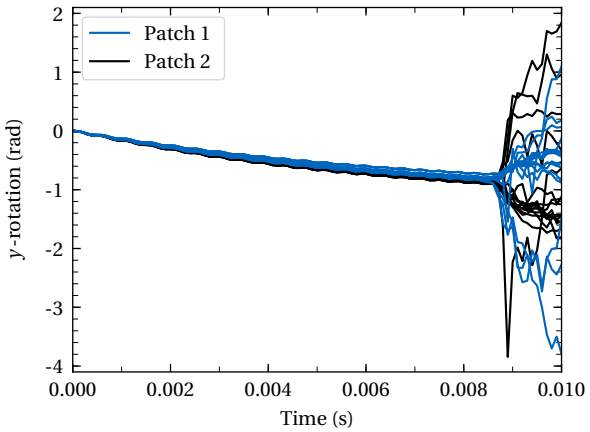

Figure 3.3: Trimmed NURBS-based multi-patch cantilever beam using standard B-Rep elements for the coupling: Rotations around the y-direction for all control points of patch 1 and patch 2, marked in blue and black in Figure 3.2. These control points are all involved in the same B-Rep element marked in red in Figure 3.2.

specifically defined as the NURBS parameters ξ and η, respectively. Also the boundary curve parameter $\tilde{\Theta}$ is now specifically defined as the trimming curve parameter $\tilde{\xi}$. The current angle between two patches is defined as the angle φ between the master and slave surface unit normal vectors $\boldsymbol{a}_3^{\mathrm{m}}$ and $\boldsymbol{a}_3^{\mathrm{s}}$, see Figure 3.4. Since $\boldsymbol{a}_{\mathrm{t}}$ is perpendicular to both $\boldsymbol{a}_3^{\mathrm{m}}$ and $\boldsymbol{a}_3^{\mathrm{s}}$, φ describes the rotation around $\boldsymbol{a}_{\mathrm{t}}$.

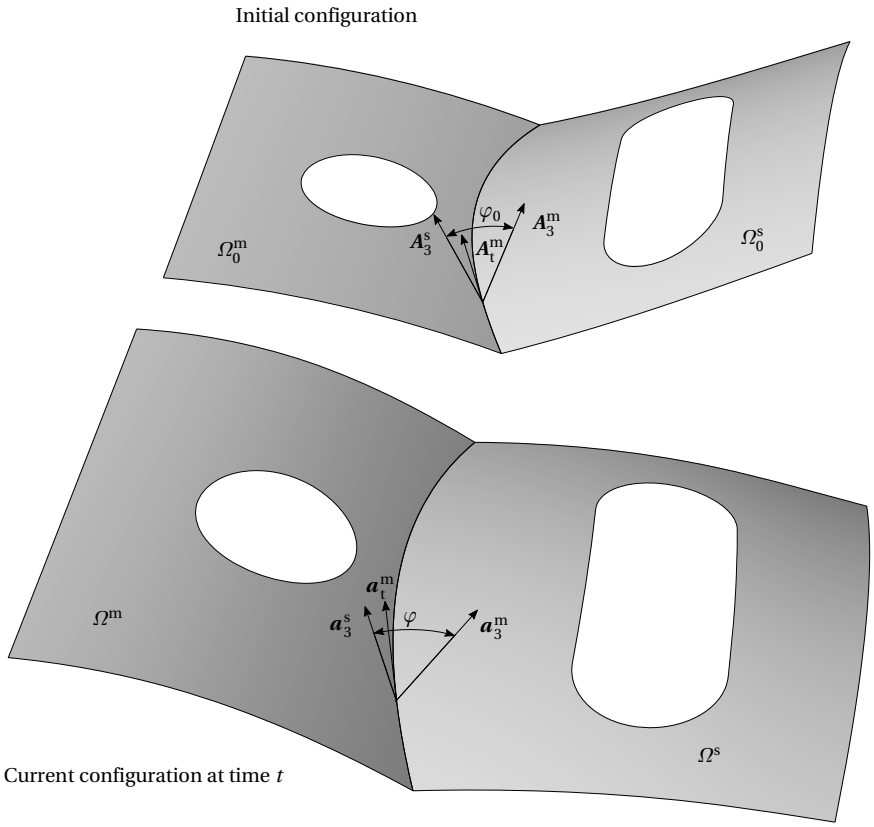

Figure 3.4: Coupling kinematics between two trimmed NURBS surfaces (master and slave).

The unit normal vectors $\boldsymbol{a}_3^{(i)}$, $(i) = \mathrm{m}, \mathrm{s}$ on the master and slave surface $\mathbf{S}^{\mathrm{m}}$ and $\mathbf{S}^{\mathrm{s}}$, respectively, are defined as

$$\boldsymbol{a}_3^{(i)} = \frac{\hat{\boldsymbol{a}}_3^{(i)}}{\|\hat{\boldsymbol{a}}_3^{(i)}\|}, \tag{3.64}$$

$$\hat{\boldsymbol{a}}_3^{(i)} = \boldsymbol{a}_1^{(i)} \times \boldsymbol{a}_2^{(i)}, \tag{3.65}$$

with the surface tangent vectors $\boldsymbol{a}_1^{(i)}$ and $\boldsymbol{a}_2^{(i)}$ along the ξ- and η-directions

$$\boldsymbol{a}_1^{(i)} = \frac{\partial \mathbf{S}^{(i)}}{\partial \xi} = \sum_A \frac{\partial N_A^{(i)}}{\partial \xi} \mathbf{P}_A, \tag{3.66}$$

$$\boldsymbol{a}_2^{(i)} = \frac{\partial \mathbf{S}^{(i)}}{\partial \eta} = \sum_A \frac{\partial N_A^{(i)}}{\partial \eta} \mathbf{P}_A. \tag{3.67}$$

Differentiating the master surface $\mathbf{S}^{\mathrm{m}}$ with respect to the curve parameter $\tilde{\xi}$ of curve $\mathbf{C}(\tilde{\xi})$ and normalization gives the unit tangent vector on the master (trimming) curve as

$$\boldsymbol{a}_{\mathrm{t}} = \frac{\hat{\boldsymbol{a}}_{\mathrm{t}}}{\|\hat{\boldsymbol{a}}_{\mathrm{t}}\|}, \quad \hat{\boldsymbol{a}}_{\mathrm{t}} = \frac{\partial \mathbf{S}^m}{\partial \tilde{\xi}} = \frac{\partial \mathbf{S}^m}{\partial \xi}\frac{\partial \xi}{\partial \tilde{\xi}} + \frac{\partial \mathbf{S}^m}{\partial \eta}\frac{\partial \eta}{\partial \tilde{\xi}}. \tag{3.68}$$

As mentioned above, φ shall be expressed with translational DOFs only. This can be done via the scalar and cross product definitions

$$\boldsymbol{a} \cdot \boldsymbol{b} = \|\boldsymbol{a}\| \|\boldsymbol{b}\| \cos(\theta), \tag{3.69}$$

$$\boldsymbol{a} \times \boldsymbol{b} = \|\boldsymbol{a}\| \|\boldsymbol{b}\| \sin(\theta)\, \boldsymbol{n}, \tag{3.70}$$

where $\boldsymbol{a}, \boldsymbol{b} \in \mathbb{R}^3$, are two arbitrary three-dimensional vectors with their Euclidean norms $\|\boldsymbol{a}\|$, $\|\boldsymbol{b}\|$; θ is the angle between $\boldsymbol{a}$ and $\boldsymbol{b}$, and $\boldsymbol{n} \in \mathbb{R}^3$ is a unit vector normal to $\boldsymbol{a}$ and $\boldsymbol{b}$. Transferred to the present case in Figure 3.4, φ and φ_0 can be expressed as

$$\cos(\varphi) = \boldsymbol{a}_3^{\mathrm{m}} \cdot \boldsymbol{a}_3^{\mathrm{s}}, \tag{3.71}$$
$$\sin(\varphi) = \boldsymbol{a}_{\mathrm{t}}^{\mathrm{m}} \cdot (\boldsymbol{a}_3^{\mathrm{m}} \times \boldsymbol{a}_3^{\mathrm{s}}), \tag{3.72}$$

and

$$\cos(\varphi_0) = \boldsymbol{A}_3^{\mathrm{m}} \cdot \boldsymbol{A}_3^{\mathrm{s}}, \tag{3.73}$$
$$\sin(\varphi_0) = \boldsymbol{A}_{\mathrm{t}}^{\mathrm{m}} \cdot (\boldsymbol{A}_3^{\mathrm{m}} \times \boldsymbol{A}_3^{\mathrm{s}}), \tag{3.74}$$

as in [47]. This establishes a direct relation between φ and the translational DOFs in $\mathbf{P}_A$ via Eqs. (3.64)–(3.68).

Since the aim is to preserve the initial angle φ_0 (at $t = 0$) between two patches, the constraint should be on the deviation between the current and the initial angle $\psi = (\varphi - \varphi_0) = 0$. Because ψ should be kept small and close to zero, $\psi \approx \sin(\psi)$ holds and the constraint [47] can be formulated as

$$g^{\tan}(\tilde{\xi}) = \sin(\psi) = 0 \tag{3.75}$$
$$= \sin(\varphi - \varphi_0) = 0 \tag{3.76}$$
$$= \sin(\varphi)\cos(\varphi_0) - \cos(\varphi)\sin(\varphi_0) = 0 \tag{3.77}$$
$$= \boldsymbol{a}_{\mathrm{t}}^{\mathrm{m}} \cdot (\boldsymbol{a}_3^{\mathrm{m}} \times \boldsymbol{a}_3^{\mathrm{s}})\cos(\varphi_0) - (\boldsymbol{a}_3^{\mathrm{m}} \cdot \boldsymbol{a}_3^{\mathrm{s}})\sin(\varphi_0) = 0, \tag{3.78}$$

where the superscript 'tan' indicates the rotational coupling around the curve tangent $\boldsymbol{a}_{\mathrm{t}}$ and where the trigonometric addition theorems are exploited in order to enable using Eqs. (3.71) and (3.72) directly. The same applies for $\cos(\varphi_0)$ and $\sin(\varphi_0)$ evaluated at $t = 0$.

Please note that

- for $\varphi_0 = 0°$: $\cos(\varphi_0) = 1$, $\sin(\varphi_0) = 0$ and the constraint simplifies to $g^{\tan} = \sin(\varphi) = \boldsymbol{a}_{\mathrm{t}}^{\mathrm{m}} \cdot (\boldsymbol{a}_3^{\mathrm{m}} \times \boldsymbol{a}_3^{\mathrm{s}}) = 0$,
- for $\varphi_0 = 90°$: $\cos(\varphi_0) = 0$, $\sin(\varphi_0) = 1$ and the constraint simplifies to $g^{\tan} = -\cos(\varphi) = \boldsymbol{a}_3^{\mathrm{m}} \cdot \boldsymbol{a}_3^{\mathrm{s}} = 0$.

It is also worth noting that $g^{\tan}$ is a scalar constraint, in contrast to the vector-valued constraints in Section 3.3.

Inserting the constraint into the general virtual work expression for weak penalty-based constraints (3.33) and integration along the master curve yields

$$\delta W^{\text{B-Rep,tan}} = \alpha^{\tan} \int_{\Gamma_{\mathrm{C}}^{\mathrm{m}}} g^{\tan}(\mathbf{d}^{\mathrm{disp}})\, \delta g^{\tan}(\mathbf{d}^{\mathrm{disp}})\, \mathrm{d}\Gamma = \alpha^{\tan} \int_{\Gamma_{\mathrm{C}}^{\mathrm{m}}} \sin(\varphi - \varphi_0)\, \delta \left(\sin(\varphi - \varphi_0)\right) \mathrm{d}\Gamma, \tag{3.79}$$

where $\mathbf{d}^{\mathrm{disp}}$ again denotes the vector of control point displacements and $\alpha^{\tan}$ the corresponding penalty factor. For the sake of brevity, the superscript 'disp' is skipped within the remainder of this section, since only translational DOFs are involved anyway. Thus, the vector of control point displacements is in the following denoted as $\mathbf{d} = \{\ldots, \mathbf{d}_A^T, \ldots\}^T$, with $\mathbf{d}_A^T = \{\mathrm{u}_{A1}, \mathrm{u}_{A2}, \mathrm{u}_{A3}\}^T$.

3.4.3 Element formulation for Dirichlet boundary conditions

This type of angular constraint can, of course, also be used to enforce rotational Dirichlet boundary conditions. In this case only one domain Ω with one boundary Γ is considered and the slave unit normal vector $\boldsymbol{a}_3^{\mathrm{s}}$ is formally substituted with a prescribed Dirichlet normal vector $\boldsymbol{a}_3^{\mathrm{D}}$. The superscript m on the master side is skipped for brevity. In accordance to the coupling case Eqs. (3.71)–(3.74), the trigonometric functions for the angles φ^{D} and φ_0^{D} are defined as

$$\cos(\varphi^{\mathrm{D}}) = \boldsymbol{a}_3 \cdot \boldsymbol{a}_3^{\mathrm{D}}, \tag{3.80}$$
$$\sin(\varphi^{\mathrm{D}}) = \boldsymbol{a}_{\mathrm{t}} \cdot (\boldsymbol{a}_3 \times \boldsymbol{a}_3^{\mathrm{D}}), \tag{3.81}$$

and

$$\cos(\varphi_0^{\mathrm{D}}) = \boldsymbol{A}_3 \cdot \boldsymbol{A}_3^{\mathrm{D}}, \tag{3.82}$$
$$\sin(\varphi_0^{\mathrm{D}}) = \boldsymbol{A}_{\mathrm{t}} \cdot (\boldsymbol{A}_3 \times \boldsymbol{A}_3^{\mathrm{D}}). \tag{3.83}$$

This gives the constraint

$$g^{\tan}(\tilde{\xi}) = \sin(\psi^{\mathrm{D}}) = 0 \tag{3.84}$$
$$= \sin(\varphi^{\mathrm{D}} - \varphi_0^{\mathrm{D}}) = 0 \tag{3.85}$$
$$= \sin(\varphi^{\mathrm{D}})\cos(\varphi_0^{\mathrm{D}}) - \cos(\varphi^{\mathrm{D}})\sin(\varphi_0^{\mathrm{D}}) = 0 \tag{3.86}$$
$$= \boldsymbol{a}_{\mathrm{t}} \cdot (\boldsymbol{a}_3 \times \boldsymbol{a}_3^{\mathrm{D}})\cos(\varphi_0^{\mathrm{D}}) - (\boldsymbol{a}_3 \cdot \boldsymbol{a}_3^{\mathrm{D}})\sin(\varphi_0^{\mathrm{D}}) = 0, \tag{3.87}$$

and the virtual work

$$\delta W^{\text{B-Rep,tan}} = \alpha^{\tan} \int_{\Gamma_{\mathrm{D}}} \sin(\varphi^{\mathrm{D}} - \varphi_0^{\mathrm{D}})\, \delta\left(\sin(\varphi^{\mathrm{D}} - \varphi_0^{\mathrm{D}})\right) \mathrm{d}\Gamma, \tag{3.88}$$

for weakly enforced penalty-based Dirichlet boundary conditions.

3.4.4 Control point forces and stiffness matrix for coupling conditions

Based on the general form of the potential for a weakly enforced penalty constraint as given in Eq. (3.35), the potential for this coupling constraint can be computed as

$$W^{\text{B-Rep,tan}} = \frac{1}{2}\alpha^{\tan} \int_{\Gamma_{\mathrm{C}}} \sin^2(\varphi - \varphi_0)\, \mathrm{d}\Gamma. \tag{3.89}$$

The corresponding control point force is obtained by differentiating the potential with respect to control point displacements:

$$\mathbf{f}^{\text{B-Rep,tan}} = \frac{\partial W^{\text{B-Rep,tan}}}{\partial \mathbf{d}} = \alpha^{\tan} \int_{\Gamma_{\mathrm{C}}} g^{\tan}(\mathbf{d}) \frac{\partial g^{\tan}(\mathbf{d})}{\partial \mathbf{d}}\, \mathrm{d}\Gamma, \tag{3.90}$$
$$\mathbf{f}_A^{\text{B-Rep,tan}} = \frac{\partial W^{\text{B-Rep,tan}}}{\partial \mathbf{d}_A} = \alpha^{\tan} \int_{\Gamma_c} g^{\tan}(\mathbf{d}) \frac{\partial g^{\tan}(\mathbf{d})}{\partial \mathbf{d}_A}\, \mathrm{d}\Gamma. \tag{3.91}$$

The corresponding tangential stiffness matrix[1] is then computed as

$$\mathbf{K}^{\text{B-Rep,tan}} = \frac{\partial^2 W^{\text{B-Rep,tan}}}{\partial \mathbf{d} \partial \mathbf{d}} = \alpha^{\tan} \int_{\Gamma_c} \frac{\partial g^{\tan}(\mathbf{d})}{\partial \mathbf{d}} \otimes \frac{\partial g^{\tan}(\mathbf{d})}{\partial \mathbf{d}}\, \mathrm{d}\Gamma, \tag{3.92}$$
$$\mathbf{K}_{AB}^{\text{B-Rep,tan}} = \frac{\partial^2 W^{\text{B-Rep,tan}}}{\partial \mathbf{d}_A \partial \mathbf{d}_B} = \alpha^{\tan} \int_{\Gamma_c} \frac{\partial g^{\tan}(\mathbf{d})}{\partial \mathbf{d}_A} \otimes \frac{\partial g^{\tan}(\mathbf{d})}{\partial \mathbf{d}_B}\, \mathrm{d}\Gamma. \tag{3.93}$$

The constrained derivatives involved in the force and stiffness matrix definitions in Eqs. (3.90) and (3.92) are computed next. For this reason, the cross product in Eq. (3.78) is rewritten in matrix form

$$g^{\tan}(\mathbf{d}) = \boldsymbol{a}_{\mathrm{t}}^{\mathrm{m}} \cdot \left(\left[\boldsymbol{a}_3^{\mathrm{m}}\times\right]\boldsymbol{a}_3^{\mathrm{s}}\right)\cos(\varphi_0) - (\boldsymbol{a}_3^{\mathrm{m}} \cdot \boldsymbol{a}_3^{\mathrm{s}})\sin(\varphi_0) = 0, \tag{3.94}$$

with the skew-symmetric matrix

$$\left[\boldsymbol{a}_3^{\mathrm{m}}\times\right] = \begin{bmatrix} 0 & -a_{33}^{\mathrm{m}} & a_{32}^{\mathrm{m}} \\ a_{33}^{\mathrm{m}} & 0 & -a_{31}^{\mathrm{m}} \\ -a_{32}^{\mathrm{m}} & a_{31}^{\mathrm{m}} & 0 \end{bmatrix}. \tag{3.95}$$

For the derivatives with respect to $\mathbf{d}_A$ one needs to differentiate between master $\mathbf{d}_A^{\mathrm{m}}$ and slave $\mathbf{d}_A^{\mathrm{s}}$ coordinates. By using the product rule and the identity $\left[\boldsymbol{a}_3^{\mathrm{m}}\times\right]\boldsymbol{a}_3^{\mathrm{s}} = -\left[\boldsymbol{a}_3^{\mathrm{s}}\times\right]\boldsymbol{a}_3^{\mathrm{m}}$, the constraint derivatives with respect to master coordinates can be written as

$$\frac{\partial g^{\tan}(\mathbf{d})}{\partial \mathbf{d}_A^{\mathrm{m}}} = \left[\left(\left[\boldsymbol{a}_3^{\mathrm{m}}\times\right]\boldsymbol{a}_3^{\mathrm{s}}\right) \cdot \frac{\partial \boldsymbol{a}_{\mathrm{t}}^{\mathrm{m}}}{\partial \mathbf{d}_A^{\mathrm{m}}} + \boldsymbol{a}_{\mathrm{t}}^{\mathrm{m}} \cdot \left(-\left[\boldsymbol{a}_3^{\mathrm{s}}\times\right]\frac{\partial \boldsymbol{a}_3^{\mathrm{m}}}{\partial \mathbf{d}_A^{\mathrm{m}}}\right)\right]\cos(\varphi_0) - \left(\boldsymbol{a}_3^{\mathrm{s}} \cdot \frac{\partial \boldsymbol{a}_3^{\mathrm{m}}}{\partial \mathbf{d}_A^{\mathrm{m}}}\right)\sin(\varphi_0) = 0. \tag{3.96}$$

[1] The constraint is assumed to be linear and thus the second derivative contribution is neglected here. Within this thesis, this only has an effect on the eigenvalue analysis, since no stiffness matrix is used for explicit analysis anyway.

With $\left[\boldsymbol{a}_3^{\mathrm{m}}\times\right]\boldsymbol{a}_3^{\mathrm{s}}=\boldsymbol{a}_{\mathrm{t}}^{\mathrm{m}}$ it can be seen that the first term in Eq. (3.96) vanishes

$$\boldsymbol{a}_{\mathrm{t}}^{\mathrm{m}}\cdot\frac{\partial\boldsymbol{a}_{\mathrm{t}}^{\mathrm{m}}}{\partial\mathbf{d}_A^{\mathrm{m}}}=0, \tag{3.97}$$

since the derivative of a unit vector is perpendicular to the unit vector, leading to a scalar product equal to zero. Equation (3.96) therefore simplifies to

$$\frac{\partial g^{\tan}(\mathbf{d})}{\partial\mathbf{d}_A^{\mathrm{m}}}=\boldsymbol{a}_{\mathrm{t}}^{\mathrm{m}}\cdot\left(-\left[\boldsymbol{a}_3^{\mathrm{s}}\times\right]\frac{\partial\boldsymbol{a}_3^{\mathrm{m}}}{\partial\mathbf{d}_A^{\mathrm{m}}}\right)\cos(\varphi_0)-\left(\boldsymbol{a}_3^{\mathrm{s}}\cdot\frac{\partial\boldsymbol{a}_3^{\mathrm{m}}}{\partial\mathbf{d}_A^{\mathrm{m}}}\right)\sin(\varphi_0)=0, \tag{3.98}$$

The only derivative left to evaluate is then $\partial\boldsymbol{a}_3^{\mathrm{m}}/\partial\mathbf{d}_A^{\mathrm{m}}$. By using Eq. (3.64), $\partial\boldsymbol{a}_3^{\mathrm{m}}/\partial\mathbf{d}_A^{\mathrm{m}}$ can be expressed as

$$\frac{\partial\boldsymbol{a}_3^{\mathrm{m}}}{\partial\mathbf{d}_A^{\mathrm{m}}}=\frac{1}{\left(\|\hat{\boldsymbol{a}}_3^{\mathrm{m}}\|\right)^2}\left(\frac{\partial\hat{\boldsymbol{a}}_3^{\mathrm{m}}}{\partial\mathbf{d}_A^{\mathrm{m}}}\|\hat{\boldsymbol{a}}_3^{\mathrm{m}}\|-\hat{\boldsymbol{a}}_3^{\mathrm{m}}\otimes\frac{\partial\|\hat{\boldsymbol{a}}_3^{\mathrm{m}}\|}{\partial\mathbf{d}_A^{\mathrm{m}}}\right) \tag{3.99}$$

$$=\frac{1}{\|\hat{\boldsymbol{a}}_3^{\mathrm{m}}\|}\frac{\partial\hat{\boldsymbol{a}}_3^{\mathrm{m}}}{\partial\mathbf{d}_A^{\mathrm{m}}}-\frac{1}{\|\hat{\boldsymbol{a}}_3^{\mathrm{m}}\|^3}\hat{\boldsymbol{a}}_3^{\mathrm{m}}\otimes\left(\hat{\boldsymbol{a}}_3^{\mathrm{m}}\cdot\frac{\partial\hat{\boldsymbol{a}}_3^{\mathrm{m}}}{\partial\mathbf{d}_A^{\mathrm{m}}}\right) \tag{3.100}$$

$$=\frac{1}{\|\hat{\boldsymbol{a}}_3^{\mathrm{m}}\|}\left(\mathbf{I}-\boldsymbol{a}_3^{\mathrm{m}}\otimes\boldsymbol{a}_3^{\mathrm{m}}\right)\frac{\partial\hat{\boldsymbol{a}}_3^{\mathrm{m}}}{\partial\mathbf{d}_A^{\mathrm{m}}}, \tag{3.101}$$

where the following identity is used

$$\frac{\partial\|\hat{\boldsymbol{a}}_3^{\mathrm{m}}\|}{\partial\mathbf{d}_A^{\mathrm{m}}}=\frac{1}{\|\hat{\boldsymbol{a}}_3^{\mathrm{m}}\|}\hat{\boldsymbol{a}}_3^{\mathrm{m}}\cdot\frac{\partial\hat{\boldsymbol{a}}_3^{\mathrm{m}}}{\partial\mathbf{d}_A^{\mathrm{m}}}. \tag{3.102}$$

Rewriting Eq. (3.65) as

$$\hat{\boldsymbol{a}}_3^{\mathrm{m}}=\boldsymbol{a}_1^{\mathrm{m}}\times\boldsymbol{a}_2^{\mathrm{m}}=\left[\boldsymbol{a}_1^{\mathrm{m}}\times\right]\boldsymbol{a}_2^{\mathrm{m}}=-\boldsymbol{a}_2^{\mathrm{m}}\times\boldsymbol{a}_1^{\mathrm{m}}=-\left[\boldsymbol{a}_2^{\mathrm{m}}\times\right]\boldsymbol{a}_1^{\mathrm{m}}, \tag{3.103}$$

the derivative of the master normal vector $\hat{\boldsymbol{a}}_3^{\mathrm{m}}$ with respect to the vector of master displacements $\mathbf{d}_A^{\mathrm{m}}$ in Eq. (3.101) can be expressed in terms of the master surface tangent vectors $\boldsymbol{a}_1^{\mathrm{m}}$ and $\boldsymbol{a}_2^{\mathrm{m}}$:

$$\frac{\partial\hat{\boldsymbol{a}}_3^{\mathrm{m}}}{\partial\mathbf{d}_A^{\mathrm{m}}}=-\left[\boldsymbol{a}_2^{\mathrm{m}}\times\right]\frac{\partial\boldsymbol{a}_1^{\mathrm{m}}}{\partial\mathbf{d}_A^{\mathrm{m}}}+\left[\boldsymbol{a}_1^{\mathrm{m}}\times\right]\frac{\partial\boldsymbol{a}_2^{\mathrm{m}}}{\partial\mathbf{d}_A^{\mathrm{m}}}. \tag{3.104}$$

With

$$\frac{\partial\boldsymbol{a}_1^{\mathrm{m}}}{\partial\mathbf{d}_A^{\mathrm{m}}}=\begin{bmatrix}\frac{\partial N_A^{\mathrm{m}}}{\partial\xi} & 0 & 0\\ 0 & \frac{\partial N_A^{\mathrm{m}}}{\partial\xi} & 0\\ 0 & 0 & \frac{\partial N_A^{\mathrm{m}}}{\partial\xi}\end{bmatrix},\quad \frac{\partial\boldsymbol{a}_2^{\mathrm{m}}}{\partial\mathbf{d}_A^{\mathrm{m}}}=\begin{bmatrix}\frac{\partial N_A^{\mathrm{m}}}{\partial\eta} & 0 & 0\\ 0 & \frac{\partial N_A^{\mathrm{m}}}{\partial\eta} & 0\\ 0 & 0 & \frac{\partial N_A^{\mathrm{m}}}{\partial\eta}\end{bmatrix}, \tag{3.105}$$

Eq. (3.104) simplifies to

$$\frac{\partial\hat{\boldsymbol{a}}_3^{\mathrm{m}}}{\partial\mathbf{d}_A^{\mathrm{m}}}=-\frac{\partial N_A^{\mathrm{m}}}{\partial\xi}\left[\boldsymbol{a}_2^{\mathrm{m}}\times\right]+\frac{\partial N_A^{\mathrm{m}}}{\partial\eta}\left[\boldsymbol{a}_1^{\mathrm{m}}\times\right]. \tag{3.106}$$

The constraint derivative $\partial g^{\tan}(\mathbf{d})/\partial\mathbf{d}_A^{\mathrm{m}}$ with respect to master control point displacements is now obtained by combining Eqs. (3.106), (3.101) and (3.98).

The constraint derivative $\partial g^{\tan}(\mathbf{d})/\partial\mathbf{d}_A^{\mathrm{s}}$ with respect to slave coordinates is very similar, because the first term of Eq. (3.96) vanishes. The equivalent expressions for the slave side are then given as

$$\frac{\partial g^{\tan}(\mathbf{d})}{\partial\mathbf{d}_A^{\mathrm{s}}}=\boldsymbol{a}_{\mathrm{t}}^{\mathrm{m}}\cdot\left(\left[\boldsymbol{a}_3^{\mathrm{m}}\times\right]\frac{\partial\boldsymbol{a}_3^{\mathrm{s}}}{\partial\mathbf{d}_A^{\mathrm{s}}}\right)\cos(\varphi_0)-\left(\boldsymbol{a}_3^{\mathrm{m}}\cdot\frac{\partial\boldsymbol{a}_3^{\mathrm{s}}}{\partial\mathbf{d}_A^{\mathrm{s}}}\right)\sin(\varphi_0)=0, \tag{3.107}$$

with

$$\frac{\partial\boldsymbol{a}_3^{\mathrm{s}}}{\partial\mathbf{d}_A^{\mathrm{s}}}=\frac{1}{\|\hat{\boldsymbol{a}}_3^{\mathrm{s}}\|}\left(\mathbf{I}-\boldsymbol{a}_3^{\mathrm{s}}\otimes\boldsymbol{a}_3^{\mathrm{s}}\right)\frac{\partial\hat{\boldsymbol{a}}_3^{\mathrm{s}}}{\partial\mathbf{d}_A^{\mathrm{s}}},\quad\text{and}\quad\frac{\partial\hat{\boldsymbol{a}}_3^{\mathrm{s}}}{\partial\mathbf{d}_A^{\mathrm{s}}}=-\frac{\partial N_A^{\mathrm{s}}}{\partial\xi}\left[\boldsymbol{a}_2^{\mathrm{s}}\times\right]+\frac{\partial N_A^{\mathrm{s}}}{\partial\eta}\left[\boldsymbol{a}_1^{\mathrm{s}}\times\right]. \tag{3.108}$$

Control point forces and stiffness matrices can now be obtained by inserting the master and slave constraint derivatives into Eqs. (3.90) and (3.92), respectively. Since this gave rather lengthy equations, stating the complete formulas for the control point force vectors and the stiffness matrix is omitted here.

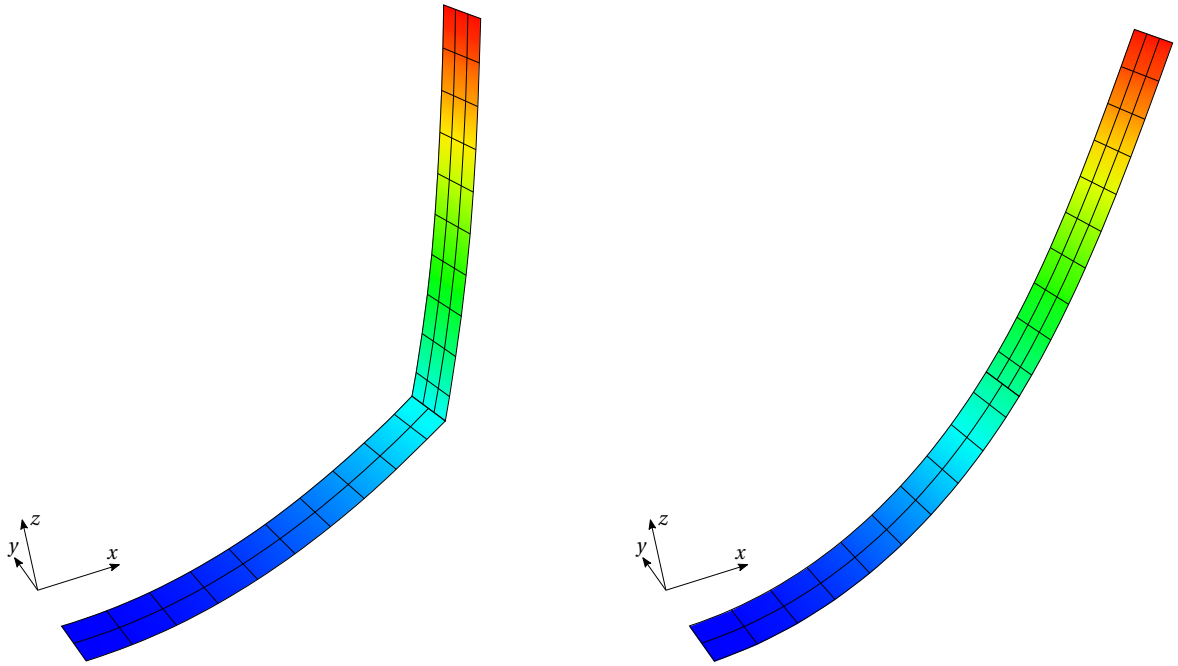

(a) Standard B-Rep element formulation.

(b) Enhanced B-Rep element formulation.

Figure 3.5: Trimmed NURBS-based multi-patch cantilever beam: Comparison of the deformed shapes at $t = 0.009\,\mathrm{s}$ between two explicit dynamic analyses using the standard B-Rep element formulation in (a) and the enhanced B-Rep element formulation in (b). The color plots indicate z-displacements.

3.4.5 Control point forces and stiffness matrix for Dirichlet boundary conditions

With the potential along the Dirichlet boundary Γ_{D}

$$W^{\text{B-Rep,tan}} = \frac{1}{2}\alpha^{\tan}\int_{\Gamma_{\mathrm{D}}} \sin^2(\varphi^{\mathrm{D}} - \varphi_0^{\mathrm{D}})\,\mathrm{d}\Gamma, \tag{3.109}$$

and Eqs. (3.90) and (3.92), computing the control point force vector and the stiffness matrix for the case of Dirichlet boundary conditions is straightforward. One only has to substitute (i) φ resp. φ_0 with φ^{D} resp. φ_0^{D} and (ii) $\boldsymbol{a}_3^{\mathrm{s}}$ with a prescribed Dirichlet normal vector $\boldsymbol{a}_3^{\mathrm{D}}$. Since $\boldsymbol{a}_3^{\mathrm{D}}$ is independent of control point displacements, only constraint derivatives with respect to one domain $\partial \boldsymbol{a}_3/\partial \mathbf{d}_A$ need to be considered, i.e. no distinction between master and slave domains is required.

3.4.6 Trimmed multi-patch cantilever beam with the enhanced B-Rep element formulation

Finally, the effectiveness of the enhanced B-Rep element formulation and the additional constraint on the shell normals shall be demonstrated by means of the cantilever beam example already used for the problem description in Section 3.4.1. The same model with the same material and analysis parameters as defined in Figure 3.2 is used, but now with the enhanced instead of the standard B-Rep element formulation. Figure 3.5 provides a comparison between the deformed shapes at $t = 0.009\,\mathrm{s}$ obtained by explicit dynamic analyses using the standard (Figure 3.5a) and the enhanced B-Rep element formulation (Figure 3.5b). As clearly visible, no kink along the coupling edge appears when using the enhanced B-Rep element formulation, thus indicating its effectiveness and rotational coupling accuracy. A comparison of the y-rotations over time for both B-Rep element formulations is provided in Figure 3.6. In accordance to Figure 3.5b, the rotations obtained with the enhanced B-Rep element formulation in Figure 3.6b show a plausible behavior without large unrealistic values.

To conclude, the additional rotational constraint imposed on the shell normals and thus on translational DOFs, is an effective mean to eliminate the rotational coupling deficiencies observed with the standard B-Rep element formulation.

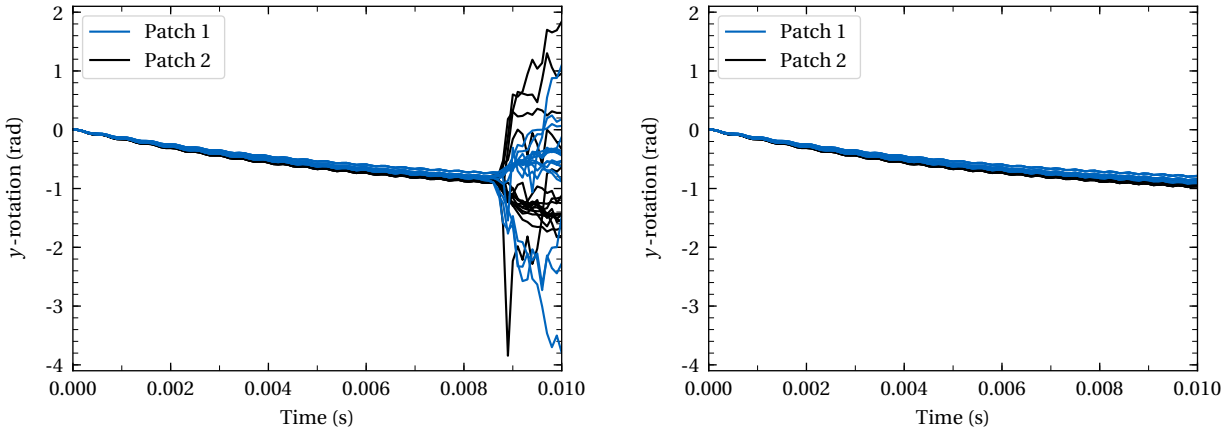

(a) Standard B-Rep element formulation.

(b) Enhanced B-Rep element formulation.

Figure 3.6: Trimmed NURBS-based multi-patch cantilever beam: Comparison of rotations around the y-direction between two explicit dynamic analyses using the standard B-Rep element formulation in (a) and the enhanced B-Rep element formulation in (b), cf. Figure 3.5. Control points of patch 1 and patch 2, marked in blue and black in Figure 3.2 are considered. These control points are all involved in the same B-Rep element marked in red in Figure 3.2.

3.5 Numerical stability and time step estimation

As described in Section 2.9, explicit time integration schemes are only stable if the time step size is smaller than a critical value. For the central difference method used within this thesis, this critical time step can be determined via condition (2.67). The corresponding derivation via a linear stability analysis, as provided in the Appendix A, shows that condition (2.67) only holds for symmetric and positive semidefinite system mass and stiffness matrix, and if a Rayleigh damping matrix is used [54]. Moreover, Section 2.9 described several common time step estimates based on the stability condition (2.67). The aim of this section is to demonstrate (i) that condition (2.67) remains valid and (ii) which of the presented time step estimates to use for problems with weak penalty-based B-Rep elements.

3.5.1 Stability for weak penalty-based coupling and boundary conditions

The explicit central difference method is shown to be stable if the time step size does not exceed a critical time step determined via (2.67). This, however, only holds if (i) a Rayleigh damping matrix is used and (ii) the system mass and stiffness matrix are symmetric and positive semidefinite. In the following, the use of a Rayleigh damping matrix is presumed, that is, the damping matrix is defined as a linear combination of $\mathbf{M}$ and $\mathbf{K}$. Thus, premise (i) is fulfilled. The task is now to show that premise (ii) is fulfilled when using penalty-based B-Rep elements; for the standard B-Rep element formulation this was previously shown by Leidinger et al. [54]. To this end, the underlying shell mass matrix $\mathbf{M}^{\mathrm{S}}$ and shell stiffness matrix $\mathbf{K}^{\mathrm{S}}$ are presumed as symmetric and positive semidefinite. Introducing B-Rep elements does not introduce additional mass, therefore $\mathbf{M} = \mathbf{M}^{\mathrm{S}}$ is symmetric and positive semidefinite. For the investigations on the stiffness matrix, $\mathbf{K}$ shall be separated into a shell and a B-Rep penalty contribution, while the latter may involve B-Rep stiffness contributions from displacement, rotation and shell normal constraints (tan):

$$\mathbf{K} = \mathbf{K}^{\mathrm{S}} + \mathbf{K}^{\mathrm{P}} = \mathbf{K}^{\mathrm{S}} + \mathbf{K}^{\text{B-Rep,disp}} + \mathbf{K}^{\text{B-Rep,rot}} + \mathbf{K}^{\text{B-Rep,tan}}. \tag{3.110}$$

Since the shell stiffness $\mathbf{K}^{\mathrm{S}}$ is presumed to be symmetric and positive semidefinite, the task is to show that this is also the case for $\mathbf{K}^{\mathrm{P}}$. The symmetry of the displacement, rotation and shell normal (tan) constraint stiffness matrices is evident from the symmetric definitions in Eqs. (3.42), (3.43) and (3.92), respectively. The penalty stiffness matrices from the displacement and rotation constraints are formally identical and can be written as

$$\mathbf{K}^{\text{B-Rep,disp}} = \alpha \int_{\Gamma} \mathbf{\Phi}^T \mathbf{\Phi} \, \mathrm{d}\Gamma, \quad \mathbf{K}^{\text{B-Rep,rot}} = \alpha \int_{\Gamma} \mathbf{\Phi}^T \mathbf{\Phi} \, \mathrm{d}\Gamma. \tag{3.111}$$

To show the positive semidefiniteness of $\mathbf{K}^{\text{B-Rep,disp}}$ and $\mathbf{K}^{\text{B-Rep,rot}}$, the following theorem is deployed, see also [54].

Theorem 3.1 (Positive definiteness of a matrix)
Let $\boldsymbol{z} \in \mathbb{R}^n$, $n \in \mathbb{N}$ be a non-zero real column vector and $\mathbf{A} \in \mathbb{R}^{n \times n}$ a symmetric real matrix. Then, $\mathbf{A}$ is called positive definite if $\boldsymbol{z}^T \mathbf{A} \boldsymbol{z} > 0$ for all non-zero $\boldsymbol{z} \in \mathbb{R}^n$. Similarly, $\mathbf{A}$ is called positive semidefinite if $\boldsymbol{z}^T \mathbf{A} \boldsymbol{z} \geqslant 0$ for all $\boldsymbol{z} \in \mathbb{R}^n$.

By pre- and post-multiplying Eq. (3.111) with $\boldsymbol{z}^T$ and $\boldsymbol{z}$, respectively, putting $\boldsymbol{z}^T$ and $\boldsymbol{z}$ into the integral and re-ordering terms gives

$$\boldsymbol{z}^T \mathbf{K}^{\text{B-Rep,disp}} \boldsymbol{z} = \alpha \int_\Gamma \boldsymbol{z}^T \boldsymbol{\Phi}^T \boldsymbol{\Phi} \boldsymbol{z} \, \mathrm{d}\Gamma = \alpha \int_\Gamma (\boldsymbol{\Phi}\boldsymbol{z})^T (\boldsymbol{\Phi}\boldsymbol{z}) \, \mathrm{d}\Gamma = \alpha \int_\Gamma \boldsymbol{b}^T \mathbf{I} \, \boldsymbol{b} \, \mathrm{d}\Gamma, \tag{3.112}$$

with the introduced vector $\boldsymbol{b} = \boldsymbol{\Phi}\boldsymbol{z}$. Since the identity matrix $\mathbf{I}$ is positive definite, the integrand $\boldsymbol{b}^T \mathbf{I} \, \boldsymbol{b}$ is non-zero, if the vector $\boldsymbol{b}$ is non-zero. The latter, however, is in general not guaranteed. Therefore, the integrand $\boldsymbol{b}^T \mathbf{I} \, \boldsymbol{b}$ can only be assumed to be non-negative. Together with a non-negative penalty factor α, $\boldsymbol{z}^T \mathbf{K}^{\text{B-Rep,disp}} \boldsymbol{z}$ is non-negative. This shows that $\mathbf{K}^{\text{B-Rep,disp}}$ is symmetric and positive semidefinite for a non-negative penalty factor α. The same of course applies for $\mathbf{K}^{\text{B-Rep,rot}}$.

With the same assumption of a non-negative penalty factor α it can be seen that the stiffness matrix for the shell normal constraint (tan) in the form

$$\mathbf{K}^{\text{B-Rep,tan}} = \alpha \int_\Gamma \left(\frac{\partial g}{\partial \mathbf{d}} \right)^T \left(\frac{\partial g}{\partial \mathbf{d}} \right) \mathrm{d}\Gamma \tag{3.113}$$

is also positive semidefinite. To this end $\mathbf{K}^{\text{B-Rep,tan}}$ is again pre- and postmultiplied with $\boldsymbol{z}^T$ and $\boldsymbol{z}$, respectively. By performing the same operations as above, one can write

$$\boldsymbol{z}^T \mathbf{K}^{\text{B-Rep,tan}} \boldsymbol{z} = \alpha \int_\Gamma \boldsymbol{z}^T \left(\frac{\partial g}{\partial \mathbf{d}} \right)^T \left(\frac{\partial g}{\partial \mathbf{d}} \right) \boldsymbol{z} \, \mathrm{d}\Gamma = \alpha \int_\Gamma \left(\frac{\partial g}{\partial \mathbf{d}} \boldsymbol{z} \right)^T \left(\frac{\partial g}{\partial \mathbf{d}} \boldsymbol{z} \right) \mathrm{d}\Gamma = \alpha \int_\Gamma b^2 \, \mathrm{d}\Gamma, \tag{3.114}$$

with the introduced scalar value $b = \frac{\partial g}{\partial \mathbf{d}} \boldsymbol{z} \geq 0$. Since the integrand b^2 is always non-negative, also the stiffness matrix for the shell normal constraint is positive semidefinite for a non-negative penalty factor.

In conclusion, the stability condition (2.67) remains valid when enforcing weak penalty-based coupling and boundary conditions via B-Rep edge elements.

3.5.2 Stable time step estimation

The previous section showed that condition (2.67) can be used to determine the critical time step size for problems including penalty-based B-Rep edge elements. Since condition (2.67) requires multiple evaluations of the maximum system eigenvalue during nonlinear analysis, computationally more efficient estimates as described in Section 2.9.4 are commonly used within practical FEA. The question that arises is whether these estimates are able to account for the effect of weak penalty-based coupling and boundary conditions on the critical time step size, i.e. for penalty-based B-Rep edge elements.

The heuristic element estimate for the critical time step is based on a characteristic element length. In the literature, one can find various definitions of the characteristic length for different types of elements within both FEA and IGA [14, 45, 81]. However, none of these estimates accounts for the influence of B-Rep elements, preventing their direct application to Explicit IBRA.

The nodal estimates based on the Gershgorin circle theorem and the Power iteration method, on the other hand, aim at approximating the maximum system eigenvalue directly. That is, these estimates account for all effects represented in the system matrix $\mathbf{M}^{-1}\mathbf{K}$ and are therefore applicable to any kind of system in the form of Eq. (2.65), for which condition (2.67) holds [54]. This includes penalty-based coupling and boundary conditions, which are accounted for in the global stiffness matrix $\mathbf{K}$.

In conclusion, both the nodal estimate and the Power iteration method can be used to efficiently estimate the critical time step size for problems with penalty-based B-Rep edge elements [54].

3.6 Summary and conclusion of Chapter 3

This chapter presents the adaptations required for the extension of IBRA to (i) explicit dynamics and (ii) Reissner-Mindlin shell theory. To achieve the latter, two novel B-Rep edge element formulations for RM shells with rotational DOFs are proposed in Section 3.3 and Section 3.4, respectively. The standard B-Rep element formulation enforces displacement and rotational continuity directly via the corresponding translational and rotational DOFs. Although this is shown to be sufficient from a mechanical point of view, the rotational coupling quality may be poor in dynamic large deformation problems due to occasionally appearing inaccuracies in the rotational DOFs of trimmed elements. The enhanced B-Rep element formulation eliminates these deficiencies by enforcing additional translation-based

coupling constraints on the shell normals. A comparison of results for a trimmed multi-patch cantilever beam obtained with the standard and the enhanced B-Rep element formulation shows the effectiveness of the additional constraint on the shell normals. Based on the derived stiffness matrices, Section 3.5 shows that the proposed B-Rep element formulations maintain the symmetry and positive semidefiniteness of the system mass and stiffness matrices. Thus, the stability condition (2.67) can also be used for problems with penalty-based B-Rep elements. Finally, it is shown that all time step estimates that aim at estimating the maximum system eigenvalue in condition (2.67) directly, also remain applicable when using B-Rep elements; an important component for efficient explicit analysis of practical problems such as vehicle crash simulations.

Chapter 4

Stable time step size in an Explicit IBRA setting

After having shown that the explicit central difference scheme maintains its conditional stability within an Explicit IBRA setting, this chapter specifically investigates the different influencing factors on the size of the stable time step. Section 4.1 describes the effect of continuity and boundary elements in open knot vector patches on the time step, while Section 4.2 shows how trimming can be used to eliminate the time step restricting influence of boundary elements. Section 4.3 studies the effect of trimming itself, and especially the role of small trimmed elements in explicit analysis. Section 4.4 describes the effect of penalty-based B-Rep edge elements on the stable time step. Finally, in Section 4.5 a local selective mass scaling approach is proposed as a measure to compensate for a possible decrease in time step size caused by penalty-based B-Rep elements. Sections 4.1–4.4 expand on preliminary exploratory work conducted within the Master's theses of Murugan [144] and Pasch [145], and a student project of Lian [146]. The local selective mass scaling approach was first implemented and tested within a student project by Pasch [147]. All these studies were supervised by the author of this dissertation.

4.1 Effect of continuity and boundary elements on the time step

A remarkable property of B-spline and NURBS basis functions is the higher continuity across element boundaries, in the following denoted as inter-element continuity. In standard FEA based on Lagrange polynomials, the inter-element continuity is limited to C^0, while NURBS-based IGA allows for C^{p-1}. This section describes the effect of this higher continuity on the eigenfrequencies and thus on the critical time step size in explicit analysis.

As described in Chapter 2, the shape and thus the inter-element continuity of the n basis functions within a NURBS patch of degree p are defined by the knot vector $\Xi = \{\xi_1, \xi_2, \ldots, \xi_{n+p+1}\}$. More specifically, the inter-element continuity is determined as C^{p-m_i}, where m_i is the multiplicity of the knot value ξ_i. In case a knot ξ_i has multiplicity $m_i = p$, the continuity of the basis reduces to C^0. This implies that, at this knot, one basis function is equal to one, while all others are equal to zero, see Figure 2.1. In that case, the basis is said to be *interpolatory* at ξ_i [121]. That is, a NURBS curve generated from such a knot vector passes through the corresponding control point at ξ_i. In a similar manner, this of course also applies to NURBS surfaces. For $m_i = p+1$ the basis becomes discontinuous (C^{-1}), forming a patch boundary. In CAD programs the first and the last knot values (ξ_1 and ξ_{n+p+1}) are therefore commonly defined with multiplicity $m_i = p+1$, see also Figure 2.1. Such a knot vector is denoted as an *open* or *clamped* knot vector. Thus, for open knot vectors the multiplicity of the first and the last knot value is prescribed. This affects the shape of the p first and last basis functions in the $p-1$ first and last elements[1]. This can also be interpreted as a reduction of continuity towards patch boundaries.

To summarize, regardless of whether interior or boundary knots are considered, varying the multiplicity of a knot alters the shape and the inter-element continuity of basis functions. Since mass and stiffness matrix entries are essentially determined by basis functions, the question arises, whether the type of basis function also affects the eigenfrequencies and thus the stable explicit time step of the model.

In their work on stable time step estimates for explicit IGA [81], Adam et al. already found that inter-element continuity is decisive for the critical time step, see Table 2 in [81]. That is, the higher the continuity, the higher the critical time

[1] For the sake of brevity, the $p-1$ elements and p basis functions at the boundary of an open knot vector curve are denoted as *boundary* elements and *boundary* basis functions. The same applies to the $p-1$ element and p basis function rows at the boundary of open knot vector surface patches. Please note that these *boundary* elements have nothing to do with the elements in the Boundary Element Method (BEM).

step. In [81] the authors also found that in open knot vector patches with an inter-element continuity of C^{p-1}, the boundary elements require a smaller time step than interior elements. The authors suggested two approaches to remedy this negative effect of boundary elements, which will be discussed later in this section. Before that, it is expedient to analyze the effect of shape and inter-element continuity of basis functions on the resulting mass and stiffness matrix entries (M_A and K_{AB}), and their impact on the eigenvalue problem

$$(\mathbf{K}-\omega_I^2\mathbf{M})\mathbf{y}_I=(\mathbf{K}-\lambda_I\mathbf{M})\mathbf{y}_I=0 \quad \text{or} \quad (\mathbf{M}^{-1}\mathbf{K}-\omega_I^2\mathbf{I})\mathbf{y}_I=(\mathbf{M}^{-1}\mathbf{K}-\lambda_I\mathbf{I})\mathbf{y}_I=0. \tag{4.1}$$

Via this eigenvalue problem the matrix entries M_A and K_{AB} indeed determine the eigenfrequencies ω_A and thus the critical time step size

$$\Delta t_{\text{crit}}=\frac{2}{\omega_{\max}}. \tag{4.2}$$

To demonstrate this, one-dimensional bar and two-dimensional shell models with varying continuity are studied here.

4.1.1 Open knot vector patches with C^0 inter-element continuity

At first, NURBS patches with C^0 inter-element continuity shall be considered (NURBS patches with C^{p-1} continuity follow in Section 4.1.2) in order to investigate the effect on the eigenfrequencies and the size of the critical time step in explicit analysis for different polynomial degrees p. For this purpose, one-dimensional bar and two-dimensional shell models with the following properties are considered unless otherwise stated:

- A uniform open knot vector with C^0 inter-element continuity, i.e. a p-refined knot vector generated from a linear knot vector.
- A control point distribution defined such that the Jacobian J_1 of the mapping from the parameter space to the geometry space is constant throughout the patch, which is standard in CAD programs. This corresponds to a uniform control point distribution for patches with C^0 inter-element continuity.
- Linear elastic, isotropic and homogeneous material behavior without damping.

One-dimensional bar model

The one-dimensional NURBS-based bar models with constant cross-sectional area and $p=1$ to 4 considered here are generated from a linear C^0 open knot vector $\Xi=\{0,0,1,2,3,4,5,6,6\}$ via p-refinement. That is, as the order is elevated by one, the multiplicity of each distinct knot value is increased by one as well. The resulting basis functions for $p=1$ to 4 are depicted in the upper part of Figure 4.1b. It can be seen that the continuity drops to C^0 at element boundaries and that all elements have identical basis functions. However, for $p>1$ the basis functions within an element vary. Without loss of generality, the mass density ρ, the cross-sectional area A and the Young's modulus E are set to $\rho=A=E=1$ in the following. The values in all subsequent plots are provided in consistent units. The control point distributions leading to a constant Jacobian $J_1=1$ are given in Figure 4.1a. For the one-dimensional bar models considered here, the entries of the lumped mass matrix are computed as

$$M_A=\int_V \rho\, N_A \,\mathrm{d}V=\rho\, A\int_x N_A\,\mathrm{d}x=\rho\, A\int_\xi N_A\left|\frac{\partial x}{\partial \xi}\right|\mathrm{d}\xi, \tag{4.3}$$

and the entries of the stiffness matrix as

$$K_{AB}=\int_V \frac{\partial N_A}{\partial x}E\frac{\partial N_B}{\partial x}\,\mathrm{d}V=E\,A\int_x \frac{\partial N_A}{\partial x}\frac{\partial N_B}{\partial x}\,\mathrm{d}x=E\,A\int_\xi\left(\frac{\partial N_A}{\partial \xi}\frac{\partial \xi}{\partial x}\right)\left(\frac{\partial N_B}{\partial \xi}\frac{\partial \xi}{\partial x}\right)\left|\frac{\partial x}{\partial \xi}\right|\mathrm{d}\xi. \tag{4.4}$$

From Eq. (4.3) one can see that, via the integral, the control point mass M_A is directly proportional to the area under the basis function N_A. In fact, the area under the basis function remains the only distinguishing quantity since the Jacobian $J_1=|\partial x/\partial \xi|$ and all material parameters are constant throughout the bar. The control point mass M_A therefore varies with the varying shape and support of the basis functions, which can be seen in Figure 4.1b. The stiffness matrix entries K_{AB} in Eq. (4.4) on the other hand, are computed from the basis function derivatives $N_A'(\xi)=\partial N_A/\partial \xi$, which also vary for the different types of basis function, see Figure 4.2.

In order to show the influence of different types of basis functions on mass and stiffness, Figure 4.1a depicts control point eigenfrequencies computed from lumped mass and lumped stiffness matrices, which are obtained by row summing of absolute values. For $p=1$, 2, the varying mass and stiffness values counterbalance, leading to constant

nodal eigenfrequencies. For $p = 3, 4$ on the contrary, the control point eigenfrequencies vary periodically throughout the patch and within an element. A general observation is the following: The further a control point is located away from a C^0 continuity, the lower its eigenfrequency.

Since all elements are identical here, the maximum element eigenfrequencies depicted in Figure 4.1b are constant throughout the patch. It is worth noting that the eigenfrequencies increase with increasing p. This can be explained by the following facts: (i) the area under the basis functions decreases with increasing p, which gives smaller control point masses, see Eq. (4.3), (ii) the maximum values of the basis function derivatives increase with increasing p, which gives larger stiffness entries, see Eq. (4.4). From Eq. (4.1) and the eigenfrequency of a single DOF mass-spring-system

$$\omega = \sqrt{\lambda} = \sqrt{\frac{k}{m}} \tag{4.5}$$

it can be seen that a smaller mass and a higher stiffness leads to a higher eigenfrequency and via Eq. (4.2) to a smaller critical time step.

Another explanation for the higher eigenfrequencies with increasing p can be found in the control point distribution in Figure 4.1a. For p-refinement, increasing p by one introduces one new basis function in each element, that is, n_{el} new basis functions in total, where n_{el} is the number of elements. Thus, the higher p, the higher the number of control points and the closer the control points are located to each other. For example for $p = 4$ the number of control points is by $3n_{\text{el}}$ times higher than for $p = 1$. This must lead to smaller control point masses and via the stiffness formula of a spring with length l

$$k = \frac{EA}{l} \tag{4.6}$$

also to higher stiffness, where l can be interpreted as the distance between control points.

Two-dimensional shell model

For the two-dimensional case, the effects and dependencies are very similar. To show this, square plates with a side length of $l = 10\,\text{mm}$ and a discretization of 10×10 Reissner-Mindlin shell elements for $p = 1$ to 4 are considered as depicted in Figure 4.3. The model is again generated from linear C^0 open knot vectors $\Xi = \mathcal{H} = \{0, 0, 1, 2, 3, 4, 5, 6, 7, 8, 9, 10, 10\}$ via p-refinement, maintaining C^0 continuity at element boundaries. The control point distributions of the plate for the different p-refinement levels and a constant Jacobian $J_1 = 1$ are depicted in Figure 4.3. It can be seen that, due to the enforced C^0 continuity, the number of control points again strongly increases with p. The mass density ρ, the Young's modulus E, the shell thickness h and the Poisson's ratio ν are, for simplicity, defined as $\rho = E = h = 1$ and $\nu = 0.3$. The values in the corresponding plots are again provided in consistent units.

As mentioned in Section 2.6.2, the RM shell elements use a lumped mass matrix in which the rotational inertias are scaled such that the corresponding eigenmodes do not control the critical time step size. Thus, only considering the translational DOFs, eigenmodes and eigenfrequencies of the shell is sufficient for studying the influence on the time step size in this section.

Figure 4.4 depicts the maximum element eigenfrequency distribution of all four configurations $p = 1$ to 4 via a heat map of the parameter space. The eigenfrequencies are normalized with respect to the linear case and the elements are colored in accordance to their maximum eigenfrequency. The colorbar scales are identical for all four subplots. Because of the enforced C^0 inter-element continuity, all elements within a patch have equal maximum element eigenfrequencies. For the same reasons as in the one-dimensional bar model, the eigenfrequencies increase with p. For instance the maximum element eigenfrequency for $p = 4$ is 1.93 times higher than for $p = 1$. This means that p-refinement of C^0 continuous NURBS models would reduce the critical time step size in explicit analysis – a clearly unfavorable behavior.

4.1.2 Open knot vector patches with maximum C^{p-1} inter-element continuity

In the previous section p-refined NURBS models with C^0 inter-element continuity as in standard FEA are studied and it is found that elevating the order has a negative effect on the time step size. This section deals with k-refined open knot vector NURBS models with higher inter-element continuity up to C^{p-1}. According to Adam et al. [81], a positive effect of higher continuity is expected.

Hereafter, one-dimensional bar and two-dimensional shell models with the following properties are considered unless otherwise stated:

- A uniform open knot vector now with maximum C^{p-1} inter-element continuity, i.e. a k-refined knot vector, which only has interior knots of multiplicity $m_i = 1$.

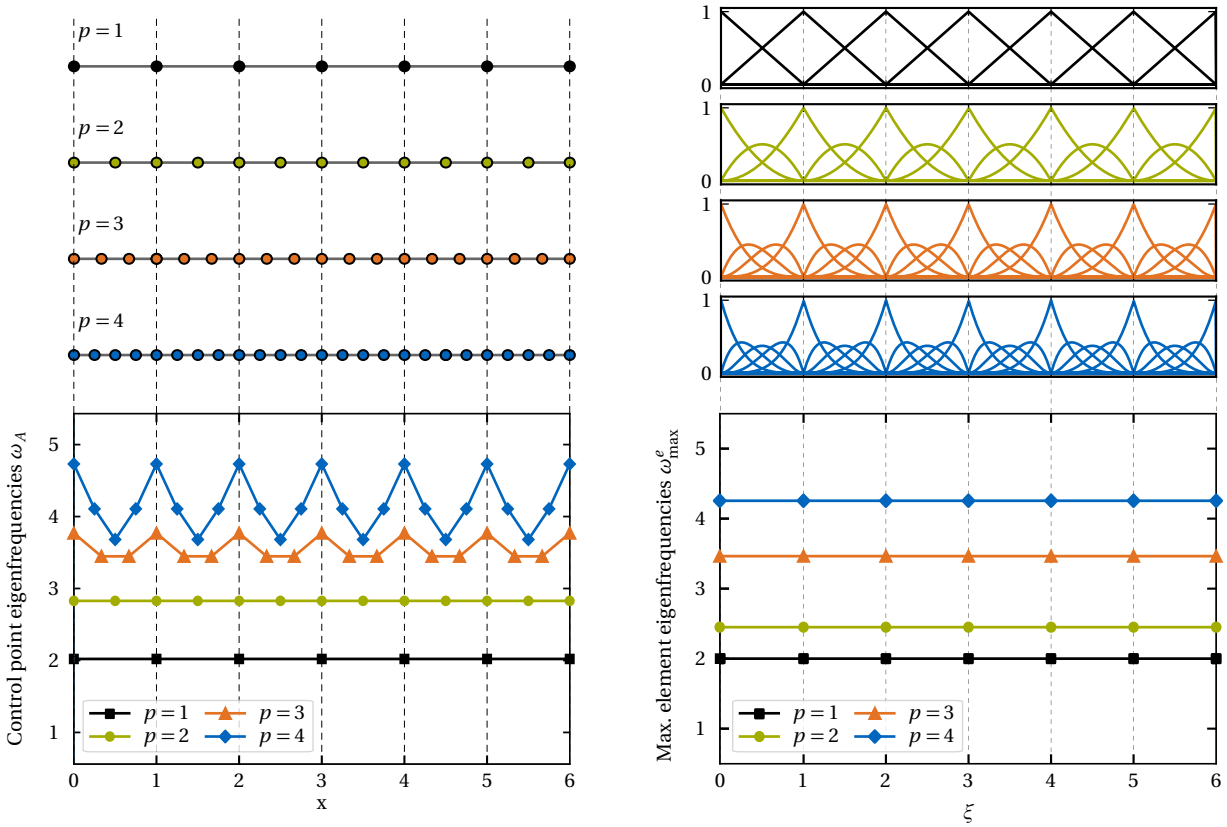

(a) Control point distributions in the geometry space (top) and control point eigenfrequencies ω_A computed from lumped mass and lumped stiffness matrices (bottom).

(b) Basis functions (top) and maximum element eigenfrequencies $\omega^e_{\max}$ (bottom).

Figure 4.1: One-dimensional bar problem C^0: Models of polynomial degree $p = 1$ to 4, generated from an open knot vector with six elements (for $p = 1$: $\Xi = \{0,0,1,2,3,4,5,6,6\}$, for $p > 1$: p-refined Ξ with C^0 continuity between interior elements, i.e. interior knots of multiplicity $m_i = p$). Black dashed lines indicate element boundaries.

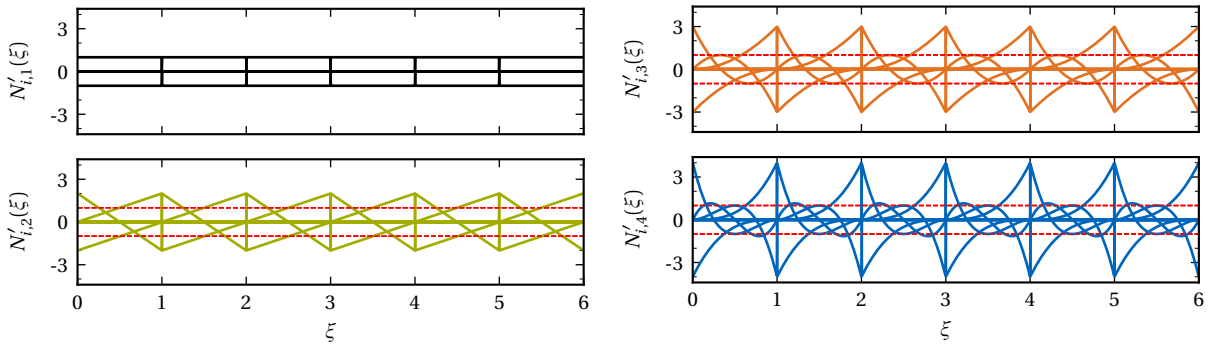

Figure 4.2: One-dimensional bar problem C^0: Derivatives $N'_{i,p}(\xi)$ of the basis functions for $p = 1$ to 4 depicted in Figure 4.1b. Red dashed lines indicate the level for $p = 1$.

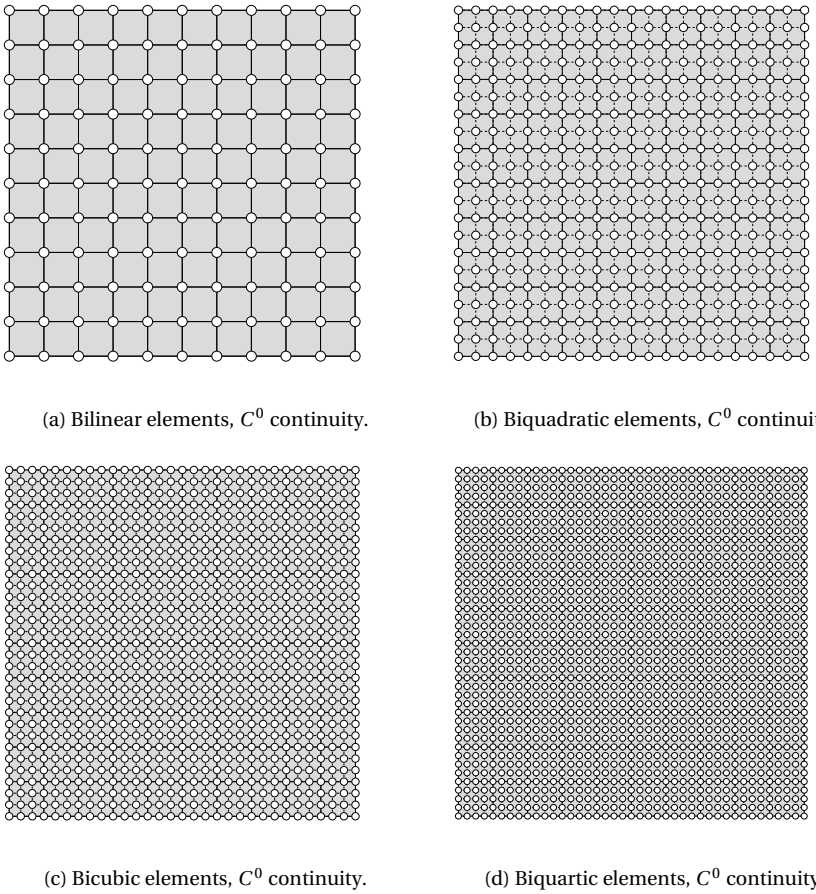

(a) Bilinear elements, C^0 continuity.

(b) Biquadratic elements, C^0 continuity.

(c) Bicubic elements, C^0 continuity.

(d) Biquartic elements, C^0 continuity.

Figure 4.3: Two-dimensional square plate problem C^0: Shell models with 10×10 isogeometric elements, C^0 inter-element continuity and $p = 1$ to 4 in (a) to (d), showing the elements and the control point distributions in the geometry space. The NURBS patches are generated from open knot vectors with ten elements (for $p = 1$: $\Xi = \mathcal{H} = \{0,0,1,2,3,4,5,6,7,8,9,10,10\}$, for $p > 1$: p-refined Ξ and $\mathcal{H}$ with $m_i = p$ multiplicity of interior knot values).

- A control point distribution defined such that the Jacobian J_1 of the mapping from the parameter space to the geometry space is constant throughout the patch, which is standard in CAD programs. For $p > 1$ this leads to an accumulation of control points near patch boundaries, see the upper part of Figure 4.5a.
- Linear elastic, isotropic and homogeneous material behavior without damping.

One-dimensional bar model

To demonstrate the effect of higher continuity on the time step, a one-dimensional NURBS-based bar model with a constant cross-sectional area and an open knot vector $\Xi = \{0,0,1,2,3,4,5,6,6\}$ for $p = 1$ is considered as a starting point. By applying k-refinement for $p = 2$ to 4, only the multiplicity of the first and last knot value is increased to $p+1$. The multiplicity of all other knot values remains to be $m_i = 1$, leading to C^{p-1} inter-element continuity. Without loss of generality, the model properties are again set to $\rho = A = E = 1$ and the values in the corresponding plots are given in consistent units. The control point distributions leading to a constant Jacobian $J_1 = 1$ are given in Figure 4.5a. The resulting basis functions for $p = 1$ to 4 with C^{p-1} inter-element continuity are depicted in the upper part of Figure 4.5b. Comparing these figures with the p-refined bar model in Figure 4.1, one can immediately recognize two major differences: (i) The number of control points and basis functions for $p > 1$ is much lower, since k-refinement only introduces one instead of n_{el} new basis function per order elevation; (ii) the elements differ with regard to their basis functions. More precisely, the support of a basis function reduces towards the patch boundary, i.e. towards a point of reduced continuity. Thereby also the shape of the basis function changes. In the following, the $p-1$ elements and p basis functions at the patch boundary are denoted as *boundary* elements and *boundary* basis functions in order to distinguish them from *interior* elements and *interior* basis functions.

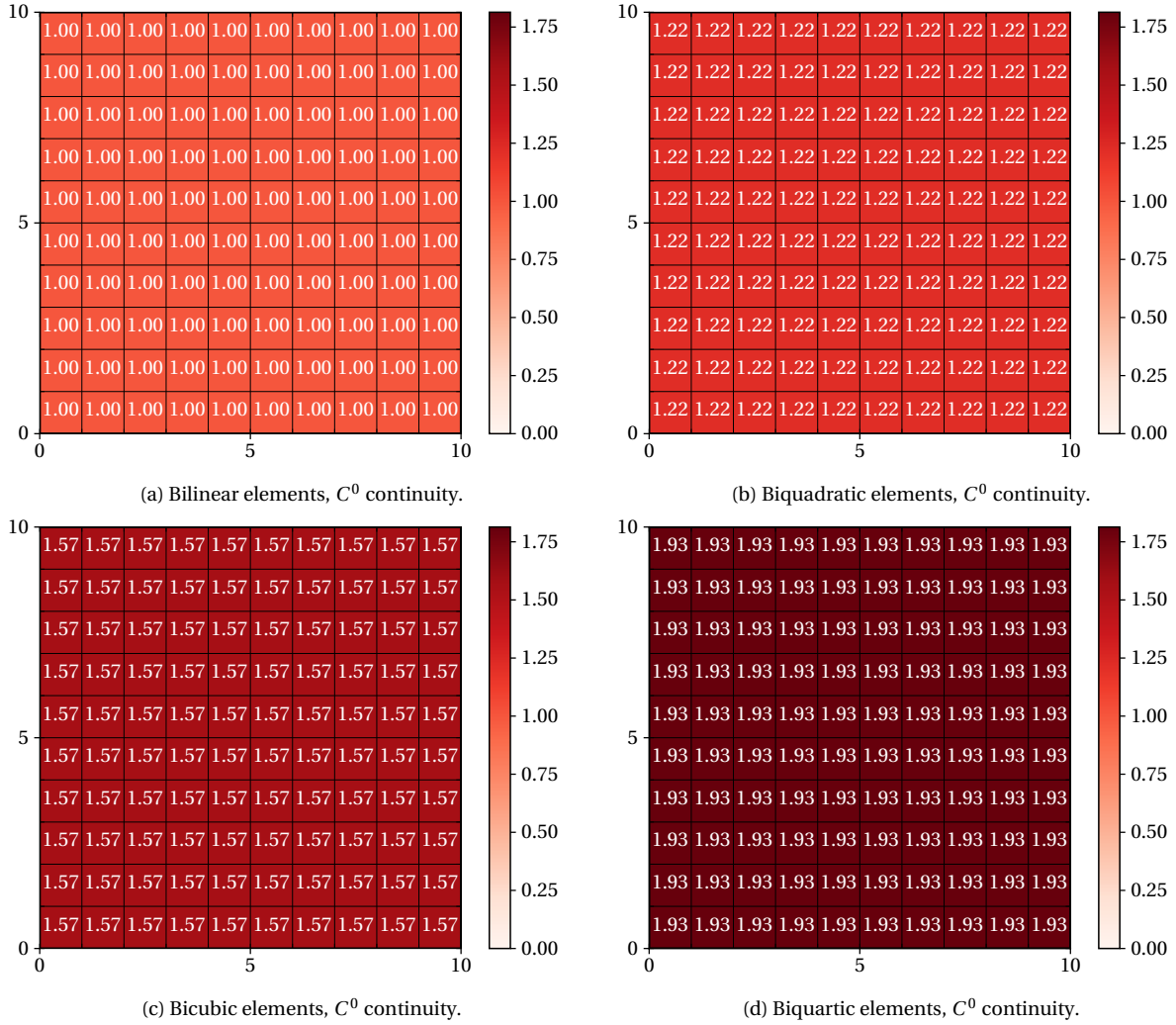

(a) Bilinear elements, C^0 continuity.

(b) Biquadratic elements, C^0 continuity.

(c) Bicubic elements, C^0 continuity.

(d) Biquartic elements, C^0 continuity.

Figure 4.4: Two-dimensional square plate problem C^0: Maximum element eigenfrequencies $\omega^e_{\max}$ for polynomial degrees $p = 1$ to 4 in (a) to (d). The element eigenfrequencies are normalized with respect to linear elements.

As in the previous section, the effect of the different types of basis functions on the time step shall be explained by means of the eigenvalue problem (4.1) and Eqs. (4.2), (4.3) and (4.4). Via Eq. (4.3) the control point mass M_A is directly proportional to the area under the basis function N_A. For internal basis functions with full support on $p+1$ uniform knot spans, the area under the basis function is equal to the element length, i.e. $\int_\xi N_A \,\mathrm{d}\xi = 1$ in the present case. As depicted in Figure 4.5b, the area under boundary basis functions N_A is smaller than for interior basis functions and even decreases with increasing p. Hence, boundary control points have a lower mass than internal control points.

The stiffness entries of boundary elements show a contrary behavior, since the basis function derivatives instead of the basis function values appear in the integral in Eq. (4.4). Figure 4.5b clearly shows that the internal basis functions flatten out with increasing p, while boundary basis functions get steeper with increasing p. Thus, the maximum derivative values of boundary basis functions for $p > 1$ are higher than in the linear case ($p = 1$), while the derivative values of internal basis functions are lower. The basis function derivatives $N'_A(\xi) = \partial N_A / \partial \xi$ for $p = 1$ to 4 are depicted in Figure 4.6, approving these observations. By recalling Eq. (4.4) it becomes obvious that, due to the varying basis function derivatives, (i) stiffness entries of boundary elements are higher than those of interior elements and that (ii) for $p > 1$ the boundary/interior stiffness entries are higher/lower than in the linear case.

Equation (4.1) explains that boundary elements with higher stiffness and lower mass entries have a higher eigenfrequency and thus require a smaller critical time step compared to interior elements. Figure 4.5 clearly confirms this effect by means of control point eigenfrequencies ω_A in Figure 4.5a and maximum element eigenfrequencies $\omega^e_{\max}$ in Figure 4.5b. For the linear case ($p = 1$), all control point and maximum element eigenfrequencies are constant since no boundary basis functions and elements exist; all elements are equivalent. For higher p the nodal and maximum element eigenfrequencies at the boundary are higher than in the interior and higher than in the linear case. For $p = 4$,

for instance, boundary elements have an approximately 2.6 times higher eigenfrequency than interior elements. Please note that the nodal eigenfrequencies are computed from lumped mass and lumped stiffness matrices obtained through row summing of absolute values. The nodal eigenfrequencies can therefore only be used as a rough and conservative estimate of the maximum system eigenfrequency. Nevertheless, the effect of boundary elements is clearly visible. Through the element eigenvalue inequality [49, 135, 136], the element eigenfrequencies in Figure 4.5b can also be used as a conservative estimate of the maximum system eigenfrequency.

The effect of boundary elements can, to some extent, also be intuitively explained by the control point distributions shown in Figure 4.5a: at the patch boundaries, the control point distribution is denser in order to achieve a constant Jacobian J_1. For a constant mass density of the material, these boundary control points therefore need to have lower mass. Moreover, a smaller distance between control points leads to stiffer elements. This can again be explained by the analytical formula for the stiffness of a one-dimensional bar in Eq. (4.6). The lower mass in combination with a higher stiffness at patch boundaries then leads to higher eigenfrequencies.

Comparing with the results for the p-refined C^0 NURBS models one can furthermore recognize that the eigenfrequencies of interior elements with $p > 1$ are (i) lower than for linear elements ($p = 1$) and (ii) decrease with increasing p. Since the $p = 1$ case is identical to linear finite elements based on Lagrange polynomials, this means that interior higher-order C^{p-1} NURBS elements would allow for a larger time step size in explicit dynamic simulations than linear finite elements.

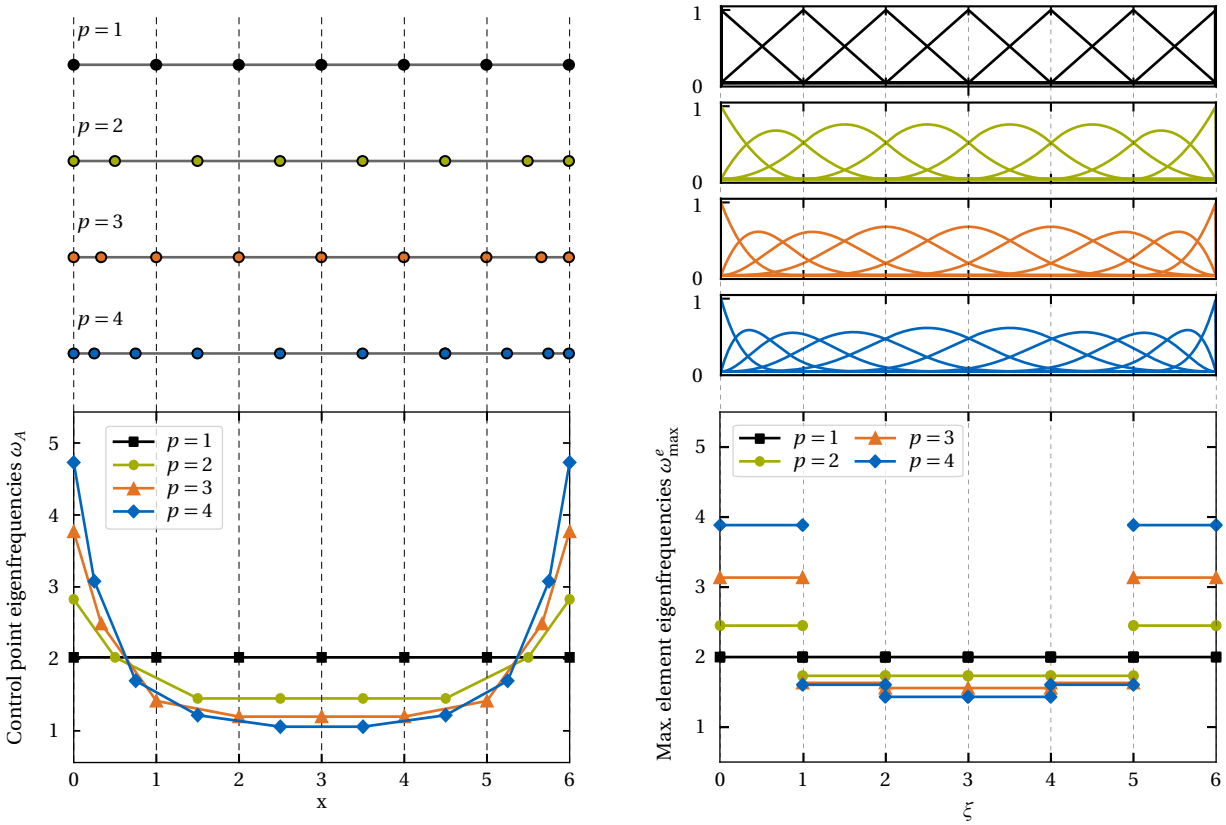

(a) Control point distributions in the geometry space (top) and control point eigenfrequencies ω_A computed from lumped mass and lumped stiffness matrices (bottom).

(b) Basis functions (top) and maximum element eigenfrequencies $\omega^e_{\max}$ (bottom).

Figure 4.5: One-dimensional bar problem C^{p-1}: Models of polynomial degree $p = 1$ to 4, generated from an open knot vector with six elements (for $p = 1$: $\Xi = \{0,0,1,2,3,4,5,6,6\}$, for $p > 1$: k-refined Ξ with C^{p-1} continuity between interior elements, i.e. interior knots of multiplicity $m_i = 1$). Black dashed lines indicate element boundaries.

Two-dimensional shell model

Next, the effect of higher inter-element continuity and boundary elements on the eigenfrequency and the critical time step size is studied for two-dimensional shell models. To this end, the same square plate geometry as in Figure 4.3 is considered. The difference is that the model is now generated from linear C^0 open knot vectors

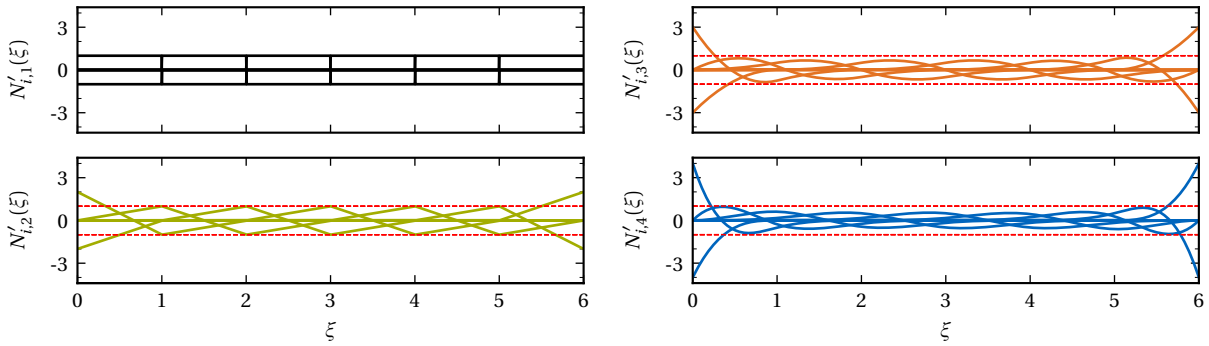

Figure 4.6: One-dimensional bar problem C^{p-1}: Derivatives $N'_{i,p}(\xi)$ of the basis functions for $p = 1$ to 4 depicted in Figure 4.5b. Red dashed lines indicate the level for $p = 1$.

$\Xi = \mathcal{H} = \{0,0,1,2,3,4,5,6,7,8,9,10,10\}$ via k-refinement, which increases the continuity at element boundaries to C^{p-1}. The control point distributions of the plate for the different k-refinement levels and a constant Jacobian $J_1 = 1$ are depicted in Figure 4.7. In contrast to the p-refinement case, now only one control point row and column is added per elevated degree, leading to a much lower number of control points. The distance between interior control points even remains the same for all degrees.

Figure 4.8 depicts the maximum element eigenfrequencies of the square plate model for $p = 1$ to 4. The element eigenfrequencies are normalized with respect to linear elements. Each element is colored in accordance to the level of its maximum eigenfrequency. As for the one-dimensional bar model, for $p = 1$ all elements are equivalent with identical eigenfrequencies ($\omega^E_{\max} = 2.39$ without normalization). For $p = 2$ to 4, the effect of boundary elements is again clearly visible: the $(p-1)$ boundary element rows and columns have higher eigenfrequencies than interior elements and linear elements. In this two-dimensional problem, *corner* elements appear, for which the boundary effect enters from two directions and therefore is even more pronounced. For $p = 4$, for example, the corner elements have an approximately 2.55 times higher eigenfrequency than interior elements.

Compared to the p-refined shell model with C^0 inter-element continuity, one can again see two beneficial effects: (i) the eigenfrequencies of higher-order interior elements are lower than for the linear case ($p = 1$) and (ii) even decrease with increasing p.

For completeness, the maximum element eigenfrequencies of the quartic shell model with C^1 and C^2 inter-element continuity are provided in Figure 4.9. The shell models with C^1 and C^2 inter-element continuity in Figure 4.9a and Figure 4.9b consist of 10×10 isogeometric elements and are generated from the uniform open knot vectors $\Xi = \mathcal{H} = \{0,0,0,0,0,1,1,1,2,2,2,\ldots,9,9,9,10,10,10,10,10\}$ and $\Xi = \mathcal{H} = \{0,0,0,0,0,1,1,2,2,\ldots,9,9,10,10,10,10,10\}$, respectively. The element eigenfrequencies are normalized with respect to linear elements. The colorbar scales of both subplots are identical. As can be seen, the eigenfrequencies of the C^1 continuous model are slightly higher than the ones of the C^2 continuous model. Also the time step restricting boundary effect is again clearly visible. Comparing with Figure 4.4d and Figure 4.8d, one can conclude that the higher the inter-element continuity, the lower the eigenfrequencies and the larger the critical time step.

Interpretation via characteristic element length

These continuity effects can be described in yet another way, for which a one-dimensional bar problem is again considered. A common explanation of the critical time step in explicit analysis is that the information in the analysis must propagate faster than the wave speed c of the material in order for the analysis to be stable. This is a physical interpretation of the stability condition

$$\Delta t \leq \min_e \frac{l_c^e}{c}, \tag{4.7}$$

where l_c^e is a characteristic element length. By studying the explicit central difference scheme, for instance, one can see that for (higher-order) C^0 finite elements information propagates only across one element within each time step. This is because the support of C^0 basis functions is limited to two elements. From this it becomes plausible that linear bar elements have a characteristic length equal to their spatial extent, i.e. equal to the distance between the two nodes/control points. For higher-order p-refined elements with C^0 continuity the spatial extent is the same, but additional nodes/control points are introduced within the element, i.e. the distance between nodes/control points becomes smaller, see Figure 4.1a. Since also the critical time step is smaller than for linear elements, higher-order C^0

elements can be said to have a reduced characteristic element length, which is usually considered via an additional factor in Eq. (4.7), see for instance [49, 81, 134]. In contrast to that, *interior* higher-order and higher-continuity NURBS elements obtained via k-refinement have larger support ($p+1$ elements for C^{p-1}) and information therefore propagates further than only one element per time step. Also the distance between the outermost control points is larger for a given physical element length. The larger critical time step of *interior* higher-order and higher-continuity NURBS elements can therefore be interpreted as an increased characteristic element length. Boundary elements also have only limited support and can therefore not benefit from the higher continuity, leading to a smaller time step than interior elements.

Eliminating the boundary effect

For standard FEA with C^0 inter-element continuity higher-order elements lead to a smaller time step; in IGA, interior elements with C^{p-1} inter-element continuity would allow for larger time steps. From these investigations one can conclude that removing the negative effect of higher-order boundary elements would increase the critical time step size in explicit analysis to a level even higher than in the linear (finite element) case. This would enable efficient usage of higher-order elements in explicit analysis such as crash or metal forming simulations. Adam et al. [81] proposed two approaches that allow removing the boundary effect:

- The first suggestion is to increase the physical extent of boundary elements. In accordance to the explanations above, this can be interpreted as: (i) Introducing a higher Jacobian J_1 of the mapping from the parameter to the geometry space. This increases the control point mass and reduces the values of basis function derivatives with respect to physical coordinates at the boundaries. (ii) Reducing the control point density, which increases mass and reduces stiffness.
- The second suggestion is the use of unclamped (non-open) knot vectors, which yields identical basis functions with full support as for interior elements.

The first remedy of increasing the size of boundary elements requires a coarser discretization at patch boundaries and may therefore lead to poor accuracy if boundary effects are of interest [81]. It furthermore requires suitable preprocessing capabilities in order to be practically applicable. Using unclamped knot vectors, on the other hand, is an elegant remedy as it does not impair analysis results. However, this approach either requires CAD programs able to generate patches with unclamped knot vectors or preprocessing capabilities to convert open (clamped) knot vector patches into unclamped ones, see [81]. The authors in [81] also mentioned mass scaling as a general approach to increase time step size in explicit analysis, but did not further elaborate on it, because of the drawback of artificially added mass. Nonetheless, mass scaling is common in practical vehicle crash simulations and selectively scaling the mass of only the boundary control points as needed would also limit its negative impact on the dynamic response of the model.

Besides these suggestions, a novel, effective and practically applicable approach for eliminating the boundary effect is proposed in the next section: Trimming.

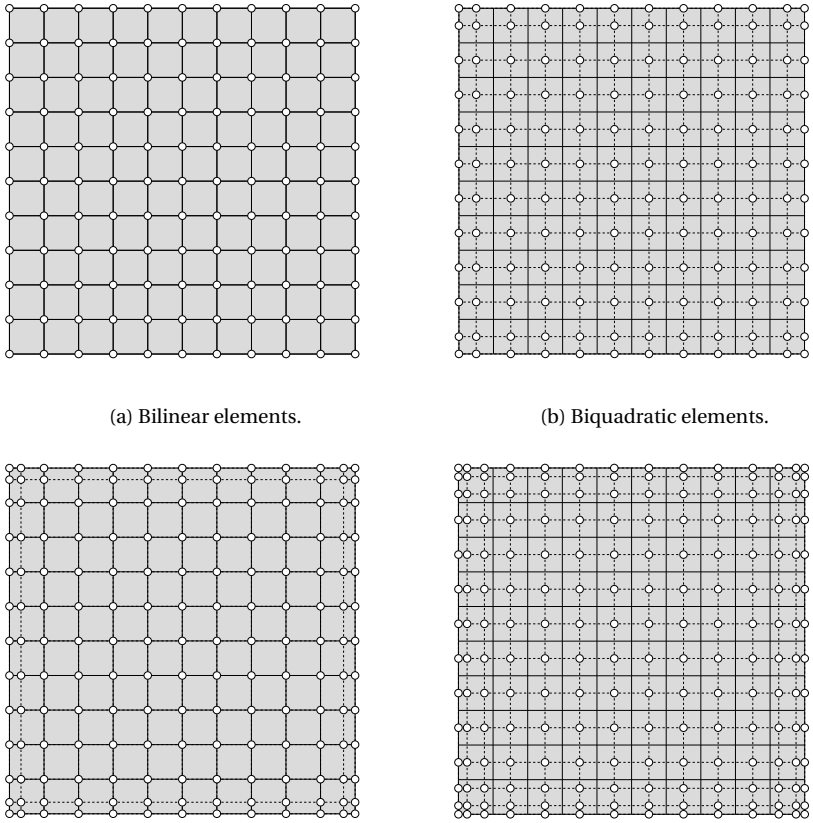

(a) Bilinear elements.

(b) Biquadratic elements.

(c) Bicubic elements.

(d) Biquartic elements.

Figure 4.7: Two-dimensional square plate problem C^{p-1}: Shell models with 10×10 isogeometric elements and $p = 1$ to 4 in (a) to (d), showing the elements and the control point distributions in the geometry space. The NURBS patches are generated from an open knot vector with ten elements (for $p = 1$: $\Xi = \mathcal{H} = \{0,0,1,2,3,4,5,6,7,8,9,10,10\}$, for $p > 1$: k-refined Ξ and $\mathcal{H}$ with C^{p-1} continuity between interior elements, i.e. interior knots of multiplicity $m_i = 1$).

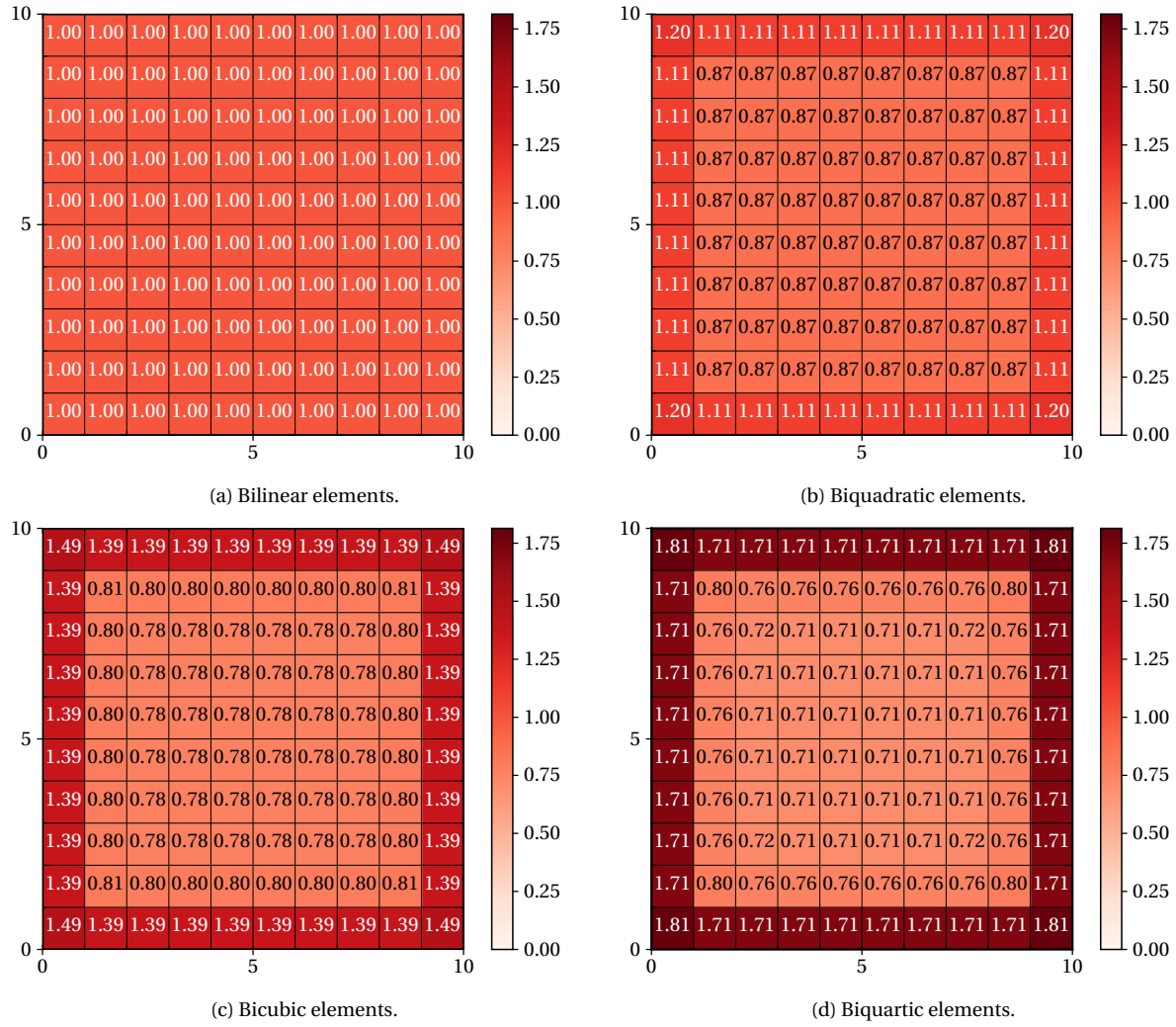

(a) Bilinear elements.

(b) Biquadratic elements.

(c) Bicubic elements.

(d) Biquartic elements.

Figure 4.8: Two-dimensional square plate problem C^{p-1}: Maximum element eigenfrequencies $\omega^e_{\max}$ for polynomial degrees $p = 1$ to 4 in (a) to (d). The element eigenfrequencies are normalized with respect to linear elements.

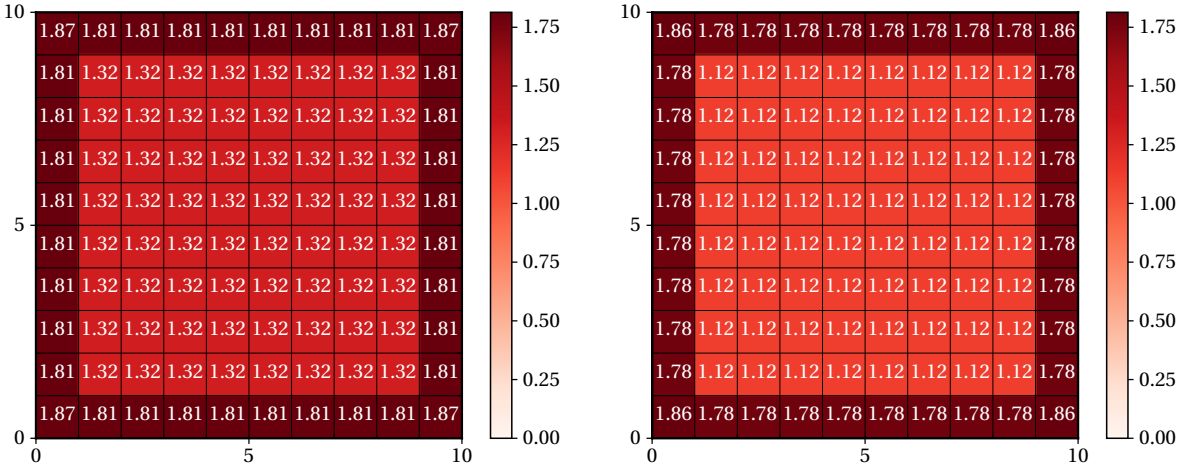

(a) Biquartic elements, C^1 continuity.

(b) Biquartic elements, C^2 continuity.

Figure 4.9: Two-dimensional square plate problem C^1 and C^2, $p = 4$: Maximum element eigenfrequencies $\omega^e_{\max}$ for C^1 and C^2 inter-element continuity in (a) and (b). The element eigenfrequencies are normalized with respect to linear elements.

4.2 Eliminating the boundary effect through trimming

In this section, trimming is proposed as a remedy to eliminate the time step restricting effect of boundary elements in open knot vector patches of higher order and higher continuity. As described in Section 2.2, directed trimming loops divide the domain into visible/material and void domains. In order for the time step restricting boundary effect to disappear, all boundary elements must be located in a void domain. The most obvious approach would be to trim exactly along the knot lines that separate interior from boundary elements. For one-dimensional bar models one only needs to trim at the corresponding knot values. Anyway, in order to obtain the desired model dimensions after having trimmed away the boundary elements, the original geometry needs to be larger, i.e. extended beyond the final boundary.

In the following, the one-dimensional bar and two-dimensional shell models from the previous section are again considered.

4.2.1 One-dimensional bar model

For the bar model from Figure 4.5 this extension and trimming approach is demonstrated in Figure 4.10. The bar model is extended by $(p-1)$ elements on both ends and subsequently trimmed at the desired position ($x=0, \xi=0$). Please note that Figure 4.10 only depicts the left end of the bar model and that the other end is treated equivalently. Figure 4.10a shows the trimming position in the geometry space and the fact that boundary control points located closely to each other are trimmed away. The control point eigenfrequencies ω_A, which can serve as a rough conservative estimate of the maximum system eigenfrequency, are decreased compared to Figure 4.5a. Figure 4.10b shows the trimming position in the parameter space, trimmed-off boundary elements respectively basis functions and constant element eigenvalues for each degree p. The shape of the remaining, interior basis functions is uniform and therefore similar to those generated from an unclamped knot vector. The behavior of the critical time step for the untrimmed bar model from Figure 4.5 and the trimmed bar model from Figure 4.10 for $p=1$ to 4 is given in Figure 4.11. The critical time steps plotted in Figure 4.11 are computed from the maximum system eigenfrequencies. While the critical time step for the untrimmed model decreases with an increasing p, it increases for the model with trimmed-off boundary elements.

4.2.2 Two-dimensional shell model

In Figure 4.12 the approach of extending and trimming is applied to a square plate problem with 4×4 elements and degrees $p=1$ to 4, with similar properties as the 2D models in the previous section. Now, the model is extended by $(p-1)$ elements in all four directions and subsequently trimmed along knot lines to obtain the desired dimensions. Because of trimming, only interior elements with equal maximum element eigenfrequencies remain. The element eigenfrequencies of trimmed-off boundary elements are set to zero. As in the trimmed bar model, the maximum element eigenfrequencies decrease with increasing p. Figure 4.13 provides the behavior of the critical time step for different degrees p for the untrimmed plate from Figure 4.8 and the trimmed plate from Figure 4.12, confirming the trend observed for the bar model in Figure 4.11. The critical time steps plotted in Figure 4.13 are computed from the maximum system eigenfrequencies. In this example, eliminating the boundary effect through trimming leads to an increase in time step size by +54%, +128% and +221% for $p=2$, 3 and 4, respectively.

4.2.3 Discussion

From these numerical experiments one can conclude that trimming is indeed an effective measure to eliminate the time step restricting effect of boundary elements. Trimming exactly along knot lines separating interior from boundary elements is very similar to the use of an unclamped knot vector. However, this entails a strong restriction in the design freedom, since knot lines (isocurves) needed to be located exactly on the final, desired surface boundary. Achieving this is hardly possible within current CAD programs.

Thus, for practical applicability, one must allow for arbitrary trimming curves not exactly located along knot lines. A possible automated approach for CAD would be to (i) create a model with an open knot vector as usual in CAD programs, (ii) store the boundary curve description in the geometry space, (iii) extend the surface patches beyond the boundaries by introducing $(p-1)$ element and control point rows (surface extrapolation is a standard feature in CAD systems) and (iv) trim the patch along the initial boundaries. This approach provides an automated and practically applicable procedure in CAD programs. However, it may lead to arbitrarily small trimmed elements. This gives rise to the question of whether and how such small trimmed elements affect the critical time step in explicit analysis. The next section aims at providing an answer.

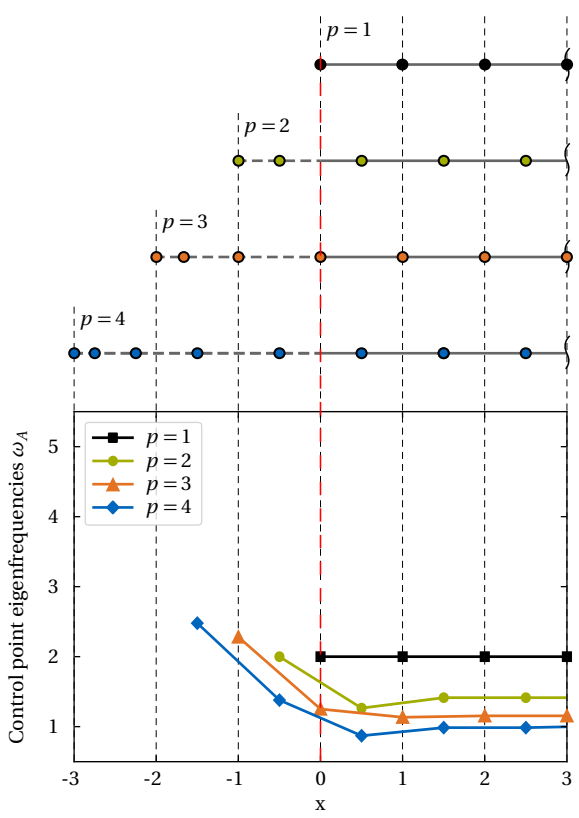

(a) Control point distributions in the geometry space (top) and control point eigenfrequencies ω_A computed from lumped mass and lumped stiffness matrices (bottom).

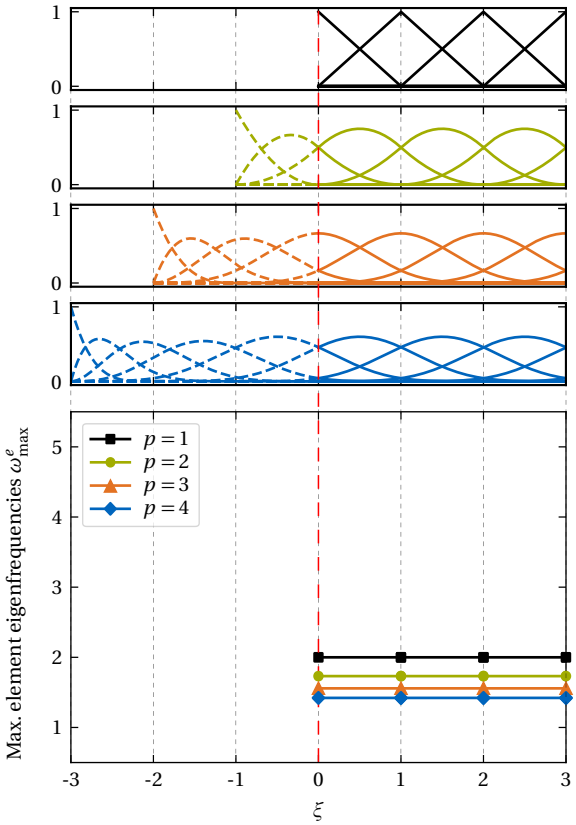

(b) Basis functions (top) and maximum element eigenfrequencies $\omega^e_{\max}$ (bottom).

Figure 4.10: One-dimensional bar problem C^{p-1} with trimmed-off boundary elements: Models of polynomial degree $p = 1$ to 4, generated from an open knot vector with $6+2(p-1)$ elements, similar to the ones in Figure 4.5.

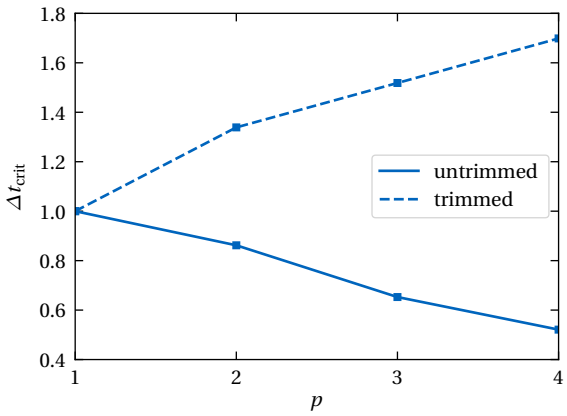

Figure 4.11: One-dimensional bar problem C^{p-1}: Comparison of the critical time step Δt_{crit} as a function of p between the untrimmed case from Figure 4.5 and the case with trimmed-off boundary elements from Figure 4.10.

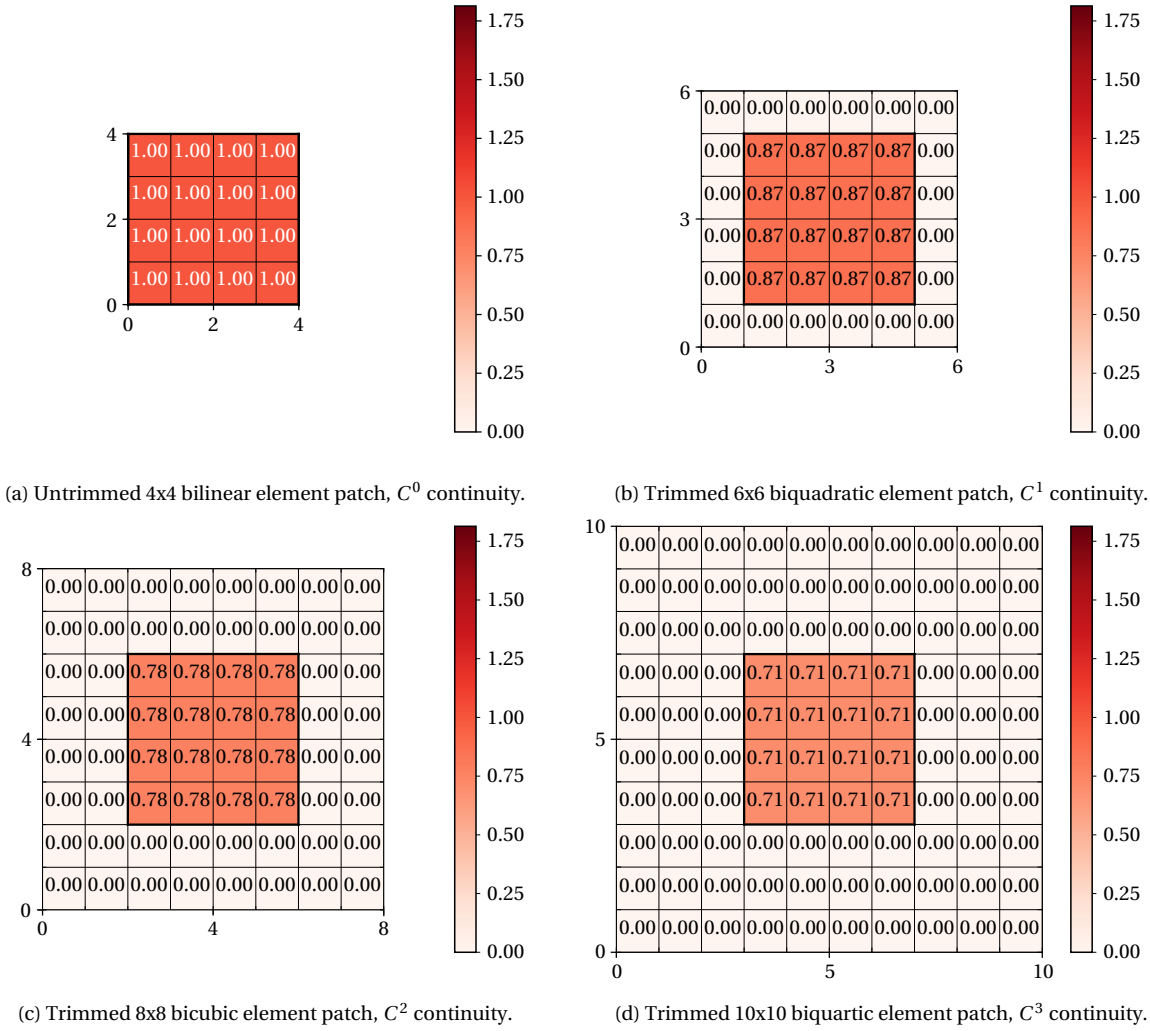

(a) Untrimmed 4x4 bilinear element patch, C^0 continuity.

(b) Trimmed 6x6 biquadratic element patch, C^1 continuity.

(c) Trimmed 8x8 bicubic element patch, C^2 continuity.

(d) Trimmed 10x10 biquartic element patch, C^3 continuity.

Figure 4.12: Two-dimensional square plate problem C^{p-1} with trimmed-off boundary elements: Maximum element eigenfrequencies $\omega^e_{\max}$ of shell models with C^{p-1} elements and $p = 1$ to 4 in (a) to (d). Except for the linear case, elements at the patch boundaries with higher eigenfrequencies (see Figure 4.8) are trimmed off and only interior elements with lower eigenfrequencies remain. The element eigenfrequencies are again normalized with respect to linear elements. The colorbar scales are identical to the ones in Figure 4.8.

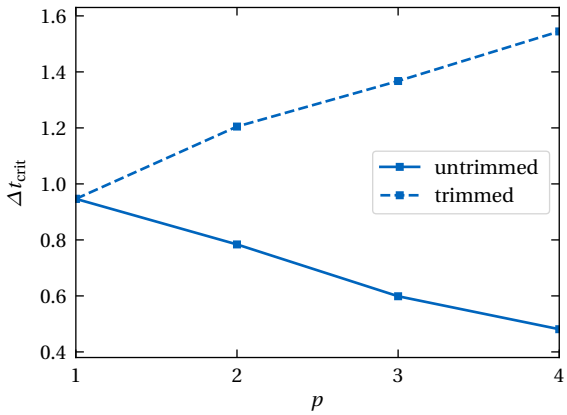

Figure 4.13: Two-dimensional square plate problem C^{p-1}: Comparison of the critical time step Δt_{crit} as a function of p between the untrimmed cases from Figure 4.8 and the cases with trimmed-off boundary elements from Figure 4.12.

4.3 Effect of trimmed element size on the time step

In this section, the effect of trimmed element size on the critical time step in explicit analysis is studied. To this end, the one-dimensional bar and two-dimensional shell models from the previous sections are again deployed. First, the effect of trimming is studied for C^0 inter-element continuity, followed by models with C^{p-1} inter-element continuity.

4.3.1 Open knot vector patches with C^0 inter-element continuity

One-dimensional bar model

To study the effect of trimmed element size for NURBS models with C^0 inter-element continuity, bar models with $p = 1$ to 4 are considered. These models are similar to the ones in Figure 4.1, but are assumed to consist of $n_{\text{el}} > 8$ elements and $n_p = n_{\text{el}}\, p + 1$ control points. The bar models are successively and symmetrically trimmed from both ends from the outside to the inside, in order to generate trimmed elements with varying size as depicted in Figure 4.14. The trimming distance measured from both endpoints in the parameter space is denoted as ξ_{t}. For each chosen ξ_{t} the maximum system eigenfrequency ω_{max} is evaluated. In Figure 4.15 the progression of ω_{max} is plotted over $\xi_{\text{t}} \in [0, 4)$, i.e. the bar is trimmed at different positions ξ_{t} within the four outermost elements on both sides. The corresponding basis functions for $p = 1$ to 4 of the first four elements are depicted above the diagram in Figure 4.15.

Figure 4.15 can be interpreted as follows:

- For all trimming positions ξ_{t}, ω_{max} increases with increasing p.
- As the trimmed element size becomes smaller, that is, as ξ_{t} approaches a knot line from below, ω_{max} increases and tends towards infinity.
- As soon as an element is trimmed off completely, e.g. for $\xi_{\text{t}} = 1 + \varepsilon$ with $\varepsilon << 1$, ω_{max} recovers and takes approximately the value of the untrimmed model.
- The progression of ω_{max} follows the same pattern in all elements, since all elements have identical basis functions.

Recalling that the critical time step in explicit analysis is inversely proportional to the maximum system eigenfrequency, one can draw the following conclusion: For explicit analysis of NURBS-based bar models with C^0 inter-element continuity, trimming is practically infeasible, because the critical time step strongly decreases as the trimmed element size decreases. This would render practical explicit analysis impossible.

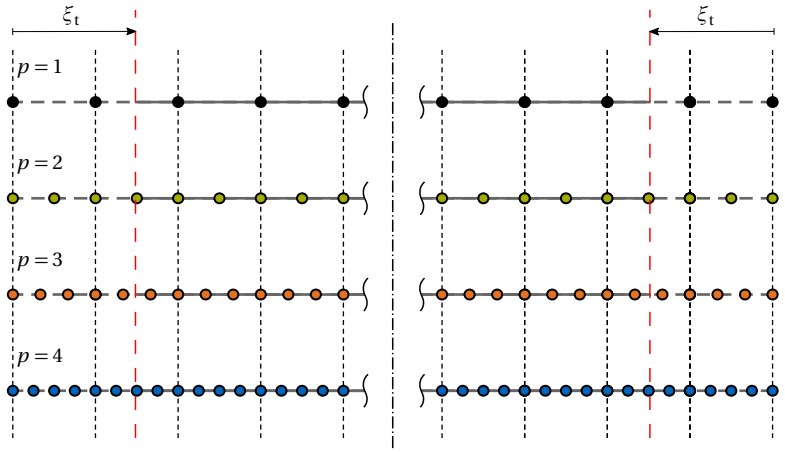

Figure 4.14: One-dimensional trimmed bar problem C^0: Models with $n_{\text{el}} > 8$ elements and C^0 inter-element continuity for $p = 1$ to 4. Colored circles indicate control points, black dashed lines indicate element boundaries and red dashed lines indicate trimming positions. The trimming distance ξ_{t} is measured from the endpoints of both sides.

One-dimensional bar model – Analytical considerations

The fact that ω_{max} tends towards infinity as the size of a trimmed C^0 element tends towards zero can also be explained analytically by studying the system matrix $\mathbf{A} = \mathbf{M}^{-1}\mathbf{K}$. For this reason, the trimmed element length δ is introduced as depicted in Figure 4.16. The following uniform open knot vectors for $p = 1$ to 3 are considered:

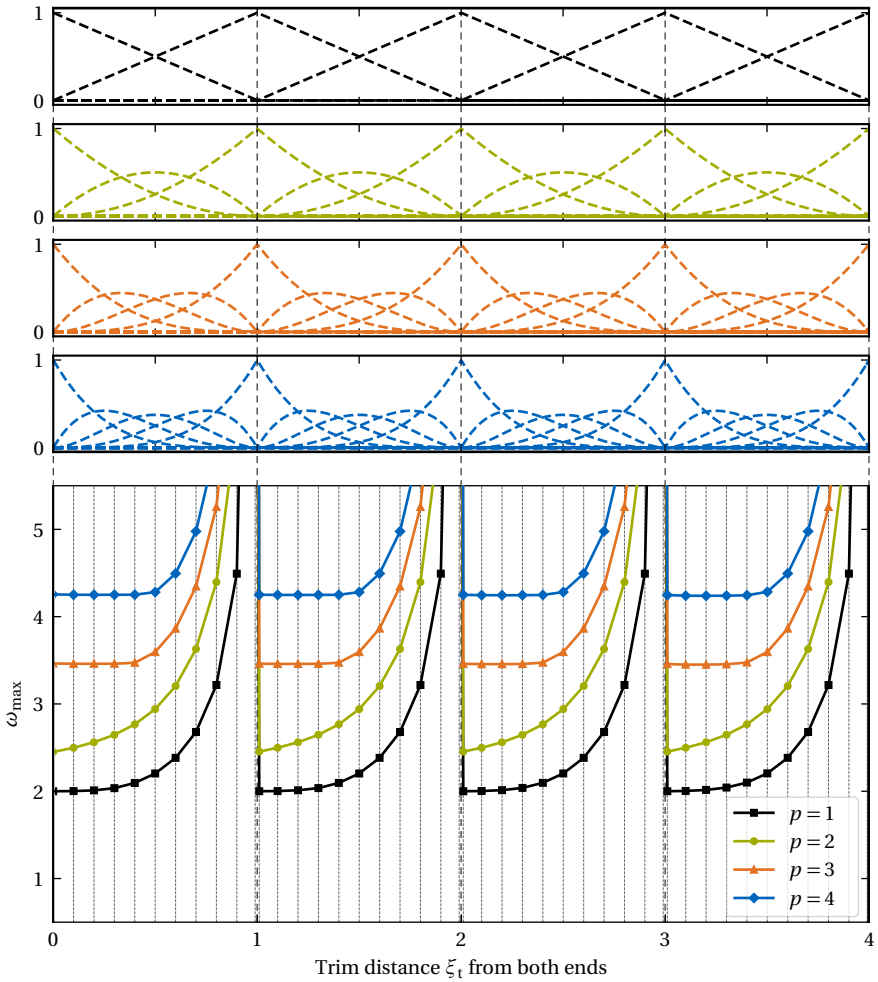

Figure 4.15: One-dimensional trimmed bar problem C^0: Basis functions and maximum system eigenfrequencies for $p=1$ to 4. The bar models are trimmed symmetrically at a distance of $\xi_t \in [0,4)$ from both ends, see Figure 4.14. Note that only the basis functions of the four outermost elements on the left are plotted.

- $p=1$: $\Xi = \{0,0,1,2,3,\ldots\}$
- $p=2$: $\Xi = \{0,0,0,1,1,2,2,3,3,\ldots\}$
- $p=3$: $\Xi = \{0,0,0,0,1,1,1,2,2,2,3,3,3,\ldots\}$

The mass and stiffness matrices are determined analytically by computing the basis functions $N_{i,p}$ and their derivatives $N'_{i,p}(\xi) = \partial N_{i,p}/\partial \xi$, and by inserting them into Eqs. (4.3) and (4.4). In the following, the trimming position is assumed to be located within the first element yielding $\xi_t = 1-\delta$.

The first 4×4 entries of the resulting system matrix $\mathbf{A}$ for $p=1$ are provided in Eq. (4.8), along with the limit $\delta \to 0$ of $\mathbf{A}$, which allows explaining the effect of small trimmed elements. Below, superscripts (p) indicate the polynomial degree. For clarity, the matrix entries A_{ij} in Eqs. (4.8), (4.10) and (4.11) are colored as follows:

- Green, if $\lim_{\delta\to 0} A_{ij} \to 0$.
- Orange, if $\lim_{\delta\to 0} A_{ij} \to \infty$.
- Black, if the leading term is independent of δ.

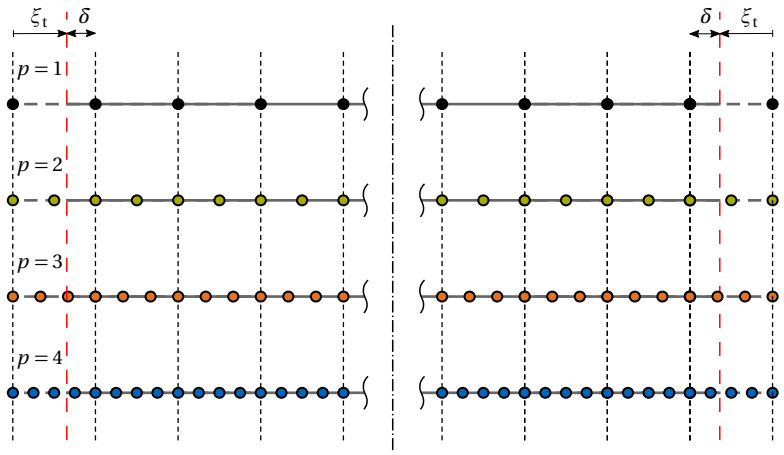

Figure 4.16: One-dimensional trimmed bar problem C^0: Models with $n_{el} > 8$ elements and C^0 inter-element continuity for $p = 1$ to 4. Colored circles indicate control points, black dashed lines indicate element boundaries and red dashed lines indicate the trimming positions within the first outermost elements. The trimming distance $\xi_t = 1-\delta$ is measured from the endpoints of both sides, δ is the trimmed element length.

$$\mathbf{A}^{(p=1)} = \mathbf{M}^{-1}\mathbf{K} = \begin{bmatrix} 2/\delta & -2/\delta & 0 & 0 & \dots \\ \frac{-\delta}{1/2+\delta-\delta^2/2} & \frac{1+\delta}{1/2+\delta-\delta^2/2} & \frac{-1}{1/2+\delta-\delta^2/2} & 0 & \dots \\ 0 & -1 & 2 & -1 & \dots \\ 0 & 0 & -1 & 2 & \dots \\ \vdots & \vdots & \vdots & \vdots & \ddots \end{bmatrix}, \quad \lim_{\delta\to 0}\mathbf{A}^{(p=1)} = \begin{bmatrix} 2/\delta & -2/\delta & 0 & 0 & \dots \\ -2\delta & 2 & -2 & 0 & \dots \\ 0 & -1 & 2 & -1 & \dots \\ 0 & 0 & -1 & 2 & \dots \\ \vdots & \vdots & \vdots & \vdots & \ddots \end{bmatrix} \tag{4.8}$$

For $p = 2$, the first 4×4 entries of $\mathbf{A}$ and $\lim_{\delta\to 0}\mathbf{A}$ are computed as

$$\mathbf{A}^{(p=2)} = \mathbf{M}^{-1}\mathbf{K} = \begin{bmatrix} \frac{4\delta^3/3}{\delta^3/3} & \frac{-8\delta^3/3+2\delta^2}{\delta^3/3} & \frac{4\delta^3/3-2\delta^2}{\delta^3/3} & 0 & \dots \\ \frac{-8\delta^3/3+2\delta^2}{-2\delta^3/3+\delta^2} & \frac{16\delta^3/3-8\delta^2+4\delta}{-2\delta^3/3+\delta^2} & \frac{-8\delta^3/3+6\delta^2-4\delta}{-2\delta^3/3+\delta^2} & 0 & \dots \\ \frac{4\delta^3/3-2\delta^2}{\delta^3/3-\delta^2+\delta+1/3} & \frac{-8\delta^3/3+6\delta^2-4\delta}{\delta^3/3-\delta^2+\delta+1/3} & \frac{4\delta^3/3-4\delta^2+4\delta+4/3}{\delta^3/3-\delta^2+\delta+1/3} & \frac{-2/3}{\delta^3/3-\delta^2+\delta+1/3} & \dots \\ 0 & 0 & \frac{-2/3}{1/3} & \frac{4/3}{1/3} & \dots \\ \vdots & \vdots & \vdots & \vdots & \ddots \end{bmatrix}, \tag{4.9}$$

$$\lim_{\delta\to 0}\mathbf{A}^{(p=2)} = \begin{bmatrix} 4 & 6/\delta & -6/\delta & 0 & \dots \\ 2 & 4/\delta & -4/\delta & 0 & \dots \\ -6\delta^2 & -12\delta & 4 & -2 & \dots \\ 0 & 0 & -2 & 4 & \dots \\ \vdots & \vdots & \vdots & \vdots & \ddots \end{bmatrix}. \tag{4.10}$$

The first 5×5 entries of the mass and stiffness matrices $\mathbf{M}$ and $\mathbf{K}$ for $p = 3$ are given as

$$M_1 = \delta^4/4, \quad M_2 = -3\delta^4/4+\delta^3, \quad M_3 = 3\delta^4/4-2\delta^3+3\delta^2/2, \quad M_4 = -\delta^4/4+\delta^3-3\delta^2/2+\delta-1/4, \quad M_5 = 1/4,$$
$$K_{11} = 9\delta^5/5, \quad K_{12} = -27\delta^5/5+9\delta^4/2, \quad K_{13} = 27\delta^5/5-9\delta^4+3\delta^3, \quad K_{14} = -9\delta^5/5+9\delta^4/2-3\delta^3,$$
$$K_{22} = 81\delta^5/5-27\delta^4+12\delta^3, \quad K_{23} = -81\delta^5/5+81\delta^4/2-33\delta^3+9\delta^2, \quad K_{24} = 27\delta^5/5-18\delta^4+21\delta^3-9\delta^2,$$
$$K_{33} = 81\delta^5/5-54\delta^4+66\delta^3-36\delta^2+9\delta, \quad K_{34} = -27\delta^5/5+45\delta^4/2-36\delta^3+27\delta^2-9\delta,$$
$$K_{44} = 9\delta^5/5-9\delta^4+18\delta^3-18\delta^2+9\delta+9/5, \quad K_{45} = -9/10, \quad K_{55} = 6/5,$$

and the resulting system matrix in the limit $\delta \to 0$ as

$$\mathbf{A}^{(p=3)} = \mathbf{M}^{-1}\mathbf{K}, \quad \lim_{\delta\to 0}\mathbf{A}^{(p=3)} = \begin{bmatrix} 36\delta/5 & 18\delta & 12/\delta & 12/\delta & 0 & \dots \\ 9\delta/2 & 12 & 9/\delta & -9/\delta & 0 & \dots \\ 2\delta & 6 & 6/\delta & -6/\delta & 0 & \dots \\ 12\delta & -36\delta^2 & -36\delta & 36/5 & -18/5 & \dots \\ 0 & 0 & 0 & -18/5 & 24/5 & \dots \\ \vdots & \vdots & \vdots & \vdots & \vdots & \ddots \end{bmatrix}. \tag{4.11}$$

The remaining entries A_{ij} not given in Eqs. (4.8), (4.10) and (4.11) do not depend on δ and are either zero or finite, except for the last $(p+1)\times(p+1)$ entries, which are identical to the first $(p+1)\times(p+1)$ entries. From the matrices $\lim_{\delta\to 0}\mathbf{A}$ it can be seen that the pth entry in the main diagonal, which corresponds to the pth basis function, tends towards infinity:

$$\lim_{\delta\to 0} A_{pp} = \lim_{\delta\to 0}\frac{c}{\delta} = \infty, \tag{4.12}$$

where c is a positive constant depending on the polynomial degree p. Since the considered bar model is symmetric, the same applies for pth last entry in the main diagonal A_{kk}, $k = n_p + 1 - p$. Because all main diagonal entries are positive,

$$\lim_{\delta\to 0}\operatorname{tr}(\mathbf{A}) = \lim_{\delta\to 0}\left(2\frac{c}{\delta} + \sum_{i\neq p,k} A_{ii}\right) = \infty, \quad k = n_p + 1 - p \tag{4.13}$$

where $\operatorname{tr}(\mathbf{A})$ denotes the trace of $\mathbf{A}$. The fact that the trace of an $n_p \times n_p$ matrix is equal to the sum of all its eigenvalues

$$\operatorname{tr}(\mathbf{A}) = \sum_{i=1}^{n_p}\lambda_i, \tag{4.14}$$

shows that

$$\lim_{\delta\to 0}\sum_{i=1}^{n_p}\lambda_i = \lim_{\delta\to 0}\left(2\frac{c}{\delta} + \sum_{i\neq p,k} A_{ii}\right) = \lim_{\delta\to 0} 2\frac{c}{\delta} = \infty. \tag{4.15}$$

That is, the sum of all eigenvalues tends towards infinity. In the last step in Eq. (4.15), the sum over the $(n_p - 2)$ finite values A_{ii} is neglected as it is small compared to c/δ. From Eq. (4.15) one can conclude that at least one eigenvalue λ_i must tend towards infinity as $\delta \to 0$. This can be shown by assuming an eigenvalue $\lambda = C/\delta$ with a positive constant C of order $\mathcal{O}(1)$. For $p = 3$, for example, the determinant associated with the eigenvalue problem $(\mathbf{A} - \lambda\mathbf{I})\mathbf{y} = 0$ in the limit $\delta \to 0$ can then be written as

$$\left|\lim_{\delta\to 0}\left(\mathbf{A}^{(p=3)} - C/\delta\,\mathbf{I}\right)\right| = \begin{vmatrix} 36\delta/5 - C/\delta & 18\delta & 12/\delta & 12/\delta & 0 & \dots \\ 9\delta/2 & 12 - C/\delta & 9/\delta & -9/\delta & 0 & \dots \\ 2\delta & 6 & 6/\delta - C/\delta & -6/\delta & 0 & \dots \\ 12\delta & -36\delta^2 & -36\delta & 36/5 - C/\delta & 0 & \dots \\ 0 & 0 & 0 & -18/5 & 24/5 - C/\delta & \dots \\ \vdots & \vdots & \vdots & \vdots & \vdots & \ddots \end{vmatrix} = 0 \tag{4.16}$$

Compared to the orange entries of order $\mathcal{O}(1/\delta)$, the green and black entries of order $\mathcal{O}(\delta)$ and $\mathcal{O}(1)$, respectively, can be neglected. Because no entries of order $\mathcal{O}(1/\delta)$ appear below the main diagonal, the matrix $(\mathbf{A}^{(p=3)} - \lambda\mathbf{I})$ becomes

an upper triangular matrix, for which the determinant is just the product of its diagonal entries:

$$\left|\lim_{\delta\to 0}\left(\mathbf{A}^{(p=3)}-C/\delta\,\mathbf{I}\right)\right| \approx \begin{vmatrix} -C/\delta & 0 & 12/\delta & 12/\delta & 0 & \dots \\ 0 & -C/\delta & 9/\delta & -9/\delta & 0 & \dots \\ 0 & 0 & 6/\delta - C/\delta & -6/\delta & 0 & \dots \\ 0 & 0 & 0 & -C/\delta & 0 & \dots \\ 0 & 0 & 0 & 0 & -C/\delta & \dots \\ \vdots & \vdots & \vdots & \vdots & \vdots & \ddots \end{vmatrix} = (-C/\delta)^{n_p-2}\left(\frac{6-C}{\delta}\right)^2 = 0 \tag{4.17}$$

Equation (4.17) is fulfilled for $C = 6$ and thus $\lambda = 6/\delta$ is an eigenvalue of $\mathbf{A}$ that tends towards infinity for small trimmed elements. Please note that the bar is assumed to be trimmed symmetrically on both ends, which is the reason why the eigenvalue $\lambda = 6/\delta$ has multiplicity 2. In the same way it can be shown that $\lambda = 2/\delta$ is an eigenvalue for $p = 1$ and that $\lambda = 4/\delta$ is an eigenvalue for $p = 2$.

To summarize, for one-dimensional bar models with C^0 inter-element continuity, it is shown that one system eigenvalue of $\mathbf{A} = \mathbf{M}^{-1}\mathbf{K}$ tends to infinity as one trimmed element length δ approaches zero. Consequently, also one system eigenfrequency tends to infinity as δ approaches zero, leading to an infinitely small critical time step in explicit analysis.

Two-dimensional shell model

To study the effect of trimmed element size for two-dimensional shell models with C^0 inter-element continuity, the square plate models from Figure 4.3 and Figure 4.4 for $p = 1$ to 4 are again considered. Now, these models are trimmed by two smaller, rotated squares such that a large variety of trimmed element sizes is achieved, see Figure 4.17. The square with a diagonal of 8.4 mm forms an outer loop, while the smaller square with a diagonal of 3.6 mm forms an inner loop.

Figure 4.18 depicts the trimmed shell models for $p = 1$ to 4 with the elements colored according to the level of their maximum element eigenfrequencies. The eigenfrequencies are again normalized with respect to linear untrimmed elements. The maximum level of the colorbar corresponds to the maximum eigenfrequency of the quartic model in Figure 4.18d. The results can be interpreted as follows:

- For all degrees p the maximum element eigenfrequencies of trimmed elements are higher than those of untrimmed elements.
- The smaller the trimmed element size, the higher the eigenfrequencies for all p.
- The higher the degree p, the higher the eigenfrequencies of both trimmed and untrimmed elements.

These findings are in accordance with those from the one-dimensional bar model. One can thus conclude that trimming in combination with NURBS-based bar and shell models with C^0 inter-element continuity, may lead to arbitrarily small explicit time steps in case of arbitrarily small trimmed elements. Since small trimmed elements can, in general, not be avoided in industrial models, trimmed C^0 NURBS patches can be classified as infeasible for practical explicit analyses. For the same reason, the concept of trimming is also expected to be infeasible for explicit analysis of standard finite element models based on C^0 Lagrange polynomials. However, the behavior of trimmed NURBS models with higher inter-element continuity still remains to be clarified. This is the subject of the following section.

4.3.2 Open knot vector patches with maximum C^{p-1} inter-element continuity

One-dimensional bar model

The aim of this section is to study whether higher inter-element continuity improves the time step restricting effect of the trimmed element size in C^0 NURBS patches observed above. To this end, the bar models from Figure 4.5 with C^{p-1} inter-element continuity are again considered, but now with a number of $n_{el} > 8$ elements and $n_p = n_{el} + p$ control points as illustrated in Figure 4.19. As in the previous section, the bar models are successively and symmetrically trimmed at a distance ξ_t from both ends in order to generate trimmed elements with varying size. The maximum system eigenfrequency ω_{max} is again evaluated and plotted over $\xi_t \in [0, 4)$ in Figure 4.20. The corresponding basis functions for $p = 1$ to 4 of the four outermost elements are again depicted above the diagram in Figure 4.20.

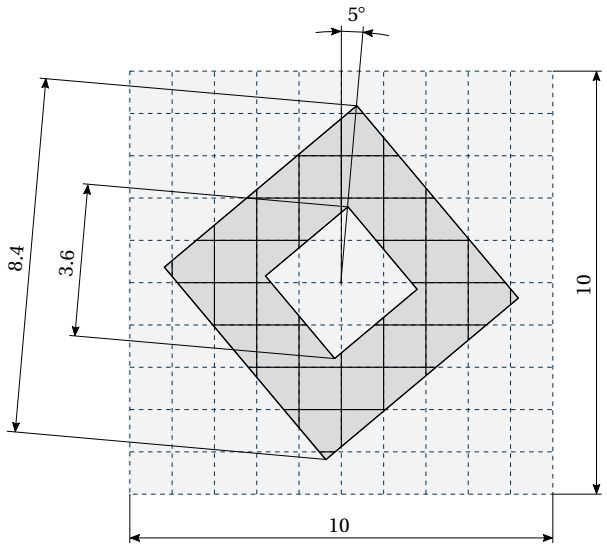

Figure 4.17: Two-dimensional trimmed square plate problem: Shell model with 10×10 isogeometric elements. The square plate is trimmed by two smaller concentric and rotated squares, resulting in a square shell model with a square cut-out.

The behavior plotted in Figure 4.20 differs substantially from the C^0 case in Figure 4.15:

- For the untrimmed case ($\xi_t = 0$), ω_{max} still increases with increasing p.
- The maximum eigenfrequency ω_{max} only tends to infinity for $p = 1$ as the trimmed element size becomes smaller. This is because for $p = 1$ the model is still C^0 continuous. This behavior is the same within all elements, since the linear basis functions are again identical in all elements.
- For higher degrees ($p > 1$) one has to differentiate between the $p-1$ boundary elements and the remaining interior elements. As described in Section 4.1.2, boundary elements possess the highest eigenfrequencies and therefore restrict the time step. Section 4.2 furthermore showed that trimming off boundary elements completely eliminates this effect. Figure 4.20 now demonstrates the behavior for trimming within (boundary) elements. When increasing the trim position ξ_t within the first boundary element, ω_{max} decreases immediately for $p = 2$ to 4. For $p = 2$ it slightly increases again after around $\xi_t = 0.5$, but clearly stays finite as ξ_t approaches the first element boundary. This is in clear contrast to the behavior of an increase towards infinity observed in the C^0 case. For $p = 3, 4$, ω_{max} decreases steadily with an increasing ξ_t and reaches a level lower than the untrimmed linear ω_{max} at $\xi_t = 1$.
- By comparing with the basis functions above the diagram, one can see that for $p = 2$ the boundary effect is removed after the first outermost element is trimmed off. At this point, ω_{max} drops instantaneously. Further increasing the trimming position ξ_t then gives the same progression within all elements for $p = 2$: ω_{max} first slightly increases and then decreases to a finite value shortly before the element boundary.
- For $p = 3, 4$ the maximum eigenfrequency even decreases further with increasing ξ_t until the $p-1$ boundary elements are trimmed off. Trimming within an interior element seems to have no effect on the maximum eigenfrequency at all.

These results show that the higher inter-element continuity for $p > 1$ completely removes the time step restricting effect of small trimmed elements observed in C^0 continuous NURBS models. Quite the contrary, trimming can even increase the critical time step.

One-dimensional bar model – Analytical considerations

The positive effect of higher inter-element continuity shall now be explained by means of the resulting system matrix $\mathbf{A} = \mathbf{M}^{-1}\mathbf{K}$. In analogy to the C^0 bar models in Figure 4.16, C^{p-1} bar models are trimmed within the first outermost elements, yielding a trimmed element length of $\delta = 1 - \xi_t$, see Figure 4.21. The mass and stiffness matrices are again

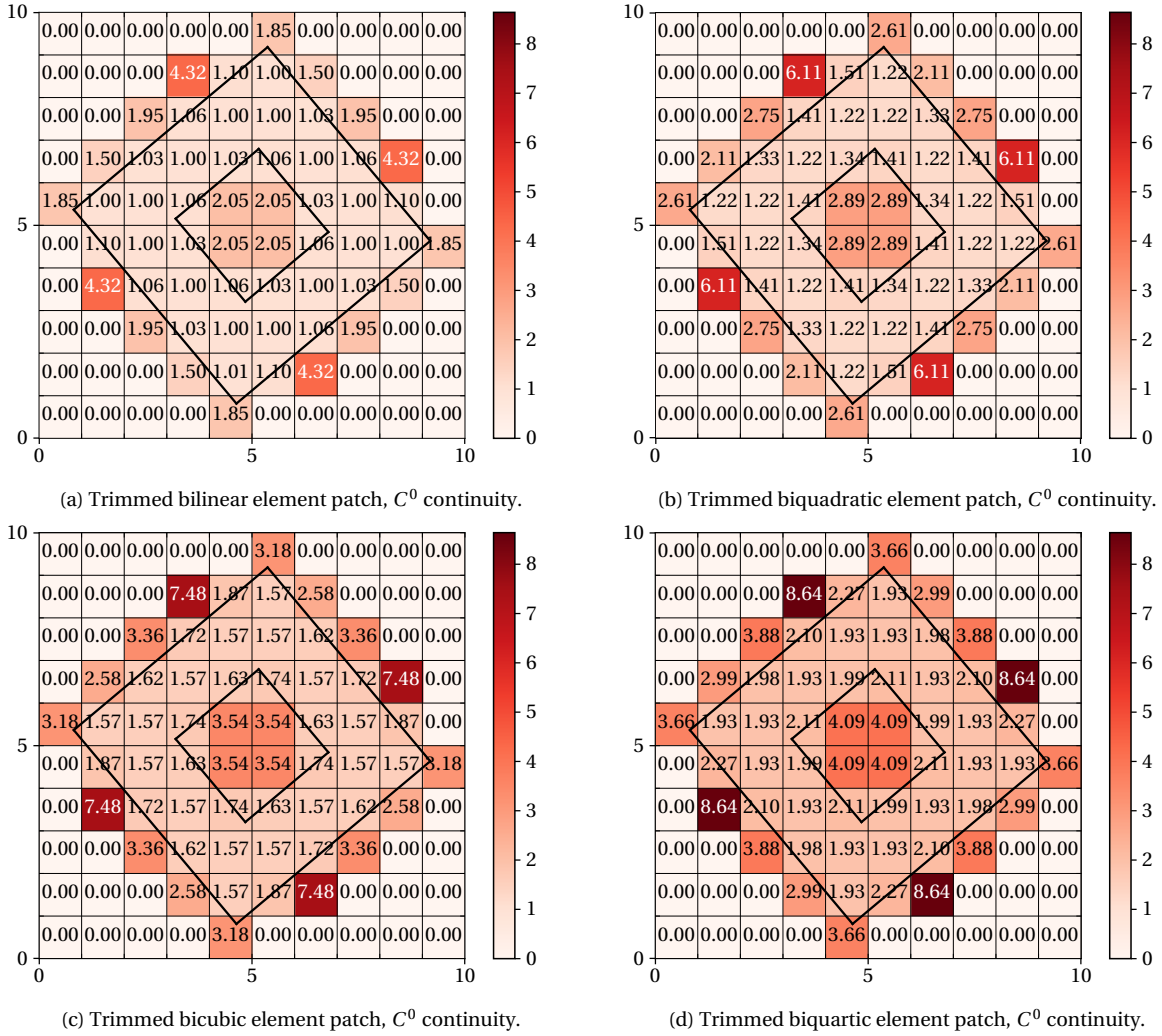

(a) Trimmed bilinear element patch, C^0 continuity.

(b) Trimmed biquadratic element patch, C^0 continuity.

(c) Trimmed bicubic element patch, C^0 continuity.

(d) Trimmed biquartic element patch, C^0 continuity.

Figure 4.18: Two-dimensional trimmed square plate problem C^0: Maximum element eigenfrequencies $\omega^e_{\max}$ of shell models generated from different patches with C^0 isogeometric elements and $p = 1$ to 4 in (a) to (d). The element eigenfrequencies are again normalized with respect to untrimmed linear elements. For all degrees the maximum element eigenfrequencies are sensitive to small trimmed elements.

determined analytically by computing the basis functions $N_{i,p}$ and the corresponding derivatives $N'_{i,p}(\xi) = \partial N_{i,p}/\partial \xi$, and by inserting the resulting expressions into Eqs. (4.3) and (4.4). The following uniform open knot vectors are used:

- $p = 1$: $\Xi = \{0, 0, 1, 2, 3, \ldots\}$
- $p = 2$: $\Xi = \{0, 0, 0, 1, 2, 3, \ldots\}$
- $p = 3$: $\Xi = \{0, 0, 0, 0, 1, 2, 3, \ldots\}$

For $p = 1$ the highest possible continuity is $C^{p-1} = C^0$, so the results are the same as in Section 4.3.1, see Eq. (4.8). The first 4×4 entries of the resulting system matrix $\mathbf{A}$ for $p = 2$ and the corresponding limit $\delta \to 0$ are given as

$$\mathbf{A}^{(p=2)} = \mathbf{M}^{-1}\mathbf{K} = \begin{bmatrix} \frac{4\delta^3/3}{\delta^3/3} & \frac{\delta^2-2\delta^3}{\delta^3/3} & \frac{-\delta^2+2/3\delta^3}{\delta^3/3} & 0 & \ldots \\ \frac{\delta^2-2\delta^3}{1/6+\delta/2+\delta^2/2-\delta^3/2} & \frac{1/3+\delta-3\delta^2+3\delta^3}{1/6+\delta/2+\delta^2/2-\delta^3/2} & \frac{-1/6-\delta+2\delta^2-\delta^3}{1/6+\delta/2+\delta^2/2-\delta^3/2} & \frac{-1/6}{1/6+\delta/2+\delta^2/2-\delta^3/2} & \cdots \\ \frac{-\delta^2+2/3\delta^3}{5/6+\delta/2-\delta^2/2+\delta^3/6} & \frac{-1/6-\delta+2\delta^2-\delta^3}{5/6+\delta/2-\delta^2/2+\delta^3/6} & \frac{2/3+\delta-\delta^2+\delta^3/3}{5/6+\delta/2-\delta^2/2+\delta^3/6} & \frac{-1/3}{5/6+\delta/2-\delta^2/2+\delta^3/6} & \cdots \\ 0 & -1/6 & -1/3 & 1 & \ldots \\ \vdots & \vdots & \vdots & \vdots & \ddots \end{bmatrix}, \tag{4.18}$$

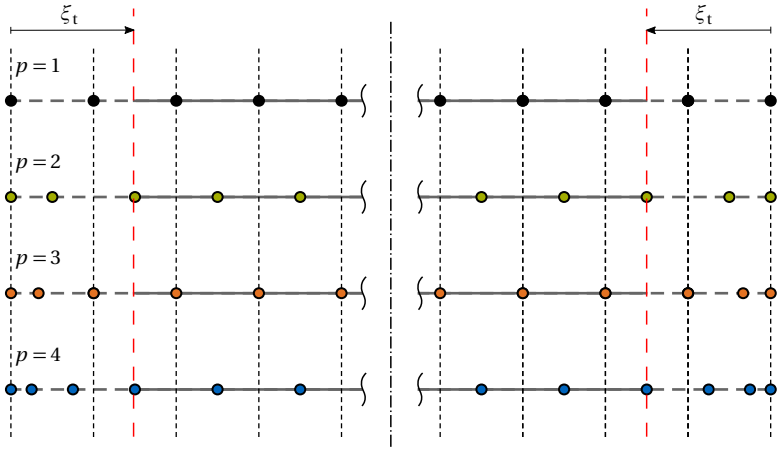

Figure 4.19: One-dimensional trimmed bar problem C^{p-1}: Models with $n_{el} > 8$ elements and C^{p-1} inter-element continuity for $p = 1$ to 4. Colored circles indicate control points, black dashed lines indicate element boundaries and red dashed lines indicate trimming positions. The trimming distance ξ_t is measured from the endpoints of both sides.

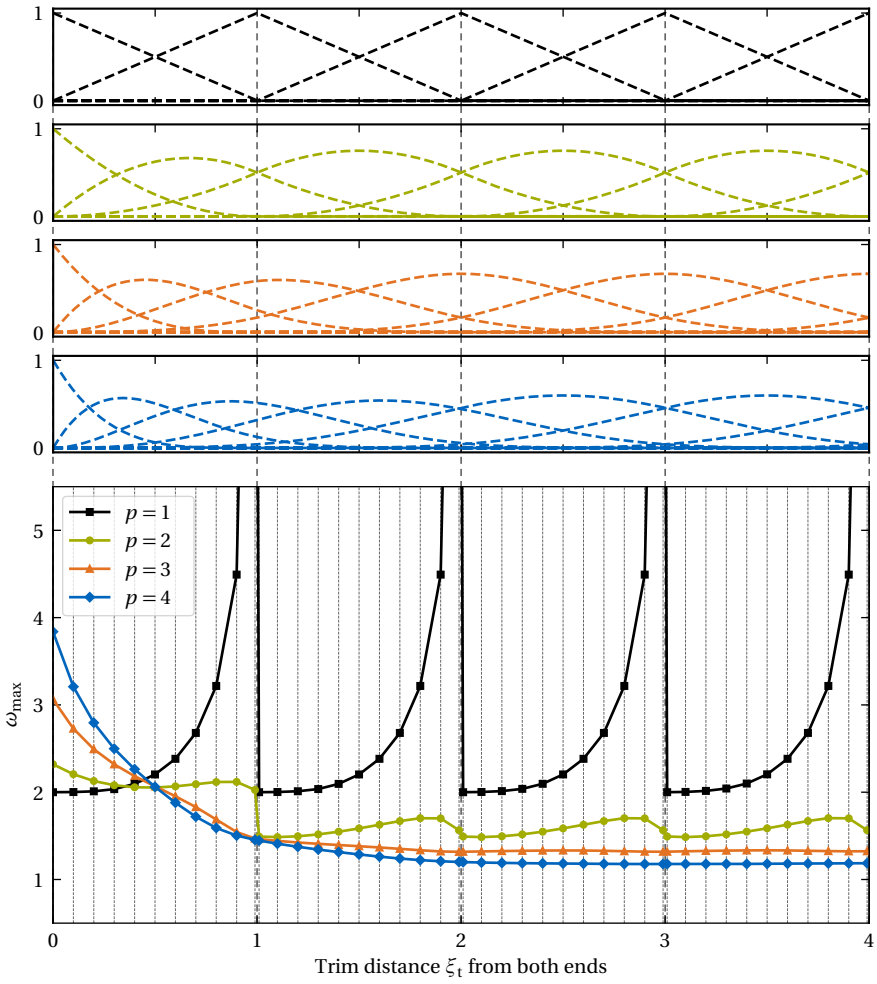

Figure 4.20: One-dimensional trimmed bar problem C^{p-1}: Basis functions and maximum system eigenfrequencies for $p = 1$ to 4. The bar models are trimmed symmetrically at a distance of ξ_t from both ends. Note that only the basis functions of the four outermost elements on the left are plotted.

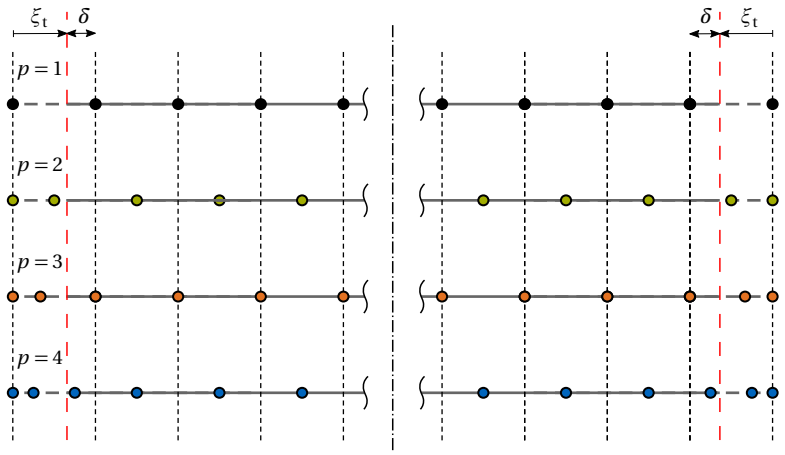

Figure 4.21: One-dimensional trimmed bar problem C^{p-1}: Models with $n_{el} > 8$ elements and C^{p-1} inter-element continuity for $p = 1$ to 4. Colored circles indicate control points, black dashed lines indicate element boundaries and red dashed lines indicate trimming positions. The trim position $\xi_t = 1 - \delta$ is measured from the endpoints of both sides, δ is the trimmed element length.

$$\lim_{\delta\to 0} \mathbf{A}^{(p=2)} = \begin{bmatrix} 4 & 3/\delta & -3/\delta & 0 & \dots \\ 6\delta^2 & 2 & -1 & -1 & \dots \\ -6\delta^2/5 & -1/5 & 4/5 & -2/5 & \dots \\ 0 & -1/6 & -1/3 & 1 & \dots \\ \vdots & \vdots & \vdots & \vdots & \ddots \end{bmatrix}. \tag{4.19}$$

For $p = 3$ the first 5×5 entries of the mass and stiffness matrices are given as

$$M_1 = \delta^4/4, \quad M_2 = -7\delta^4/16 + \delta^3/4 + 3\delta^2/8 + \delta/4 + 1/16,$$
$$M_3 = 11\delta^4/48 - 5\delta^3/12 - \delta^2/8 + 7\delta/12 + 23/48, \quad M_4 = -\delta^4/24 + \delta^3/6 - \delta^2/4 + \delta/6 + 23/24,$$
$$K_{11} = 9\delta^5/5, \quad K_{12} = -63\delta^5/20 + 9\delta^4/8 + 3\delta^3/4, \quad K_{13} = 33\delta^5/20 - 15\delta^4/8 - \delta^3/4,$$
$$K_{14} = -3\delta^5/10 + 3\delta^4/4 - \delta^3/2, \quad K_{22} = 441\delta^5/80 - 63\delta^4/16 - 15\delta^3/8 + 9\delta^2/8 + 9\delta/16 + 9/80,$$
$$K_{23} = -231\delta^5/80 + 69\delta^4/16 - \delta^3/8 - 9\delta^2/8 - 3\delta/16 + 1/20, \quad K_{24} = 21\delta^5/40 - 3\delta^4/2 + 5\delta^3/4 - 3\delta/8 - 3/20,$$
$$K_{33} = 121\delta^5/80 - 55\delta^4/16 + 13\delta^3/8 + 5\delta^2/8 + \delta/16 + 23/80,$$
$$K_{34} = -11\delta^5/40 + \delta^4 - 5\delta^3/4 + \delta^2/2 + \delta/8 - 2/15, \quad K_{44} = \delta^5/20 - \delta^4/4 + \delta^3/2 - \delta^2/2 + \delta/4 + 37/60,$$

and the resulting system matrix in the limit $\delta \to 0$ as

$$\mathbf{A}^{(p=3)} = \mathbf{M}^{-1}\mathbf{K}, \quad \lim_{\delta\to 0} \mathbf{A}^{(p=3)} = \begin{bmatrix} 36\delta/5 & 3/\delta & -1/\delta & -2/\delta & 0 & \dots \\ 12\delta^3 & 9/5 & 4/5 & -12/5 & A_{25} & \dots \\ -12\delta^3/23 & 9/5 & 4/5 & -12/5 & A_{35} & \dots \\ -12\delta^3/23 & 12/115 & 3/5 & 32/115 & A_{45} & \dots \\ 0 & A_{52} & A_{53} & A_{54} & A_{55} & \dots \\ \vdots & \vdots & \vdots & \vdots & \vdots & \ddots \end{bmatrix}. \tag{4.20}$$

The color scheme from Section 4.3.1 is again used for clarity. All matrix entries not specified in Eqs. (4.18) and (4.20) are again either zero or finite, except for the last $(p+1)\times(p+1)$ entries, which are identical to the first $(p+1)\times(p+1)$ entries. From the matrices in Eqs. (4.18) and (4.20) one can immediately see one main difference to the C^0 cases: No orange entries of order $\mathcal{O}(1/\delta)$ appear in the main diagonal. This implies that the trace of $\mathbf{A}$ remains bounded and, via Eq. (4.14) and the assumption of only non-negative eigenvalues, also that all eigenvalues are bounded. Increasing

the trimming position to $1 \leq \xi_t = 2 - \delta < 2$, $2 \leq \xi_t = 3 - \delta < 3$, etc. gives qualitatively similar results, i.e. bounded eigenvalues and eigenfrequencies as depicted in Figure 4.20. This proves the previous observation that bar models with higher order ($p > 1$) and higher continuity (C^{p-1}) elements do not suffer from high eigenfrequencies and small critical time steps in case of small trimmed elements.

Two-dimensional shell model

The C^{p-1} continuous shell models from Figure 4.7 are now trimmed as depicted in Figure 4.17 in order to confirm the positive effect of higher continuity for two-dimensional trimmed models.

The maximum element eigenvalues of linear, quadratic, cubic and quartic trimmed NURBS models with C^{p-1} inter-element continuity are depicted in Figure 4.22. The elements are again colored according to the level of their maximum element eigenfrequency and normalized with respect to linear untrimmed elements. The maximum level of the colorbar corresponds to the maximum eigenfrequency of the linear model in Figure 4.22a. The results of this experiment show the following:

- The results for the linear case in Figure 4.22a are the same as in Figure 4.18a, since the model is still only C^0 continuous.
- For $p = 2$ to 4 the effect of small trimmed elements is nearly removed completely, which can be seen by comparing Figs. 4.22b–4.22d with Figs. 4.18b–4.18d, respectively. For $p = 4$, for instance, the highest maximum element eigenfrequency is around 9.1 times lower than in the C^0 case.
- Except for some (boundary) elements in the $p = 2$ case, all (trimmed) maximum element eigenfrequencies are smaller than those of the untrimmed linear elements.

Please note again that maximum element eigenfrequencies only provide an upper bound for the maximum system eigenfrequency, which determines the critical time step. To demonstrate the actual impact on explicit analysis, the critical time steps of the C^0 models from Figure 4.18 and the C^{p-1} models from Figure 4.22 are plotted in Figure 4.23. While Δt_{crit} reduces with increasing p for the C^0 models, Δt_{crit} increases significantly with increasing p for the C^{p-1} models. For C^0 inter-element continuity, Δt_{crit} approximately halves when increasing p from one to four. For C^{p-1} inter-element continuity, on the contrary, Δt_{crit} increases by a factor of 2.8. The ratio between trimmed and untrimmed element area of the smallest element in these models is 8.45×10^{-4}. In practical models, the trimmed element size may be arbitrarily small, which would scale up the difference in time step size between C^0 and C^{p-1} models even more. It should also be noted that the effect of boundary elements is not completely removed for the C^{p-1} models.

4.3.3 Summary and conclusion of this section

The results observed in this section demonstrate that trimming in explicit analysis is only practically feasible for elements with higher order ($p > 1$) *and* higher continuity ($> C^0$). Regardless of whether a model is trimmed or not, higher order *without* higher continuity (i.e. C^0) gives even smaller time steps than in the case of linear elements. Furthermore, for infinitely small trimmed elements with C^0 inter-element continuity, the time step also becomes infinitely small. This clearly demonstrates the superiority of isogeometric elements with higher inter-element continuity over standard finite elements in terms of time step size and trimming in explicit analysis.

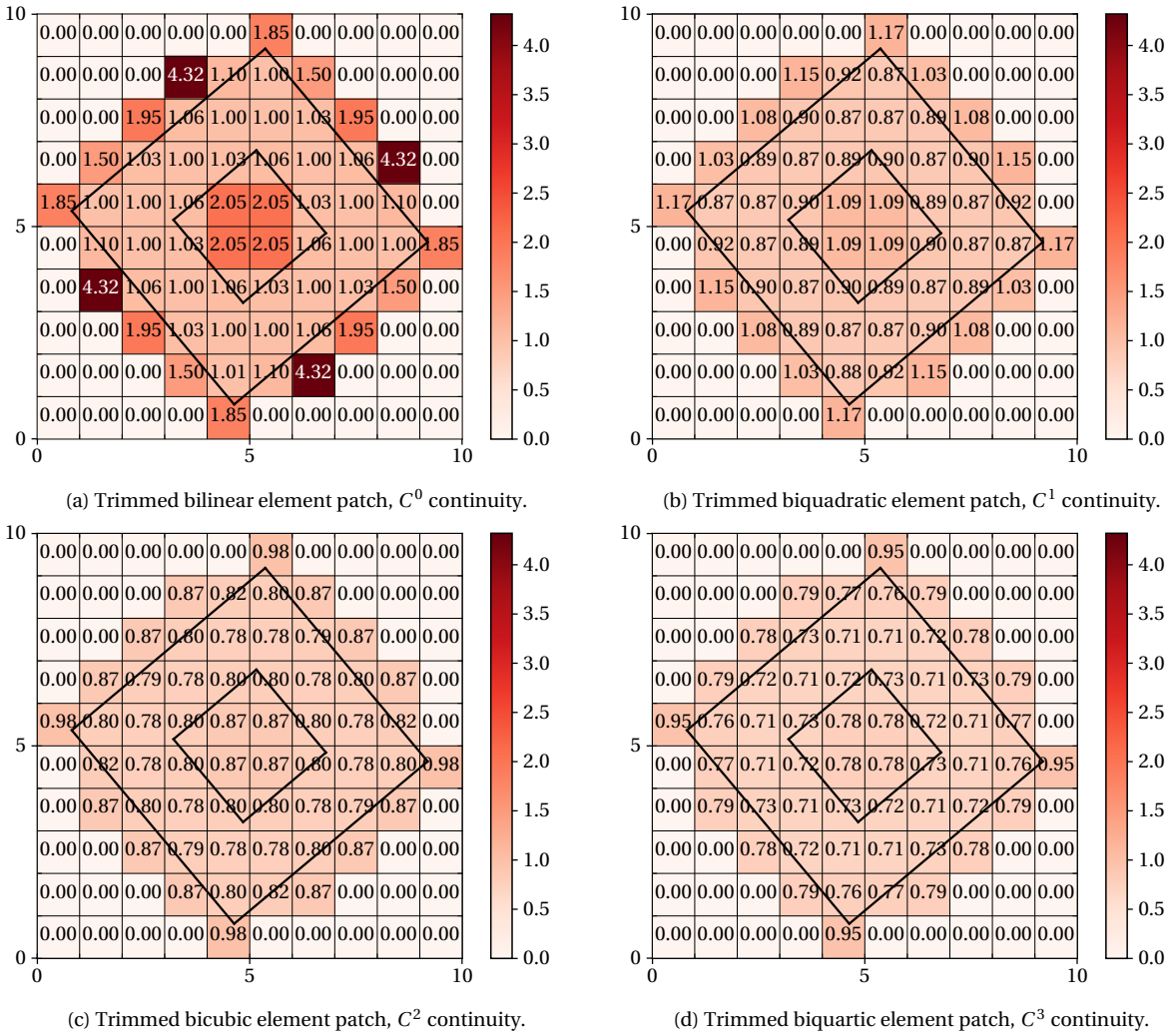

(a) Trimmed bilinear element patch, C^0 continuity.

(b) Trimmed biquadratic element patch, C^1 continuity.

(c) Trimmed bicubic element patch, C^2 continuity.

(d) Trimmed biquartic element patch, C^3 continuity.

Figure 4.22: Two-dimensional trimmed square plate problem C^{p-1}: Maximum element eigenfrequencies $\omega^e_{\max}$ of a trimmed square plate generated from different patches with isogeometric elements of $p = 1$ to 4 in (a) to (d) with C^{p-1} inter-element continuity. Small trimmed elements only cause high element eigenfrequencies for the linear case in (a), while for higher orders in (b) to (d) the element eigenfrequencies are much less sensitive to the trimmed element size. The element eigenfrequencies are again normalized with respect to untrimmed linear elements.

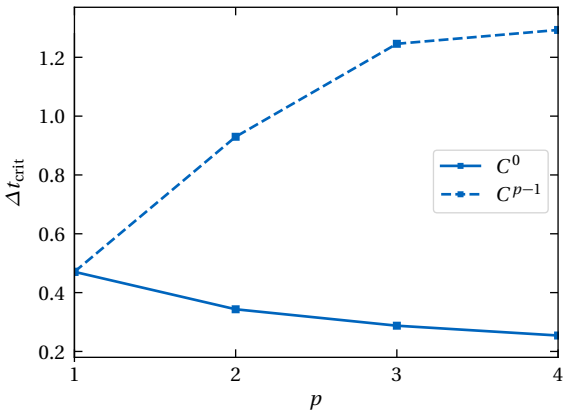

Figure 4.23: Two-dimensional trimmed square plate problem, C^0 versus C^{p-1}: Comparison of the critical time step Δt_{crit} as a function of p between the cases with C^0 and C^{p-1} inter-element continuity from Figures 4.18 and 4.22, respectively. The critical time step is computed from the maximum system eigenfrequency.

4.4 Effect of weak penalty-based boundary conditions on the time step

Applying coupling or Dirichlet boundary conditions in a weak integral sense, for example via a penalty approach, generally introduces stiffness into the system. And as described above, higher stiffness generally leads to higher eigenfrequencies and thus smaller explicit time steps. In the present case of IBRA, penalty-based B-Rep elements add stiffness to the underlying shell structure. The question to be answered is to what extent the critical time step size suffers from the introduced penalty stiffness within Explicit IBRA.

This section therefore aims at providing a general understanding of the relation between the penalty factor and time step size, along with a suitable a priori time step estimate. It furthermore investigates the combined effect of penalty boundary conditions and trimming, again by means of simple one-dimensional bar and two-dimensional shell models.

4.4.1 General relation between penalty factor and time step size

For the subsequent studies, the total stiffness matrix $\mathbf{K}$ is separated into its shell and penalty contributions $\mathbf{K}^{\mathrm{S}}$ and $\mathbf{K}^{\mathrm{P}}$, respectively, see Eqs. (2.33), (3.37) and (3.110), leading to an eigenvalue problem of the form

$$\left[\mathbf{M}^{-1}(\mathbf{K}^{\mathrm{S}}+\mathbf{K}^{\mathrm{P}})\right]\mathbf{y}=\lambda\mathbf{y}. \tag{4.21}$$

While the shell stiffness is prescribed for a given discretization and a given material, the magnitude of the penalty stiffness is strongly dependent on the chosen penalty factor α. For an easier understanding it is beneficial to consider two cases:

- Case I: low relative penalty factors $\alpha_r = \frac{\alpha}{E} << 1$,
- Case II: high relative penalty factors $\alpha_r = \frac{\alpha}{E} >> 1$,

where E denotes the Young's modulus. For case I, the penalty stiffness is small compared to the shell stiffness and can therefore be neglected in the eigenvalue problem (4.21). This gives the well-known eigenvalue problem and critical time step for shells as

$$(\mathbf{M}^{-1}\mathbf{K}^{\mathrm{S}})\mathbf{y}=\lambda\mathbf{y}, \tag{4.22}$$

$$\Delta t^{\mathrm{S}}_{\mathrm{crit}}=\frac{2}{\sqrt{\lambda^{\mathrm{S}}_{\mathrm{max}}}}=\frac{2}{\omega^{\mathrm{S}}_{\mathrm{max}}}. \tag{4.23}$$

For case II, the penalty stiffness dominates over the shell stiffness and therefore the latter can be neglected within the eigenvalue problem. Assuming a constant penalty factor α within the system[2] gives the following eigenvalue problem

$$(\mathbf{M}^{-1}\mathbf{K}^{\mathrm{P}})\mathbf{y}=(\mathbf{M}^{-1}\alpha\check{\mathbf{K}}^{\mathrm{P}})\mathbf{y}=\alpha(\mathbf{M}^{-1}\check{\mathbf{K}}^{\mathrm{P}})\mathbf{y}=\alpha\check{\lambda}^{\mathrm{P}}\mathbf{y}=\lambda^{\mathrm{P}}\mathbf{y}, \tag{4.24}$$

where $\check{\mathbf{K}}^{\mathrm{P}}$ and $\check{\lambda}^{\mathrm{P}}$ denote the penalty stiffness matrix and an eigenvalue for $\alpha=1$, respectively. From this, the critical time step for dominating penalty stiffness can be computed as

$$\Delta t^{\mathrm{P}}_{\mathrm{crit}}=\frac{2}{\omega^{\mathrm{P}}_{\mathrm{max}}}=\frac{2}{\sqrt{\alpha\check{\lambda}^{\mathrm{P}}_{\mathrm{max}}}}=\frac{1}{\sqrt{\alpha}}\frac{2}{\check{\omega}^{\mathrm{P}}_{\mathrm{max}}} \tag{4.25}$$

Equation (4.25) reveals that for case II the critical time step is inversely proportional to $\sqrt{\alpha}$, that is, the time step decreases with an increasing penalty factor. It is worth noting that the relation in Eq. (4.25) is applicable to any kind of penalty approach or model, since all information about the detailed penalty formulation, the material and the discretization are accounted for in $\check{\omega}^{\mathrm{P}}_{\mathrm{max}}$. Determining $\check{\omega}^{\mathrm{P}}_{\mathrm{max}}$ in a pre-processing step is relatively cheap because only the DOFs involved in penalty-based boundary conditions are non-zero. Applying the logarithm to Eq. (4.25) yields

$$\log\left(\Delta t^{\mathrm{P}}_{\mathrm{crit}}\right)=-\frac{1}{2}\log(\alpha)+\log\left(\frac{2}{\check{\omega}^{\mathrm{P}}_{\mathrm{max}}}\right). \tag{4.26}$$

[2] In this eigenvalue problem a lumped mass matrix and a penalty stiffness matrix are considered, which do not couple different types of DOFs (for instance no coupling between x- and y-translations or between translations and rotations). This allows to decouple the equation system, to define individual penalty factors for each type of DOF or even smaller subdomains, and consequently to set up individual eigenvalue problems of the same type as (4.24). The highest eigenvalue of all subproblems would be the critical one. However, this thesis is restricted to one penalty factor for the whole system.

Plotting $\Delta t^{\mathrm{P}}_{\mathrm{crit}}$, and $\Delta t^{\mathrm{S}}_{\mathrm{crit}}$ from Eq. (4.23) as a function of α in a double-logarithmic diagram yields two straight curves as schematically shown in Figure 4.24. From Eq. (4.26), the constant slope of the $\Delta t^{\mathrm{P}}_{\mathrm{crit}}$ curve can be identified as $-\frac{1}{2}$. Modifying the discretization or the physical model would only shift the $\Delta t^{\mathrm{P}}_{\mathrm{crit}}$ curve upwards or downwards, but would not change its slope. The point at which both curves intersect can be computed as

$$\Delta t^{\mathrm{S}}_{\mathrm{crit}} = \Delta t^{\mathrm{P}}_{\mathrm{crit}} \tag{4.27}$$

$$\frac{2}{\omega^{\mathrm{S}}_{\mathrm{max}}} = \frac{1}{\sqrt{\alpha}} \frac{2}{\breve{\omega}^{\mathrm{P}}_{\mathrm{max}}} \quad \Rightarrow \quad \alpha' = \left(\frac{\omega^{\mathrm{S}}_{\mathrm{max}}}{\breve{\omega}^{\mathrm{P}}_{\mathrm{max}}} \right)^2 . \tag{4.28}$$

This penalty factor α' is of practical importance because it indicates the highest possible α that does not lead to a reduction in time step size. A similar estimation of the penalty factor can be found in [47, 145][3]. The actual critical time step can then be estimated via

$$\Delta t_{\mathrm{crit}} = \min(\Delta t^{\mathrm{S}}_{\mathrm{crit}}, \Delta t^{\mathrm{P}}_{\mathrm{crit}}). \tag{4.29}$$

Of course, the actual transition between $\Delta t^{\mathrm{S}}_{\mathrm{crit}}$ and $\Delta t^{\mathrm{P}}_{\mathrm{crit}}$ at α' will not be perfectly sharp, but rather smooth. However, as will be shown below, this bilinear progression is a reasonable approximation.

From Figure 4.24 it is now clear that the time step for small penalty factors is determined by the shell and that only large penalty factors $\alpha/E >> 1$ lead to a reduction in time step size; in fact, for $\alpha/E >> 1$ the time step is directly proportional to $1/\sqrt{\alpha}$.

The behavior of $\Delta t^{\mathrm{S}}_{\mathrm{crit}}$ and $\omega^{\mathrm{S}}_{\mathrm{max}}$ with respect to trimming, polynomial degree and continuity is shown in the previous sections. The question that remains to be answered is how $\breve{\omega}^{\mathrm{P}}_{\mathrm{max}}$ behaves in combination with trimming (especially small trimmed elements), for different polynomial degrees and different h-refinement levels. These effects are investigated in the following sections. The behavior with respect to inter-element continuity is of less interest, since the time step for trimmed NURBS shells demands for highest possible continuity anyway.

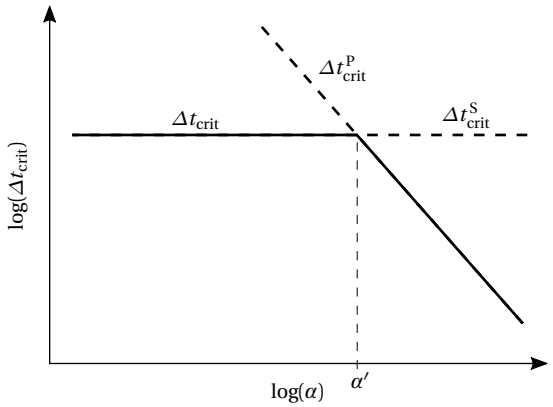

Figure 4.24: Generic relation between critical time step size Δt_{crit} and the penalty factor α.

4.4.2 One-dimensional bar model

The main objectives of this section are (i) studying the behavior of $\breve{\omega}^{\mathrm{P}}_{\mathrm{max}}$ for trimming and different polynomial degrees $p = 1$ to 4 and (ii) approving the general relation between critical time step and penalty factor shown in Figure 4.24 by means of one-dimensional bar problems.

For this purpose, bar models with varying trimming position similar to the ones in the Figure 4.21 are used, but with additional penalty-based Dirichlet boundary conditions applied on both trimmed ends, see Figure 4.25. As mentioned above, only models with C^{p-1} inter-element continuity are considered, since maximum continuity is desired for a reasonable time step size in trimmed shell problems.

In Figure 4.26, the maximum eigenfrequency $\breve{\omega}^{\mathrm{P}}_{\mathrm{max}}$ from the eigenvalue problem (4.24) only including penalty stiffness is plotted as a function of the trim position ξ_{t}. From this plot, the following effects can be identified

[3] A detailed study on the definition of penalty factors within Explicit IBRA is ongoing at the time this PhD thesis is written; results may be found in the corresponding Master's thesis by Theresa Pasch [145], supervised by the author.

- For $p = 1$, the behavior within all four trimmed elements is identical, while for $p = 2$ to 4 a boundary effect again appears.
- For untrimmed models $\check{\omega}^{\mathrm{P}}_{\max}$ increases with increasing p. This behavior reverses as soon as one half of the outermost element is trimmed off, i.e. then a lower p leads to a lower $\check{\omega}^{\mathrm{P}}_{\max}$.
- None of the four curves tends towards infinity as the trim position ξ_{t} approaches a knot line. The $p = 1$ curve indeed increases as the trimmed element size tends towards zero, but finally tends towards a finite value. For $p = 2$ to 4, $\check{\omega}^{\mathrm{P}}_{\max}$ steadily decreases with an increasing trim position ξ_{t}, especially within the first element, and seems to be practically independent of the trimmed element size as soon as the boundary effect is eliminated.

These results have three important positive implications for trimmed NURBS shells with penalty-based boundary conditions:

- The critical time step $\Delta t^{\mathrm{P}}_{\mathrm{crit}}$ stays finite as the trimmed element size tends towards zero, see Eq. (4.25).
- The penalty factor α' until which penalty boundary conditions have no effect on the time step size stays finite as the trimmed element size tends towards zero, see Eq. (4.28).
- For $p > 1$ the eigenfrequency $\check{\omega}^{\mathrm{P}}_{\max}$ is practically independent of the trimmed element size. This means that the same penalty factor α for different B-Rep edge elements, leads to similar maximum eigenfrequencies and thus similar critical time steps, independent of the size of the underlying trimmed shell element. Thus, with respect to time step size it is sufficient to use one consistent penalty factor throughout the system (provided that material properties and discretization are uniform).

For completeness, the overall maximum eigenfrequency $\omega_{\max}$ including shell and penalty stiffness contributions is provided in Figure 4.27. This plot is basically a combination of the plots from Figure 4.20 and Figure 4.26, showing the practical applicability of trimmed NURBS shells with $p > 1$ and penalty-based boundary conditions in explicit analysis.

Figure 4.28 provides the relation between the critical time step Δt_{crit} and the relative penalty factor $\alpha_r = \alpha / E$ for the bar models $p = 1$ to 4 with four different trimming positions ξ_{t}. The four plots Figure 4.28a–4.28d show that the bilinear approximation in Figure 4.24 is expedient for different trimming positions and all considered p. It can also be seen that the penalty factor α' at which the time step starts to decrease varies between the cases. For the case without trimming ($\xi_{\mathrm{t}} = 0$, Figure 4.28a) the time step decreases with p for all α_r. With a trim position of $\xi_{\mathrm{t}} = 0.5$ (Figure 4.28b) the time step size is nearly identical for all degrees p, cf. Figure 4.27. For $\xi_{\mathrm{t}} = 3.5$ (Figure 4.28c), the boundary effect is completely removed and the time step now increases with increasing p. For $\xi_{\mathrm{t}} = 3.9$ (Figure 4.28d) the trend is similar, but the small trimmed element size now leads to a larger difference between the cases $p = 1$ and $p > 1$. Regardless of that, for $\alpha > \alpha'$, all curves decrease with a slope of $-1/2$ in the double-logarithmic plot, independent of trimming position and degree.

4.4.3 One-dimensional bar model – Analytical considerations

As in the previous sections, the behavior of eigenfrequencies with respect to small trimmed elements can be explained analytically via the mass and stiffness matrix entries. Now the focus is on the role of the penalty stiffness. The lumped mass matrix entries M_A and stiffness matrix entries K_{AB} for the one-dimensional bar models are again computed according to Eqs. (4.3) and (4.4). The stiffness matrix entries for penalty-based Dirichlet boundary conditions applied to trimmed bar models are computed as

$$K^{\mathrm{P}}_{AB} = \alpha N_A(\xi) N_B(\xi), \tag{4.30}$$

where the basis functions $N_A(\xi)$ and $N_B(\xi)$ are evaluated at the trim position ξ_{t}. With a uniform open knot vector $\mathcal{H} = \{0,0,1,2,3,4,\ldots\}$ and a trim position $\xi_{\mathrm{t}} = 1-\delta$, the resulting system matrix including shell and penalty stiffness contributions for $p = 1$ is computed as

$$\mathbf{A}^{(p=1)} = \mathbf{M}^{-1}(\mathbf{K}^{\mathrm{S}} + \mathbf{K}^{\mathrm{P}}) = \begin{bmatrix} \frac{\delta+\alpha\delta^2}{\delta^2/2} & \frac{-\delta-\alpha(\delta-\delta^2)}{\delta^2/2} & 0 & 0 & \ldots & \\ \frac{-\delta-\alpha(\delta-\delta^2)}{-\delta^2/2+\delta+1/2} & \frac{(1+\delta)+\alpha(\delta^2-2\delta+1)}{-\delta^2/2+\delta+1/2} & \frac{-1}{-\delta^2/2+\delta+1/2} & 0 & \ldots & \\ 0 & -1 & 2 & -1 & \ldots & \\ 0 & 0 & -1 & 2 & \ldots & \\ \vdots & \vdots & \vdots & \vdots & \vdots & \ddots \end{bmatrix}. \tag{4.31}$$

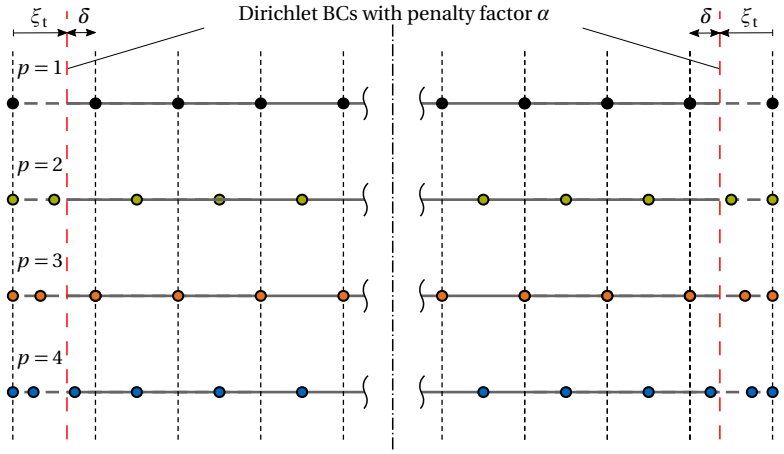

Figure 4.25: One-dimensional trimmed bar problem C^{p-1} with Dirichlet boundary conditions: Models with $n_{\text{el}} > 8$ elements, penalty-based Dirichlet boundary conditions weakly enforced at both ends and C^{p-1} inter-element continuity for $p = 1$ to 4. Colored circles indicate control points, black dashed lines indicate element boundaries and red dashed lines indicate the trimming positions within the first outermost elements. The trimming distance $\xi_t = 1 - \delta$ is measured from the endpoints of both sides, δ is the trimmed element length.

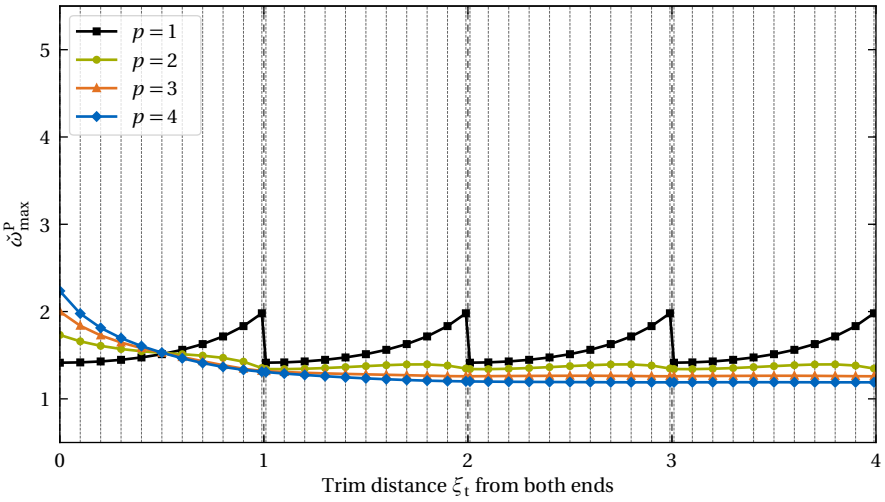

Figure 4.26: One-dimensional trimmed bar problem C^{p-1} with Dirichlet boundary conditions: Maximum eigenfrequencies $\breve{\omega}^{\text{P}}_{\text{max}}$ only including the penalty stiffness contribution $\mathbf{K}^{\text{P}}$. The bar models with $p = 1$ to 4 are trimmed symmetrically at a distance of $\xi_t \in [0, 4)$ from both ends. A relative penalty factor of $\alpha_r = 1$ is used.

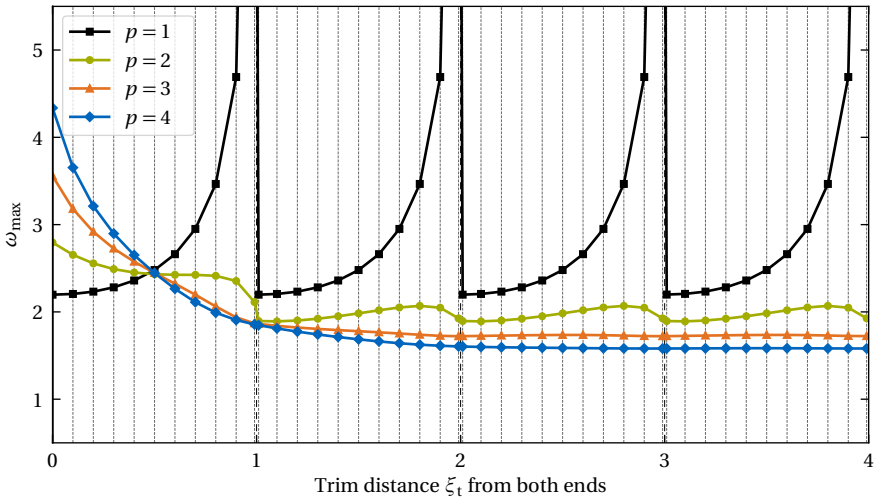

Figure 4.27: One-dimensional trimmed bar problem C^{p-1} with Dirichlet boundary conditions: Maximum system eigenfrequencies $\omega_{\max}$ including the shell and the penalty stiffness contributions $\mathbf{K}^{\mathrm{S}}$ and $\mathbf{K}^{\mathrm{P}}$. The bar models with $p=1$ to 4 are trimmed symmetrically at a distance of $\xi_t \in [0,4)$ from both ends. A relative penalty factor of $\alpha_r = 1$ is used.

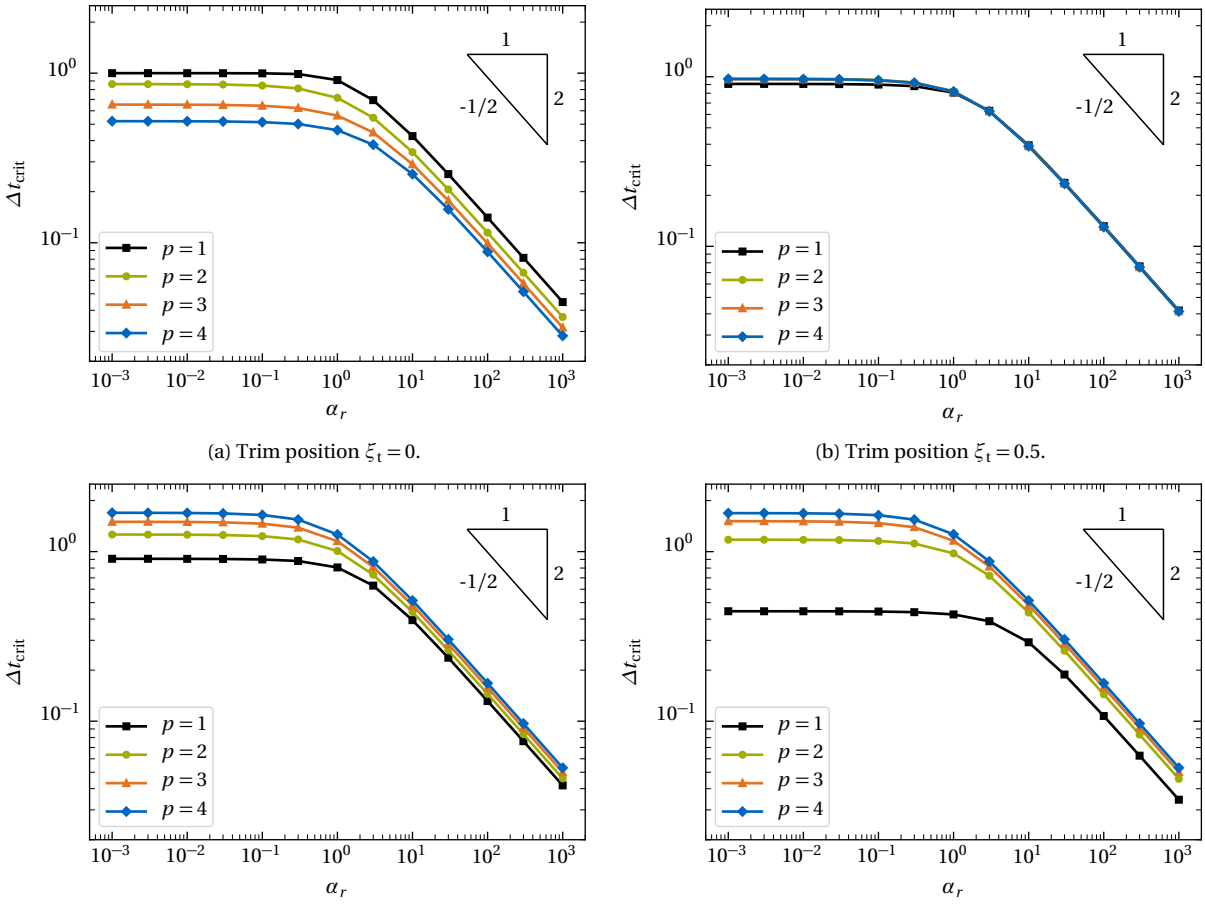

(a) Trim position $\xi_t = 0$.

(b) Trim position $\xi_t = 0.5$.

(c) Trim position $\xi_t = 3.5$.

(d) Trim position $\xi_t = 3.9$.

Figure 4.28: One-dimensional trimmed bar problem C^{p-1} with Dirichlet boundary conditions: Critical time step size Δt_{crit} versus relative penalty factor $\alpha_r = \alpha/E$ for different trim positions ξ_t (see Figure 4.25–4.27) and polynomial degrees $p=1$ to 4.

In the limit $\delta \to 0$ the matrix $\mathbf{A}^{(p=1)}$ simplifies to

$$\lim_{\delta\to 0}\left(\mathbf{A}^{(p=1)}\right) = \begin{bmatrix} 2/\delta+2\alpha & -2/\delta-2\alpha/\delta & 0 & 0 & \dots \\ -2\delta-2\alpha\delta & 2+2\alpha & -2 & 0 & \dots \\ 0 & -1 & 2 & -1 & \dots \\ 0 & 0 & -1 & 2 & \dots \\ \vdots & \vdots & \vdots & \vdots & \vdots & \ddots \end{bmatrix}, \tag{4.32}$$

in which entries tending towards infinity and zero are colored in orange and green, respectively. For $p=2$ with a uniform open knot vector $\mathcal{H}=\{0,0,0,1,2,3,4,\dots\}$ the first 3×3 penalty stiffness entries are obtained as

$$K_{11}^{\mathrm{P}} = \alpha\delta^4, \quad K_{12}^{\mathrm{P}} = \alpha\delta^2/2\left(1+2\delta-3\delta^2\right), \quad K_{13}^{\mathrm{P}} = \alpha/2\left(\delta^2-2\delta^3+\delta^4\right), \quad K_{22}^{\mathrm{P}} = \alpha/4\left(1+4\delta-2\delta^2-12\delta^3+9\delta^4\right),$$
$$K_{23}^{\mathrm{P}} = \alpha/4\left(1-6\delta^2+8\delta^3-3\delta^4\right), \quad K_{33}^{\mathrm{P}} = \alpha/4\left(1-4\delta+6\delta^2-4\delta^3+\delta^4\right),$$

which yields the matrix $\mathbf{A}^{(p=2)}$ in the limit $\delta \to 0$:

$$\lim_{\delta\to 0}\left(\mathbf{A}^{(p=2)}\right) = \begin{bmatrix} 4+3\alpha\delta & 3/\delta+3\alpha/(2\delta) & -3/\delta+3\alpha/(2\delta) & 0 & \dots \\ 6\delta^2+3\alpha\delta^2 & 2+3\alpha/2 & -1+3\alpha/2 & -1 & \dots \\ -6\delta^2/5+3\alpha\delta^2/5 & -1/5+3\alpha/10 & 4/5+3\alpha/10 & -2/5 & \dots \\ 0 & -1/6 & -1/3 & 1 & \dots \\ \vdots & \vdots & \vdots & \vdots & \vdots & \ddots \end{bmatrix}. \tag{4.33}$$

For the cubic case $p=3$ and a uniform open knot vector $\mathcal{H}=\{0,0,0,0,1,2,3,4,\dots\}$ the first 4×4 penalty stiffness entries are

$$K_{11}^{\mathrm{P}} = \alpha\delta^6, \quad K_{12}^{\mathrm{P}} = \alpha\delta^3/4\left(-7\delta^3+3\delta^2+3\delta+1\right), \quad K_{13}^{\mathrm{P}} = \alpha\delta^3/12\left(11\delta^3-15\delta^2-3\delta+7\right),$$
$$K_{14}^{\mathrm{P}} = \alpha\delta^3/6\left(-\delta^3+3\delta^2-3\delta+1\right), \quad K_{22}^{\mathrm{P}} = \alpha/16\left(49\delta^6-42\delta^5-33\delta^4+4\delta^3+15\delta^2+6\delta+1\right),$$
$$K_{23}^{\mathrm{P}} = \alpha\left(-48\delta^6/77+23\delta^5/8+3\delta^4/16-23\delta^3/12-\delta^2/16+3\delta/8+7/48\right),$$
$$K_{24}^{\mathrm{P}} = \alpha\left(7\delta^6/24-\delta^5+9\delta^4/8-\delta^3/3-\delta^2/8+1/24\right),$$
$$K_{33}^{\mathrm{P}} = \alpha\left(121\delta^6/144-55\delta^5/24+53\delta^3/48+61\delta^3/36-67\delta^2/48-7\delta/24+49/144\right),$$
$$K_{34}^{\mathrm{P}} = \alpha\left(-11\delta^6/72+2\delta^5/3-25\delta^4/24+5\delta^3/9+5\delta^2/24-\delta/3+7/72\right),$$
$$K_{44}^{\mathrm{P}} = \alpha\left(\delta^6/36-\delta^5/6+5\delta^4/12-5\delta^3/9+5\delta^2/12-\delta/6+1/36\right).$$

The system matrix $\mathbf{A}^{(p=3)}$ in the limit $\delta \to 0$ can then be written as

$$\lim_{\delta\to 0}\left(\mathbf{A}^{(p=3)}\right) = \begin{bmatrix} 36\delta/5+4\alpha\delta^2 & 3/\delta+\alpha/\delta & -1/\delta+7\alpha/(3\delta) & -2/\delta-2\alpha/(3\delta) & 0 & \dots \\ 12\delta^3+4\alpha\delta^3 & 9/5+\alpha & 4/5+7\alpha/3 & -12/5+2\alpha/3 & A_{25} & \dots \\ -12\delta^3/23+28\alpha\delta^3/23 & 12/115+7\alpha/23 & 3/5+49\alpha/69 & 32/115+14\alpha/69 & A_{35} & \dots \\ -12\delta^3/23+4\alpha\delta^3/23 & -18/115+\alpha/23 & -16/115+7\alpha/69 & 74/115+2\alpha/69 & A_{45} & \dots \\ 0 & A_{52} & A_{53} & A_{54} & A_{55} & \dots \\ \vdots & \vdots & \vdots & \vdots & \vdots & \ddots \end{bmatrix}. \tag{4.34}$$

All other entries not provided in (4.32), (4.33) and (4.34) are either zero or finite, except for the last $(p+1)\times(p+1)$ entries, which are identical to the first $(p+1)\times(p+1)$ entries.

Recalling that the trace of a matrix is equal to the sum of all eigenvalues, one can see the following from the matrices $\mathbf{A}$ in the limit $\delta \to 0$ in (4.32), (4.33) and (4.34):

- The penalty-related terms in the main diagonal all remain bounded or tend to zero for $\delta \to 0$ in all three cases $p = 1,2,3$. Recalling the fact that the trace of a matrix is equal to the sum of its eigenvalues, see Eq. (4.14), and assuming only positive eigenvalues, this implies that also all eigenvalues remain bounded. As a result, penalty boundary conditions do not introduce terms that would cause high eigenfrequencies and small time steps in case of small trimmed shell elements.
- For $p = 1$, the first entry A_{11} contains a finite α term, while for $p > 1$ the α term in the first entry tends to zero as $\delta \to 0$. This is the reason why $\check{\omega}^{\mathrm{P}}_{\max}$ increases (towards a value of 2 in the present example) for $p = 1$ as $\delta \to 0$, which is not the case for $p > 1$.
- All other terms not including α originate from the shell elements and are identical to the ones in Section 4.3.2. Therefore, only the $p = 1$ case possesses a main diagonal entry and thus also an eigenvalue/eigenfrequency tending to infinity for $\delta \to 0$. The main diagonal entries for $p = 2,3$ are all finite or tend to zero. These differences in the matrix entries explain the qualitatively different behavior between $p = 1$ and $p > 1$ in Figure 4.27.

4.4.4 Two-dimensional shell model

The effect of penalty-based boundary conditions shall now be analyzed for two-dimensional trimmed NURBS shell models. Finally, also the effect of mesh refinement via knot insertion is studied.

For this purpose, trimmed square plate models similar to the ones in the previous sections with 10×10 elements, the same material properties and C^{p-1} inter-element continuity are considered. Additionally, penalty-based translational Dirichlet boundary conditions are applied to all four edges. Figure 4.29 depicts the considered shell models with four well-selected trim positions ξ_{t}.

The critical time step Δt_{crit} as a function of the relative penalty factor $\alpha_r = \alpha / E$ for the four trim positions ξ_{t} is given in Figure 4.30. These plots are very similar to the plots of the one-dimensional bar case in Figure 4.28 and therefore allow drawing similar conclusions regarding the value of α' and different trim positions ξ_{t}. The diagrams in Figure 4.30 are also in accordance with the behavior previously reported in [54]. One can furthermore see that the bilinear approximation from Figure 4.24 is also well-suited for two-dimensional trimmed NURBS shell problems and that the curves still decrease with a slope of $-1/2$ for $\alpha > \alpha'$.

In order to also demonstrate the effect of mesh refinement via knot insertion on NURBS shells with penalty-based boundary conditions, the untrimmed configuration[4] from Figure 4.29a with $p = 3$ is considered in four different mesh refinement levels from 5×5 to 20×20 elements, maintaining C^{p-1} continuity. The behavior of the critical time step for these four meshes is plotted in Figure 4.31 and can be interpreted as follows: The finer the mesh, the smaller the critical time step Δt_{crit}. This effect is more pronounced in the region of $\alpha < \alpha'$, in which the shell stiffness dominates. This is because the shell stiffness matrix entries increase with a finer mesh, while the mass matrix entries decrease. For the region of $\alpha > \alpha'$ the difference between the meshes is smaller, because the penalty stiffness entries are hardly affected by the shell element size. The main difference is therefore caused by the varying mass matrix entries.

4.4.5 Summary and conclusion of this section

The main findings of this section regarding the influence of penalty-based boundary conditions on the critical time step can be summarized as follows:

- Penalty-based boundary conditions can indeed reduce the critical time step size, but only for penalty factors larger than a certain value ($\alpha > \alpha'$). This value α' can be determined by solving separate eigenvalue problems for the shell contribution ($\omega^{\mathrm{S}}_{\max}$) and the penalty contribution ($\check{\omega}^{\mathrm{P}}_{\max}$), see Eq. (4.28).
- For NURBS patches with $p > 1$ and an inter-element continuity of C^{p-1}, the critical time step is insensitive to the size of trimmed shell elements involved in penalty-based boundary conditions. Thus, a feasible time step size can be achieved even if penalty-based boundary and coupling conditions are applied to NURBS models with arbitrarily small trimmed elements.
- In order to achieve a certain critical time step size one consistent penalty factor α can be used for all B-Rep edge elements, independent of the size of the underlying trimmed shell element.

The behavior of the time step size in more complex examples including penalty-based coupling conditions is demonstrated in Chapter 7.

[4] Considering a trimmed configuration in this refinement study would vary the trim positions within elements and therefore cause different effects on the time step for different refinement levels. To avoid this, the untrimmed configuration is chosen.

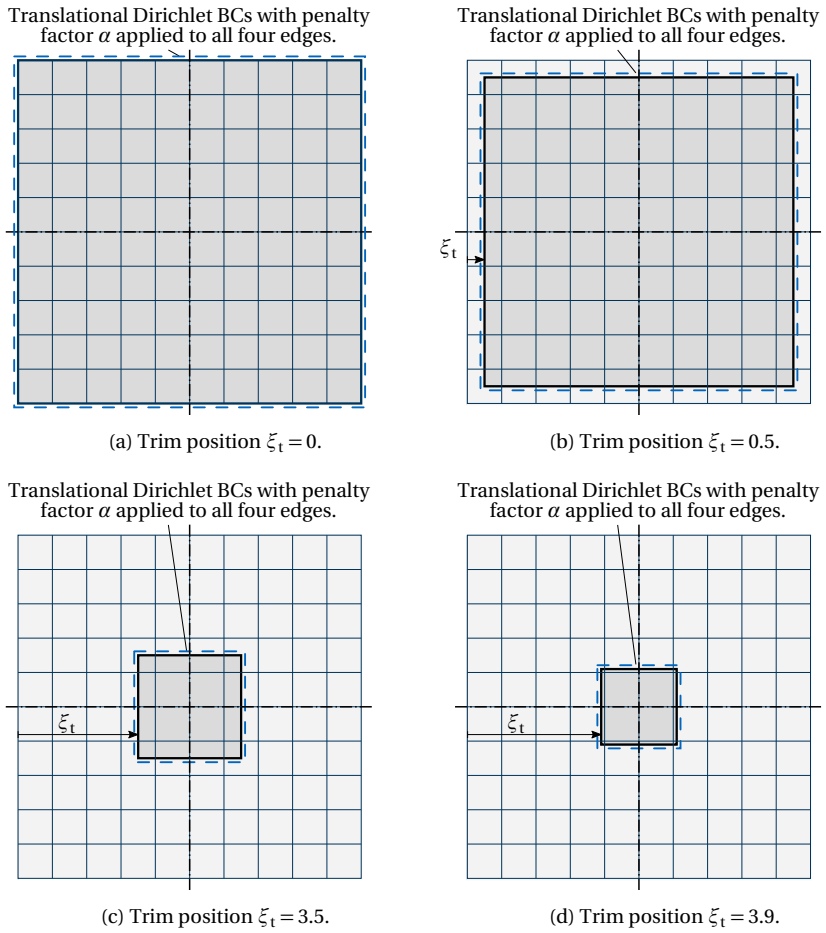

(a) Trim position $\xi_t = 0$.

(b) Trim position $\xi_t = 0.5$.

(c) Trim position $\xi_t = 3.5$.

(d) Trim position $\xi_t = 3.9$.

Figure 4.29: Two-dimensional trimmed square plate problem C^{p-1} with Dirichlet boundary conditions: Double symmetric shell models with 10×10 isogeometric elements, polynomial degrees $p = 1$ to 4, C^{p-1} inter-element continuity and four different trimming configurations defined by the trim position ξ_t. Penalty-based Dirichlet boundary conditions are weakly enforced on all four (trimmed) edges.

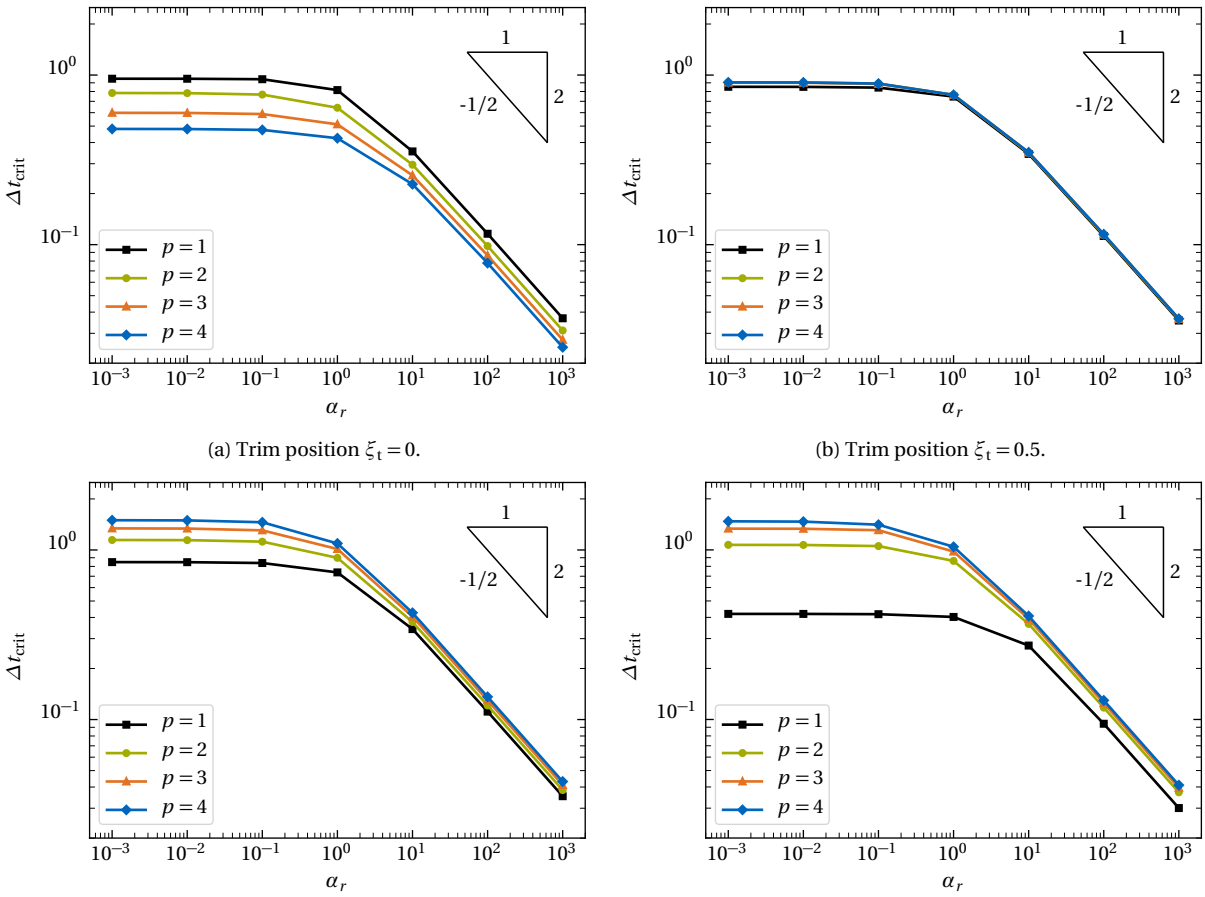

(a) Trim position $\xi_t = 0$.

(b) Trim position $\xi_t = 0.5$.

(c) Trim position $\xi_t = 3.5$.

(d) Trim position $\xi_t = 3.9$.

Figure 4.30: Two-dimensional trimmed square plate problem C^{p-1} with Dirichlet boundary conditions: Critical time step size Δt_{crit} versus relative penalty factor $\alpha_r = \alpha/E$ for different trim positions ξ_t (see Figure 4.29), C^{p-1} inter-element continuity and $p = 1$ to 4.

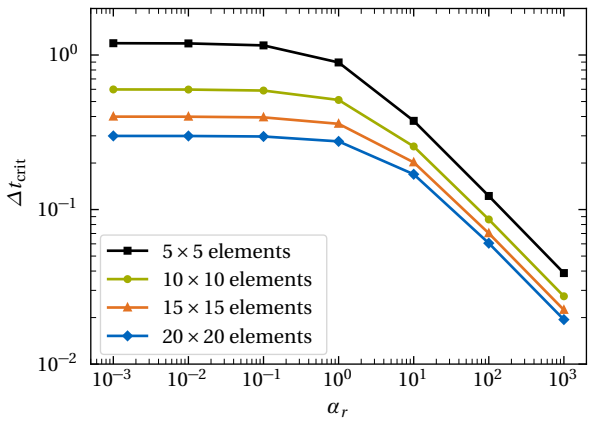

Figure 4.31: Two-dimensional trimmed square plate problem C^{p-1} with Dirichlet boundary conditions: Critical time step size Δt_{crit} versus relative penalty factor $\alpha_r = \alpha/E$ for the untrimmed model $\xi_t = 0$ from Figure 4.30 with different mesh refinement levels, C^{p-1} inter-element continuity and $p = 3$.

4.5 Local selective mass scaling for penalty-based B-Rep elements

4.5.1 Introduction

The previous section demonstrated the behavior of the critical time step with respect to penalty-based boundary and coupling conditions. As shown in [54], in many cases accurate results are obtained without a restriction in time step size. In case penalty-based B-Rep elements, however, lead to a reduced critical time step, mass scaling is a convenient way to overcome this issue. In fact, mass scaling is employed in basically every practical vehicle crash simulation with standard explicit FEA.

As described in Section 3.3, penalty-based boundary and coupling conditions only add stiffness to control points involved in the corresponding B-Rep edge element formulations. Furthermore, the introduced stiffness is distributed to control points according to the value of their basis function along the respective B-Rep edge element, see for instance Eqs. (3.42), (3.43), (3.53) and (3.54). Thus, in order to minimize the amount of added mass, it is expedient to only scale the involved control points and only to the extent required for balancing the impact of added stiffness on the time step. That is, a local selective approach specifically scaling control points depending on the introduced stiffness is desired. The difficulty is, however, to determine a suitable scaling factor for each control point. This section proposes a simple yet effective local selective mass scaling approach based on the Gershgorin circle theorem [81, 138–140] and control point (nodal) time step estimates.

4.5.2 The local selective mass scaling approach

In the following, it is expedient to consider three different undamped systems with $n_{\mathrm{DOF}} \times n_{\mathrm{DOF}}$ mass and stiffness matrices, where n_{DOF} denotes the number of degrees of freedom.

System I – No penalty-based B-Rep elements, no mass scaling: This system is described by a lumped mass matrix $\mathbf{M}$ and a stiffness matrix $\mathbf{K}^{\mathrm{S}}$ with shell contributions only. The critical time step without B-Rep elements is then computed as

$$\Delta t_{\mathrm{crit}}^{\mathbf{M}^{-1}\mathbf{K}^{\mathrm{S}}} = \frac{2}{\omega_{\max}^{\mathbf{M}^{-1}\mathbf{K}^{\mathrm{S}}}} = \frac{2}{\sqrt{\lambda_{\max}^{\mathbf{M}^{-1}\mathbf{K}^{\mathrm{S}}}}} = \frac{2}{\max\limits_{k}\sqrt{\lambda_{k}^{\mathbf{M}^{-1}\mathbf{K}^{\mathrm{S}}}}}, \quad k = 1, \ldots, n_{\mathrm{DOF}}. \tag{4.35}$$

System II – Penalty-based B-Rep elements, no mass scaling: This system is described by a lumped mass matrix $\mathbf{M}$, a stiffness matrix with shell and penalty contributions $\mathbf{K} = \mathbf{K}^{\mathrm{S}} + \mathbf{K}^{\mathrm{P}}$, and a critical time step including B-Rep elements of

$$\Delta t_{\mathrm{crit}}^{\mathbf{M}^{-1}\mathbf{K}} = \frac{2}{\omega_{\max}^{\mathbf{M}^{-1}\mathbf{K}}} = \frac{2}{\sqrt{\lambda_{\max}^{\mathbf{M}^{-1}\mathbf{K}}}} = \frac{2}{\max\limits_{k}\sqrt{\lambda_{k}^{\mathbf{M}^{-1}\mathbf{K}}}}, \quad k = 1, \ldots, n_{\mathrm{DOF}}. \tag{4.36}$$

Due to the penalty stiffness introduced by B-Rep elements, the critical time step of System II will be smaller than or equal to the one of System I.

System III – Penalty-based B-Rep elements, mass scaling: This system is described by a *scaled* lumped mass matrix $\hat{\mathbf{M}}$, a stiffness matrix with shell and penalty contributions $\mathbf{K} = \mathbf{K}^{\mathrm{S}} + \mathbf{K}^{\mathrm{P}}$, and a critical time step

$$\Delta t_{\mathrm{crit}}^{\hat{\mathbf{M}}^{-1}\mathbf{K}} = \frac{2}{\omega_{\max}^{\hat{\mathbf{M}}^{-1}\mathbf{K}}} = \frac{2}{\sqrt{\lambda_{\max}^{\hat{\mathbf{M}}^{-1}\mathbf{K}}}} = \frac{2}{\max\limits_{k}\sqrt{\lambda_{k}^{\hat{\mathbf{M}}^{-1}\mathbf{K}}}}, \quad k = 1, \ldots, n_{\mathrm{DOF}}. \tag{4.37}$$

The aim of the local selective mass scaling approach is to determine the scaled mass matrix $\hat{\mathbf{M}}$, such that the critical time step without penalty-based B-Rep elements (System I) is achieved, i.e. such that a (possible) time step restricting effect by B-Rep elements is eliminated. This leads to the requirement

$$\Delta t_{\mathrm{crit}}^{\hat{\mathbf{M}}^{-1}\mathbf{K}} \overset{!}{\geq} \Delta t_{\mathrm{crit}}^{\mathbf{M}^{-1}\mathbf{K}^{\mathrm{S}}}. \tag{4.38}$$

As described above, each control point involved in a penalty-based B-Rep element receives a particular amount of stiffness depending on the value of its basis function along the B-Rep edge element. Thus, for each control point a particular amount of mass scaling is required to balance the impact on the critical time step. The difficult task now is to assign the right amount of mass to each control point – as little as possible, but as much as needed. A simple yet effective way to break down this requirement onto the control point level is to use the nodal time step estimate based on the Gershgorin circle theorem, see Section 2.9.4, Eqs. (2.75)–(2.77). Applied to System III, which includes

mass scaling, the nodal time step estimate gives a conservative estimation of the maximum system eigenvalue $\lambda_{\max}^{\hat{\mathbf{M}}^{-1}\mathbf{K}}$ via the maximum eigenvalue of the system with a lumped stiffness matrix $\tilde{\mathbf{K}}$:

$$\lambda_{\max}^{\hat{\mathbf{M}}^{-1}\mathbf{K}} \leq \lambda_{\max}^{\hat{\mathbf{M}}^{-1}\tilde{\mathbf{K}}} = \max_{A,i}\left(\frac{\tilde{K}_{AiAi}}{\hat{M}_{AiAi}}\right). \tag{4.39}$$

Herein the index $A = \{1,\dots,n\}$ represents a control point and $i = \{1,\dots,6\}$ the degree of freedom (three translations and three rotations). This upper bound $\lambda_{\max}^{\hat{\mathbf{M}}^{-1}\tilde{\mathbf{K}}}$ can be interpreted as the maximum real value of all Gershgorin discs

$$\hat{\mathcal{D}}_{Ai}\left(\frac{K_{AiAi}}{\hat{M}_{AiAi}}, \sum_{Bj\neq Ai}|K_{AiBj}|\right), \tag{4.40}$$

see also Section 2.9.4. Based on the individual maxima of each Gershgorin disc, i.e. the entries of the lumped matrix $\hat{\mathbf{M}}^{-1}\tilde{\mathbf{K}}$, one can formally assign a critical time step $\Delta t_{Ai}^{\hat{\mathbf{M}}^{-1}\tilde{\mathbf{K}}}$ to each DOF:

$$\Delta t_{Ai}^{\hat{\mathbf{M}}^{-1}\tilde{\mathbf{K}}} = \frac{2}{\sqrt{\frac{\tilde{K}_{AiAi}}{\hat{M}_{AiAi}}}}. \tag{4.41}$$

Based on that, a conservative lower bound for the critical time step of the mass-scaled System III can be computed as

$$\Delta t_{\text{crit}}^{\hat{\mathbf{M}}^{-1}\tilde{\mathbf{K}}} = \min_{A,i}\left(\Delta t_{Ai}^{\hat{\mathbf{M}}^{-1}\tilde{\mathbf{K}}}\right) \leq \Delta t_{\text{crit}}^{\hat{\mathbf{M}}^{-1}\mathbf{K}}. \tag{4.42}$$

Through Eq. (4.42), requirement (4.38) can be formulated in terms of control point specific time steps as

$$\Delta t_{\text{crit}}^{\hat{\mathbf{M}}^{-1}\mathbf{K}} \geq \Delta t_{\text{crit}}^{\hat{\mathbf{M}}^{-1}\tilde{\mathbf{K}}} = \min_{A,i}\left(\Delta t_{Ai}^{\hat{\mathbf{M}}^{-1}\tilde{\mathbf{K}}}\right) \overset{!}{\geq} \Delta t_{\text{crit}}^{\mathbf{M}^{-1}\mathbf{K}^{\text{S}}}. \tag{4.43}$$

which is stronger than requirement (4.38) and thus conservative. Equation (4.43) is equivalent to the requirement that all Gershgorin discs[5] $\hat{\mathcal{D}}_{Ai}$ of System III must be entirely located below the maximum eigenvalue of System I. The basic requirement to be fulfilled within the proposed mass scaling approach can then be concisely formulated as

$$\Delta t_{Ai}^{\hat{\mathbf{M}}^{-1}\tilde{\mathbf{K}}} \overset{!}{\geq} \Delta t_{\text{crit}}^{\mathbf{M}^{-1}\mathbf{K}^{\text{S}}} \quad \forall\, Ai. \tag{4.44}$$

With Eq.(4.39) and the relation between critical time step and maximum eigenvalue similar to Eq.(4.37), the required control point mass to achieve $\Delta t_{\text{crit}}^{\mathbf{M}^{-1}\mathbf{K}^{\text{S}}}$ can be computed as

$$\hat{M}_{AiAi} \geq \frac{1}{4}\tilde{K}_{AiAi}\left(\Delta t_{\text{crit}}^{\mathbf{M}^{-1}\mathbf{K}^{\text{S}}}\right)^2. \tag{4.45}$$

In order to obtain an actual mass scaling factor, both sides of (4.45) are divided by the unscaled control point mass M_{AiAi}, which, together with the nodal estimate for System II

$$\Delta t_{\text{crit}}^{\mathbf{M}^{-1}\tilde{\mathbf{K}}} = \frac{2}{\sqrt{\frac{\tilde{K}_{AiAi}}{M_{AiAi}}}}, \tag{4.46}$$

leads to a formula for the control point mass scaling factor:

$$f_{Ai} = \frac{\hat{M}_{AiAi}}{M_{AiAi}} = \left(\frac{\Delta t_{\text{crit}}^{\mathbf{M}^{-1}\mathbf{K}^{\text{S}}}}{\Delta t_{Ai}^{\mathbf{M}^{-1}\tilde{\mathbf{K}}}}\right)^2. \tag{4.47}$$

Thus, the mass scaling factor is computed from the ratio between the desired time step and the respective nodal time step of System II. Please note that the '≥' is replaced by a '=', since the lowest possible mass scaling is desired. From Eq. (4.47) one can see that there are possibly six ($i = 1-6$) mass scaling factors per control point A. In practice, a control point has exactly *one* translational and *one* rotational mass. Therefore the largest of the three translational and the largest of the three rotational mass scaling factors are chosen as the effective control point mass scaling

[5] In fact, the Gershgorin circle theorem does not claim that every disc contains an eigenvalue. Since requirement (4.43) considers all discs $\hat{\mathcal{D}}_{Ai}$, this means that there is a chance that control points may be scaled to a higher amount than necessary.

factors. Furthermore mass scaling factors smaller than one are not permitted. This leads to the final formulas for the translational and rotational mass scaling factors:

$$f_A^{\text{disp}} = \max\left(1,\ \max_{i \in \mathcal{M}_{\text{i}}^{\text{disp}}} \left(f_{Ai}\right)\right), \tag{4.48}$$

$$f_A^{\text{rot}} = \max\left(1,\ \max_{i \in \mathcal{M}_{\text{i}}^{\text{rot}}} \left(f_{Ai}\right)\right), \tag{4.49}$$

where $\mathcal{M}_{\text{i}}^{\text{disp}}$ and $\mathcal{M}_{\text{i}}^{\text{rot}}$ are the sets of translational and rotational matrix indices, respectively.

Of course, instead of the critical time step $\Delta t_{\text{crit}}^{\mathbf{M}^{-1}\mathbf{K}^{\text{S}}}$ of System I without penalty-based B-Rep elements, any desired time step $\Delta \bar{t}$ can be specified in Eq. (4.47), leading to the generalized form

$$f_{Ai} = \frac{\hat{M}_{AiAi}}{M_{AiAi}} \geq \left(\frac{\Delta \bar{t}}{\Delta t_{Ai}^{\mathbf{M}^{-1}\tilde{\mathbf{K}}}}\right)^2. \tag{4.50}$$

Due to the conservative nature of this approach, a higher critical time step than the one specified in (4.50) may be achieved. For the same reason also control points not involved in B-Rep edge element formulations may be scaled even though this is not necessary to achieve the desired time step. Control points not involved in B-Rep edge element formulations are therefore excluded from this mass scaling approach.

4.5.3 Minimal numerical example – two-dimensional shell model

The working principle of the local selective mass scaling approach shall now be demonstrated by means of two-dimensional (trimmed) square plate problems, similar to the ones in Figure 4.29. Here, penalty-based translational Dirichlet boundary conditions are applied via B-Rep edge elements along all four edges.

As an example that includes trimming, the square plate with cubic shell elements trimmed at $\xi_{\text{t}} = 0.5$ is studied in more detail here. Figure 4.32 depicts the control point mass distributions for the case without mass scaling (Figure 4.32a) and with mass scaling for $\alpha_r = 1$, 10 and 100 (Figs. 4.32b–4.32d). In accordance to Eqs. (4.47)–(4.49) the control points are scaled such that the critical time step of the case without penalty boundary conditions is achieved. In these figures the control point volume represents the corresponding control point mass. All control points are colored according their added mass normalized by the heaviest untrimmed and unscaled control point mass of the model $m_{\max} = \max_A(M_{AA})$. A value of added mass equal to one, for instance, means that the mass of the scaled control point is increased by the mass of the heaviest control point.

From Figure 4.32a, one can recognize the initial unscaled control point masses and the fact that control points associated with trimmed elements are smaller, i.e. have lower mass. Figures 4.32b–4.32d clearly show that only the $p+1=4$ outer control point rows and columns involved in B-Rep edge elements are scaled. They furthermore show that each control point receives a different amount of mass; in fact, the specific amount required to balance the introduced penalty stiffness. For $\alpha_r = 1$, the maximum mass added to a control point is only $0.057\, m_{\max}$, while this value increases to $1.05\, m_{\max}$ for $\alpha_r = 10$ and $11.97\, m_{\max}$ for $\alpha_r = 100$. This corresponds to a total mass increase of $\Delta m = +3.6\%$, $+62.3\%$ and $+861.3\%$, respectively. However, it should be noted that for this simple model the total mass increase is not meaningful, since a majority of the control points (144 out of 169) are involved in B-Rep element formulations. In practical models a much smaller fraction of control points is expected to be involved in B-Rep element formulations, yielding a much smaller total mass increase.

A more meaningful quantity is the mass scaling factor per shell element, depicted in Figure 4.32. For instance an element mass scaling factor of two means that the element mass doubled compared to its initial unscaled mass. Figures 4.33b–4.33d show that the present mass scaling approach also leads to a specific element scaling, which scales shell elements close to B-Rep edge elements the most. Shell elements without control points involved in B-Rep edge elements are consequently not scaled. For $\alpha_r = 1$, 10 and 100 the maximum shell element mass scaling factors are 1.41, 5.84 and 55. As a comparison, in practical vehicle crash simulations with explicit FEA, element mass scaling factors of up to 400 are typically permitted as long as the total mass increase of the model remains within an acceptable range.

In accordance with Figures 4.30a–4.30d, Figures 4.34a–4.34c depict mass scaling results for trimmed square plate models with different trimming positions ($\xi_{\text{t}} = 0$, 0.5 and 1.9) and polynomial degrees $p = 1$ to 4. These figures plot the critical time steps without mass scaling (solid lines), together with the required maximum shell element mass scaling factors required to obtain Δt_{crit} without the influence of penalty boundary conditions (dashed lines). As can be seen for all trim positions ξ_{t}, the required mass scaling factor correlates with the required increase in time step

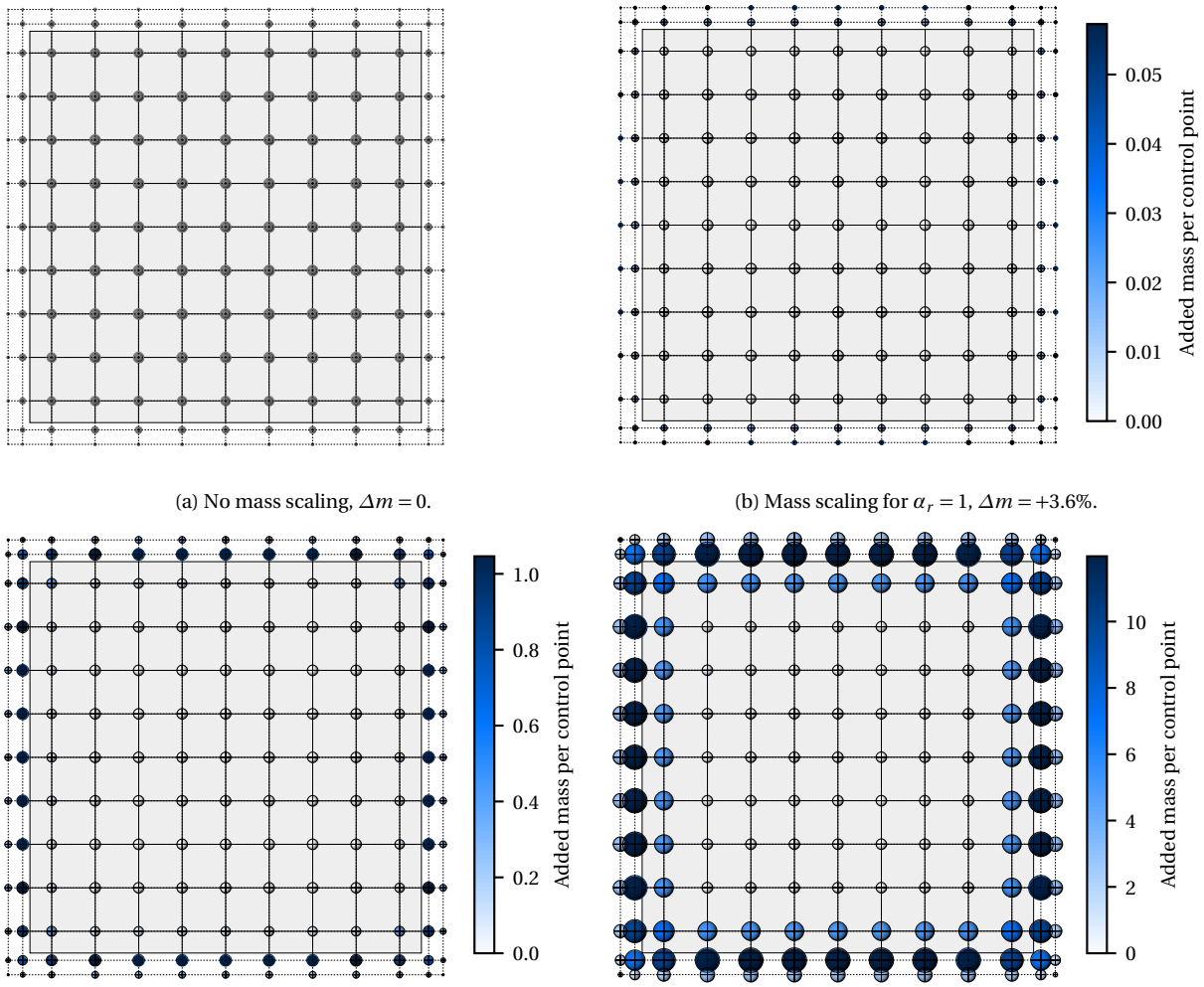

(a) No mass scaling, $\Delta m = 0$.

(b) Mass scaling for $\alpha_r = 1$, $\Delta m = +3.6\%$.

(c) Mass scaling for $\alpha_r = 10$, $\Delta m = +62.3\%$.

(d) Mass scaling for $\alpha_r = 100$, $\Delta m = +861.3\%$.

Figure 4.32: Two-dimensional trimmed square plate problem C^{p-1} with Dirichlet boundary conditions: Mass scaling results per control point for different relative penalty factors $\alpha_r = \alpha/E = 1$ to 100, a trim positions $\xi_t = 0.5$ (see Figure 4.29b) and a polynomial degree $p = 3$. The control point mass is scaled such that the critical time step without penalty boundary conditions is reached. The added mass per control point indicated by the colorbar is normalized with respect to the highest untrimmed and unscaled control point mass. The sphere volume of the control points represents the control point mass.

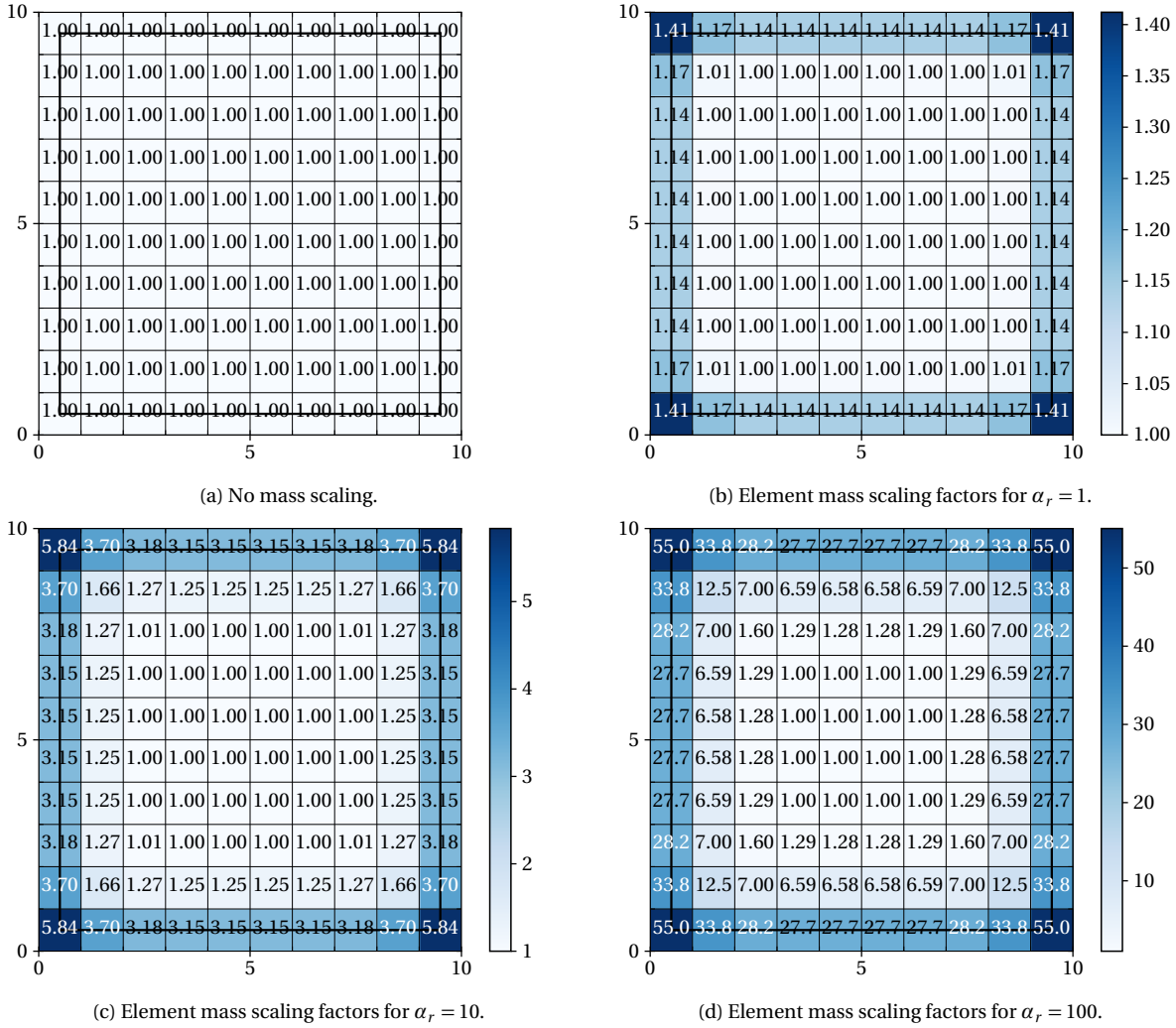

(a) No mass scaling.

(b) Element mass scaling factors for $\alpha_r = 1$.

(c) Element mass scaling factors for $\alpha_r = 10$.

(d) Element mass scaling factors for $\alpha_r = 100$.

Figure 4.33: Two-dimensional trimmed square plate problem C^{p-1} with Dirichlet boundary conditions: Mass scaling factor per element for different relative penalty factors $\alpha_r = \alpha/E = 1$ to 100, a trim positions $\xi_t = 0.5$ (see Figure 4.29b) and a polynomial degree $p = 3$. The control point mass is scaled such that the critical time step without penalty boundary conditions is reached. Elements are colored according to the factor of (trimmed) element mass increase (m^e_{scaled}/m^e).

size – the higher the time step decrease through penalty, the more mass scaling is required to achieve the time step without penalty. Furthermore, no specific influence of the trimmed element size on the required amount of mass scaling can be identified. The reason why the max. element mass scaling factors do not exactly start from one (= no mass scaling) for small penalty factors is the fact that the proposed mass scaling approach is conservative. Thus, a small amount of mass scaling will be applied even if actually not necessary[6].

Remark 4.1: In this example, translational Dirichlet boundary conditions are applied. For rotational Dirichlet boundary or coupling conditions, also rotational masses needed to be scaled accordingly as described in Eq. (4.49). However, as stated in Section 2.6.2 and [14, 73], the rotational masses are already significantly scaled in order to prevent a time step restriction by rotational modes, which is common also in explicit FEA, see [45, 131, 132]. This scaling is acceptable since the rotational masses have a relatively low impact on the overall solution accuracy. The amount of additional rotational mass scaling for B-Rep elements will therefore not be predominant and no further investigations on rotational mass scaling are conducted in this thesis.

[6] The unexpected reduction of the max. element mass scaling factor at $\alpha_r = 10^0$ for $p = 1$ in (c) is very likely caused by the fact that some shell and penalty stiffness entries have very similar magnitude and therefore nearly vanish. This leads to a smaller row sum and thus to a smaller time step estimate than for the case with lower penalty factors.

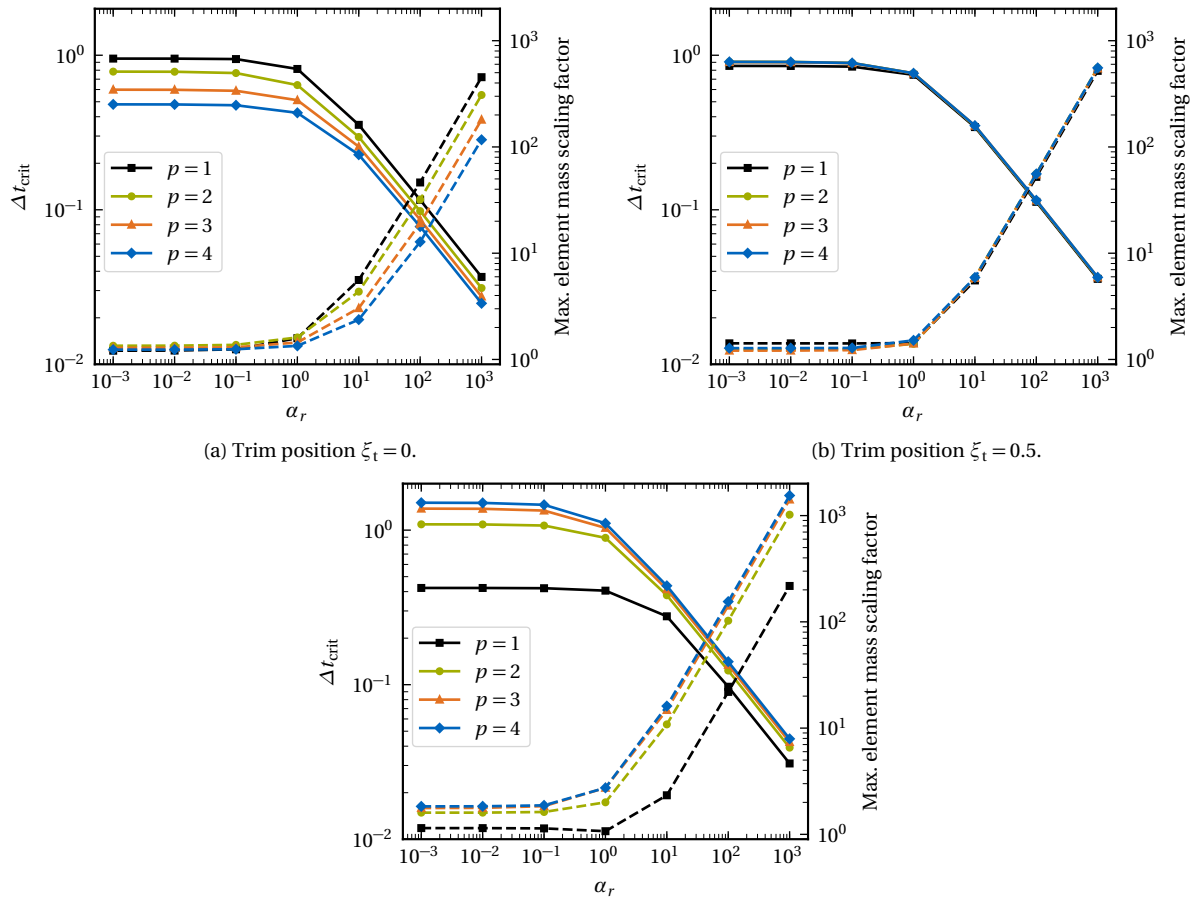

(a) Trim position $\xi_t = 0$.

(b) Trim position $\xi_t = 0.5$.

(c) Trim position $\xi_t = 1.9$.

Figure 4.34: Two-dimensional trimmed square plate problem C^{p-1} with Dirichlet boundary conditions: Critical time step size Δt_{crit} without mass scaling (solid lines) and maximum element mass scaling factor required to obtain the critical time step without penalty boundary conditions (dashed lines) versus relative factor $\alpha_r = \alpha / E$ for different trim positions ξ_t (see Figure 4.29) and polynomial degrees $p = 1$ to 4.

4.5.4 Summary and discussion of this section

The local selective mass scaling approach proposed in this section is a simple and effective way to eliminate the effect of penalty-based boundary and coupling conditions on the time step, while keeping the artificially added control point mass low. The latter is achieved by determining control point specific scaling factors based on the introduced penalty stiffness. The proposed mass scaling approach is simple because it only needs the desired time step size, the lumped control point masses and the lumped stiffnesses as an input. This neither requires the assembly of the whole stiffness matrix nor the solution of the full eigenvalue problem. Moreover, this scaling of masses only needs to be performed once in the preprocessing step, in case the penalty stiffness is not intended to change during the simulation. An increase in shell eigenfrequencies, for instance caused by strongly compressed elements in a crash simulation, would either result in a smaller overall time step or could be handled via standard mass scaling approaches as in standard explicit FEA. The proposed mass scaling approach is effective because it always assures that the desired time step is achieved. In fact, the proposed method is conservative in the sense that slightly more mass than actually required is added, which makes it not the optimal solution.

One idea to determine the minimum required scaling factor for each control point is to set up an optimization problem in the preprocessing step with the objective to reduce the individual mass scaling factors and under the constraint that the desired time step is achieved. The mass scaling distribution obtained by the proposed approach would certainly be an excellent starting point for this optimization problem.

In the end, there is always a trade-off between computational cost (time step size) and accuracy (amount of mass added), and the simulation engineer needs to define which amount of mass scaling to permit for the problem at hand. In Chapter 7 the proposed mass scaling approach is demonstrated on several more complex examples.

4.6 Summary and conclusion of Chapter 4

This chapter provides a systematic study on the stable time step size in an Explicit IBRA setting. This includes (i) the effect of inter-element continuity, (ii) the negative effect of boundary elements and corresponding remedies to remove it, (iii) the effect of trimming and especially small trimmed elements for models with different inter-element continuity, (iv) the effect of penalty-based boundary and coupling conditions and (v) mass scaling for B-Rep elements. The main findings and novelties from this chapter can be summarized as follows:

- Trimming off the $p-1$ boundary element rows and columns of a patch is a simple, effective and practically applicable approach to eliminate their time step restricting effect. In this way, the stable time step size of the presented two-dimensional shell examples could be increased by +54%, +128% and +221% for $p = 2$, 3 and 4, respectively. With trimmed-off boundary elements, the stable time step is found to even increase with p, while it decreases with p if this is not the case. This is in accordance with the results in [81], in which the boundary effect was removed by using open knot vectors or extended boundary elements.
- Higher inter-element continuity is found to be the key aspect for the applicability of trimming in explicit analysis. More precisely, for a maximum inter-element continuity of C^{p-1} and $p \geq 2$, the stable time step size is found to be practically independent of the trimmed element size (for interior elements). For C^0 inter-element continuity, on the other hand, the stable time step size strongly depends on the trimmed element size and actually tends towards zero as the trimmed element size approaches zero. It can therefore be concluded that explicit analysis of trimmed models with C^0 inter-element continuity is practically infeasible. However, practically more important is the finding and understanding that trimmed models with C^{p-1} and $p \geq 2$ can be efficiently used in explicit analysis.
- Penalty-based boundary conditions can lead to a reduced stable time step size in case the penalty factor α is higher than a certain value α'. Below this value, the stable time step is found to be practically independent of α. For patches with C^{p-1} and $p \geq 2$ it is furthermore shown that the size of trimmed shell elements involved in penalty-based boundary conditions, has no significant effect on the critical time step size. This means that, from a time step point of view, a consistent penalty factor can be used throughout the whole model, independent of the size of underlying trimmed shell elements – a finding that strongly facilitates the suitable definition of the penalty factor.
- To compensate a possibly negative effect of penalty-based boundary conditions on the time step, a local selective mass scaling approach for control points involved in B-Rep elements is proposed. This simple and effective approach specifically scales the mass of affected control points based on their added penalty stiffness. To achieve this, control point specific (nodal) time steps are computed via lumped stiffness matrices and the Gershgorin circle theorem. Based on that, the proposed method scales the mass of affected control points such that their control point specific time step is above the desired time step size.

Chapter 5

Stabilization of small trimmed elements / light control points

5.1 Introduction

The two previous chapters introduced Explicit IBRA for trimmed multi-patch B-Rep NURBS models and studied the influencing factors like trimming and penalty coupling on the critical time step size in explicit analysis, respectively. This chapter deals with numerical instabilities associated with trimmed models in explicit analysis.

Industrial B-Rep models can consist of a vast number of patches, including various trimming loops to represent complex shapes, holes, cut-outs or beadings. Consequently, isogeometric NURBS elements may be trimmed in various different ways and at arbitrary locations, leading to trimmed elements with varying sizes, including extremely small trimmed elements. Hence, in industrial B-Rep models, small trimmed elements are ubiquitous and inevitable. During isogeometric analysis, such elements often cause numerical problems. In fact, small trimmed elements lead to ill-conditioned system matrices. In most cases mentioned in the literature, see Section 1.2.4, numerical problems arise when solving equation systems including such ill-conditioned system matrices. However, in explicit dynamic analysis numerical problems arise even though the total system matrices are not assembled and the equation system is not actually solved.

This chapter provides a detailed investigation on the numerical instabilities associated with trimmed B-Rep NURBS models in explicit dynamic isogeometric analysis. Section 5.2 investigates (i) the effects of small trimmed elements on the numerical model, (ii) the reasons for these numerical instabilities, (iii) the related symptoms, furthermore (iv) attempts to characterize and classify the instability, (v) deals with numerical problems in multi-patch models and (vi) provides requirements for a potential stabilization scheme. In Section 5.3, a stabilization method based on penalty constraints is presented as a remedy. Section 5.4 demonstrates that the classical stability condition and time step estimation based on the maximum system eigenvalue for explicit dynamics, remain applicable with the proposed stabilization approach. In order to quantify unstable behavior and the effectiveness of the stabilization method, appropriate error measures are introduced in Section 5.5. In Section 5.6, the proposed stabilization method is successfully applied to two minimal numerical problems, namely to a trimmed single- and a trimmed multi-patch cantilever beam. The work presented in this chapter builds upon studies and developments conducted within the Master's thesis of Kwon [148], supervised by the author of this dissertation.

5.2 Stability issues in explicit analysis of trimmed NURBS shells

5.2.1 Small trimmed elements and light control points

As described in Section 2.2, trimming operations do not change the underlying surface description, but only disregard the part of the domain located on the right hand side of a directed trimming curve. In CAD models in general, a NURBS surface can be trimmed with arbitrary trimming curves, potentially leading to arbitrarily small trimmed elements. Figure 5.1a depicts a trimmed double curved shell with two relatively small trimmed elements highlighted in orange. As a consequence of these two small trimmed elements, the basis functions of control points P_3 and P_9 (highlighted in orange in Figure 5.1a) have only very limited support on the material domain as shown in Figure 5.1b–5.1d. The

basis functions belonging to control points P_1, P_2 and P_8 in dark gray in Figure 5.1a, do not have any support on the material domain as depicted in Figure 5.1e. Therefore, P_1, P_2 and P_8 do no longer contribute to the solution, which is why they are denoted as *inactive* control points. During analysis, inactive control points are disregarded and fixed at their initial positions. Control points with trimmed basis functions, i.e. basis functions which do not have full support on the material domain, are denoted as *trimmed* control points in this thesis.

Small trimmed elements and the consequently small support of basis functions as, for example, highlighted in orange in Figure 5.1, cause the corresponding control points to have small mass and small stiffness matrix entries. This becomes obvious when considering a simple one-dimensional bar problem like the one in Figure 5.2. For such a bar problem the lumped control point masses M_A are computed as

$$M_A = \int_V \rho\, N_A \,\mathrm{d}V = \rho\, A \int_x N_A \,\mathrm{d}x = \rho\, A \int_\xi N_A \left|\frac{\partial x}{\partial \xi}\right| \mathrm{d}\xi, \tag{5.1}$$

where the mass density ρ and the cross-section area A are assumed to be constant throughout the beam. The corresponding stiffness matrix entries can be computed as

$$K_{AB} = \int_V \frac{\partial N_A}{\partial x} E \frac{\partial N_B}{\partial x} \,\mathrm{d}V = E\, A \int_x \frac{\partial N_A}{\partial x} \frac{\partial N_B}{\partial x} \,\mathrm{d}x = E\, A \int_\xi \left(\frac{\partial N_A}{\partial \xi}\frac{\partial \xi}{\partial x}\right)\left(\frac{\partial N_B}{\partial \xi}\frac{\partial \xi}{\partial x}\right)\left|\frac{\partial x}{\partial \xi}\right| \mathrm{d}\xi, \tag{5.2}$$

with a uniform Young's modulus E. Depending on the trimming position ξ_t, the size of a trimmed element varies and therefore also the integration domains in Eqs. (5.1) and (5.2). This makes clear that arbitrarily small elements and integration domains lead to arbitrarily small control point mass and stiffness entries. In addition to the integration domain, also the magnitude of one basis function and its derivative are approaching zero as ξ_t approaches knot values in the material domain, cf. $N_{5,2}$ in Figure 5.2. That is, also integrands in the mass and stiffness integrals in Eqs. (5.1) and (5.2) are small in case of small trimmed elements. Because of their small mass, such control points are denoted as *light* control points in this thesis.

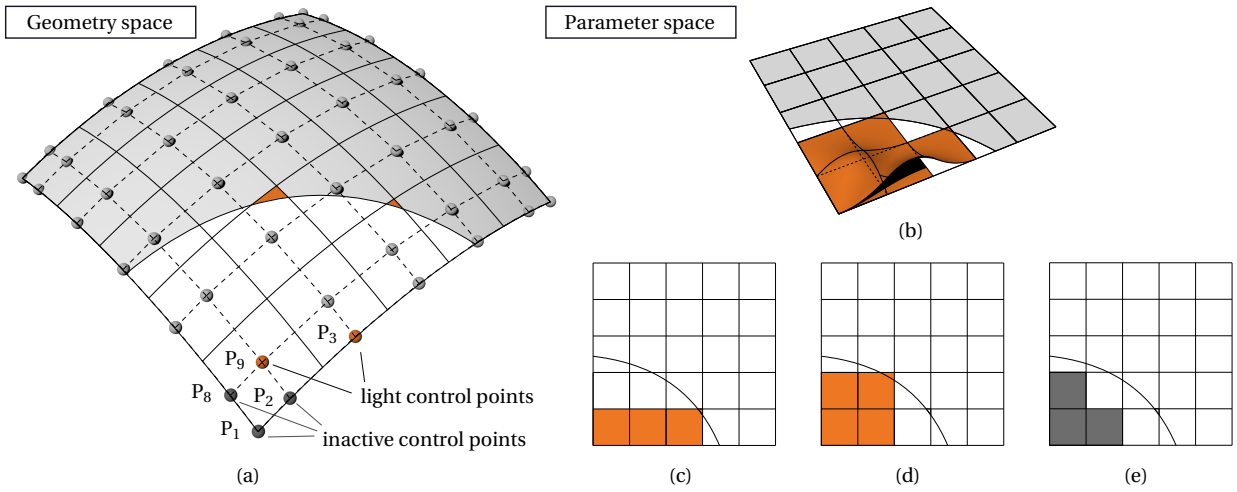

Figure 5.1: Trimmed double curved shell: In (a) the trimmed shell is depicted in geometry space with two small trimmed elements and two light control points highlighted in orange, and three inactive control points highlighted in dark gray. In (b) the trimmed parameter space is depicted along with the two basis functions of the two light control points. In (c)-(e) the trimmed parameter space is depicted with the support of the basis functions belonging to the light control points P_3 resp. P_9 highlighted in orange in (c) resp. (d), and the support belonging to the three inactive elements in dark gray in (e).

The quadratic four-element bar model in Figure 5.2 is defined by an open knot vector $\Xi = \{0,0,0,1/4,1/2,3/4,1,1,1\}$ and gets trimmed at $\xi_t = 0.55$. This causes (i) P_6 to be an inactive control point because $N_{6,2}$ has no longer support on the material domain, and (ii) P_5 to be a light control point because the support of $N_{5,2}$ on the material domain is small. Figure 5.3 clarifies this by depicting the normalized lumped mass and lumped stiffness values of control points P_5 and P_6 for different trimming positions ξ_t. Both, lumped mass and lumped stiffness values, are obtained by row summing of absolute values. It clearly shows that lumped mass and stiffness values tend towards zero as the trimming position approaches the corresponding knot values with decreasing ξ_t. For instance, for a trimmed element length of 4% of the untrimmed length, the lumped mass and stiffness values of P_5 are around 2×10^{-5} and 6×10^{-4} times smaller than in the untrimmed case, respectively.

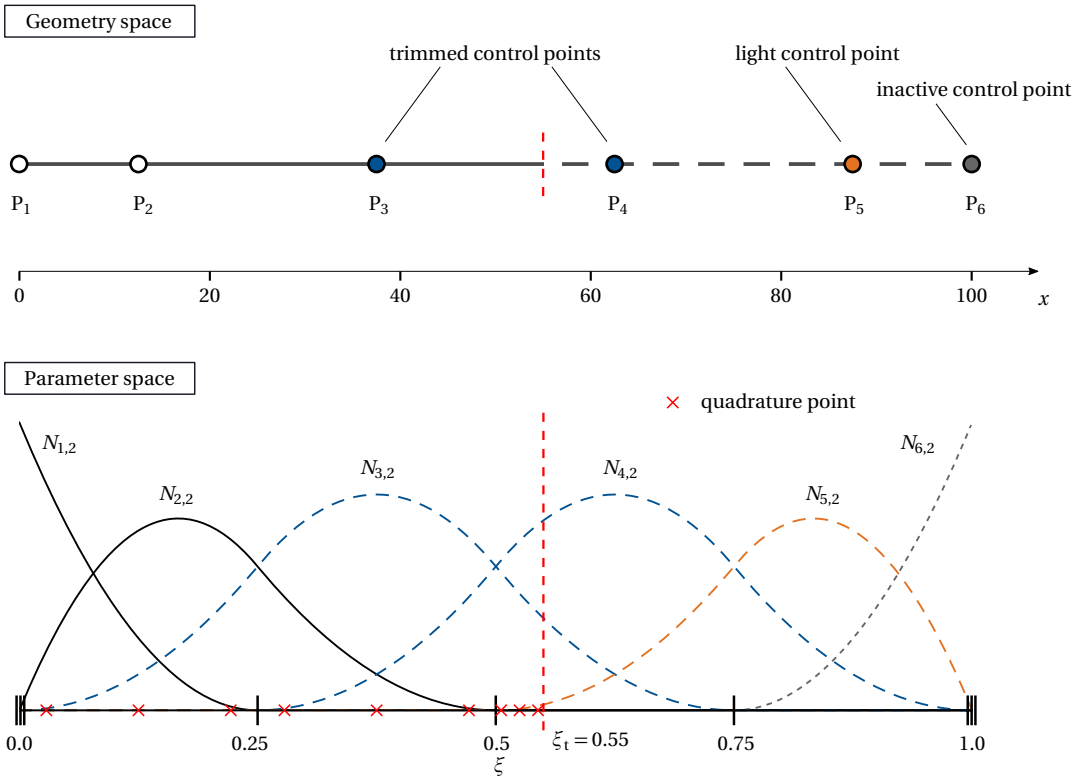

Figure 5.2: Geometry and parameter space of a one-dimensional, trimmed bar model with four quadratic elements and six control points. Control point P_6 is inactive and control point P_5 is a light control point.

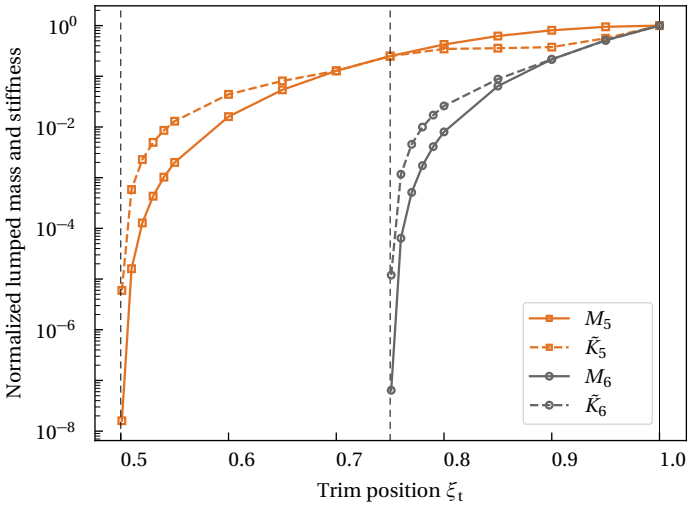

Figure 5.3: Lumped mass and stiffness values for P_5 and P_6 from Figure 5.2 for different trim positions ξ_t. The dashed black vertical lines indicate knot values. Mass and stiffness are normalized with their untrimmed values. The strong decrease of lumped mass and stiffness values with decreasing element length is clearly visible.

5.2.2 Reasons for numerical instabilities

Still, the question why small trimmed elements lead to numerical problems in explicit dynamic analysis remains to be answered. As described in Section 1.2.4, many authors have identified ill-conditioned system matrices caused by small trimmed elements as the main reason for numerical problems when solving equation systems. Therefore, the concept of condition number shall be briefly explained here for an equation system of the form $\mathbf{A}\mathbf{x} = \mathbf{b}$, with the real square matrix $\mathbf{A}$ and the real column vectors $\mathbf{x}$ and $\mathbf{b}$. Informally, the condition number $\kappa(\mathbf{A})$ quantifies how inaccuracies in the input $\mathbf{b}$ affect the accuracy of the solution $\mathbf{x}$, see for instance [149]. For a real square matrix $\mathbf{A}$, the condition number can be computed as $\kappa(\mathbf{A}) = \frac{|\lambda_{\max}|}{|\lambda_{\min}|}$, with the maximum and minimum eigenvalues $\lambda_{\max}$ and $\lambda_{\min}$ of $\mathbf{A}$. For general dynamic problems, the second order equation of motion

$$\mathbf{M}\ddot{\mathbf{u}} + \mathbf{C}\dot{\mathbf{u}} + \mathbf{K}\mathbf{u} = \mathbf{f}^{\text{ext}}, \tag{5.3}$$

needs to be considered. For implicit time integration schemes, solving Eq. (5.3) for the displacements $\mathbf{u}^{n+1}$ at time step $n+1$ involves matrix inversions of $\mathbf{M}$, $\mathbf{C}$ and $\mathbf{K}$. Consequently, the conditioning of $\mathbf{M}$, $\mathbf{C}$ and $\mathbf{K}$ is decisive for the accuracy of the results.

For explicit time integration schemes, things are usually different, because the equation system is not actually solved. To show this, the equations of motion in Eq. (5.3) at time t^n without damping are discretized in time by applying the explicit central difference scheme:

$$\frac{1}{\Delta t^2}\mathbf{M}\left(\mathbf{u}^{n+1} - 2\mathbf{u}^n + \mathbf{u}^{n-1}\right) = \mathbf{f}^{\text{ext},n} - \mathbf{K}\mathbf{u}^n. \tag{5.4}$$

One can see that the stiffness matrix only appears in $\mathbf{K}\mathbf{u}^n$, which gives the internal force vector $\mathbf{f}^{\text{int},n}$. Thus, in order to solve for $\mathbf{u}^{n+1}$ only $\mathbf{M}$ has to be inverted. By using a diagonal lumped mass matrix, the equation system can be decoupled and all computations including the matrix multiplication ($\mathbf{K}\mathbf{u}^n$) can be performed on an element level, see for instance [76]. Therefore the global matrices do not need to be assembled. To enable this for cases with damping, also $\mathbf{C}$ needed to be diagonalized. This decoupling through the use of lumped mass and lumped damping matrices makes explicit analysis very efficient. The control point accelerations can then be computed as

$$\mathbf{a}_A^n = \mathbf{M}_A^{-1}\left(\mathbf{f}_A^{\text{ext},n} - \mathbf{f}_A^{\text{int},n} + \mathbf{f}_A^{\text{B-Rep},n}\right). \tag{5.5}$$

Since, in contrast to implicit methods, the equation system is actually not solved, also numerical instability caused by small trimmed elements cannot be directly explained by the ill-conditioned mass and stiffness matrices. Therefore, the various steps within an explicit dynamic analysis with the central difference scheme shall be investigated in more detail.

Consider a mechanical system at rest or in motion with constant velocity at $t = 0$. For this system, internal and external forces[1] are in equilibrium and all control point accelerations are zero. At t^n an external force shall be applied. This external force causes an imbalance in the force equilibrium, leading to accelerations (and therefore inertia forces) at time t^n via the inverse mass in Eq. (5.5). Based on these control point accelerations, velocities at the next half time step $n+1/2$ are computed via linear extrapolation as

$$\mathbf{v}^{n+1/2} = \mathbf{v}^{n-1/2} + \Delta t\,\mathbf{a}^n. \tag{5.6}$$

These velocities $\mathbf{v}^{n+1/2}$ are in turn used to compute the displacements at the next time step $n+1$ again via linear extrapolation as

$$\mathbf{u}^{n+1} = \mathbf{u}^{n-1} + \Delta t\,\mathbf{v}^{n+1/2}. \tag{5.7}$$

The extrapolations in Eqs. (5.6) and (5.7) make clear that all obtained velocities and displacements are inherently only approximations, afflicted by more or less high errors, depending on the time step size. The internal forces for time step $n+1$ are then again computed from inexact displacements, and the control point accelerations at time step $n+1$ are again computed via the force equilibrium between external and internal forces and the mass inverse in Eq. (5.5).

Such small errors are usually not a problem in explicit analysis, because too high control point displacements are immediately penalized/stabilized by internal forces in the opposite direction. Roughly spoken, the explicit scheme balances itself to some extent from time step to time step, leading to more or less pronounced oscillations in the control point forces and accelerations. Spurious high frequency oscillations for wave equations solved with the

[1] B-Rep coupling and Dirichlet boundary conditions are considered as internal forces, while B-Rep Neumann boundary conditions are considered as external forces here.

central difference method are for example also reported in [150]. Figure 5.4 depicts such oscillations for a simple cantilever beam model dynamically loaded by an end shear force P in z-direction. In Figure 5.4a, L denotes the length of the beam, b the width, h the thickness, E the Young's modulus, ν the Poisson ratio and ρ the mass density. The same notation holds for the beam examples in subsequent sections. Displacements and forces in z-direction as well as moments w.r.t. the y-direction of three control points are plotted in Figures 5.4b–5.4d. The control point forces and moments show significant oscillations, especially for control point P_{69}, which exhibits the highest displacements. Despite that, the control point displacement response is smooth and the simulation remains stable since the time step is below the critical time step.

For light control points, on the contrary, this penalization/stabilization via internal forces is much less effective. This is because the force acting on light control points is extremely insensitive to light control point displacements, due to the extremely small stiffness related to light control points ($\mathbf{f} = \mathbf{K}\mathbf{u}$). That means that (i) the penalization/stabilization force remains low even for high light control point displacements and (ii) once a light control point shows strong oscillations it can hardly be stabilized by internal forces. This effect is even aggravated by the fact that the extremely large inverse mass of light control points in Eq. (5.5) acts as a very strong amplifier to errors in the force equilibrium.

In the following, a small uniform error $\|\mathbf{e}_A\|$ shall be considered for all control point forces $\mathbf{f}_A$. This error might be the result of (i) errors in the displacements due to the assumptions made in the central difference scheme, (ii) inaccuracies due to the use of a lumped mass matrix and scaled rotational masses, (iii) inevitable inaccuracies in the numerical integration of (trimmed) elements and (iv) round-of errors. For normal control points P_A, $\|\mathbf{e}_A\| << \|\mathbf{f}_A\|$ shall hold, i.e. the relative force error $\frac{\|\mathbf{e}_A\|}{\|\mathbf{f}_A\|}$ is small. However, for light control points P_B with $\|\mathbf{f}_B\| << \|\mathbf{f}_A\|$, the relative error $\frac{\|\mathbf{e}_A\|}{\|\mathbf{f}_B\|}$ will be significantly larger. Via the extremely large inverse light control point mass in Eq. (5.5), this error is amplified, leading to a large absolute error in the light control point accelerations, which can be hardly stabilized by internal forces as described above. Over the ten or even hundred thousand time steps in an explicit analysis, this error accumulates, probably causing the system to become unstable.

The unstable behavior of light control points can also be described in a physical manner. First, the extremely low mass means that the light control point is very sensitive to forces applied, i.e. the inertia force will be low and even a very small applied force can lead to high accelerations. Additionally, due to the small stiffness matrix entries, a light control point is only loosely connected with the material domain. This means that the forces tying the light control point to the actual shell are very low as well. This loose connection in combination with high sensitivity to forces, can lead to unpredictable behavior with high accelerations, velocities and displacements.

5.2.3 Consequences of numerical instabilities

The numerical instability related with light control points appears as strong oscillations of control point displacements, velocities, accelerations, forces, etc. It is important to note that oscillations and inaccuracies of light control point quantities are not a problem for the overall accuracy of the solution per se, because the influence of these control points on the overall solution is negligible compared to that of normal control points. However, these erroneous effects tend to propagate to (coupled) adjacent normal control points. In such case, the accuracy of the overall results is indeed affected. Moreover, extremely large values, regardless of which control point, can cause the solver to abort the simulation prematurely due to overflow errors. In LS-DYNA, in particular, the simulation either continues with useless results (indicated by 'nan' values in the output) or terminates with an error message indicating 'out-of-range velocities'.

In order to demonstrate these instabilities, the same cantilever problem as above is now solved with a trimmed model, see Figure 5.5. The model is designed and trimmed with the aim to obtain a row of small trimmed elements and subsequently a row of five light control points highlighted in orange in Figure 5.5a. Since one row of elements is completely trimmed off, there is also a row of five inactive control points highlighted in dark gray. Control points whose basis functions are partially trimmed, i.e. do not have full support, are highlighted in blue. In Figure 5.5b resp. Figure 5.5c, z-displacements resp. y-rotations, are plotted for one light control point (P_{71}), two trimmed control points (P_{70} and P_{69}) and two normal control points (P_{64} and P_{59}) of the centered control point row. It can be seen that the displacements and rotations of the light control point show excessive oscillations from the beginning, while the responses of the other control points are reasonable and smooth. But as described above, with progressing simulation time, the erroneous behavior of light control points propagates to adjacent control points and finally affects the whole model. This is shown in Figure 5.5b and Figure 5.5c from around 2×10^{-3} s. Finally, at around $t = 2.5 \times 10^{-3}$ s, the solver terminates prematurely due to the appearing instability. The unrealistic behavior of light control points prior to termination can be seen in the deformed configuration at $t = 1.33 \times 10^{-3}$ in Figure 5.5a. Despite the high displacements of light control points, the deformed model geometry at $t = 1.33 \times 10^{-3}$ seems to be still unaffected by it. This shows the almost negligible contribution of light control points to the overall solution. Because of their unpredictable behavior and loose connection to the material domain, light control points are also commonly denoted as *flying nodes* in [30].

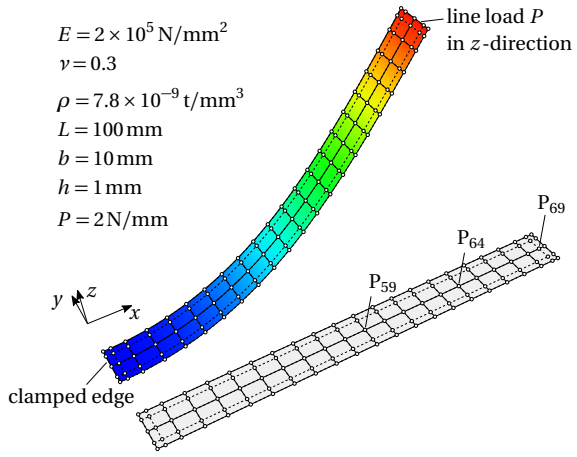

(a) Problem description and deformed configuration. The color plot indicates z-displacements.

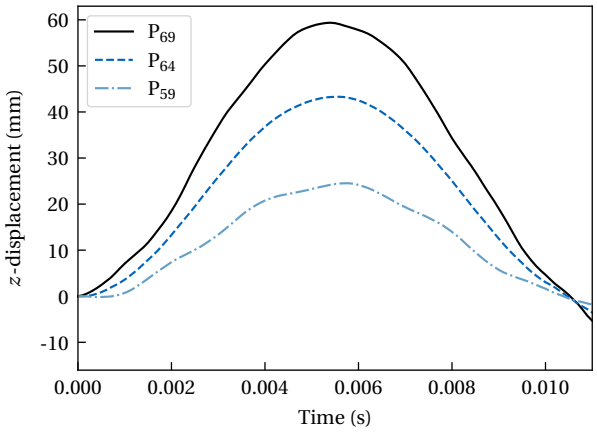

(b) Displacement response.

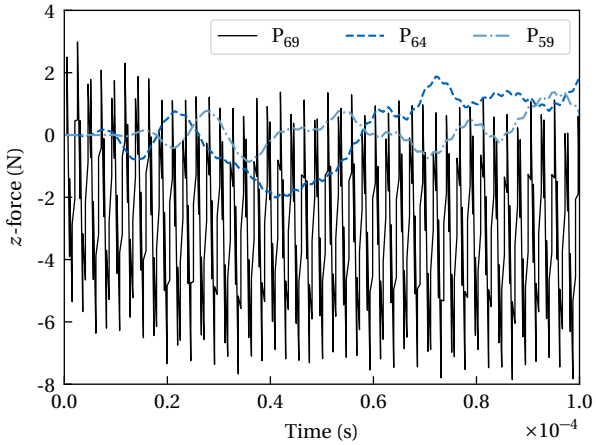

(c) Control point forces in z-direction.

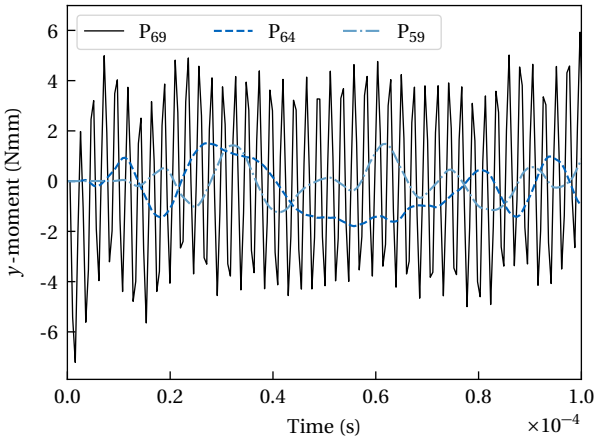

(d) Control point moments around the y-direction.

Figure 5.4: Explicit dynamic isogeometric analysis of a cantilever beam instantaneously loaded by an end shear force in z-direction. The displacement response for three control points P_{59}, P_{64} and P_{69} are plotted in (b). Corresponding control point forces and moments for each time step are plotted for the first 10^{-4} s of the simulation in (c) and (d), respectively. Please note the different time scales on the x-axis in (b), (c) and (d).

5.2.4 Type of instability

It is worth noting that numerical instabilities caused by light control points behave differently than classical instabilities caused by a time step larger than the critical value. In fact, explicit simulations involving light control points become unstable, although the critical time step for the central difference scheme is not exceeded. To clarify this issue, the classification of time integration schemes with respect to stability is briefly reviewed. In the literature, see for instance [151] and [152], the stability of time integration schemes is commonly classified into

- Unconditional and conditional stability: Implicit time integration schemes are usually unconditionally stable, while explicit time integration schemes are conditionally stable, i.e. only stable for a time step smaller than the critical time step.
- Strict and weak stability: A strictly stable time integration scheme is said to be stable for all times, whereas a strictly unstable scheme is unstable immediately after the first time step. A weakly stable time integration scheme on the contrary, is only initially stable and becomes unstable after a certain period of time. A decrease in time step size can in some cases postpone the appearance of instabilities, but in other cases cause the instability to appear even earlier, see [152]. Anyway, for weakly stable schemes, there is no critical time step size below which instability can be completely avoided. Another characteristic of a weak instability is the exponential growth of oscillation amplitudes [152].

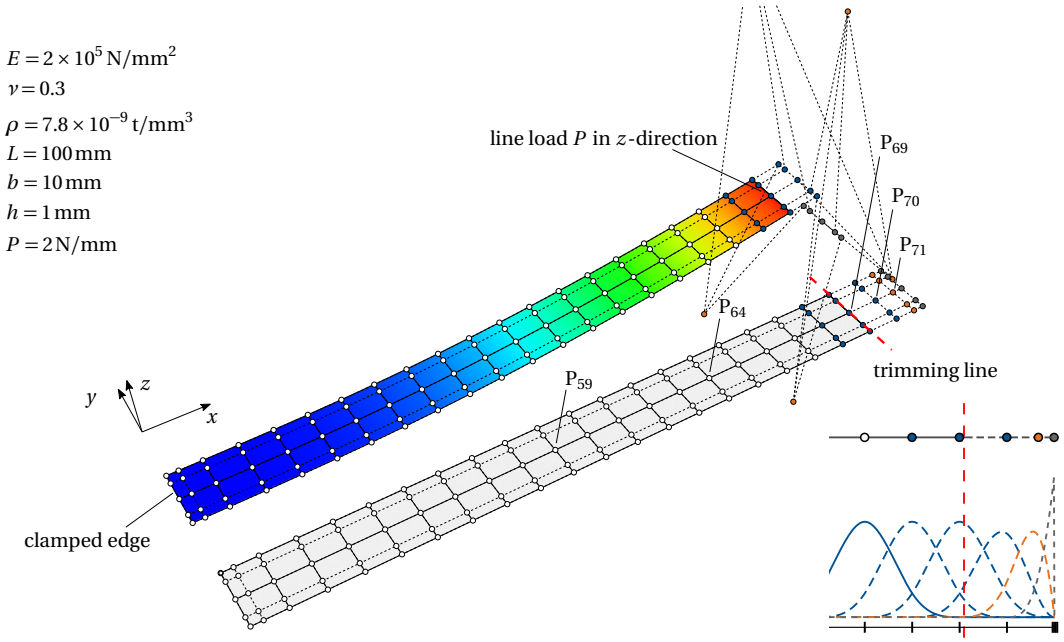

(a) Problem description and deformed configuration at $t = 0.0133\,\mathrm{s}$. The color plot indicates z-displacements.

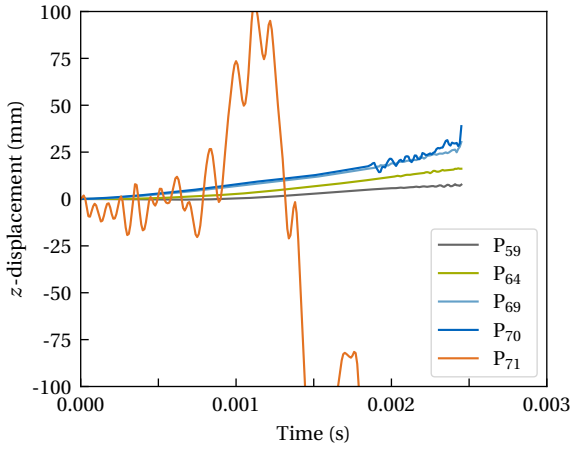

(b) z-displacement response.

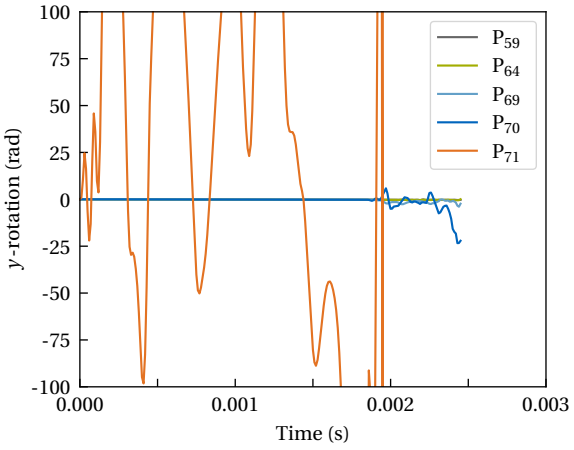

(c) y-rotation response.

Figure 5.5: Explicit dynamic isogeometric analysis of a trimmed cantilever beam instantaneously loaded by an end shear force in z-direction. The beam is designed and trimmed such that a row of five light control points is obtained as highlighted in orange in (a). The z-displacement and y-rotation response are plotted for one light control point (P_{71}), two trimmed control points (P_{70} and P_{69}) and two normal control points (P_{64} and P_{59}) of the centered control point row in (b) and (c), respectively.

The explicit central difference scheme, for instance, is (at least for linear problems) strictly stable under the condition that the time step is smaller than the critical time step and strictly unstable in case this condition is not fulfilled. However, the stability of the time integration scheme does not guarantee that the actual solution procedure remains stable. The mathematical model problem also needs to be well-posed. For example for the partitioned solution of fluid-structure-interaction problems in [152], even small violations of the continuity condition can impair the stability behavior of the solution procedure and the appearance of weak instabilities.

The instability caused by light control points shows characteristics of a weak instability, since a smaller time step cannot avoid the instability, but instead causes the instability to appear even earlier. In Figure 5.6 the trimmed cantilever problem from Figure 5.5 is solved for various time steps smaller than the critical value. The z-displacement and y-rotation responses for light control point P_{71} show that instability cannot be avoided by smaller time steps, and that it tends to occur even earlier. This can be explained by the fact that the error increases with each computation in each time step. Thus, the higher the number of steps per time, the larger the error becomes and the earlier the instability appears.

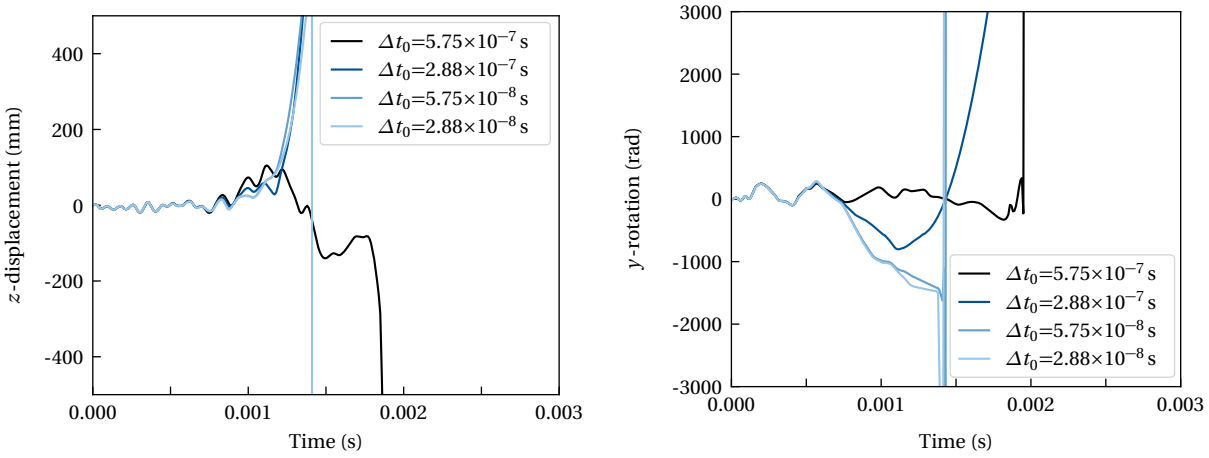

(a) z-displacement response.

(b) y-rotation response.

Figure 5.6: Explicit dynamic isogeometric analysis of a trimmed cantilever beam instantaneously loaded by an end shear force. z-displacement (a) and y-rotation responses (b) of light control point P_{71} for different initial time step sizes Δt_0. Even the largest initial time step $\Delta t_0 = 5.75 \times 10^{-7}$ is 10% below the estimated critical time step size.

5.2.5 Multi-patch problems

Weak boundary and coupling conditions are commonly enforced along trimming curves. Light control points are therefore very likely to be involved in B-Rep edge element definitions. In case of coupling or Dirichlet boundary conditions, stiffness is added to light control point entries. One could subsequently expect a positive stabilization effect for light control points. However, basis function values of light control points in B-Rep element formulations are evaluated along trimming curves. As shown in Figure 5.2, light control point basis function values are small and therefore also the added stiffness is small. Because of this, no significant stabilization effect can be expected. For the same reason, the influence of light control points on the coupling condition is also small. Nevertheless, as mentioned above the erroneous effects of light control points tend to propagate to adjacent or coupled control points. Then, the erroneous light control point behavior can even deteriorate the quality of coupling or boundary conditions, causing bad results. In that case, the weak coupling or boundary condition might still be fulfilled in an integral sense, but with strong individual oscillations in alternating directions. This effect is similar to what is often referred to as *spurious checkerboard modes* in the literature, see for instance [134].

To demonstrate the negative effect of light control points involved in weak coupling conditions, the cantilever problem from above is now modeled through two trimmed patches, see Figure 5.7. These two patches are coupled along trimming lines, which are defined such that one row of light control points is obtained in each patch (highlighted in orange). The coupling conditions in this example involve translational and rotational DOFs, as well as shell normals, i.e. the enhanced B-Rep element formulation proposed in Section 3.4 is used. From Figure 5.7 one can see two effects: First, the light control points highlighted in orange are again located at arbitrary positions. The light control points of the left patch are not even visible in this figure, due to their high displacements. Second,

the deformed cantilever beam shows a substantial kink between the coupled patches, because the erroneous light control point behavior also affects the quality of the coupling conditions.

To conclude, numerical instabilities also appear when light control points are involved in the formulation of weak boundary conditions, as in the case of coupled trimmed multi-patch models. In many instances, the coupling of trimmed patches fails and causes useless results even if the simulation does not yet abort due to instability. Resolving this issue is crucial for robust and accurate explicit multi-patch analyses.

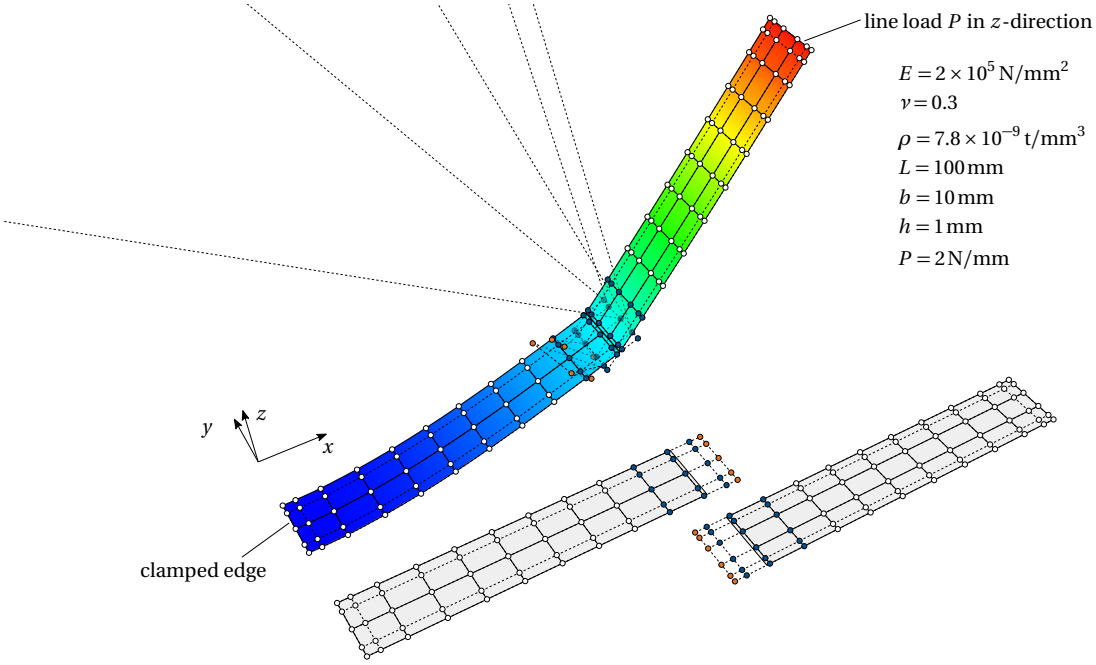

Figure 5.7: Trimmed NURBS-based multi-patch cantilever beam instantaneously loaded by an end shear force in z-direction: Problem definition and deformed shape at $t = 3.82 \times 10^{-3}$ s. Both patches are trimmed such that each patch has one row of light control points, highlighted in orange. Trimmed control points are highlighted in blue. The substantial kink between the patches occurs because the coupling conditions are affected by the erroneous behavior of light control points.

5.2.6 Stabilization

For explicit dynamic isogeometric B-Rep analysis of trimmed NURBS-based multi-patch models, the undesired phenomena described above need to be resolved. A potential stabilization scheme should incorporate the following aspects:

1. Prevention of extensively high control point displacements, velocities or accelerations in order to prevent the solver to abort prematurely.
2. Compatibility with weakly applied coupling and boundary conditions via B-Rep elements. A rigid constraint on the light control points was found to be incompatible with weak coupling conditions, leading to an over-constrained system. The issue of light control points is similar to the issues related with the fictitious domain in the Finite Cell Method (FCM). As mentioned in the PhD thesis of Schillinger [153], '[...] it is beneficial for the quality of the FCM results, if the solution fields in the fictitious domain can "move" as freely as possible to permit a smooth extension of the physical solution into the fictitious domain'. This rationale can also be transferred to light control points in IBRA [30].
3. No modification of the physical model behavior.
4. Computational efficiency and no restriction of the stable time step size in explicit analysis.
5. Applicability to complex industrial B-Rep NURBS models.
6. Easy applicability to existing explicit dynamic solvers such as LS-DYNA.

The stabilization method presented in the following section, is designed with these aspects in mind.

5.3 Penalty-based light control point stabilization

This section presents the actual light control point stabilization method, starting with a brief overview in Section 5.3.1. The identification of problematic light control points and stable adjacent control points is introduced in Section 5.3.2 and Section 5.3.3, respectively. The estimation of a suitable reference behavior for light control points is discussed in Section 5.3.4, before Section 5.3.5 presents an approach to determine control point specific penalty stabilization factors. Finally, local mass scaling of light control points and the actual penalty-based stabilization constraints are introduced in Section 5.3.6 and Section 5.3.7, respectively.

5.3.1 Overview on the stabilization method

As mentioned in the previous section, light control points in explicit dynamic analysis tend to show unpredictable behavior with extremely high displacements, velocities and accelerations in both translations and rotations. Although the influence of light control points on the overall solution is negligible, the erroneous behavior can either propagate and infect other control points or simply cause the solver to terminate prematurely due to overflow/out-of-range errors.

Because of the negligible influence of light control points, the task of the stabilization method is not to determine a highly accurate solution for light control points, but to just prevent those control points from causing numerical problems. Nevertheless, light control points are still degrees of freedom and should also be treated as such; imposing rigid constraints on light control points turned out to be not consistent with (weak) boundary conditions applied on trimmed elements. With these aspects in mind, a suitable stabilization method based on a penalty approach is developed.

Simply spoken, the stabilization method constrains each light control point to a specific virtual reference point determined via linear extrapolation of the control polygon from adjacent stable control points. The force and stiffness introduced by penalty constraints $\boldsymbol{g} = 0$ with a penalty factor β are, in a general form, given as

$$\mathbf{f} = \beta\, \boldsymbol{g}^T \frac{\partial \boldsymbol{g}}{\partial \mathbf{d}}, \tag{5.8}$$

$$\mathbf{K} = \beta \left(\frac{\partial \boldsymbol{g}}{\partial \mathbf{d}} \right)^T \frac{\partial \boldsymbol{g}}{\partial \mathbf{d}}, \tag{5.9}$$

where $\partial \boldsymbol{g} / \partial \mathbf{d}$ are the constraint derivatives with respect to control point displacements. Of course, the same applies to rotational DOFs with moments and rotations. With these formulas at hand, the main task is to develop an effective constraint formulation $\boldsymbol{g}$.

The overall stabilization procedure can be divided into the following five steps, from which 1. to 4. are preprocessing steps only performed once prior to analysis, while the final step 5. is performed at every time step during analysis:

1. Identification of light control points
2. Determination of a virtual reference point for each light control point
3. Determination of control point specific penalty factors
4. Local mass scaling of light control points
5. Enforcing stabilization constraints

Each of these steps is described in more detail in the following subsections.

5.3.2 Identification of light control points

One of the main challenges is the reliable, a priori determination of those trimmed control points that require stabilization in the analysis. Considering all trimmed control points would introduce an unnecessarily high stabilization stiffness, potentially leading to an altered physical model behavior and distorted results. Considering too few control points, on the other hand, would not solve the problem, since even a single unstable control point can destroy the whole simulation. In the literature such distinctions are made based on (i) the ratio between trimmed and untrimmed element size [71, 100], (ii) the volume fraction of the basis function support within the material domain [94], (iii) whether a basis function spans at least one element completely located in the material domain [101–106], (iv) whether the anchor of a basis function is located in the material domain [34, 107], (v) the relative position of the control point/basis function in the mesh with respect to the trimmed boundary [93], or (vi) the energy norm of basis

functions [72, 95]. However, whether a trimmed element or control point requires stabilization or not depends on the type of analysis and solution method. In order to modify the physical system as little as possible through the stabilization, the goal is to specifically stabilize only affected control points. Therefore a control point related criterion is desired. As described in the Section 5.2, problematic control points are characterized by a very low lumped mass, as the notation *light* control point implies. The criterion chosen for identifying problematic (light) control points is thus lumped control point mass. Via Eq. (5.1), the lumped control point mass is also related to the size of a trimmed element. This yields a distinction of control points in three disjoint sets $\mathcal{M}_{\text{st}}^{(i)}$, $\mathcal{M}_{\text{li}}^{(i)}$ and $\mathcal{M}_{\text{in}}^{(i)}$:

Definition 5.1: Light control points. Consider the set $\mathcal{M}$ of all control points in Ω and the subset $\mathcal{M}^{(i)} \subseteq \mathcal{M}$ of all control points in $\Omega^{(i)}$. A control point A in $\mathcal{M}^{(i)}$ is considered as a *light* control point in the set of *light* control points $\mathcal{M}_{\text{li}}^{(i)}$, if

$$0 < M_A \leq C_{\text{th}} \max_B(M_B) = m_{\text{th}}^{(i)} \quad \text{for} \quad B \in \mathcal{M}^{(i)}, \quad \text{and} \quad C_{\text{th}} \in (0,1], \tag{5.10}$$

where C_{th} is a threshold constant and $m_{\text{th}}^{(i)}$ the threshold mass for light control points in $\mathcal{M}^{(i)}$. This means that control points are identified as *light* control points, if their lumped mass M_A is smaller than a certain fraction of the maximum control point mass of the respective patch and larger than zero.

Definition 5.2: Inactive control points. A control point A in $\mathcal{M}^{(i)}$ is considered as an *inactive* control point in the set of *inactive* control points $\mathcal{M}_{\text{in}}^{(i)}$, if

$$M_A = 0. \tag{5.11}$$

Definition 5.3: Stable control points. The set of *stable* control points $\mathcal{M}_{\text{st}}^{(i)}$ in the domain $\Omega^{(i)}$ is defined as

$$\mathcal{M}_{\text{st}}^{(i)} = \mathcal{M}^{(i)} \setminus (\mathcal{M}_{\text{li}}^{(i)} \cup \mathcal{M}_{\text{in}}^{(i)}) \tag{5.12}$$

This means that all control points of a patch that are neither *light* control points nor *inactive* control points are considered as *stable*.
With the set of trimmed control points $\mathcal{M}_{\text{t}}^{(i)}$ in $\Omega^{(i)}$, the following holds:

$$\mathcal{M}_{\text{li}}^{(i)} \subseteq \mathcal{M}_{\text{t}}^{(i)} \subseteq \mathcal{M}^{(i)}. \tag{5.13}$$

Due to the tensor-product structure of NURBS surfaces, a control point in the control net can be directly connected to up to four other control points in the four grid directions. A *stable* direction is defined as follows.

Definition 5.4: Stable direction. From a light control point's perspective, a direction is considered as a *stable* direction, if the two consecutive adjacent control points in this direction are stable control points.

5.3.3 Identification of stable adjacent control points

Now that the problematic light control points are identified, a virtual reference point with reference position and rotation is required for each light control point in order to enforce stabilization constraints. The reference estimation presented below in Section 5.3.4 is based on a linear extrapolation of the control polygon, which requires the prior identification of two stable control points per grid direction (N, E, S, W) in the vicinity of light control points.

This identification procedure for stable adjacent control points is given in Algorithm 5.1, in which P(A, j, k) denotes the jth adjacent control point to light control point A in direction k, see also Figure 5.8. Algorithm 5.1 can be explained as follows: For a light control point A in $\mathcal{M}_{\text{li}}^{(i)}$, the algorithm checks whether the first ($j = 1$) and the second ($j + 1$) adjacent control point in any of the four directions ($k = 1$ to 4) are stable, i.e. within $\mathcal{M}_{\text{st}}^{(i)}$. If this is the case for at least one direction, the stable adjacent control points are stored and the search is finished. If not, the search radius is sequentially increased, i.e. next the second ($j = 2$) and the third ($j + 1$) adjacent control point in any of the four directions are checked. This search is continued until a search radius of $j = p$ is reached. In the vast majority of trimming cases stable adjacent control points are found with this approach. Further extending the search radius would reduce the quality and accuracy of the reference estimation as the physical distance between reference control points and light control point increases. Of course, different variations of this identification algorithm are conceivable, e.g. considering all stable directions found in the p vicinity instead of only the stable direction(s) in the nearest vicinity. However, the presented algorithm is found to be satisfactory.

Remark 5.1: In some rare trimming scenarios, no stable control points may be found in any of the four directions. In such a case, the stable reference control points of adjacent light control points are adopted, see the explanation in the following section and Figure 5.10.

Algorithm 5.1

Loop over light control points A in $\mathcal{M}_{\text{li}}^{(i)}$:
  Loop over the p vicinity of each light control point A, $j = 1$ to p:
    Loop over the four directions (N, E, S, W), $k = 1$ to 4:
      $\mathrm{P}(A, j, k) = j$th adjacent control point in direction k of light control point A
      If $(\mathrm{P}(A, j, k)$ **and** $\mathrm{P}(A, j+1, k))$ **in** $\mathcal{M}_{\text{st}}^{(i)}$:
        Assign reference control point R1 for light control point A in direction j:
          $\mathrm{P}_{\mathrm{R1},k}^{A} \leftarrow \mathrm{P}(A, j, k)$
        Assign reference control point R2 for light control point A in direction j:
          $\mathrm{P}_{\mathrm{R2},k}^{A} \leftarrow \mathrm{P}(A, j+1, k)$
      end
    end
    If $\mathrm{P}_{\mathrm{R1},k}^{A}$ **and** $\mathrm{P}_{\mathrm{R2},k}^{A}$ assigned for at least one direction j:
      break loop
    end
  end
end

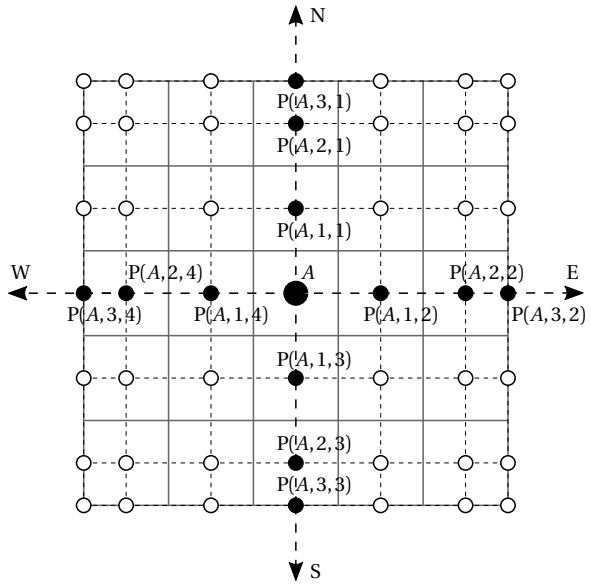

Figure 5.8: Identification of stable adjacent control points $\mathrm{P}(A, j, k)$ for light control point A in the four grid directions (N, E, S, W). Point $\mathrm{P}(A, j, k)$ denotes the jth adjacent control point in k-direction.

5.3.4 Estimation of a reference behavior

As previously mentioned, the intention is to penalize the deviation of a light control point from its virtual reference point (position and rotation), i.e. to apply forces and moments in case a light control point starts deviating from its reference. A good estimation of the reference point position and rotation is therefore crucial for a good stabilization. In this section, a simple and effective virtual reference point estimation approach is presented.

An intuitive reference position for a light control point is the linear extrapolation of the control polygon from adjacent stable control points. In the initial, undeformed state, this reference estimation is exact for plane shells. For highly curved shells, on the other hand, the deviation between the actual and the reference position in the undeformed

state depends on the refinement level. The finer the discretization, the better the reference estimation, see Figure 5.9. Depending on the trimming scenario, a light control point A can have up to four stable directions, i.e. directions in the control point grid with stable adjacent control points $B \in \mathcal{M}_{\mathrm{st}}^{(i)}$. In the deformed state, the reference positions computed from different directions do not necessarily coincide. The final virtual reference point position $\boldsymbol{x}'_A$ for a light control point A is therefore computed as the mean value of the reference positions $\boldsymbol{x}'_{A,k}$ in all $k = \{1, \dots, n_{\mathrm{d}}^A\}$ stable directions:

$$\boldsymbol{x}'_A = \frac{1}{n_{\mathrm{d}}^A} \sum_{k=1}^{n_{\mathrm{d}}^A} \boldsymbol{x}'_{A,k}. \tag{5.14}$$

In Eq. (5.14), the position $\boldsymbol{x}'_{A,k}$ of the virtual reference point for light control point A in direction k is computed via linear extrapolation of the control polygon as

$$\boldsymbol{x}'_{A,k} = \mathbf{x}_{\mathrm{R1},k}^A + (\mathbf{x}_{\mathrm{R1},k}^A - \mathbf{x}_{\mathrm{R2},k}^A) \frac{L_{1,k}^A}{L_{12,k}^A} \quad \text{with} \quad L_{1,k}^A = \|\mathbf{X}_A - \mathbf{X}_{\mathrm{R1},k}^A\|, \quad L_{12,k}^A = \|\mathbf{X}_{\mathrm{R1},k}^A - \mathbf{X}_{\mathrm{R2},k}^A\|, \tag{5.15}$$

where $L_{1,k}^A$ denotes the initial distance between the light control point A and its first stable adjacent reference control point $\mathrm{P}_{\mathrm{R1},k}^A$, and where $L_{12,k}^A$ denotes the initial distance between the first and second stable adjacent reference control point $\mathrm{P}_{\mathrm{R1},k}^A$ and $\mathrm{P}_{\mathrm{R2},k}^A$, respectively, see Figure 5.9. As for the position, the rotation $\boldsymbol{\theta}'_A$ of the virtual reference point for a light control point A is also computed as the mean value of the reference rotations $\boldsymbol{\theta}'_{A,k}$ in all $k = \{1, \dots, n_{\mathrm{d}}^A\}$ stable directions:

$$\boldsymbol{\theta}'_A = \frac{1}{n_{\mathrm{d}}^A} \sum_{k=1}^{n_{\mathrm{d}}^A} \boldsymbol{\theta}'_{A,k} \tag{5.16}$$

In geometrical accordance with a linear extrapolation of the position, the reference rotation $\boldsymbol{\theta}'_{A,k}$ in direction k is defined as

$$\boldsymbol{\theta}'_{A,k} = \boldsymbol{\theta}_{\mathrm{R1},k}^A, \tag{5.17}$$

that is, as the rotation of the first stable adjacent reference control point in direction k.

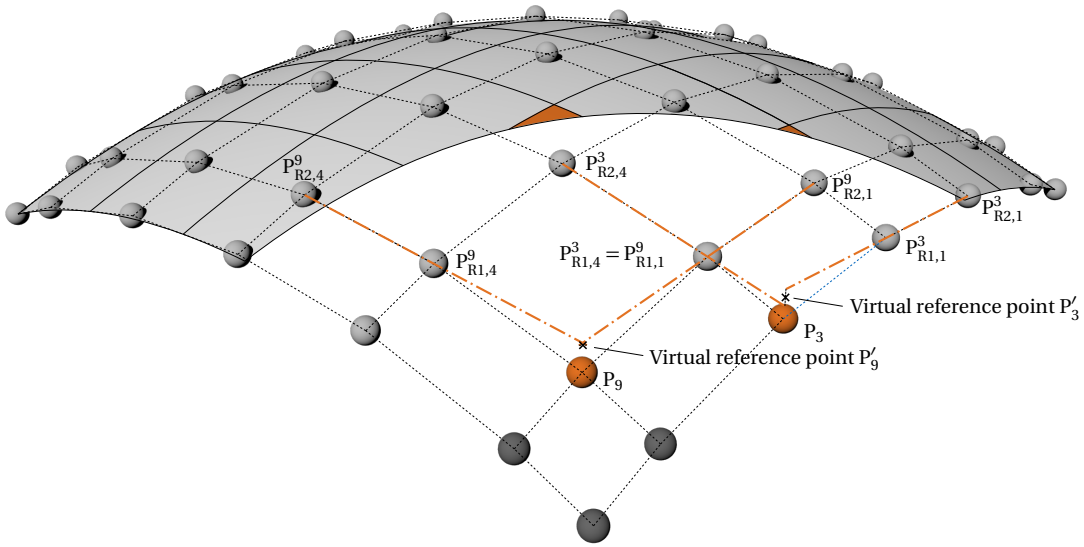

Figure 5.9: Determination of virtual reference points for the trimmed double curved shell from Figure 5.1: Two small trimmed elements and two light control points (P_3 and P_9) are highlighted in orange, the three inactive control points are highlighted in dark gray. The position of the two virtual reference points P'_3 and P'_9 for the two light control points P_3 and P_9 are determined via an averaged linear extrapolation of the control polygon from the stable adjacent reference control points ($\mathrm{P}^3_{\mathrm{R1},1}$, $\mathrm{P}^3_{\mathrm{R2},1}$, $\mathrm{P}^3_{\mathrm{R1},4}$, $\mathrm{P}^3_{\mathrm{R2},4}$) and ($\mathrm{P}^9_{\mathrm{R1},1}$, $\mathrm{P}^9_{\mathrm{R2},1}$, $\mathrm{P}^9_{\mathrm{R1},4}$, $\mathrm{P}^9_{\mathrm{R2},4}$), respectively.

Remark 5.2: As mentioned in Remark 5.1 in the previous section, there may be cases in which a light control point does not have stable adjacent control points in any of the four control grid directions. In this thesis such light

control points are denoted as *isolated* light control points. In Figure 5.10 the double curved shell model is depicted with a trimming configuration that leads to one isolated light control point highlighted in red (P_1). As can be seen, this isolated light control point has only light or inactive control points in both control grid directions. Therefore, the stable adjacent control points of the neighboring light control points P_2 and P_8 are, together with a suitable extrapolation, used to determine the virtual reference point P_1'. This is indicated by red dotdashed lines in Figure 5.10. The bonnet reinforcement structure in Section 7.3.3 includes isolated light control points, successfully stabilized via stable control points of neighboring light control points.

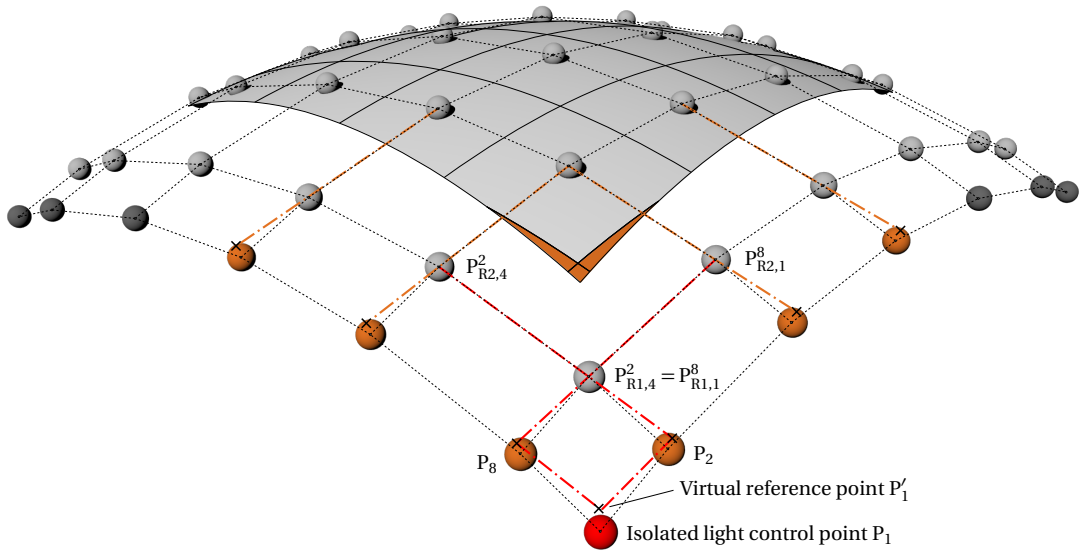

Figure 5.10: Trimmed double curved shell with five small trimmed elements and six normal light control points highlighted in orange, and one isolated light control point P_1 highlighted in red. This control point has only light (orange) and inactive control points (dark gray) in both control grid directions. The virtual reference point P_1' is defined by a suitable linear extrapolation from the stable adjacent reference control points ($P^2_{R1,4} = P^8_{R1,1}$, $P^2_{R2,4}$ and $P^8_{R2,1}$) of the neighboring light control points P_2 and P_8, as indicated by red dotdashed lines.

Remark 5.3: Also other reference estimation approaches are imaginable. One possibility would be to compute the reference position directly as the mean value of adjacent stable reference control point positions. However, this would result in a less accurate estimation, especially in large deformation scenarios, and no significant gain in computational time, since determining adjacent control points and computing initial distances is only performed once during the preprocessing step. Another possibility would be to choose an arbitrary point on the NURBS surface of the trimmed element and to solve the surface equation (2.7) for the position of the light control point. Although this seems to be more accurate at the first glance, solving the surface equation for the light control point position is again an ill-conditioned problem, which could again result in a bad reference estimation. Furthermore, no reference rotation can be computed in this way.

5.3.5 Determination of control point specific penalty factors

The next step is the determination of a specific penalty factor for each light control point. Specific penalty factors are required for two reasons. First, in order to achieve an effective stabilization, one has to ensure that the (generalized) force acting on the light control point is high enough and in the approximate range of other acting control point forces from shell and B-Rep elements. This is because the acceleration of a stabilized light control point is computed as

$$\bar{\mathbf{a}}_A^n = \overline{\mathbf{M}}_A^{-1} \left(\bar{\mathbf{f}}_A^{\text{ext},n} - \bar{\mathbf{f}}_A^{\text{int},n} + \bar{\mathbf{f}}_A^{\text{B-Rep},n} + \bar{\mathbf{f}}_A^{\text{stab},n} \right). \tag{5.18}$$

with the light control point stabilization force $\bar{\mathbf{f}}_A^{\text{stab},n}$. The stabilization would be without effect, if the stabilization force was much lower than the forces coming from shell and B-Rep elements. Second, the penalty factor must also not be too high, since the introduced stiffness would affect the critical time step of the system in explicit analysis. Thus, for an effective stabilization that does not impair the critical time step of the system, a specific and accurate penalty factor estimation for each light control point is crucial.

From Eq. (5.2) it is clear that the level of shell element forces depends on the size of the trimmed element. Therefore, a measure for the size of the trimmed element related to the light control point seems reasonable for the penalty factor estimation. Also the lumped light control point mass (see Eq. (5.1)) as a secondary quantity directly proportional to the trimmed element mass could be used to estimate the light control point penalty factor. However, this would not consider the influence of B-Rep elements and the size of the B-Rep penalty factors in Eq. (5.18). A better quantity considering all these effects, except for external loads, is stiffness.

The task is now to compute a control point related stiffness value from the overall stiffness matrix. One could use the diagonal stiffness entry of the light control point, but this would be a strong underestimation since it disregards the coupling entries to other control points. A better choice that considers these coupling entries is to compute a lumped stiffness matrix similar to the lumped mass matrix via row summing of absolute values as

$$\tilde{K}_{AiAi} = \sum_{B,j} |K_{AiBj}|, \tag{5.19}$$

where the indices $i, j = \{1,2,3,4,5,6\}$ represent the three translational $\{1,2,3\}$ and rotational $\{4,5,6\}$ entries. Since the support of NURBS basis functions is local, only a local stiffness matrix considering the control points related to the light control point A needs to be generated in the preprocessing step, which is computationally inexpensive. The specific penalty factors for the translations $\tilde{\beta}_A^{\text{disp}}$ and rotations $\tilde{\beta}_A^{\text{rot}}$ for light control point A are then computed as the mean value of the three corresponding stiffness entries

$$\tilde{\beta}_A^{\text{disp}} = \frac{1}{3}\sum_{i=1}^{3} \tilde{K}_{AiAi}, \tag{5.20}$$

$$\tilde{\beta}_A^{\text{rot}} = \frac{1}{3}\sum_{i=4}^{6} \tilde{K}_{AiAi}. \tag{5.21}$$

To sum up, the individual light control point penalty factors for translations and rotations can now be computed via local stiffness matrices considering shell and B-Rep elements. This ensures the correct amount of stabilization for all light control points with masses and stiffnesses varying by several orders of magnitude.

The final penalty factors for translations and rotations are then computed as

$$\beta_A^{\text{disp}} = \bar{\beta}\,\tilde{\beta}_A^{\text{disp}}, \tag{5.22}$$

$$\beta_A^{\text{rot}} = \bar{\beta}\,\tilde{\beta}_A^{\text{rot}}, \tag{5.23}$$

where $\bar{\beta}$ is a global penalty factor used to adjust the intensity of the stabilization.

5.3.6 Local mass scaling of light control points

Introducing a penalty stiffness between light control points and their stable adjacent control points can be seen as a kind of preconditioning for small entries in the stiffness matrix. Since the system matrix in dynamic problems is $\mathbf{M}^{-1}\mathbf{K}$, conditioning the mass matrix via local scaling of translational and rotational light control point masses also seems reasonable[2]. For explicit dynamic analysis, this localized mass scaling has two important effects: (i) it avoids a reduction in time step size due to the introduced stabilization stiffness and (ii) it reduces the error amplification effects from forces to accelerations in Eq. (5.18), caused by extremely small control point masses $\overline{\mathbf{M}}_A$. It should be noted that excessive mass scaling would impair the effectiveness of stabilization techniques for highly dynamic simulations, because of excessively high inertia effects, i.e. a high mass in combination with unaltered forces/moments in Eq. (5.18) would lead to very low accelerations.

The scaled translational and rotational masses, see Eqs. (2.34) and (2.35), of a light control point A in $\mathcal{M}_{\text{li}}^{(i)}$ are then computed as

$$\hat{M}_A = M_A f^{\text{s}} + M_\varepsilon^{(i)} \tag{5.24}$$

$$\hat{J}_A = J_A f^{\text{s}} + J_\varepsilon^{(i)}, \tag{5.25}$$

in which f^{s} is a constant mass scaling factor in the range of 10–100. Since light control points can have arbitrarily small mass, the terms $M_\varepsilon^{(i)}$ and $J_\varepsilon^{(i)}$ add extremely small translational and rotational masses ensuring that even

[2] Please note that in explicit analysis neither the stiffness nor the mass matrix is actually constructed. Here, matrices are only used to interpret the stabilization measures in a standard (implicit) FEA context.

the lightest control point possesses a minimum amount of inertia. This yields extra numerical robustness. These contributions are defined as

$$M_{\varepsilon}^{(i)} = m_{\text{th}}^{(i)} \varepsilon_{\text{l}} \tag{5.26}$$

$$J_{\varepsilon}^{(i)} = \kappa \frac{h^2}{12} m_{\text{th}}^{(i)} \varepsilon_{\text{l}}, \tag{5.27}$$

where ε_{l} is a small constant of order $\mathcal{O}(10^{-6})$–$\mathcal{O}(10^{-9})$ (for the definition of rotational inertia see also Eq. (2.35)). As can be seen, these contributions are by magnitudes smaller than the threshold mass $m_{\text{th}}^{(i)}$ below which control points are considered as light control points and thus only have an effect on the lightest control points.

In conclusion, it should be noted that mass scaling is only applied to light control points, whose mass is inherently very low, see Eq. (5.10), and thus even large scaling factors f^{s} hardly influence the overall model mass and solution.

5.3.7 Penalty-based stabilization constraints

In Section 5.3.4 above, a virtual reference point is defined for each light control point, based on position and rotation of stable adjacent control points. In this section the actual constraint formulation between virtual reference points and light control points is presented along with the corresponding derivatives required to compute control point forces/moments and stiffness.

Translational constraints

Constraints on translational DOFs can be defined in different ways. The first possibility would be to enforce the coordinates of the light control point to be the same as the coordinates of the virtual reference point, i.e. $\boldsymbol{g}^{A,\text{disp}} = \mathbf{x}_A - \boldsymbol{x}'_A = 0$. This formulation would successfully constrain the light control point to its reference, thereby avoiding extremely large displacements, velocities and accelerations. However, one has to note that the reference position is only an estimation of the actual light control point position, even in the initial state. The quality of this estimation depends on mesh refinement and surface curvature, see Figure 5.9. Due to the initial distance between the virtual reference point $\boldsymbol{x}'_A$ and the light control point $\mathbf{x}_A$, this constraint formulation leads to initial stabilization forces and consequently to initial stresses in the model.

To avoid these initial stresses, the initial distance between the virtual reference point and the light control point $(\mathbf{X}_A - \boldsymbol{X}'_A)$ is subtracted from $\boldsymbol{g}^{A,\text{disp}}$, leading to constraints on the displacements rather than on the absolute positions:

$$\boldsymbol{g}^{A,\text{disp}} = (\mathbf{x}_A - \boldsymbol{x}'_A) - (\mathbf{X}_A - \boldsymbol{X}'_A) = (\mathbf{u}_A - \boldsymbol{u}'_A) \tag{5.28}$$

This means that the light control point is enforced to have the same displacement as the virtual reference point, instead of the same position. Inserting Eqs. (5.14) and (5.15) into Eq. (5.28) and expressing all quantities via displacements finally yields the displacement constraint

$$\boldsymbol{g}^{A,\text{disp}} = \mathbf{u}_A - \frac{1}{n_{\text{d}}^A} \sum_{k=1}^{n_{\text{d}}^A} \mathbf{u}_{\text{R1},k}^A + (\mathbf{u}_{\text{R1},k}^A - \mathbf{u}_{\text{R2},k}^A) \frac{L_{1,k}^A}{L_{12,k}^A}. \tag{5.29}$$

For the computation of control point forces and stiffness matrices in Eqs. (5.8) and (5.9), constraint derivatives with respect to the displacement vector $\mathbf{d}$ are required. From Eq. (5.29) it can be seen that the only non-zero derivatives are with respect to the light control point A, and the stable adjacent reference control points $\text{P}_{\text{R1},k}^A$ and $\text{P}_{\text{R2},k}^A$. This is consistent with the fact that stabilization forces are only applied to control points involved in the constraint formulation. The constraint derivative matrix containing only the non-zero entries can be written as

$$\frac{\partial \boldsymbol{g}^{A,\text{disp}}}{\partial \mathbf{d}^{\text{disp}}} = \left[\frac{\partial \boldsymbol{g}^{A,\text{disp}}}{\partial \mathbf{u}_A}, \frac{\partial \boldsymbol{g}^{A,\text{disp}}}{\partial \mathbf{u}_{\text{R1},1}^A}, \frac{\partial \boldsymbol{g}^{A,\text{disp}}}{\partial \mathbf{u}_{\text{R2},1}^A}, \ldots, \frac{\partial \boldsymbol{g}^{A,\text{disp}}}{\partial \mathbf{u}_{\text{R1},n_{\text{d}}^A}^A}, \frac{\partial \boldsymbol{g}^{A,\text{disp}}}{\partial \mathbf{u}_{\text{R2},n_{\text{d}}^A}^A} \right]. \tag{5.30}$$

The individual non-zero constraint derivative matrices can be computed as

$$\frac{\partial \boldsymbol{g}^{A,\text{disp}}}{\partial \mathbf{u}_A} = \begin{bmatrix} 1 & 0 & 0 \\ 0 & 1 & 0 \\ 0 & 0 & 1 \end{bmatrix}, \tag{5.31}$$

$$\frac{\partial \boldsymbol{g}^{A,\mathrm{disp}}}{\partial \mathbf{u}^{A}_{\mathrm{R1},k}} = \begin{bmatrix} -\frac{1}{n^{A}_{\mathrm{d}}}\left(1+\frac{L^{A}_{1,k}}{L^{A}_{12,k}}\right) & 0 & 0 \\ 0 & -\frac{1}{n^{A}_{\mathrm{d}}}\left(1+\frac{L^{A}_{1,k}}{L^{A}_{12,k}}\right) & 0 \\ 0 & 0 & -\frac{1}{n^{A}_{\mathrm{d}}}\left(1+\frac{L^{A}_{1,k}}{L^{A}_{12,k}}\right) \end{bmatrix}, \tag{5.32}$$

$$\frac{\partial \boldsymbol{g}^{A,\mathrm{disp}}}{\partial \mathbf{u}^{A}_{\mathrm{R2},k}} = \begin{bmatrix} \frac{1}{n^{A}_{\mathrm{d}}}\frac{L^{A}_{1,k}}{L^{A}_{12,k}} & 0 & 0 \\ 0 & \frac{1}{n^{A}_{\mathrm{d}}}\frac{L^{A}_{1,k}}{L^{A}_{12,k}} & 0 \\ 0 & 0 & \frac{1}{n^{A}_{\mathrm{d}}}\frac{L^{A}_{1,k}}{L^{A}_{12,k}} \end{bmatrix}. \tag{5.33}$$

Based on this, the constraint stiffness matrix[3] for light control point A, exemplarily shown for a light control point with only one stable direction k, can then be written as

$$\mathbf{K}^{A,\mathrm{disp}} = \beta^{\mathrm{disp}}_{A} \begin{bmatrix} 1 & 0 & 0 & k_1 & 0 & 0 & k_2 & 0 & 0 \\ 0 & 1 & 0 & 0 & k_1 & 0 & 0 & k_2 & 0 \\ 0 & 0 & 1 & 0 & 0 & k_1 & 0 & 0 & k_2 \\ k_1 & 0 & 0 & k_{11} & 0 & 0 & k_{12} & 0 & 0 \\ 0 & k_1 & 0 & 0 & k_{11} & 0 & 0 & k_{12} & 0 \\ 0 & 0 & k_1 & 0 & 0 & k_{11} & 0 & 0 & k_{12} \\ k_2 & 0 & 0 & k_{12} & 0 & 0 & k_{22} & 0 & 0 \\ 0 & k_2 & 0 & 0 & k_{12} & 0 & 0 & k_{22} & 0 \\ 0 & 0 & k_2 & 0 & 0 & k_{12} & 0 & 0 & k_{22} \end{bmatrix}, \tag{5.34}$$

with

$$k_1 = -\frac{1}{n^{A}_{\mathrm{d}}}\left(1+\frac{L^{A}_{1,k}}{L^{A}_{12,k}}\right), \quad k_{11} = \frac{1}{(n^{A}_{\mathrm{d}})^2}\left(1+\frac{L^{A}_{1,k}}{L^{A}_{12,k}}\right)^2, \tag{5.35}$$

$$k_2 = \frac{1}{n^{A}_{\mathrm{d}}}\frac{L^{A}_{1,k}}{L^{A}_{12,k}}, \quad k_{22} = \left(\frac{1}{n^{A}_{\mathrm{d}}}\frac{L^{A}_{1,k}}{L^{A}_{12,k}}\right)^2, \quad k_{12} = -\frac{1}{(n^{A}_{\mathrm{d}})^2}\frac{L^{A}_{1,k}}{L^{A}_{12,k}}\left(1+\frac{L^{A}_{1,k}}{L^{A}_{12,k}}\right). \tag{5.36}$$

Rotational constraints

For stabilization constraints on rotational DOFs, considerations on initial stresses as for translational DOFs are not applicable because the initial rotations are zero anyway. Therefore the rotational constraints are defined as

$$\boldsymbol{g}^{A,\mathrm{rot}} = \boldsymbol{\theta}_A - \boldsymbol{\theta}'_A. \tag{5.37}$$

Inserting Eqs. (5.16) and (5.17) into Eq. (5.37) then yields

$$\boldsymbol{g}^{A,\mathrm{rot}} = \boldsymbol{\theta}_A - \frac{1}{n^{A}_{\mathrm{d}}}\sum_{k=1}^{n^{A}_{\mathrm{d}}} \boldsymbol{\theta}_{\mathrm{R1},k}. \tag{5.38}$$

To compute stabilization moments and stiffness, corresponding constraint derivatives are again required. For the rotational constraints only the derivatives with respect to the light control point rotation $\boldsymbol{\theta}_A$ and the reference control

[3] The constraint stiffness matrix is required for the time step estimation via the maximum system eigenvalue and to demonstrate that the overall stiffness matrix remains symmetric and positive semidefinite, which is a prerequisite for stability as shown in Section 5.4 below.

point $\mathrm{P}^A_{\mathrm{R1},k}$ are non-zero. This leads to the following constraint derivative matrix containing only the non-zero entries:

$$\frac{\partial \boldsymbol{g}^{A,\mathrm{rot}}}{\partial \mathbf{d}^{\mathrm{rot}}} = \left[\frac{\partial \boldsymbol{g}^{A,\mathrm{rot}}}{\partial \boldsymbol{\theta}_A}, \frac{\partial \boldsymbol{g}^{A,\mathrm{rot}}}{\partial \boldsymbol{\theta}^A_{\mathrm{R1},1}}, \ldots, \frac{\partial \boldsymbol{g}^{A,\mathrm{rot}}}{\partial \boldsymbol{\theta}^A_{\mathrm{R1},n^A_{\mathrm{d}}}} \right], \tag{5.39}$$

with the individual constraint derivative matrices

$$\frac{\partial \boldsymbol{g}^{A,\mathrm{rot}}}{\partial \boldsymbol{\theta}_A} = \begin{bmatrix} 1 & 0 & 0 \\ 0 & 1 & 0 \\ 0 & 0 & 1 \end{bmatrix}, \tag{5.40}$$

$$\frac{\partial \boldsymbol{g}^{A,\mathrm{rot}}}{\partial \boldsymbol{\theta}^A_{\mathrm{R1},k}} = \begin{bmatrix} -\frac{1}{n^A_{\mathrm{d}}} & 0 & 0 \\ 0 & -\frac{1}{n^A_{\mathrm{d}}} & 0 \\ 0 & 0 & -\frac{1}{n^A_{\mathrm{d}}} \end{bmatrix}. \tag{5.41}$$

The corresponding stabilization stiffness matrix, again for a light control A with only one stable direction k, can be computed as

$$\mathbf{K}^{A,\mathrm{rot}} = \beta^{\mathrm{rot}}_A \begin{bmatrix} 1 & 0 & 0 & -\frac{1}{n^A_{\mathrm{d}}} & 0 & 0 \\ 0 & 1 & 0 & 0 & -\frac{1}{n^A_{\mathrm{d}}} & 0 \\ 0 & 0 & 1 & 0 & 0 & -\frac{1}{n^A_{\mathrm{d}}} \\ -\frac{1}{n^A_{\mathrm{d}}} & 0 & 0 & \frac{1}{(n^A_{\mathrm{d}})^2} & 0 & 0 \\ 0 & -\frac{1}{n^A_{\mathrm{d}}} & 0 & 0 & \frac{1}{(n^A_{\mathrm{d}})^2} & 0 \\ 0 & 0 & -\frac{1}{n^A_{\mathrm{d}}} & 0 & 0 & \frac{1}{(n^A_{\mathrm{d}})^2} \end{bmatrix}. \tag{5.42}$$

5.4 Numerical stability and time step estimation

In Section 2.9.3, the stability condition for the explicit central difference scheme is derived in order to compute the critical time step size. It is furthermore shown that this stability condition relies on two premises: (i) use of a Rayleigh damping matrix and (ii) symmetry and positive semidefiniteness of $\mathbf{M}$ and $\mathbf{K}$. Thus, in order for the stability condition to remain valid along with the presented stabilization technique, both premises still need to be fulfilled. This shall be shown in this section.

Since the proposed stabilization method does not introduce damping, premise (i) is irrelevant and only the validity of premise (ii) for $\mathbf{M}$ and $\mathbf{K}$ remains to be shown. From Eq. (5.24) one can see that only existing mass entries of the lumped mass matrix are scaled, which means that the mass matrix remains diagonal and thus automatically symmetric. Furthermore, all mass entries remain positive and therefore $\mathbf{M}$ also remains positive-definite. From Eqs. (5.8), (5.34) and (5.42), it can also be seen that the translational and rotational stabilization stiffness matrices for a light control point are symmetric. Because these stiffness matrices are added to the shell and B-Rep element stiffness matrices, the total stiffness matrix $\mathbf{K}$ remains symmetric. Positive semidefiniteness of $\mathbf{K}^{A,\mathrm{disp}} \in \mathbb{R}^{n\times n}$ and $\mathbf{K}^{A,\mathrm{rot}} \in \mathbb{R}^{n\times n}$ in the form

$$\mathbf{K}^A = \beta \left(\frac{\partial \boldsymbol{g}}{\partial \mathbf{d}} \right)^T \frac{\partial \boldsymbol{g}}{\partial \mathbf{d}}, \tag{5.43}$$

can be shown by applying Theorem 3.1 from Section 3.5.1 in a similar manner: Pre-multiplying Eq. (5.43) with $\boldsymbol{z}^T$ and post-multiplying with $\boldsymbol{z}$ along with some reordering yields:

$$\boldsymbol{z}^T \mathbf{K}^A \boldsymbol{z} = \beta\, \boldsymbol{z}^T \left(\frac{\partial \boldsymbol{g}}{\partial \mathbf{d}} \right)^T \left(\frac{\partial \boldsymbol{g}}{\partial \mathbf{d}} \right) \boldsymbol{z} = \beta \left(\frac{\partial \boldsymbol{g}}{\partial \mathbf{d}} \boldsymbol{z} \right)^T \left(\frac{\partial \boldsymbol{g}}{\partial \mathbf{d}} \boldsymbol{z} \right) = \beta\, \boldsymbol{b}^T\, \mathbf{I}\, \boldsymbol{b}, \tag{5.44}$$

where the vector $\boldsymbol{b} = \frac{\partial \boldsymbol{g}}{\partial \mathbf{d}} \boldsymbol{z}$ and the identity matrix $\mathbf{I}$ is introduced. Since $\boldsymbol{b}^T \mathbf{I}\, \boldsymbol{b} \geq 0$ is automatically fulfilled for any vector $\boldsymbol{b}$, $\mathbf{K}^A$ is positive semidefinite as long as $\beta \geq 0$. Thus, also the total stiffness matrix $\mathbf{K}$ remains symmetric and positive semidefinite, and the stability condition (2.67) remains valid.

To conclude, this section shows that the stability condition and the corresponding time step estimations are further on applicable to models stabilized with above presented approach.

5.5 Error measures

In order to quantify the effectiveness of the proposed stabilization method for the numerical examples in Chapter 7 and Section 5.6, error measures for light control point translations and rotations are introduced. In addition to the assessment of the stabilization method, these error measures can also be used to quantify the behavior of light control points without stabilization.

The goal of the stabilization method is to prevent light control points from causing numerical problems by constraining their displacements and rotations to those of an estimated virtual reference point. Integrating the constraints $\boldsymbol{g}^{A,\mathrm{disp}}$ and $\boldsymbol{g}^{A,\mathrm{rot}}$ into the error measures in one way or another therefore seems obvious. To obtain one scalar error measure for displacements respectively rotations, the vector-valued constraints are considered via their Euclidean norm and summed up. The error measure for light control point displacements is then defined as

$$e^{\mathrm{disp}} = \sum_A \frac{\|\boldsymbol{g}^{A,\mathrm{disp}}\|}{l_{\max}\, n_{\mathrm{lcp}}} = \sum_A \frac{\|(\mathbf{u}_A - \boldsymbol{u}'_A)\|}{l_{\max}\, n_{\mathrm{lcp}}}. \tag{5.45}$$

To achieve a comparable error measure, e^{disp} is normalized with the maximum element length $l_{\max}$ and the number of light control points n_{lcp}. The error measure for light control point rotations is defined in a similar manner as

$$e^{\mathrm{rot}} = \sum_A \frac{\|\boldsymbol{g}^{A,\mathrm{rot}}\|}{2\pi\, n_{\mathrm{lcp}}} = \sum_A \frac{\|(\boldsymbol{\theta}_A - \boldsymbol{\theta}'_A)\|}{2\pi\, n_{\mathrm{lcp}}}, \tag{5.46}$$

where e^{rot} is again normalized with n_{lcp} and a rotation angle of 2π.

5.6 Minimal numerical examples

In this section, the trimmed single-patch and the trimmed multi-patch cantilever beam examples with light control points from Section 5.2 are solved with the stabilization method proposed in Section 5.3. Results with and without stabilization are compared visually and by means of the error measures introduced in the previous section. More sophisticated numerical examples with stabilized light control points are solved in Chapter 7.

5.6.1 Trimmed single-patch cantilever beam

Here it shall be shown that the proposed stabilization method allows solving the trimmed single-patch cantilever beam (one row of light control points) from Figure 5.5a without numerical instabilities. Figure 5.11 provides a comparison between the results without and with stabilization. The unstabilized configuration in Figure 5.11a shows large light control point displacements, which causes the simulation to terminate prematurely after around 2.45×10^{-3} s. The stabilized configuration in Figure 5.11b, on the other hand, shows correct light control point displacements and no premature termination. This is also clearly visible in the error measures for displacements and rotations in Figure 5.11c. The normalized displacement and rotation errors of light control points for the unstabilized configuration are high from the beginning of the simulation with values of around 10^1 and 10^2, respectively. This means (i) that the average displacement difference of a light control point from its estimated reference displacement is around 10^1 times the maximum element length and (ii) that the average rotation difference of a light control point from its estimated reference rotation is around $10^2 \times 2\pi$. At around 2.0×10^{-3} s the simulation becomes unstable and the errors increase drastically, before the simulation finally aborts. The stabilized configuration, on the contrary, shows relatively low and consistent displacement and rotation errors of approximately 10^{-4} and 10^{-2}, respectively, without instabilities. For the stabilization, control points are considered as light control points if their mass is $C_{\mathrm{th}} = 10^{-2}$ times smaller than the heaviest control point in the patch, see Eq. (5.10). A global penalty factor of $\bar{\beta} = 0.1$, see Eqs. (5.22) and (5.23), and a local mass scaling factor of $f^{\mathrm{s}} = 10$, see Eqs. (5.24) and (5.25) are used. Both configurations are solved with the same initial time step size, i.e. the time step size estimated by LS-DYNA times a safety factor of 0.9. This shows that the proposed stabilization scheme does not affect the critical time step size.

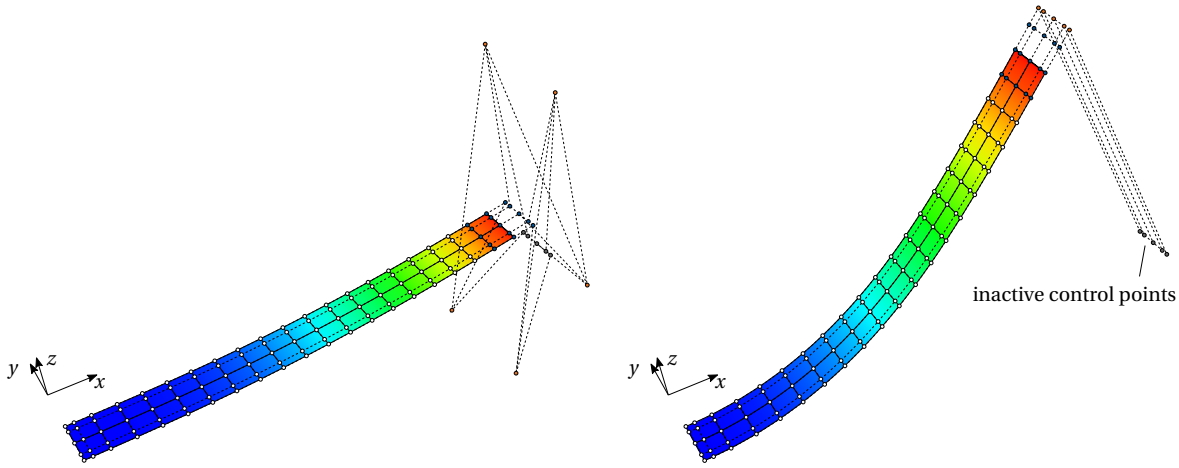

(a) Without stabilization.

(b) With stabilization.

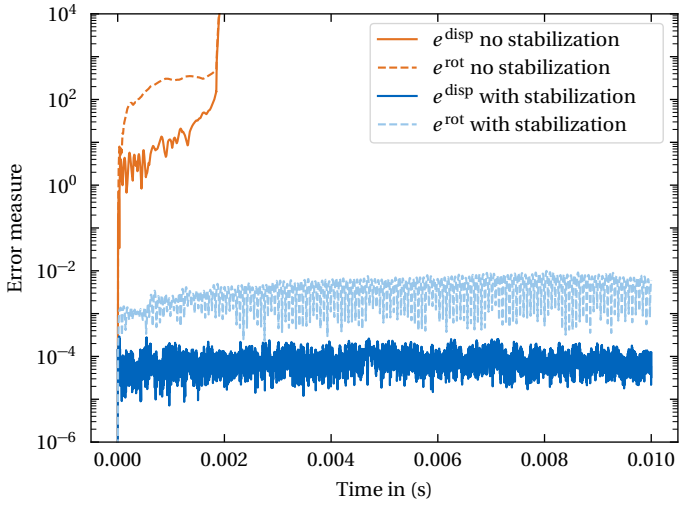

(c) Displacement and rotation error measures over time.

Figure 5.11: Trimmed single-patch cantilever beam: Comparison of deformed shapes obtained from simulations without (a) and with stabilization (b), where the color plots indicate z-displacements. Light control points are highlighted in orange, inactive control points in dark gray and trimmed control points in blue. Inactive control points are visualized in their initial configuration. The corresponding displacement and rotation error measures are depicted in (c). For the stabilization a global penalty factor of $\bar{\beta} = 0.1$ and a local mass scaling factor of $f^{\text{s}} = 10$ are used. The stabilized configuration shows the desired behavior without instabilities.

5.6.2 Trimmed multi-patch cantilever beam

The trimmed multi-patch cantilever beam from Figure 5.7 with one row of light control points in each patch is now also solved with the proposed stabilization method. The results with and without stabilization are compared in Figure 5.12. The unstabilized configuration in Figure 5.12a shows large light control point displacements and a kink between the patches due to affected coupling conditions. The unstabilized simulation terminates prematurely at around 3.94×10^{-3} s. The stabilized configuration in Figure 5.12b, on the contrary, shows light control points at the desired position and continuously coupled patches without instabilities. The error measures in Figure 5.12c clearly confirm these observations. For the unstabilized configuration, the displacement error seems to be quite constant at the beginning, while the error in the rotations increases steadily. After around 2.0×10^{-3} s also the displacement error increases significantly until the simulation becomes unstable at around 4.0×10^{-3} s, indicated by the sudden rise of errors towards infinity. The errors of the stabilized configuration show the expected stable behavior with relatively low consistent error values of around 10^{-4} to 10^{-3} over the entire simulation time. For the stabilization, the same parameter setting as above is used ($C_{\text{th}} = 10^{-2}$, $\bar{\beta} = 0.1$ and $f^{\text{s}} = 10$). As in the previous example, both configurations are solved with the same initial time step size, again indicating that the stabilization scheme does not affect the critical time step size.

To sum up, the proposed stabilization scheme enables stable simulations of examples with small trimmed elements and light control points that previously showed unstable behavior. Furthermore, no additional restriction in time step size is observed for the stabilized examples.

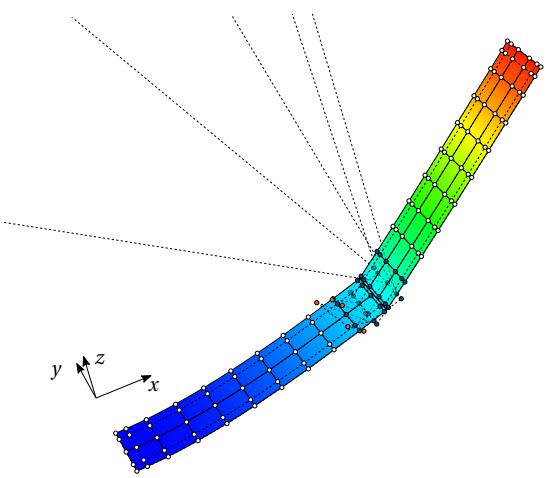

(a) Without stabilization.

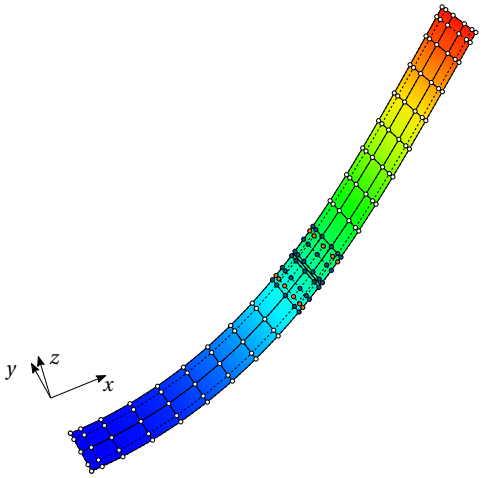

(b) With stabilization.

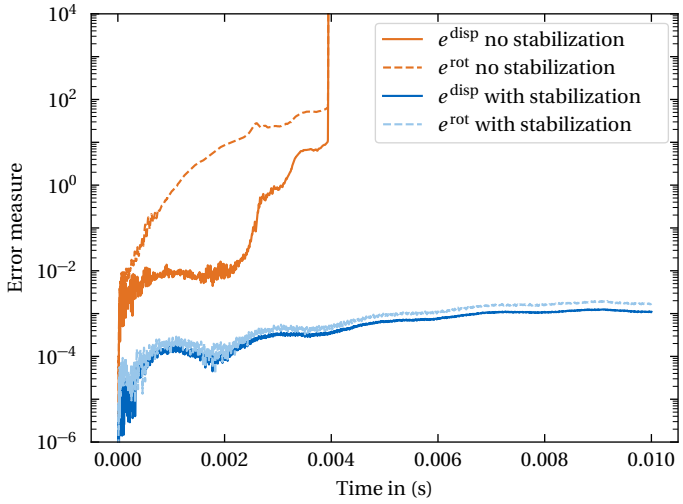

(c) Displacement and rotation error measures over time.

Figure 5.12: Trimmed multi-patch cantilever beam: Comparison of the deformed shapes obtained from simulations without (a) and with stabilization (b), where the color plots indicate z-displacements. Light control points are highlighted in orange and trimmed control points in blue. The corresponding displacement and rotation error measures are depicted in (c). For the stabilization a global penalty factor of $\bar{\beta} = 0.1$ and a local mass scaling factor of $f^{\text{s}} = 10$ are used. The stabilized configuration shows the desired behavior without instabilities.

5.7 Summary and conclusion of Chapter 5

This chapter deals with numerical instabilities in explicit dynamic isogeometric analysis caused by small trimmed NURBS elements and proposes a corresponding stabilization approach.

Section 5.2.1 first explains that small trimmed elements lead to control points with very low mass and stiffness entries – thus the designation *light* control points. Section 5.2.2 then describes that ill-conditioned mass and stiffness matrices are not the actual problem in explicit analysis, in which no equation systems are solved. The problems are in fact (i) the extreme amplification of inevitable inaccuracies in the force evaluation by extremely large inverse mass entries and (ii) the low stiffness and thereby loose connection between light control points and the material domain of the shell that hardly restricts the movement of light control points. Section 5.2.3 demonstrates that numerical instabilities caused by light control points propagate to adjacent control points, most likely leading to useless results

or premature termination due to overflow errors. Section 5.2.4 shows that light control point instabilities are not a matter of time step size, because even a time step reduction of magnitudes cannot prevent this instability to occur. Light control points rather cause the system to be only weakly stable, with instabilities evolving over simulation time. Section 5.2.5 furthermore demonstrates that the unstable behavior of light control points can also affect the quality of weak coupling conditions, clearly shown by a kink between coupled patches.

In Section 5.3, a stabilization scheme for light control points is proposed. This method tackles both aforementioned problems induced by light control points: (i) local mass scaling of light control points reduces the amplification effect of inaccuracies from forces to accelerations via lower inverse masses and (ii) penalty-based constraints introduce translational and rotational stiffness between light control points and stable adjacent control points to restrict uncontrolled light control point movement.

Section 5.4 shows that the requirements of symmetry and positive semidefiniteness on the system matrices for the stability condition are not violated by the stabilization. This allows using stable time step estimations based on the maximum system eigenvalue.

In Section 5.5, appropriate displacement and rotation error measures are introduced to quantify unstable behavior and the effectiveness of the stabilization.

The two minimal numerical examples in Section 5.6, a trimmed single-patch and a trimmed multi-patch cantilever beam including light control points, demonstrate that the proposed stabilization scheme is indeed able to eliminate the instability effects of light control points, allowing for reliable simulations without a restriction in time step size.

The advantages of the proposed stabilization approach are the following:

- Compatible with weak coupling and boundary conditions along trimmed edges.
- Computationally efficient, i.e. no time step restriction and low numerical effort.
- A non-intrusive implementation as an add-on to existing solver environments.
- Although originally designed for Reissner-Mindlin shells with rotational DOFs, the stabilization scheme is universally applicable to other shell and even solid element formulations.
- Simple implementation for 2D shell and even 3D solid problems.
- Compared to the virtual domain with low density in FCM, no additional integration points are required.

The drawback of this penalty approach is the required definition of (i) a threshold value below which a control point is considered as a light control point, (ii) a penalty factor and (iii) a local mass scaling factor. Nevertheless, the somehow heuristic identification of problematic control points, nodes or elements is, and will be required for most stabilization approaches, see the overview in Section 5.3.2. Furthermore, similar parameter settings could be used for the examples solved within this thesis.

Chapter 6

Integrated IBRA-based CAD/CAE process

The overall goal for developing Explicit IBRA is to speed up the virtual development process (for vehicle safety) via a full integration of CAD and CAE. Certainly, this requires a consistent data structure for design and analysis, well-matched interfaces and consistent bidirectional data transfer throughout the entire process. This chapter presents a prototypical implementation of such a design process, demonstrating the possibility to fully connect professional CAD and CAE software based on a smart and sophisticated exchange format. In particular, this closed design process establishes a bidirectional connection between the CAD program Rhinoceros [116] and the FEA solver LS-DYNA [45] via their corresponding application programing interfaces (APIs) and the IBRA exchange format [52], see Figure 6.1. The most distinguishing aspects of this process are:

1. The fact that geometry *and* topology information is used throughout the entire process. This enables the automatic definition of coupling conditions along edges and vertices.

2. The consistent feature-based data structure that allows identifying CAD features like holes, cut-outs, beadings or trimmed edges as such also in the analysis model. This data structure also allows to assign analysis-related information like material properties or boundary, coupling and loading conditions to features and not to individual nodes or elements as in FEA. This is a particular advantage within the various design cycles of a product development process because the same properties, coupling, boundary or loading conditions can be automatically assigned to the same features regardless of whether the model or the underlying discretization has changed.

3. The possibility to perform all design, pre- and postprocessing steps within the CAD environment.

The following sections are dedicated to different parts of this process and provide more implementation-specific information.

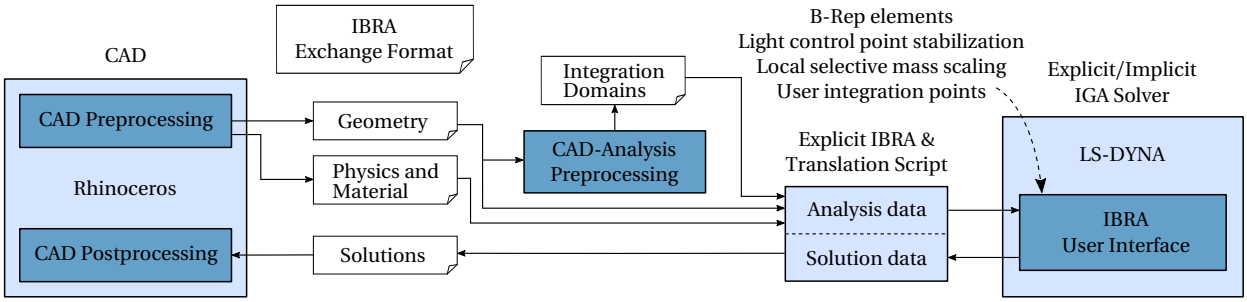

Figure 6.1: Closed design-analysis process: Prototypical implementation based on the IBRA exchange format. Figure taken from [54] in a slightly modified form.

6.1 CAD environment for design, pre- and postprocessing

Starting point for the development process shown in Figure 6.1 is the generation of a suitable B-Rep model in CAD. Since IBRA allows using NURBS-based B-Rep models for structural analysis, it is expedient to extend the scope of the CAD software from pure geometrical modeling to analysis-related pre- and postprocessing capabilities. Through this combination of design and analysis tools, switching between three different software environments for CAD, preprocessing and postprocessing can be avoided.

The design process presented within this thesis uses the already existing IBRA pre- and postprocessing plug-in TeDA (Tool to enhance Design by Analysis) [74] for the CAD system Rhinoceros [116], see Figure 6.2 and [30, 32, 52]. TeDA allows to refine the B-Rep model (knot insertion, p-refinement, k-refinement), to apply different types of boundary and loading conditions, to extract geometry and topology information and to finally output the required data in a suitable exchange format, see the following section, all within the CAD environment.

After the analysis, TeDA is able to read the *Solution* files and to visualize results on control point or integration point basis on the deformed shape directly in the CAD system. Necessary design modifications can then be directly applied to the B-Rep model and within the CAD environment. With classical FEA, design modifications are either made on the FE model only, which results in unsynchronized models for design and analysis, or on the CAD model, which then requires to generate the FE model from scratch again. As shown in [30, 32, 52], such a pre- and postprocessing environment can also be established in other CAD systems.

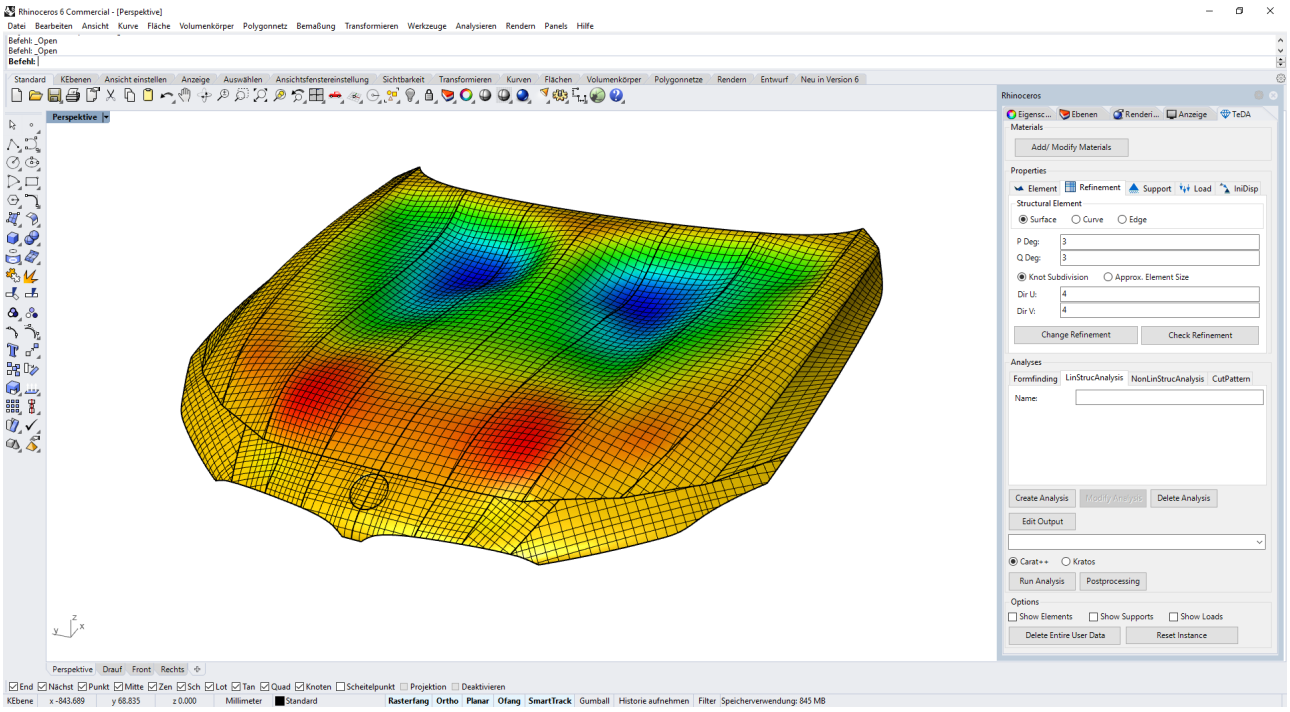

Figure 6.2: CAD environment for design, pre- and postprocessing: TeDA in Rhino.

6.2 IBRA exchange format

More important than the tools eventually used within the design process is a consistent data structure. The design process presented here relies on the IBRA exchange format proposed by Teschemacher et al. [52]. This format is based on the JavaScript Object Notation (JSON) and comprises all information required for Isogeometric B-Rep Analysis of trimmed multi-patch NURBS models. Besides geometry and topology information of the B-Rep model, this includes information on integration domains, boundary and loading conditions, material properties, and analysis results. Figure 6.3 provides a brief overview on the four data containers *Geometry*, *Integration Domains*, *Physics and Material*, and *Solutions*. Within this format, each entity is identified by a unique id, enabling a clear relation between geometric, topologic and analysis-related entities.

Another characteristic of the IBRA format are the multiple data extraction levels reaching from pure CAD data like geometry and topology information to integration points and evaluated basis functions, see Figure 6.4. These

different levels allow a flexible data extraction depending on the IGA capabilities of the solver. That is, for an advanced IGA solver it is sufficient to only extract geometry and topology data. For a standard FEA solver that does not know NURBS, one would extract already evaluated basis function values. Via TeDA, typical CAD data can be directly read from the CAD system and written to the *Geometry* container. For analysis-related data like integration points or basis function values in the *Integration Domains* container, on the other hand, an additional preprocessing step is required. In the present workflow this so-called *CAD-Analysis Preprocessing* step (see Figure 6.1) is performed by the solver CARAT++ [154] developed at the Chair of Structural Analysis at the Technical University of Munich.

A detailed description of the IBRA exchange format can be found in the corresponding open access paper [52]. The specific data extracted for usage in LS-DYNA within the present process is described in the following section.

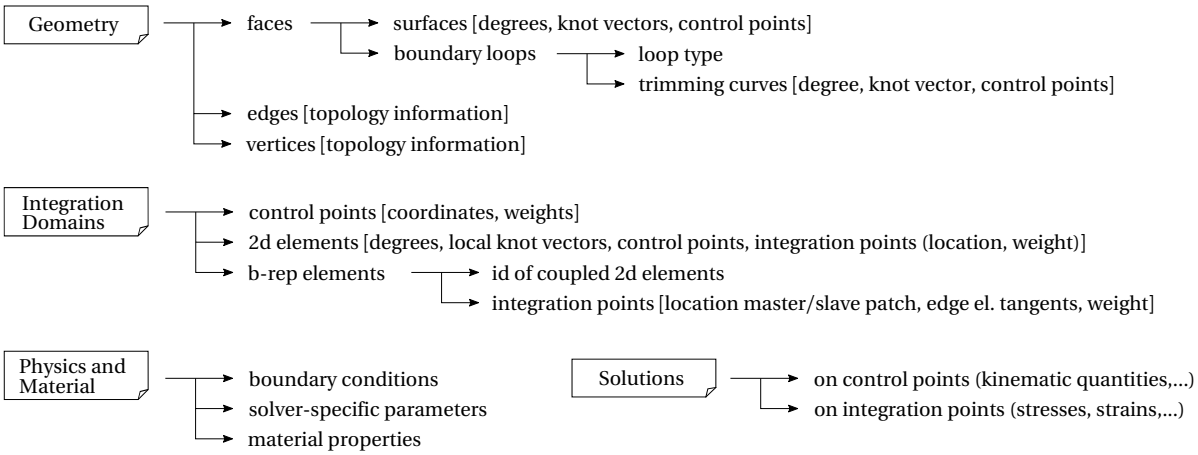

Figure 6.3: The IBRA exchange format: Essential file information [54].

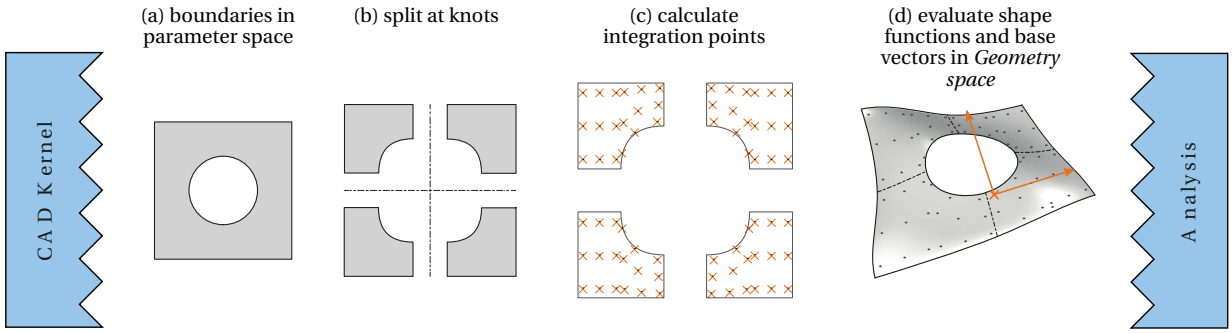

Figure 6.4: The IBRA exchange format: Overview on the different data extraction levels reaching from pure CAD (left) to full analysis data (right). Figure taken from [52] in a slightly reduced form.

6.3 Solver with IBRA interface

A solver for explicit dynamic crash analysis on trimmed B-Rep models must (i) be able to handle trimming, and to couple trimmed NURBS shells, and (ii) provide crash-relevant capabilities like explicit time integration, elasto-plastic material behavior and contact for IGA. Explicit IBRA achieves this by combining the patch coupling capabilities of IBRA with the already available crash-related features for IGA in LS-DYNA. At the time this thesis was started, the IGA functionality in LS-DYNA included: isogeometric shell and solid elements, various NURBS-based shell formulations [44, 73, 77], trimming [43], basically all standard material models, and contact for both implicit and explicit analysis as well as mass scaling for explicit IGA [14]. More information regarding the current IGA capabilities in LS-DYNA can be found in [78–80]. Referring to the different data levels of the IBRA exchange format described in the previous section, this means that LS-DYNA is able to process data on CAD level, i.e. it is sufficient to provide knot vectors, degrees, control point coordinates and trimming curve definitions of patches. Without further input, this information allows for the analysis of single-patch models and multi-patch models with matching discretization.

However, for general B-Rep models with trimmed patches and non-matching discretization, the solver must also be able to first process topology information, e.g. which faces need to be joined along which edge, and then to actually couple those faces/patches during analysis.

To achieve this, a B-Rep edge element formulation is prototypically implemented via the LS-DYNA user interface. The implementation of this B-Rep edge element can be divided into two parts: The first part is basically data processing, the second part is the implementation of the actual element formulation according to Section 3.3 and Section 3.4. The crucial aspects for the generation of B-Rep edge elements are the appropriate definition of their spatial extent and the determination of integration point locations on the master and slave patch via closest point projections in the geometry space. In the workflow presented here, B-Rep edge elements are entirely generated in the *CAD-Analysis Preprocessing* step including data on integration point and basis function level. The *Explicit IBRA* & *Translation Script* depicted in Figure 6.1 and implemented in Python [155] processes this data and translates it into an LS-DYNA readable input file. The resulting input for a fully defined B-Rep edge element implemented via the LS-DYNA user interface is given in Table 6.1. As can be seen, integration point weights and even evaluated basis function (derivative) values are provided. This kind of input is indeed not optimized for efficiency and thus not suitable for industrial applications, but keeps the implementation in the LS-DYNA Fortran user interface simple. It is furthermore worth noting that topology information is implicitly contained via the declaration of master and slave control point ids.

The *Explicit IBRA* & *Translation Script* also performs the preprocessing steps for the light control point stabilization, the local selective mass scaling scheme and the user-defined integration points. The latter enables using any kind of integration procedure, such as the AGIP [32] described in Section 2.7, in LS-DYNA. These three features are implemented via the LS-DYNA user interface as well. The corresponding input data are provided in Tables 6.2, 6.3 and 6.4.

Variable	# Entries	Description
brform	1	B-Rep edge element formulation ("0": Coupling condition, "1": Dirichlet boundary condition, "2": Neumann boundary condition)
pen	1	Penalty factor α (for *brform* = "0" and "1" only)
dofs	6	Active DOFs $\{x, y, z, rx, ry, rz\}$ ("0"/"1" for active/inactive)
vars	6	Prescribed values $\{x, y, z, rx, ry, rz\}$ (float values, for *brform* = "1" and "2" only)
nm, ns	1, 1	Number of master and slave control points
cpidm, cpids	*nm, ns*	Ids of master and slave control points
nip	1	Number of integration points (IPs)
wgts	*nip*	Integration point weights $\tilde{w}_k$ including $\tilde{J}_2$
shpm, shps	$nm \times nip$, $ns \times nip$	Master and slave basis function values at IPs $N_A^m(\xi_k, \eta_k)$, $N_B^s(\xi_k, \eta_k)$
dshpmdxi, dshpmdeta, *dshpsdxi, dshpsdeta*	$nm \times nip$, $ns \times nip$	Master and slave basis function derivatives at IPs $\frac{\partial N_A^m}{\partial \xi}(\xi_k, \eta_k)$, $\frac{\partial N_A^m}{\partial \eta}(\xi_k, \eta_k)$, $\frac{\partial N_B^s}{\partial \xi}(\xi_k, \eta_k)$, $\frac{\partial N_B^s}{\partial \eta}(\xi_k, \eta_k)$
tm1, tm2	*nip, nip*	Trimming curve tangent vector $\tilde{\boldsymbol{t}}$ on master side at IPs

Table 6.1: Input for B-Rep edge elements implemented via the LS-DYNA user interface.

Variable	# Entries	Description
spen	1	Stabilization penalty factor $\overline{\beta}$ (global)
msf	1	Mass scaling factor f^s for light control points
nlcp	1	Number of light control points (LCPs)
lcpid	*nlcp*	Ids of light control points
nscp	*nlcp*	Number of stable adjacent control points per LCP
scpid	$\sum_{A=1}^{nlcp}(nscp_A)$	Ids of stable adjacent control points
spent	*nlcp*	Control point specific stabilization penalty factor $\tilde{\beta}_A^{\text{disp}}$ (translations)
spenr	*nlcp*	Control point specific stabilization penalty factor $\tilde{\beta}_A^{\text{rot}}$ (rotations)

Table 6.2: Input for the light control point stabilization scheme implemented via the LS-DYNA user interface.

Variable	# Entries	Description
ncpt	1	Number of control points with mass scaling (translational mass)
ncpr	1	Number of control points with mass scaling (rotational mass)
cpidt	*ncpt*	Ids of control points with mass scaling (translational mass)
cpidr	*ncpr*	Ids of control points with mass scaling (rotational mass)
msft	*ncpt*	Control point specific mass scaling factor f_A^{disp} (translational mass)
msfr	*ncpr*	Control point specific mass scaling factor f_A^{rot} (rotational mass)

Table 6.3: Input for the local selective mass scaling scheme implemented via the LS-DYNA user interface.

Variable	# Entries	Description
npid	1	NURBS patch id
nel	1	Number of elements per patch
niptot	1	Total number of integration points per patch
nip	*nel*	Number of integration points per element
ipr	*niptot*	Integration point ξ-coordinate
ips	*niptot*	Integration point η-coordinate
wgt	*niptot*	Integration point weight $\bar{w}_k$ including $\tilde{J}_2$

Table 6.4: Input for the definition of user integration points in LS-DYNA.

6.4 Isogeometric analysis-aware modeling

Achieving a real benefit from an integrated IBRA-based CAD/CAE process does not only require appropriate tools, but also an appropriate and analysis-aware CAD modeling technique. The latter term *analysis-aware CAD modeling technique* is not restricted to recommendations on the parametrization of surfaces like maximum polynomial degree, minimum element size or continuity as discussed later in Section 7.3.1. It is rather concerned with the way how CAD models are generated and structured with regard to subsequent isogeometric analyses.

As already mentioned in the introduction chapter of this thesis, within industrial applications, the design and the analysis model will barely be completely identical, although theoretically possible with IGA. The three main reasons, in the author's opinion are:

- The design and the analysis model serve different purposes, each of which favors a slightly different model description. While design models need to exhibit all details necessary for collision analysis and subsequent manufacturing, analysis models require a parametrization that yields good approximation quality and an acceptable time step size in explicit analysis.
- In industrial CAD, even thin sheet metal components are modeled as hollow B-Rep volume models, i.e. as a volume only represented by its exterior surfaces. To make full vehicle (crash) simulations computationally feasible, body-in-white (BIW) components are commonly modeled as shell structures represented by the component's midsurface. Simply because of that reason, the design and the analysis model will already differ.
- In case components are not modeled as dimensionally reduced shells in the analysis, but as solids, the generation of a trivariate volume description from the hollow B-Rep model is required[1]. In that case the boundary representation may remain the same, but the model is enhanced with an additional volume discretization. Several approaches for generating trivariate spline-based solid descriptions from B-Rep models are proposed in the literature. These approaches may use immersed methods and structured spline technologies (for the Finite Cell Method see for instance [42] and for V-Reps see [156]) or boundary fitted (unstructured) spline technologies like T-splines, see [157].

Thus, simply because of these reasons, performing analysis *directly* on the CAD models we know today is not feasible. However, CAD/CAE integration is not about using only *one* model for design and analysis. It is rather about using *the same* design parameters, *the same* data base, *the same* feature-based modeling paradigm and about maintaining the connection between design and analysis instead of creating a "dead" and independent analysis model. In that sense, the concept of immersed methods suggests itself since it allows using the same feature-based data structure based on boolean trimming operations. By using immersed methods, either analysis-suitable midsurface shell models or trivariate solid models in active parametric relation to the actual B-Rep design model can be provided as a layer and result of the design process. Ideally, modifying the B-Rep design model, for instance changing the position or diameter of a hole, or the shape of a surface, would automatically update the analysis model.

For isogeometric B-Rep analysis on shells in particular, the design engineer would provide the midsurface right away with the actual B-Rep design model as an associated offset of either the outer or inner surface and perform the same boolean trimming operations on both descriptions. For most of the BIW components, the midsurface is uniquely defined and can thus be generated automatically in the CAD program. In this way, also many problems encountered with the post hoc construction of midsurfaces in probably different CAD kernels of postprocessors could be avoided. For isogeometric solid analysis, for instance using the isogeometric Finite Cell Method [42], the B-Rep model can be directly used as a "trimming surface" to define the analysis domain within a trivariate bounding box discretization.

Design modifications motivated through analysis results would then not be applied on the FEA model as done now, but right on the B-Rep model, maintaining synchronicity between the design and analysis model. Immersed models with a feature-based data structure independent of the underlying surface description would furthermore allow applying boundary conditions and connections between components directly on features such as holes or boundary edges uniquely identified by ids. In case design parameters are changed, these conditions and connections could be automatically applied to the same features. In current FEA models this is not possible (since such conditions are often applied to individual nodes that change if the mesh changes), unless the preprocessor includes a kind of feature detection algorithm and is able to artificially add metadata to the analysis model.

Such an analysis-aware modeling paradigm also considering guidelines w.r.t. the model discretization as proposed in Section 7.3.1, of course requires a little more effort (around 5–20 % as estimated by a BMW design engineer) in the geometric design phase, but will save a lot of time during the model generation process, currently taking several weeks for each of the multiple design phases.

[1] This step is aptly denoted as *model completion* in [17].

The integrated CAD/CAE process based on isogeometric B-Rep analysis presented in this thesis is focused on shell structures. However, it should again be noted that the concept behind IBRA and the integrated CAD/CAE process is not restricted to shells, and can thus also be extended to solid models – this would yield a complete solution for practical applications.

Chapter 7

Numerical examples

The numerical examples in this chapter aim at demonstrating the validity of the developments and findings presented within this thesis, in particular:

- The novel penalty-based B-Rep element formulation for Reissner-Mindlin shells with rotational DOFs;
- The enhanced B-Rep element formulation including constraints on the shell normals;
- The influence of penalty-based coupling and boundary conditions on the critical time step;
- The penalty-based light control point stabilization scheme;
- The local selective mass scaling approach for B-Rep elements.

To this end various benchmark problems reaching from linear elastic quasi-static to highly nonlinear dynamic elasto-plastic cases including contact are solved. Finally, the applicability of the proposed Explicit IBRA framework to industrial problems is demonstrated through explicit dynamic analysis of actual BMW vehicle component models.

For clarity, the examples solved in this chapter are categorized into (i) small deformation problems (Section 7.1), (ii) large deformation problems solved with light control point stabilization and the enhanced B-Rep element formulation (Section 7.2) and (iii) industrial problems (Section 7.3).

All models are generated with the workflow presented in Chapter 6 (Rhino – TeDA – Python – IBRA exchange format – LS-DYNA) and solved with LS-DYNA. IGA results are either visualized on the actual deformed NURBS geometry via TeDA in Rhino or on an auxiliary background finite element mesh via the postprocessor Animator [158]. The latter is also used to visualize FEA results.

Unless otherwise stated, all problems in this chapter are solved with (i) explicit dynamic analysis in LS-DYNA [45], (ii) the Reissner-Mindlin shell with rotational DOFs proposed in [73], (iii) $(p+1)\times(q+1)$ in-plane integration points for untrimmed elements, (iv) specific integration rules for trimmed element determined by the AGIP [32, 52] briefly explained in Section 2.7, (v) three out-of-plane integration points and (vi) one consistent penalty factor for translations and rotations.

Within this chapter E denotes the Young's modulus, E_H the tangent modulus, ν the Poisson's ratio, σ_y the yield strength, ρ the mass density, and h the shell thickness. For better comparability, the relative penalty factor $\alpha_r = \alpha/E$ is commonly used. If no units are specified, the values are provided in consistent units. Below, the term *critical time step* denotes the *initial* critical time step of the undeformed configuration.

7.1 Small deformation examples

7.1.1 Pinched cylinder

The pinched cylinder with rigid diaphragms is a popular benchmark problem of the obstacle course for linear shell analysis proposed by Belytschko et al. in [159]. In [73], Benson et al. solved this problem with an untrimmed model and the same Reissner-Mindlin shell formulation used in this thesis. Solving this linear elastic benchmark problem with trimmed multi-patch NURBS models shall confirm the correct formulation and implementation of

the standard B-Rep element formulation for Reissner-Mindlin shells with rotational DOFs proposed in Section 3.3 and [54]. Solving this intrinsically static problem as quasi-static with explicit analysis shall illustrate the relation between the penalty factor α and the critical time step size for coupling conditions; in Section 4.4 already the relation for Dirichlet boundary conditions is presented. The following results are already published in [54].

The problem description including material, model and load parameters is given in Figure 7.1. Due to the symmetric nature of this problem it suffices to only consider one eight of the cylinder. The corresponding symmetry and boundary conditions along the four edges are applied in a strong sense via single point constraints. As shown in Figure 7.1, the model is artificially split into two trimmed patches by a smaller cylinder with an axis of rotation in z-direction through point A. These two open knot vector patches with C^{p-1} continuity are only trimmed by the smaller cylinder and exhibit a discretization corresponding to 16×16 and 17×17 elements in the untrimmed case. During analysis, both patches are coupled via standard B-Rep edge elements. In order to achieve a quasi-static simulation, the load P is monotonically increased over a simulation time of $t_e = 0.1$.

The explicit analysis results for different polynomial degrees $p = q = 2$ to 5 are depicted in Figure 7.2. In Figure 7.2a, the displacement of the load application point A (top diagram) and the corresponding critical time step size (bottom diagram) are plotted versus the relative penalty factor α_r. As can be seen from the top diagram, the displacements for all degrees, except for the $p = q = 2$, converge towards the reference solution of $u = 1.8248 \times 10^{-5}$ [159] as the penalty factor increases. The fact that the displacements for the quadratic case converge towards the solution of a quadratic untrimmed model with 16×16 elements ($p = q = 2$ untr.) indicates that a finer discretization is required to achieve the reference solution, see also [73]. Regardless of that, all solutions in Figure 7.2a almost converged for $\alpha_r = 10^{-1}$. The bottom diagram confirms the trend observed for Dirichlet boundary conditions in Section 4.4. Again, one can consider basically two cases:

- Case I: For small penalty factors $\alpha_r << \alpha_r' \approx 10^0$, the critical time step[1] is independent of α, because the introduced penalty stiffness is small compared to the shell stiffness. For this case, the time step is entirely determined by the shell, see Eq. (4.23) in Section 4.4.1. Due to the presence of boundary elements in the model, the time step decreases with increasing degree, cf. Section 4.1 and Section 4.2. Because of the small penalty factor, the solution accuracy for Case I is poor.
- Case II: For larger penalty factors $\alpha_r >> \alpha_r' \approx 10^0$, the time step is determined by the penalty stiffness and decreases with a slope of $-1/2$ in the double-logarithmic diagram, see Eq. (4.25) in Section 4.4.1. The high penalty factor of this case yields high solution accuracy, but small time steps.

However, there is a feasible penalty range (highlighted in light blue) between these two cases in which α is sufficiently high ($> 10^{-1}$) to obtain accurate results and still low enough ($< 10^1$) to not or only slightly decrease the time step. This feasible penalty range shows that explicit analyses of trimmed penalty-coupled NURBS shells can be both accurate and, in terms of time step size, also efficient. The scaled deformed shape of a cubic NURBS model with $\alpha_r = 1$ is depicted in Figure 7.2b. The accurate results obtained for this example confirm the correct formulation and implementation of the standard B-Rep element formulation.

7.1.2 Plate dynamically loaded by a uniform pressure

The intention behind this benchmark example from [160] is to examine the behavior of the penalty-based standard B-Rep element formulation and trimmed multi-patch shell models in a highly dynamic problem including plasticity. Moreover, this problem shall assess the applicability of the local selective mass scaling approach proposed in Section 4.5. In [73], Benson et al. solved this benchmark problem with the same Reissner-Mindlin shell formulation used in this thesis, but with an untrimmed model. The following results, except for the considerations regarding mass scaling, are already published in [54].

The problem description of the simply supported plate under pressure load modeled with elastic-perfectly-plastic material behavior (material type 3 *MAT_PLASTIC_KINEMATIC in LS-DYNA) is provided in Figure 7.3. The plate model consists of two open knot vector patches with a discretization of 8×8 resp. 9×9 elements in the untrimmed case and maximum C^{p-1} inter-element continuity. The two patches are trimmed and coupled along a B-spline curve defined by the control points $P_1 = (-6, 2, 0)$, $P_2 = (-1, 3, 0)$, $P_3 = (4, 1, 0)$ and $P_4 = (6, -4, 0)$, see Figure 7.3. Boundary conditions are applied in a strong sense, i.e. by fixing the translational DOFs of the control points along the four outer edges. The uniform pressure load is applied instantaneously at $t = 0$ and held constant for $t > 0$. Since this problem

[1] For all benchmark examples in Section 7.1 and 7.2, the critical time step size is obtained via the maximum system eigenvalue and Eq. (2.67) without damping. The computed critical time step size turned out to coincide almost perfectly with the critical time step size obtained in numerical experiments, i.e. it is observed that only slightly larger time steps immediately cause instabilities, while time steps only a bit smaller never lead to instabilities. There are only a few rare cases, in which the simulation finishes without instabilities for time steps larger than the computed critical time step.

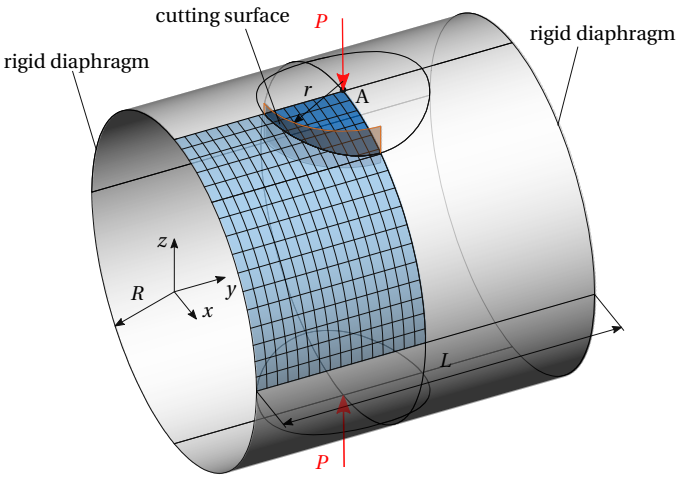

$E = 3 \times 10^6$
$\nu = 0.3$
$\rho = 7.33 \times 10^{-7}$
$L = 600$
$R = 300$
$r = 140$
$h = 3$
$P = 1$

Figure 7.1: Pinched cylinder: Problem description. The one-eight cylinder model consists of two trimmed patches split by a smaller cylinder of radius r. Figure taken from [54].

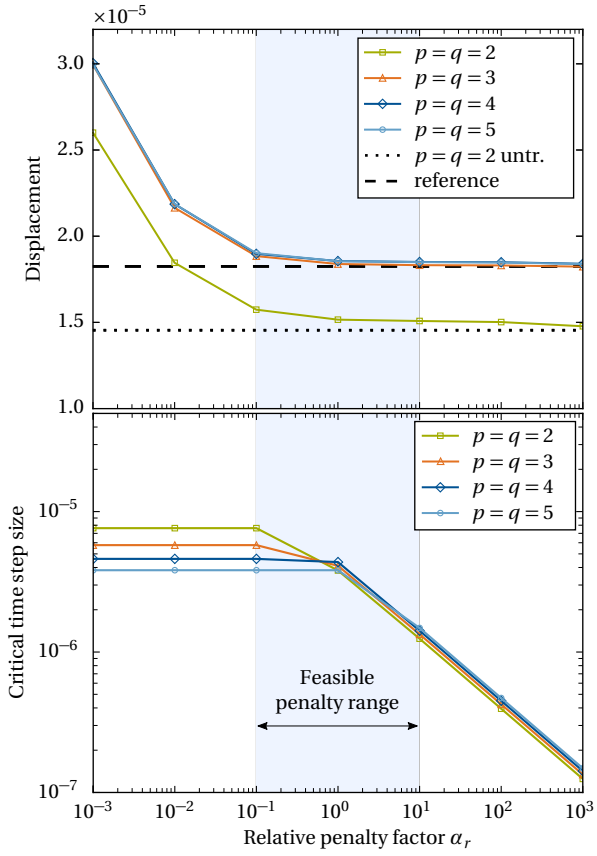

(a) Displacement of point A (top) and critical time step size (bottom) versus the relative penalty factor α_r for different polynomial degrees $p = q$. The light blue area indicates the feasible penalty factor range for achieving accurate results with a reasonable time step size.

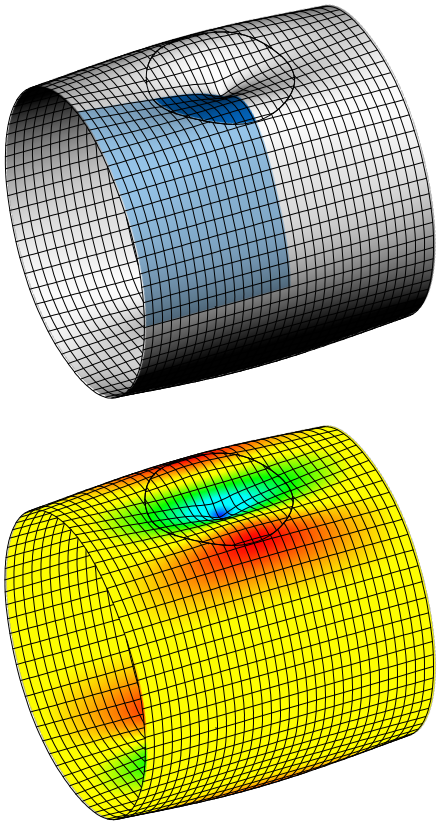

(b) Deformed shape of a configuration with cubic NURBS elements and a relative penalty factor $\alpha_r = 1$ with indicated patches (top) and z-displacement (bottom).

Figure 7.2: Pinched cylinder: Analysis results for a one-eighth cylinder model consisting of two trimmed patches with a non-matching discretization. Figure taken from [54].

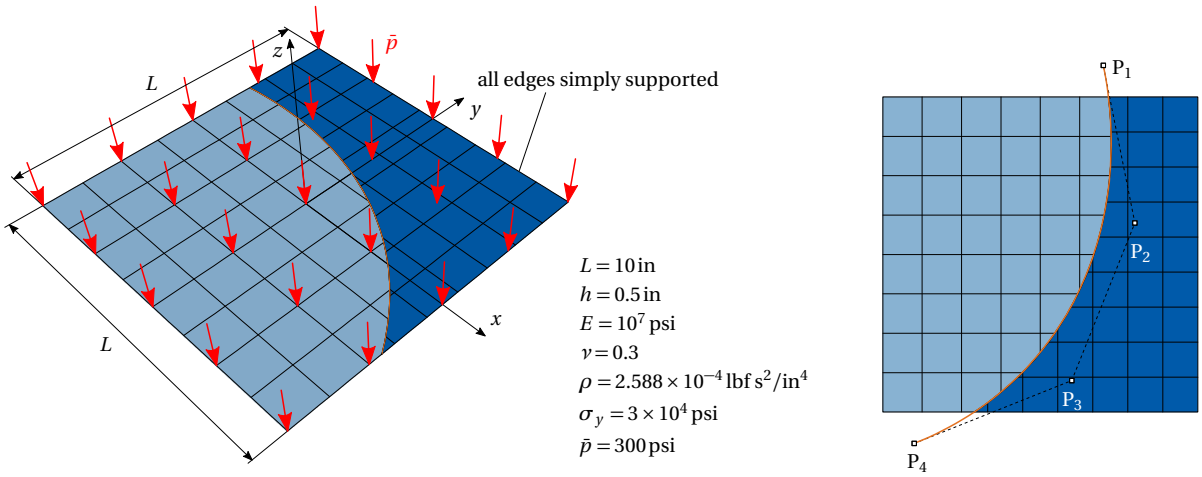

Figure 7.3: Plate dynamically loaded by a uniform pressure: Problem description. Figure taken from [54].

causes relatively small deformations, neither the enhanced B-Rep element formulation described in Section 3.4 nor the light control point stabilization from Chapter 5 is required and applied. Thus, the problem is solved as in [54].

The simulation results for all considered degrees $p = q = 2,3,4$ are depicted in Figure 7.4. Displacement responses of the patch center point over time for the quadratic, cubic and quartic case are shown in Figure 7.4a - 7.4c, respectively. The solutions for different penalty factors $\alpha_r = 10^{-3}$ to $\alpha_r = 10^2$ are compared with the corresponding solution of untrimmed models with a discretization of 8×8 elements, see also [73]. The relation between the penalty factor α and the critical time step size is depicted in Figure 7.4d, along with the deformed shape of a cubic configuration with $\alpha_r = 1$. The behavior is similar for all degrees $p = 2$ to 4: The higher the penalty factor, the smaller the deviation to the untrimmed reference solution. As can be seen, already the solutions for $\alpha_r = 1$ match the reference solution almost perfectly such that a further increase of α_r does not yield a significantly higher accuracy. However, what a further increase of α_r does yield is a decrease in critical time step size, see Figure 7.4d. As can be seen, a penalty factor of around $\alpha_r = 1$ gives both accurate results and an acceptable time step size[2].

Yet, the reduction in time step size can be prevented by using the local selective mass scaling approach presented in Section 4.5. Figure 7.5 visualizes the results of this mass scaling approach applied to configurations with cubic NURBS patches and penalty factors of $\alpha_r = 10^{-1}$ and $\alpha_r = 10^0$. For both configurations, the time step size without penalty coupling is inserted into Eq. (4.50) as the desired time step size to be achieved. For $\alpha_r = 10^{-1}$ only a minor reduction in time step size from 4.63×10^{-6} s (without penalty) to 3.13×10^{-6} s needs to be compensated by mass scaling. As Figure 7.5a shows, this only requires scaling of a few control points which are close to the patch boundaries and involved in B-Rep element formulations. The corresponding basis functions of these control points are *boundary* basis functions (see Section 4.1) and therefore have higher nodal eigenfrequencies than control points in the interior of the patch. This of course also applies to the outermost control points, but the translational DOFs of those control points are fixed by strong boundary conditions and therefore irrelevant for stability; the mass scaling approach considers this. For $\alpha_r = 10^{-1}$ this results in a total mass increase of $\Delta m = +1.7\%$ and a maximum added control point mass of $0.186\, m_{\text{max}}$, where m_{max} is the maximum control point mass in the model. For the configuration with $\alpha_r = 10^0$, on the other hand, a time step reduction from 4.63×10^{-6} s (without penalty) to 1.13×10^{-6} s needs to be compensated, which requires more control points to be scaled and by a higher amount. As shown in Figure 7.5b, now several control points in the vicinity of the trimming curve are scaled, all by a specific mass scaling factor depending on their nodal eigenfrequency. This results in a total mass increase of $\Delta m = +8.1\%$ and a maximum added control point mass of $0.34\, m_{\text{max}}$.

Scaling control point masses is of course a model modification and the question is to which extent this modification affects the solution, especially for highly dynamic problems with significant inertia effects. In order to assess this, the displacement responses with and without mass scaling are compared in Figure 7.6. While the deviation for $\alpha_r = 10^{-1}$ with a mass increase of $\Delta m = +1.7\%$ is negligible, a phase lag is apparent in the solution for $\alpha_r = 10^0$ with a mass increase of $\Delta m = +8.1\%$. However, since this is just a small academic benchmark example, no general statement regarding the acceptable amount of mass scaling can be given. For larger practical models, the portion of scaled

[2] The reason why the critical time step starts decreasing already for lower relative penalty factors compared to other examples is the relatively coarse discretization used here. Because of that, the shell stiffness/eigenfrequency is relatively low and the penalty stiffness/eigenfrequency starts to dominate already for smaller penalty factors, see Section 4.4.1 and Eq. (4.28).

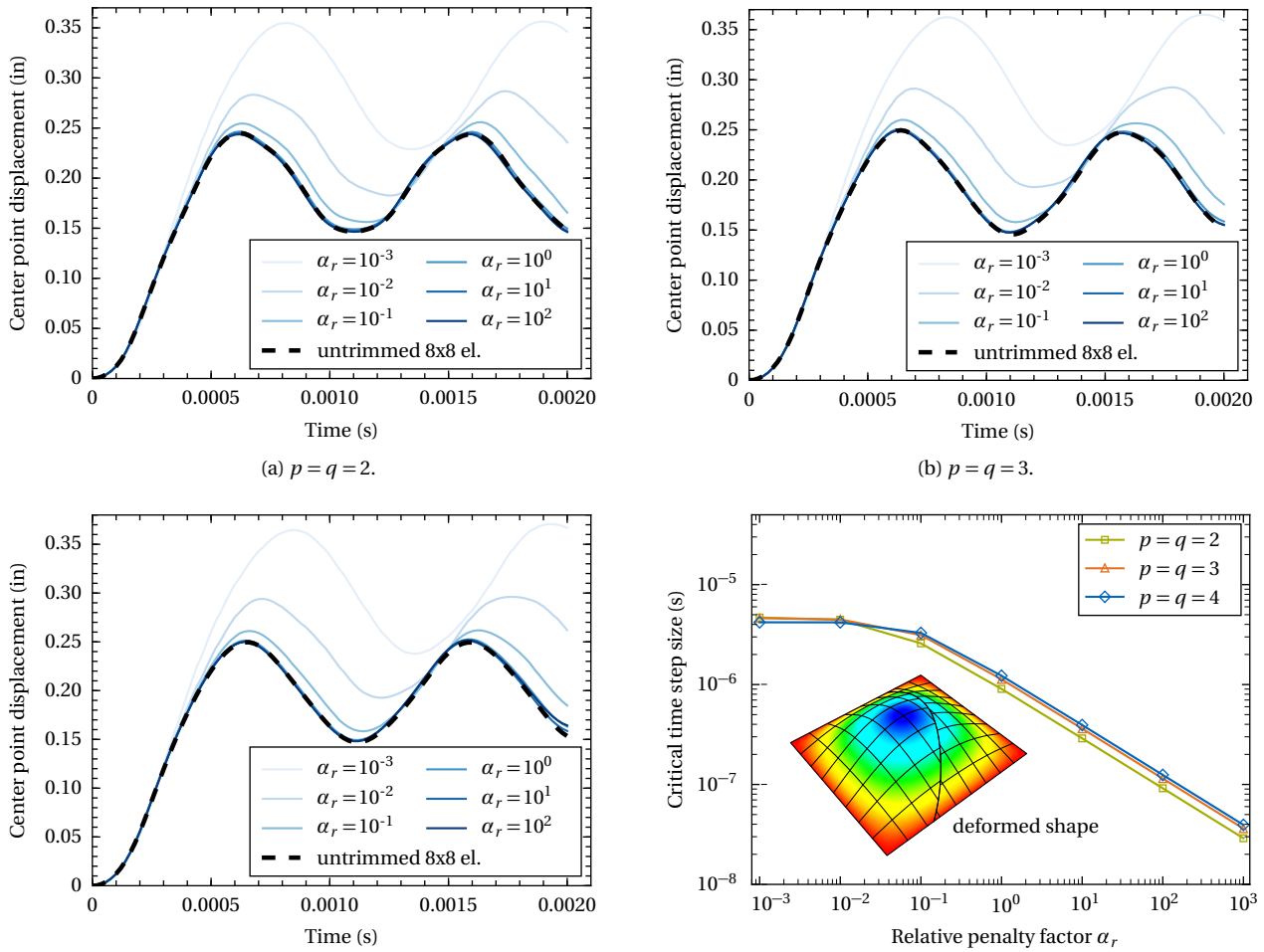

(a) $p = q = 2$.

(b) $p = q = 3$.

(c) $p = q = 4$.

(d) Critical time step size for different penalty factors.

Figure 7.4: Plate dynamically loaded by a uniform pressure: Center point displacement over time for different relative penalty factors α_r compared to the untrimmed solutions with 8x8 elements for quadratic, cubic, and quartic NURBS in (a)–(c). Critical time step size as a function of α_r in (d). Figure taken from [54].

control points (which are involved in B-Rep element formulations) and thus the effect on the solution is expected to be much smaller though[3].

In conclusion, this example shows that the standard B-Rep element formulation allows coupling trimmed NURBS patches both accurately and efficiently even in highly dynamic problems including plasticity. It is furthermore shown that a possible decrease in time step size due to penalty coupling can be removed effectively by means of local selective mass scaling of control points involved in B-Rep element formulations.

[3] It should be noted that the local selective mass scaling approach for B-Rep elements also scales rotational masses accordingly. However, as already mentioned in Section 2.6.2 and 4.5.3, rotational masses are scaled with relatively high factors by default such that the rotational modes do not restrict the time step [14, 45, 73, 131, 132]. Furthermore, the influence of the rotational control point mass on the solution accuracy is small compared to the influence of the translational control point mass. Thus, the focus of the discussions is on scaled translational masses.

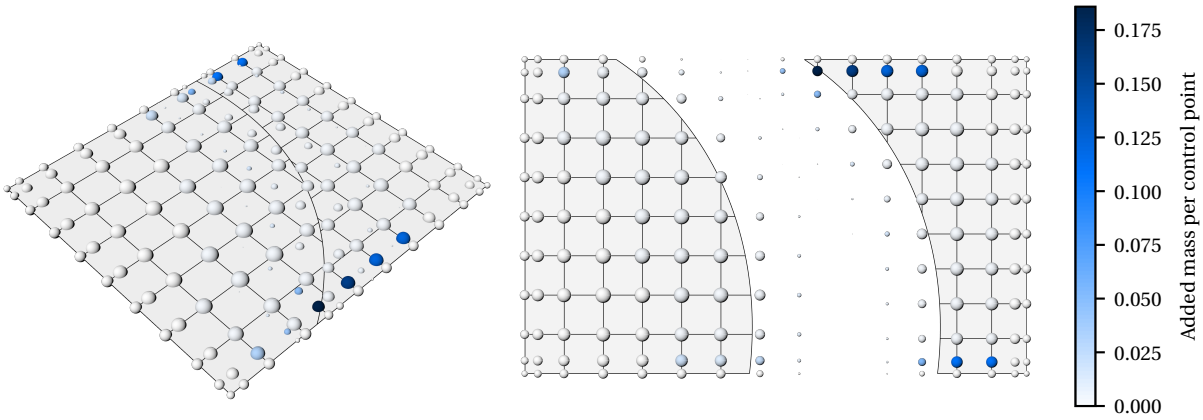

(a) Local selective mass scaling for $\alpha_r = 10^{-1}$ with $\Delta m = +1.7\%$.

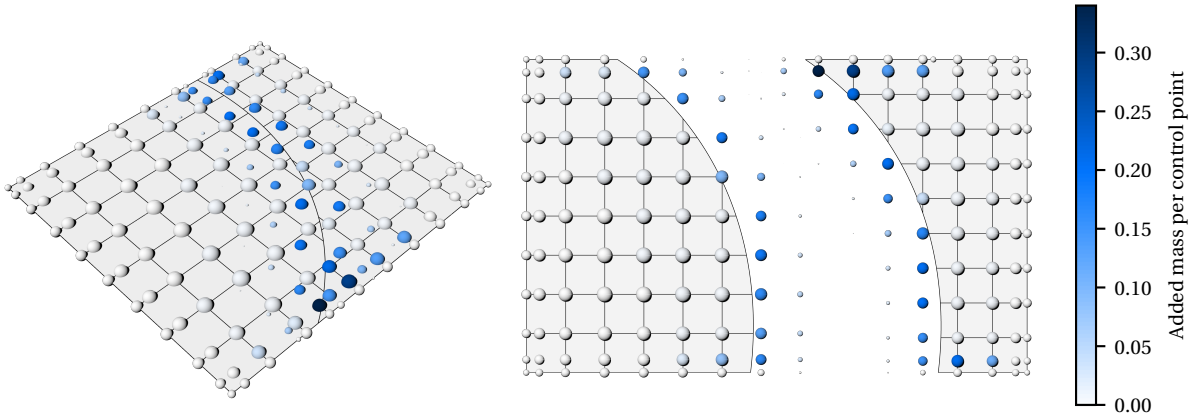

(b) Local selective mass scaling for $\alpha_r = 10^{0}$ with $\Delta m = +8.1\%$.

Figure 7.5: Plate dynamically loaded by a uniform pressure: Visualization of local selective mass scaling for cubic NURBS patches with $\alpha_r = 10^{-1}$ (a) and $\alpha_r = 1$ (b). The control point mass is scaled such that the critical time step without penalty coupling is reached. The added mass per control point indicated by the colorbar is normalized with respect to the highest unscaled control point mass. The sphere volume of the control points represents the control point mass.

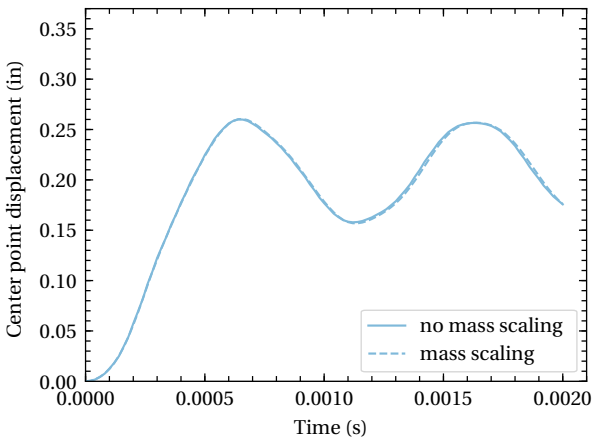

(a) $\alpha_r = 10^{-1}$.

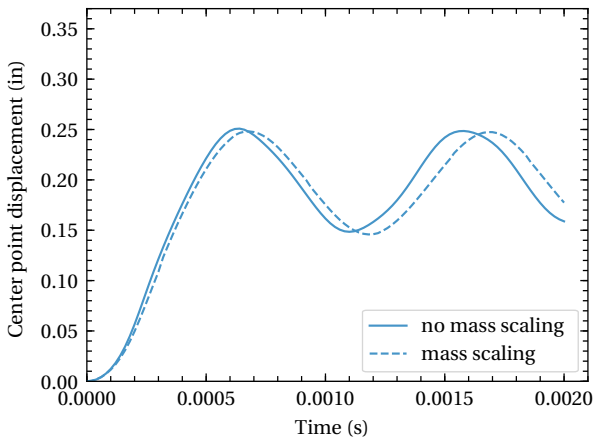

(b) $\alpha_r = 10^{0}$.

Figure 7.6: Plate dynamically loaded by a uniform pressure: Center point displacement response for the cubic configuration with and without local selective mass scaling for $\alpha_r = 10^{-1}$ (a) and $\alpha_r = 10^{0}$ (b).

7.2 Large deformation examples

7.2.1 Pinched cylinder with large deformations

The purpose of this pinched cylinder example with higher loads and large deformations [142] is to study: (i) The ability of Explicit IBRA to solve problems with large deformations and nonlinear snap-through behavior modeled through penalty-coupled trimmed NURBS shells, (ii) the validity and necessity of the enhanced B-Rep element formulation presented in Section 3.4, (iii) the effectiveness of the light control point stabilization proposed in Chapter 5 and (iv) the applicability of the local selective mass scaling approach proposed in Section 4.5.

In [142] this problem is solved through an implicit static analysis without inertia effects. It is worth noting that performing an explicit dynamic analysis with inertia effects causes significant oscillations after the snap-through which are not apparent in the implicit static reference solution.

This benchmark example was previously solved with Explicit IBRA in [54], but with a trimming configuration that avoided small trimmed elements and thus the necessity of light control point stabilization. Furthermore, with the trimming configuration in [54] accurate results were obtained without constraints on the shell normals, i.e. with the standard instead of the enhanced B-Rep element formulation. However, the trimming configuration used here, see Figure 7.7, involves small trimmed elements and therefore requires stabilization of light control points. Moreover, as shown below, more accurate results are obtained with the enhanced B-Rep element formulation.

The problem setup is described in Figure 7.7. As in the previous pinched cylinder example, only one eighth of the cylinder is modeled with corresponding symmetry boundary conditions applied in a strong sense. A smaller cylinder with an axis of rotation in z-direction through point A splits the model into two patches. These two patches with C^{p-1} continuity are generated from open knot vectors and exhibit a discretization corresponding to 32×32 and 33×33 elements in the untrimmed case. This relatively fine discretization is required to accurately capture the nonlinear snap-through behavior. During analysis, both patches are coupled via enhanced B-Rep edge elements. The load P is linearly increased to $P_{\max}$ over the simulation time of $t = 0.1$.

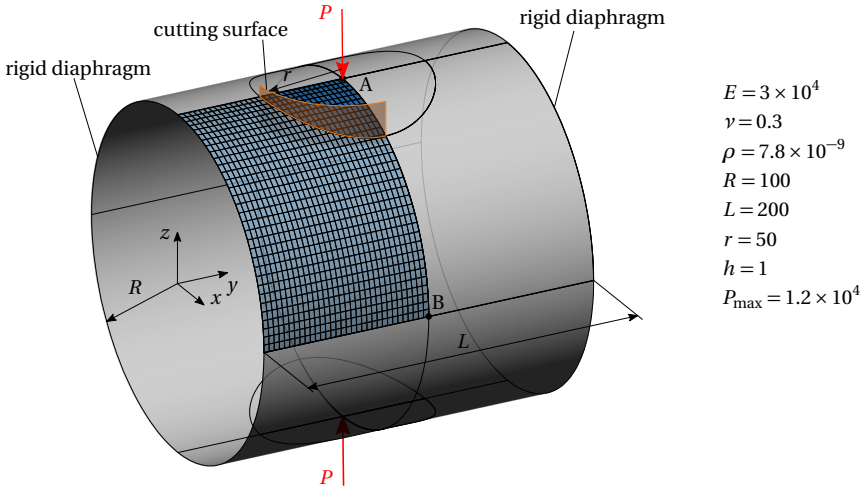

Figure 7.7: Pinched cylinder with large deformations: Problem description.

The force-deformation curves of the pinch force P versus the radial deflections of points A and B for a model with cubic elements and varying penalty factors are plotted in Figure 7.8a. For comparison, Figure 7.8a also provides an explicit dynamic FEA solution with 64×64 Belytschko-Tsay elements (FE ref) as well as implicit static (IGA stat) and explicit dynamic (IGA ref) solutions of an untrimmed IGA model with 32×32 cubic elements.

From Figure 7.8a it can be seen that the explicit solutions oscillate around the implicit static solution due to the inertia effects appearing after the snap-through. The reference solutions obtained through explicit IGA and FEA match very well. The solutions involving trimming and coupling (in blue) converge towards the reference IGA solution as α_r increases. For $\alpha_r \geq 10^{-1}$ the solutions are hardly distinguishable and almost perfectly match the reference IGA solution. In Figure 7.8b the initial critical time step size is plotted as a function of the penalty factor α_r. In this example the critical time step is practically independent of the penalty factor until $\alpha_r = 10^0$ and only starts decreasing for higher penalty factors. Comparing the results from Figure 7.8a and 7.8b, shows that accurate solutions are obtained without a (significant) restriction in time step size for $\alpha_r = 10^{-1}$ to $\alpha_r = 10^0$. The deformed shape of a configuration with $\alpha_r = 1$ depicted in Figure 7.9 shows smooth results without visible discontinuities across the coupling edge.

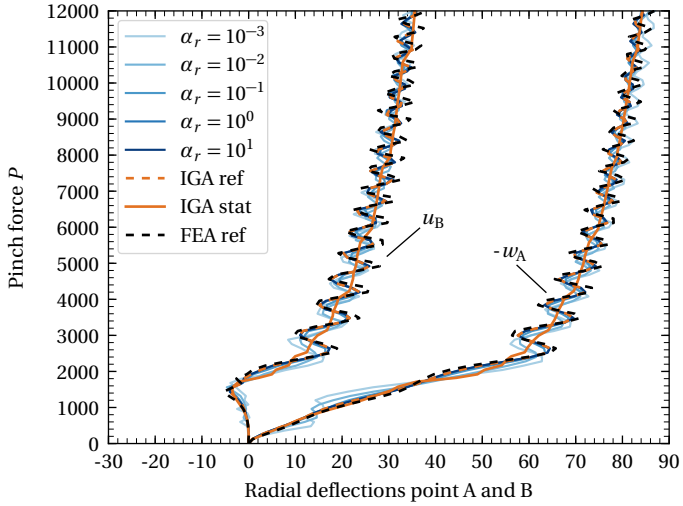

(a) Force versus radial deflection responses: Explicit dynamic solutions of the trimmed configuration with different penalty factors α_r (in blue) compared to explicit dynamic untrimmed IGA (IGA ref) and FEA solutions (FEA ref). The implicit static solution of an untrimmed IGA model (IGA stat) is also plotted for comparison.

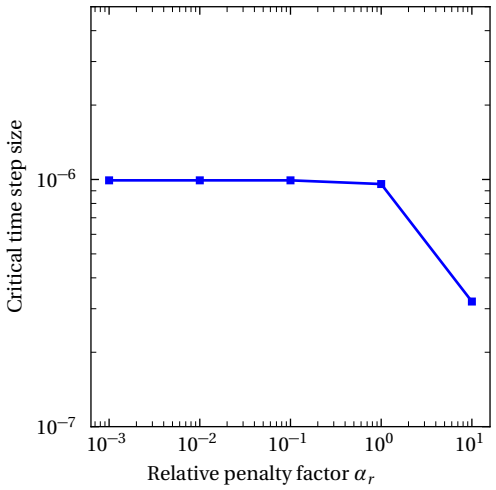

(b) Critical time step size as a function of the relative penalty factor α_r.

Figure 7.8: Pinched cylinder with large deformations: Accuracy and critical time step size for a model with cubic elements and different penalty factors α_r.

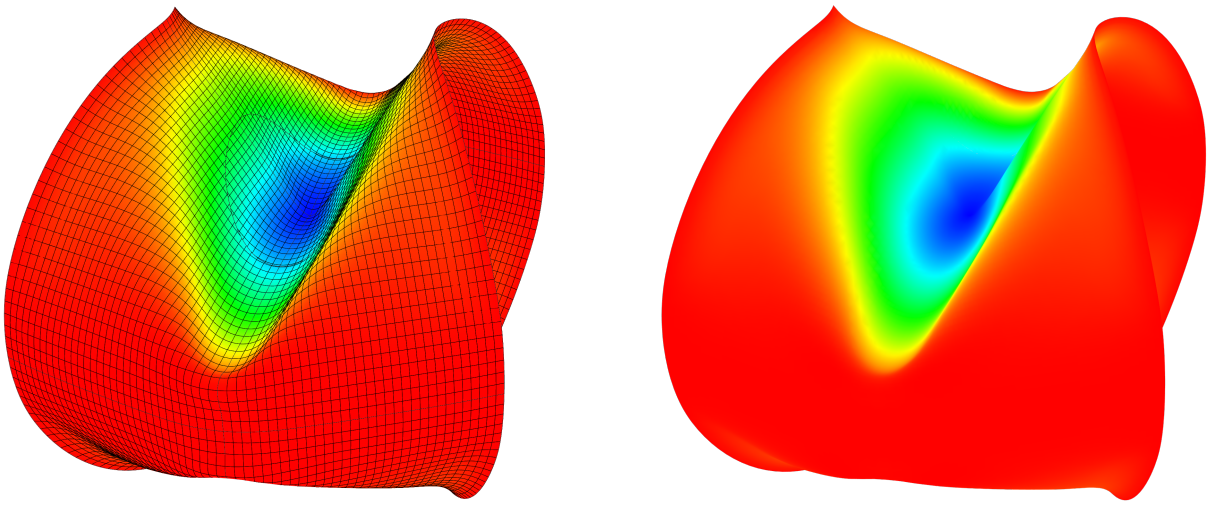

(a) (b)

Figure 7.9: Pinched cylinder with large deformations: Deformed shapes of a configuration with $\alpha_r = 1$ at $t = 0.1$ with (a) and without indicated knot lines (b). The color plot indicates z-displacements.

In order to achieve such accurate and stable results two measures are required: (i) the use of the enhanced B-Rep element formulation including coupling of shell normals as described in Section 3.4 and (ii) stabilization of light control points with the approach presented in Chapter 5. In Figure 7.10 results obtained with the standard and the enhanced B-Rep element formulation are compared. As can be seen from Figure 7.10a, the force-deflection response without coupling of shell normals (standard) deviates significantly from the reference solution. Until a force P of around 1000, the response is in good agreement with the reference solution, but then appears to be stiffer which causes the snap-through to occur later. The reason for this is a kink along the coupling edge as shown in the top image of Figure 7.10b. With constraints on the shell normals (enhanced) this discontinuity along the coupling edge can be avoided, see the bottom image of Figure 7.10b. Due to this postponed snap-through, the subsequent oscillations show larger magnitudes.

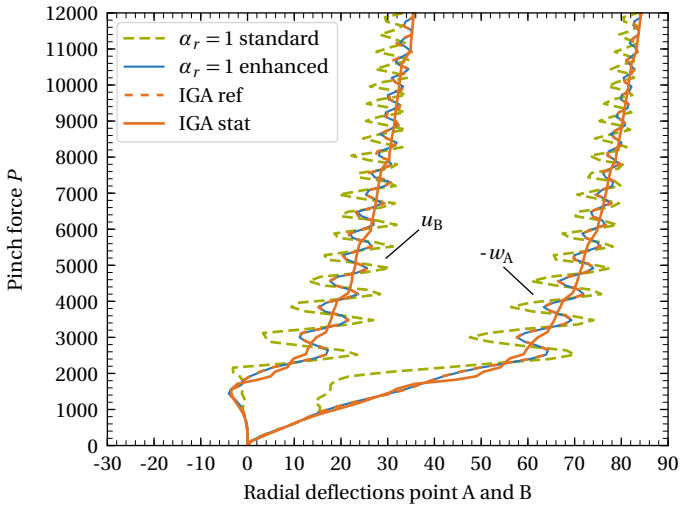

(a) Force versus radial deflection responses: Solutions without (standard) and with constraints on the shell normals (enhanced) are compared to explicit dynamic (IGA ref) and implicit static (IGA stat) solutions of untrimmed models.

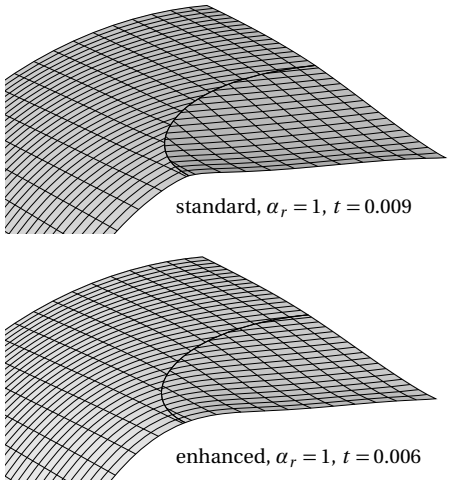

(b) Comparison of deformed shapes: The standard B-Rep element formulation (top) yields a kink along the coupling edge, while the enhanced formulation (bottom) achieves G^1 continuity.

Figure 7.10: Pinched cylinder with large deformations: Solutions with the standard and the enhanced B-Rep element formulation, clearly showing the necessity for enhanced B-Rep elements in this example.

The necessity for stabilizing light control points caused by small trimmed elements is shown in Figures 7.11 and 7.12. In Figure 7.11 deformed shapes including control points of simulations with and without stabilization are visualized. Again, all control points with a mass lower than 1 % of the maximum control point mass of the respective patch are considered as light control points ($C_{\text{th}} = 0.01$, see Section 5.3.2). For the stabilization, a global penalty factor of $\bar{\beta} = 0.01$ and a local mass scaling factor of $f^{\text{s}} = 10$ are used, see Section 5.3.5 and 5.3.6, respectively. Figure 7.12 depicts the displacement and rotation error measures proposed in Section 5.5. These error measures basically indicate how well the light control point constraints for displacements and rotations are fulfilled, see Eqs. (5.45) and (5.46). For explicit analysis without stabilization, the displacements and rotations of light control points grow quickly towards infinite values, causing the analysis to become unstable already at around $t = 0.004$. The analysis with stabilization, on the other hand, finishes as expected and produces accurate results. The error measures for the stabilized configuration in Figure 7.12 remain at a level of around 10^{-2}, confirming the successful stabilization. Here, it is worth recalling that an error of $e^{\text{disp}} \approx 10^{-2}$ indicates that the displacement of a light control point deviates from its estimated reference position by around 1 % of the maximum element length of the model on average. Moreover, an error of $e^{\text{rot}} \approx 10^{-2}$ indicates that the rotation of a light control point deviates from its estimated reference rotation by around 1 % of a full rotation (2π) on average.

Finally, the performance of the local selective mass scaling approach proposed in Section 4.5 shall be assessed. As mentioned above, in this example accurate results are obtained for penalty factors that do not cause a significant reduction in time step size ($\alpha_r = 10^{-1}$ to $\alpha_r = 10^{0}$). Nevertheless, for demonstration reasons, a penalty factor of $\alpha_r = 10^{1}$ is chosen, which causes the critical time step to reduce from 9.92×10^{-7} to 3.21×10^{-7}. The aim now is to apply local selective mass scaling such that a stable analysis with $\alpha_r = 10^{1}$ *and* the original time step of 9.92×10^{-7} can be performed.

The result of the local selective mass scaling approach is depicted in Figure 7.13, where the control points are colored according to their added mass normalized by the maximum control point mass of the model. The control point volume is directly proportional to the control point mass. As visible, control points in the vicinity of the coupling edge are specifically scaled according to their nodal eigenfrequencies. In this case, local selective mass scaling leads to a maximum added control point mass of 3.1 m_{max} and a total mass increase of $\Delta m = +16\%$. Figure 7.14 shows the effect of this mass increase on the solution accuracy. Until the snap-through inertia effects do not play a significant role and the results with and without mass scaling therefore coincide perfectly. After the snap-through the solution with mass scaling oscillates slightly slower, but with a similar magnitude and still around the implicit static solution. Thus, in this example, local selective mass scaling allows recovering the desired time step size without a significant deterioration of solution accuracy.

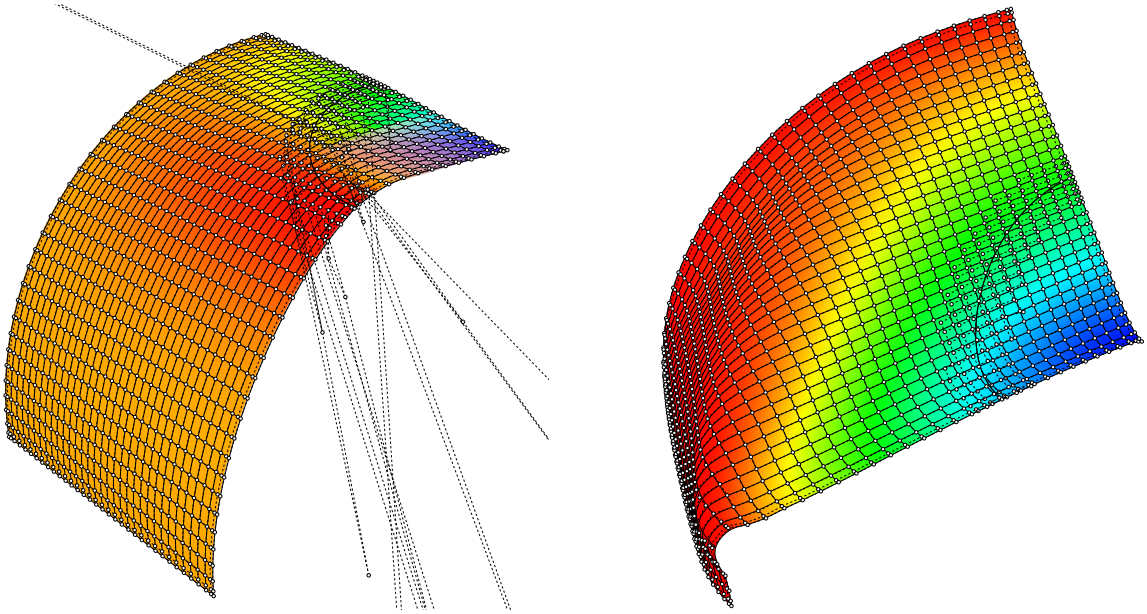

(a) Without light control point stabilization, $t = 0.004$.

(b) With light control point stabilization, $t = 0.1$.

Figure 7.11: Pinched cylinder with large deformations: Comparison of analysis results without and with light control point stabilization. Control points and control nets are visualized by black circles with white filling and dashed lines, respectively. The analysis without stabilization in (a) becomes unstable after $t = 0.004$, which can be seen from the extremely high displacements of light control points. The stabilized solution in (b) finishes and the stabilized light control points behave as intended ($\bar{\beta} = 0.01$, $f^{\mathrm{s}} = 10$, $C_{\mathrm{th}} = 0.01$).

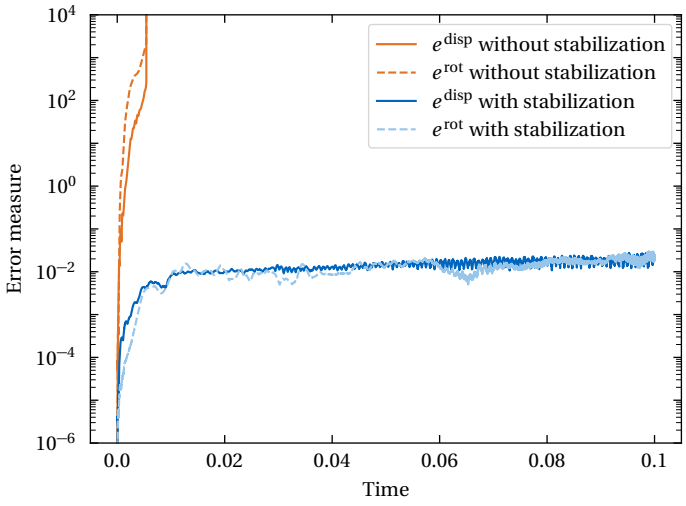

Figure 7.12: Pinched cylinder with large deformations: Comparison of displacement and rotation error measures for solutions without and with light control point stabilization ($\alpha_r = 1$, $\bar{\beta} = 0.01$, $f^{\mathrm{s}} = 10$, $C_{\mathrm{th}} = 0.01$)

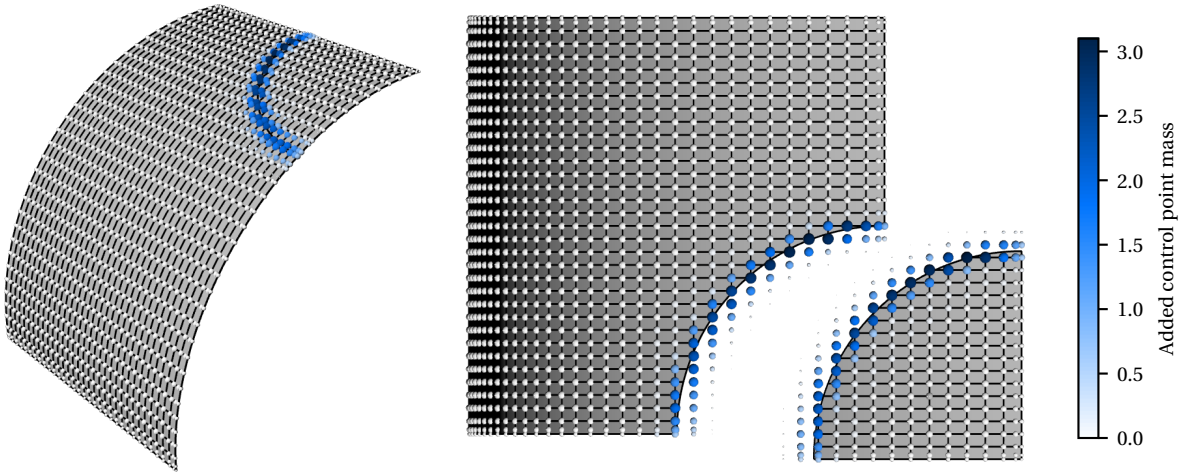

Figure 7.13: Pinched cylinder with large deformations: Results of the local selective mass scaling approach for increasing the critical time step of a configuration with $\alpha_r = 10$ from 3.21×10^{-7} to 9.92×10^{-7} (+309%). The added mass per control point indicated by the colorbar is normalized with respect to the highest unscaled control point mass. The sphere volume of the control points represents the control point mass.

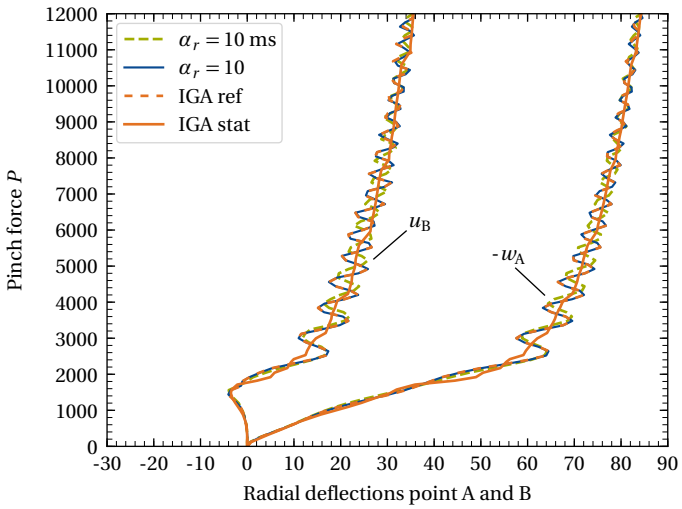

Figure 7.14: Pinched cylinder with large deformations: Comparison of force versus radial deflection responses for explicit analysis with ($\alpha_r = 10$ ms) and without ($\alpha_r = 10$) mass scaling as depicted in Figure 7.13. Explicit dynamic (IGA ref) and implicit static (IGA stat) solutions of untrimmed models are plotted for comparison.

To conclude, this pinched cylinder example shows the ability of Explicit IBRA to accurately solve large deformation problems with penalty-coupled trimmed NURBS shells and without a (significant) reduction in time step size. Furthermore it shows that:

- Coupling translations and rotations along the coupling edge as done in [54] may not always be sufficient for Reissner-Mindlin shells with rotational DOFs. Additionally coupling shell normals based on translational DOFs via the enhanced B-Rep element formulation yields higher accuracy and robustness.
- Light control points caused by small trimmed elements may lead to stability problems in explicit analysis. The light control point stabilization method proposed in this thesis is able to resolve this issue and enables stable explicit analysis of high accuracy without a reduction in time step size.
- Local selective mass scaling is an effective way to eliminate a possible time step reduction caused by penalty-based B-Rep elements, while keeping the added mass and the impact on the solution low.

7.2.2 Dynamic buckling of an energy absorbing tube

This benchmark problem shall demonstrate the applicability of Explicit IBRA and penalty-coupled trimmed NURBS shells to highly nonlinear and dynamic crash-type problems including large deformations, elasto-plastic material behavior and contact. This energy absorbing tube example shall furthermore highlight the importance of the enhanced B-Rep element formulation (with coupling constraints on the shell normals) and the light control point stabilization scheme. The latter becomes relevant because the tube is now modeled with cubic instead of quadratic NURBS elements as in [54]; the higher the degree, the more control points have support on trimmed elements and the higher is the probability of instabilities to be caused by light control points.

The problem setup is described in Figure 7.15. Model dimensions, material properties and boundary conditions are similar to the buckling square tube solved in [44, 73, 161]. However, in order to highlight the superior modeling abilities of NURBS compared to linear finite elements, the edges of the present model are rounded with a radius r. For the analysis, only a quarter of the double-symmetric problem is modeled with the corresponding symmetry and boundary conditions applied in a strong sense via single point constraints. The motion of the tube's top edge is prescribed by a constant velocity in z-direction. A tilted plane splits the quarter tube into an upper and a lower part modeled by trimmed patches with a discretization corresponding to 30×40 and 33×43 elements in the untrimmed case, respectively. Dynamic buckling of the tube is triggered by a small perturbation of $\pm 0.05\,\text{mm}$ applied to control points at $z = h_\text{p} = 64\,\text{mm}$ on both faces ($+0.05\,\text{mm}$ in x-direction on the y-z-face and $-0.05\,\text{mm}$ in y-direction on the x-z-face). The material behavior is defined as elasto-plastic with linear plastic hardening and modeled with material type 3 *MAT_PLASTIC_KINEMATIC in LS-DYNA. To consider self-contact the standard single surface contact algorithm in LS-DYNA [161] is applied to an auxiliary background mesh with $p \times q$ linear finite elements per NURBS element. The integration point locations and weights for trimmed elements are determined by the point elimination algorithm [43], firmly implemented in LS-DYNA.

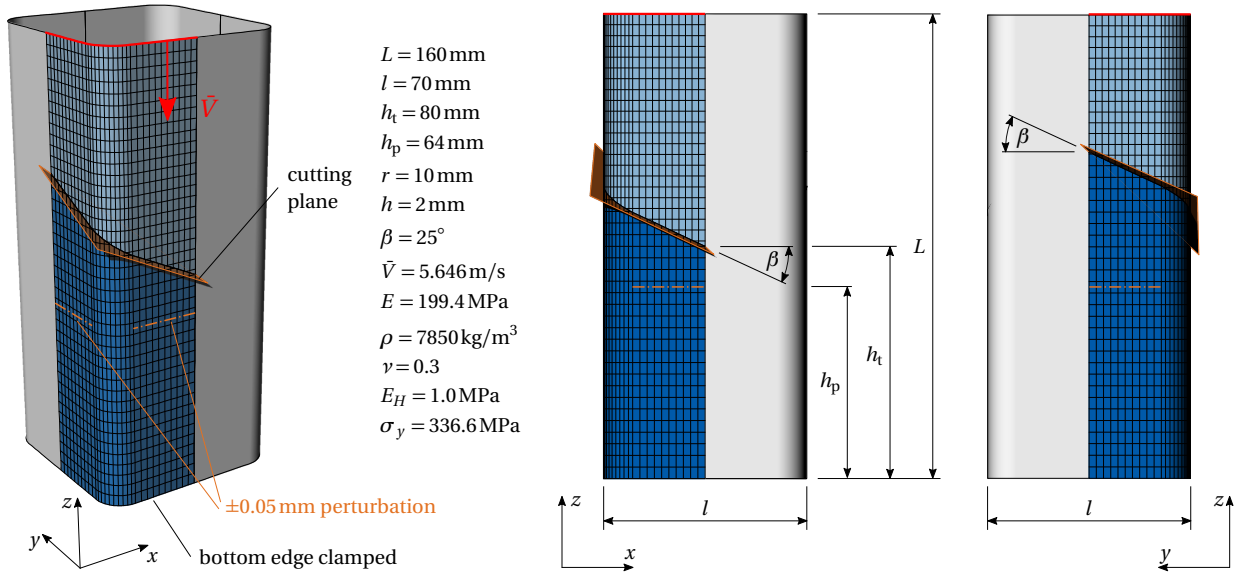

Figure 7.15: Dynamic buckling of an energy absorbing tube: Problem description and mesh. The two patches are discretized with meshes corresponding to 30×40 (bottom patch) resp. 33×43 elements (top patch) in the untrimmed case. Figure similar as in [54].

Figure 7.16 depicts the dynamic buckling process of a configuration with $\alpha_r = 1$ via a sequence of six deformed shapes. Even though the introduced perturbation is relatively small, the buckling process is triggered as intended. Please note that this problem is highly sensitive to imperfections and that even minor variations in the discretization are sufficient to alter the folding pattern. Although a varying discretization, trimming and coupling are indeed such imperfections, the resultant force response in Figure 7.17a agrees very well with the response of an untrimmed model with 30×40 cubic elements. Also the deformed shapes at $t = 0.020\,\text{s}$ shown in Figure 7.17b are in good agreement. This confirms the validity and accuracy of Explicit IBRA and the underlying B-Rep element formulation for patch coupling.

However, in order to achieve such results, two measures are again required: (i) The enhanced B-Rep element formulation including coupling constraints on the shell normals and (ii) stabilization of light control points.

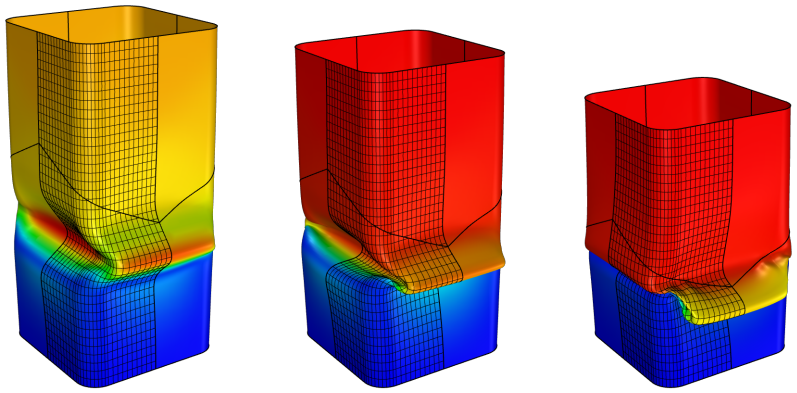

(a) $t = 0.002\,\mathrm{s}$ (b) $t = 0.004\,\mathrm{s}$ (c) $t = 0.008\,\mathrm{s}$

(d) $t = 0.012\,\mathrm{s}$ (e) $t = 0.016\,\mathrm{s}$ (f) $t = 0.020\,\mathrm{s}$

Figure 7.16: Dynamic buckling of an energy absorbing tube: Deformed shapes of a configuration with cubic NURBS elements and $\alpha_r = 1$. The color plot indicates total displacements (magnitude of the displacement vector).

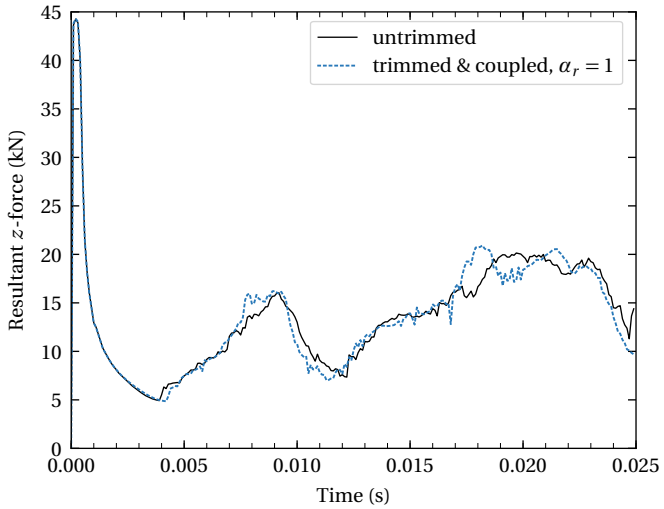

(a) Resultant z-force over time.

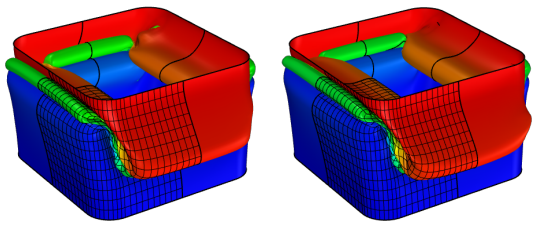

(b) Deformed shapes at $t = 0.020\,\mathrm{s}$. Untrimmed model (left) and trimmed, penalty-coupled model (right).

Figure 7.17: Dynamic buckling of an energy absorbing tube: Comparison of results between an untrimmed model with 30×40 cubic elements and a penalty-coupled trimmed model ($\alpha_r = 1$) with cubic elements and the mesh provided in Figure 7.15.

In Figure 7.18, the previously presented results are compared with the response of a configuration with the standard B-Rep element formulation, i.e. without constraints on the shell normals. As can be seen, the three responses are in good agreement until around $t = 0.0105\,\text{s}$, but then start to differ. The reason for this deviation is depicted in Figure 7.18b: For the configuration without the coupling constraints on the shell normals (left), the desired G^1 continuity between patches cannot be maintained. This leads to a distinct kink along the coupling edge, clearly visible when following the isolines across the coupling edge. Such coupling deficiencies obviously affect the folding pattern and the force response. The configuration with the shell normal coupling constraint (right), on the other hand, shows a smooth surface with no visible discontinuities.

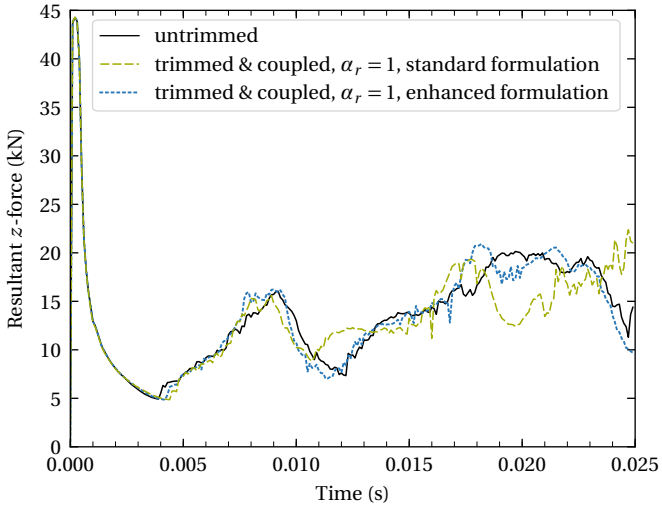

(a) Resultant z-force over time.

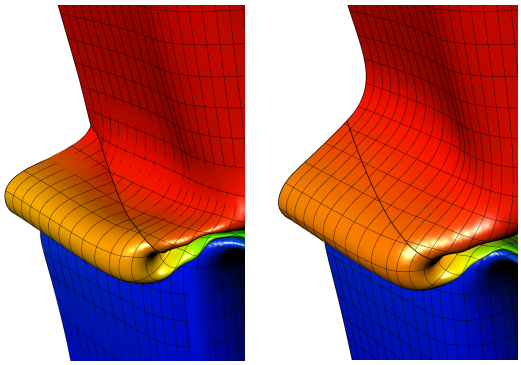

(b) Deformed shapes of configurations without (left) and with constraints on the shell normals (right) at $t = 0.0107\,\text{s}$.

Figure 7.18: Dynamic buckling of an energy absorbing tube: Comparison of results between penalty-coupled trimmed models ($p = q = 3$, $\alpha_r = 1$) with the standard and the enhanced B-Rep element formulation. The result for an untrimmed model with 30×40 cubic elements is plotted for comparison. Subfigure (b) shows deformed shapes at the moment ($t = 0.0107\,\text{s}$) when the force responses in (a) start to deviate significantly.

Simulation results of configurations without and with light control point stabilization are provided in Figure 7.19. The configuration without stabilization in Figure 7.19a shows light control points with unrealistic behavior and extremely high displacements. Over time this behavior propagates to adjacent control points until the entire simulation becomes unstable at around $t = 0.01\,\text{s}$. For the stabilized configuration shown in Figure 7.19a, on the contrary, light control points behave as intended and the simulation finishes. The corresponding error measures indicating the effectiveness of the stabilization are depicted in Figure 7.20. While the errors for the configuration without stabilization rise quickly, the errors for the stabilized configuration remain below a level of around 10^{-2}. The sudden increase of the displacement error e^{disp} at around $t = 0.01\,\text{s}$ can be explained as follows: At that time the fold of the top patch gets in contact with the area around the coupling edge, which leads to additional contact forces acting on light control points. The stabilization scheme is able to balance these additional contact forces, but the error slightly increases. This contact situation is also expected to be the main reason why this example requires higher stabilization parameters than other examples, i.e. a stabilization penalty factor of $\tilde{\beta} = 1.0$ and a light control point mass scaling factor of $f^{\text{s}} = 100$, resulting in a total mass increase of 1.1 %. The increased mass scaling factor of $f^{\text{s}} = 100$ is required to counterbalance the effect of added stabilization stiffness on the critical time step. Although a mass scaling factor of 100 may seem to be high, it should be noted that this scaling is only applied to light control points, which have a very low mass by definition. In fact, in this thesis a control point is only considered as a light control point if its mass is lower than 1 % of the maximum control point mass in the corresponding patch ($C_{\text{th}} = 0.01$). This means that in the worst case a light control point is scaled up to the mass of the heaviest control point. However, the average light control point mass in this example is only 0.13 % of the maximum control point mass of both patches.

This example allows drawing the following conclusions:

1. Explicit IBRA for trimmed multi-patch NURBS shells is able to accurately solve highly nonlinear, dynamic crash-type problems including large deformations, plasticity, structural instability and contact.
2. The enhanced B-Rep element formulation of RM shells comprising coupling conditions for translational DOFs, rotational DOFs and shell normals achieves excellent coupling accuracy even in extreme deformation cases.

3. The proposed light control point stabilization scheme enables robust explicit dynamic analysis of penalty-coupled trimmed NURBS shells with arbitrarily small elements, large deformations, plasticity and contact. Furthermore, this stabilization scheme does neither impair the solution quality nor the critical time step size.

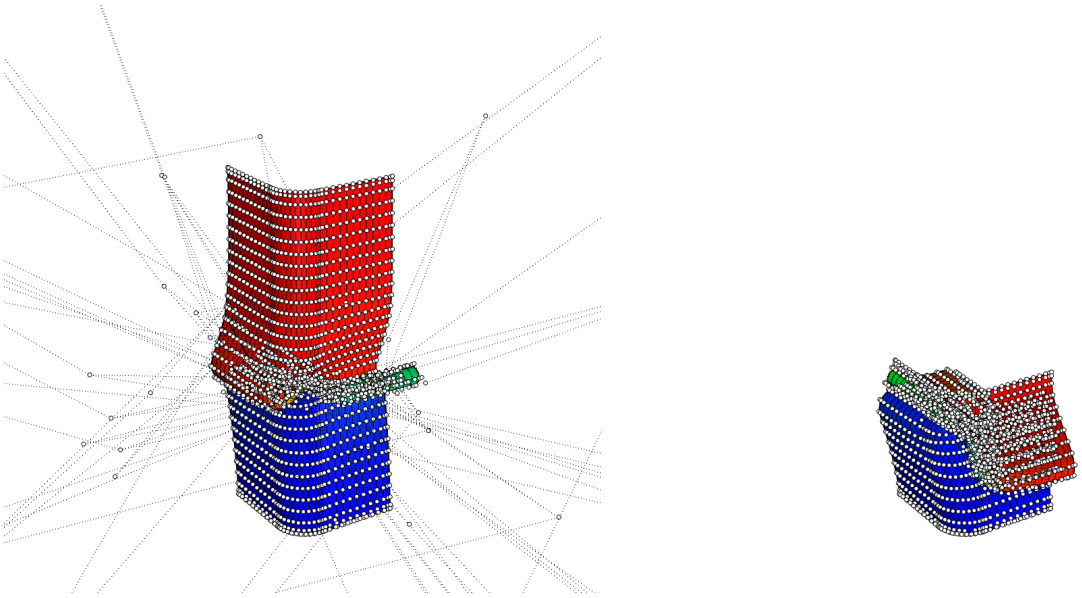

(a) Without light control point stabilization, $t = 0.009\,\mathrm{s}$.

(b) With light control point stabilization, $t = 0.02\,\mathrm{s}$.

Figure 7.19: Dynamic buckling of an energy absorbing tube: Comparison of analysis results without and with light control point stabilization. Control points and control nets are visualized by black circles with white filling and dashed lines, respectively. The analysis without stabilization in (a) becomes unstable after around $t = 0.01\,\mathrm{s}$, which can be seen from the extremely high displacements of light control points. The stabilized solution in (b) finishes and the stabilized light control points behave as intended ($\alpha_r = 1$, $\bar{\beta} = 1.0$, $f^{\mathrm{s}} = 100$, $C_{\mathrm{th}} = 0.01$).

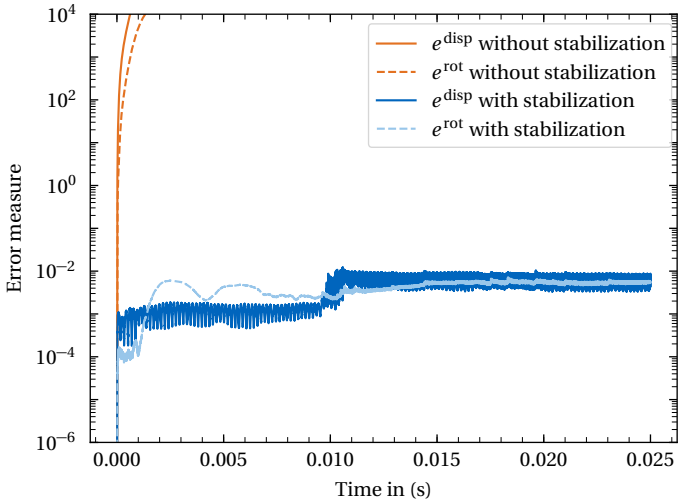

Figure 7.20: Dynamic buckling of an energy absorbing tube: Displacement and rotation error measures for simulations with and without light control point stabilization ($\alpha_r = 1$, $\bar{\beta} = 1.0$, $f^{\mathrm{s}} = 100$, $C_{\mathrm{th}} = 0.01$).

7.3 Industrial examples

In this final section, two actual BMW vehicle component models, namely the exterior skin and the reinforcement structure of an engine bonnet are considered. These industrial examples shall demonstrate the ability of Explicit IBRA and the related methods to solve explicit dynamic industry-type problems on trimmed multi-patch NURBS models.

7.3.1 Excursus on analysis-suitable CAD modeling within industrial applications

Before dealing with the actual numerical examples, this short excursus provides some remarks on analysis-suitable CAD modeling, crucial for the future industrial usage of IBRA.

At the time the bonnet models studied below were created, the BMW design engineers of course did not have analysis-suitability in mind, because for FEA completely new simulation models following well-defined modeling guidelines are generated anyway. To obtain accurate results in an efficient manner, IGA/IBRA models also need to fulfill certain IGA-specific modeling criteria. Thus, performing the analysis on the initial CAD models depicted in Figure 7.21a and Figure 7.31a, is not recommended although generally possible, see for instance [54]. Developing such IGA-specific modeling guidelines, vital for industrial applications of IGA, is subject of current research. Some guidelines models in explicit isogeometric (crash) analysis certainly have to follow are:

1. A prescribed minimum patch and element size to obtain reasonable time steps.
2. A maximum polynomial degree. In order to capture local deformations or local effects like wrinkling, the model requires a relatively fine discretization and a moderate polynomial degree. In surface patches with high polynomial degrees and high continuity (C^{p-1}), occasionally observed in industrial B-Rep models, local effects propagate due to the large support of basis functions. With the current integration rules using $p \times q$ or $(p-1)\times(q-1)$ integration points per element, a high polynomial degree furthermore becomes inefficient.
3. Preferably a uniform element size as well as uniform and maximum inter-element continuity.

Furthermore, the number of internal coupling edges can be easily reduced by merging patches obviously belonging to the same geometric surface. Another way to increase efficiency is to extend patches beyond their physical model boundaries and to subsequently trim off the time step restricting boundary elements, as shown in Section 4.2. So far, design engineers and CAD algorithms hardly considered these modeling aspects, because it was simply not necessary for the geometric representation. The bonnet exterior skin and the reinforcement structure depicted in Figure 7.21b and Figure 7.31b largely conform with the three guidelines described above. To achieve this, narrow and geometrically similar surface patches are merged and their polynomial degree of up to $p = 13$ is reduced to a maximum of $p = 4$. In a final step both models are refined by inserting internal knots with multiplicity $m_i = 1$ via a fully automated algorithm. Directly considering such modeling guidelines in future CAD models, will enable isogeometric analysis on models without or with a minimum number of modifications. That this is technically feasible is shown by the IGA capabilities recently implemented in the commercial preprocessor ANSA [162, 163].

7.3.2 Engine bonnet exterior skin

This example of a dynamically loaded bonnet exterior skin shall demonstrate that Explicit IBRA is able to achieve good results with a reasonable time step size and that both the light control point stabilization scheme and the local selective mass scaling approach for B-Rep elements are applicable to large problems with multiple trimmed patches.

The initial CAD model and the guideline-conforming analysis model are shown in Figure 7.21. The refined guideline-conforming bonnet model (half model due to symmetry) incorporating 10 trimmed NURBS patches, 2,714 active cubic and quartic shell elements[4] with an average element length of around 22 mm, and 1,122 B-Rep edge elements is depicted in Figure 7.22 along with the problem description. Clamped boundary conditions are applied in a weak sense via Dirichlet B-Rep elements along the outer edges. A uniform pressure distribution is instantaneously applied at $t = 0$ s and held constant afterwards. The material behavior is assumed to be linear elastic isotropic. In this example, the point elimination algorithm [43] is used for the numerical integration of trimmed elements. As a reference, the problem is also solved on the actual finite element model of the bonnet, consisting of 95,784 linear elements with an average element size of around 4 mm.

Figure 7.24 depicts the scaled deformed shape of the bonnet at $t = 0.10$ s, solved with the enhanced B-Rep element formulation, a penalty factor of $\alpha_r = 1$ and stabilized light control points. In this example, the application of weak

[4] Please note that for maximum inter-element continuity (C^{p-1}), multiple internal knots are removed. This step was not done in the bonnet model presented in [54]. Otherwise the models are identical.

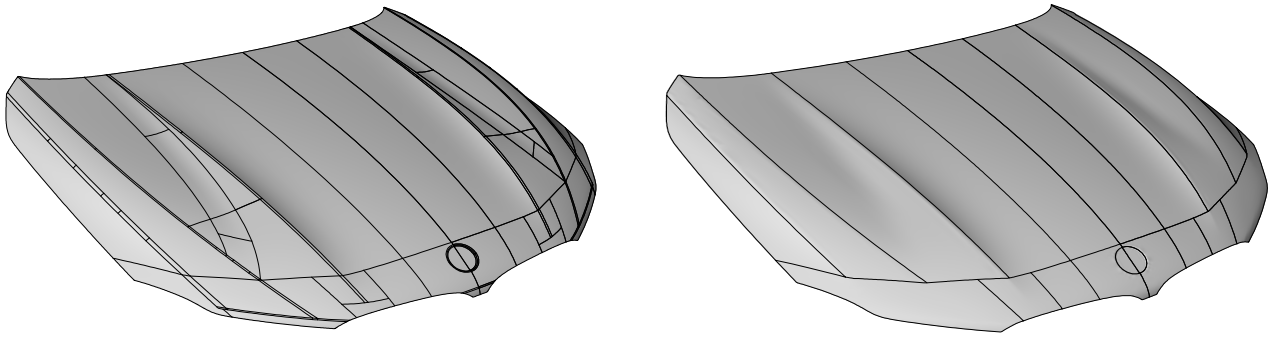

(a) (b)

Figure 7.21: BMW engine bonnet exterior skin: Initial CAD model (a) and guideline-conforming model (b). Surface patch boundaries are indicated by black lines. Figure taken from [54].

$L = 1547\,\text{mm}$ $H = 290.2\,\text{mm}$ $E = 2.1 \times 10^5\,\text{N/mm}^2$ $\rho = 7850\,\text{kg/m}^3$

$W = 1751\,\text{mm}$ $h = 1\,\text{mm}$ $\nu = 0.3$ $\bar{p} = 1 \times 10^{-3}\,\text{N/mm}^2$

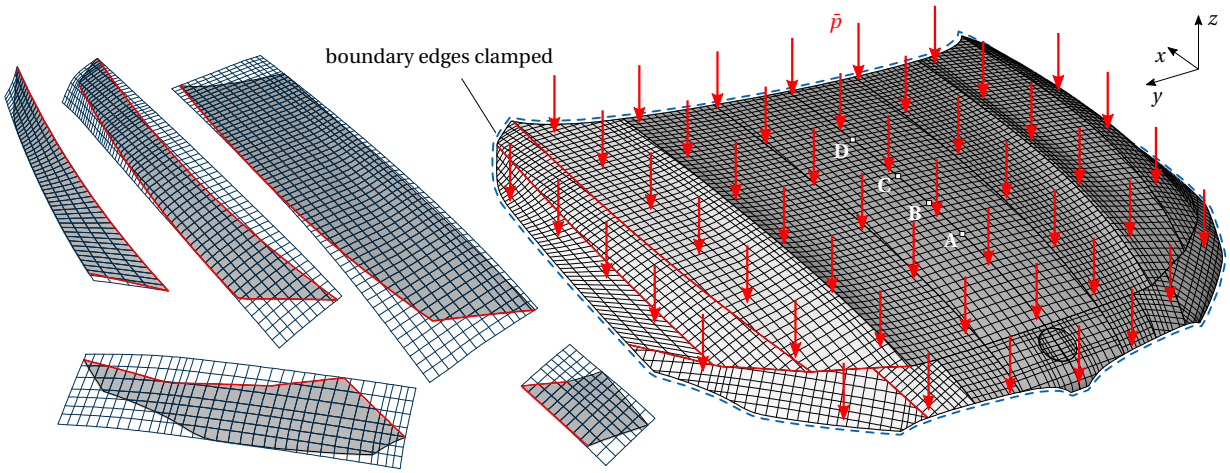

(a) Problem description and NURBS discretization: Clamped boundary edges are indicated by blue dashed curves. Points A–D are measurement positions. Five trimmed patches are exemplarily shown with their untrimmed configuration and coupling edges highlighted in red.

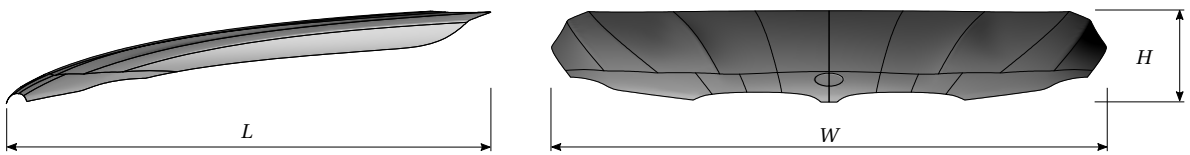

(b) CAD geometry and main model dimensions.

Figure 7.22: BMW engine bonnet exterior skin loaded by a uniform pressure: The guideline-conforming analysis model (half model) consists of 10 trimmed NURBS patches with 2,714 active cubic and quartic shell elements (average element length around 22 mm). Weak penalty and coupling conditions are applied via 1,122 B-Rep edge elements. Figure taken from [54] in a slightly modified form.

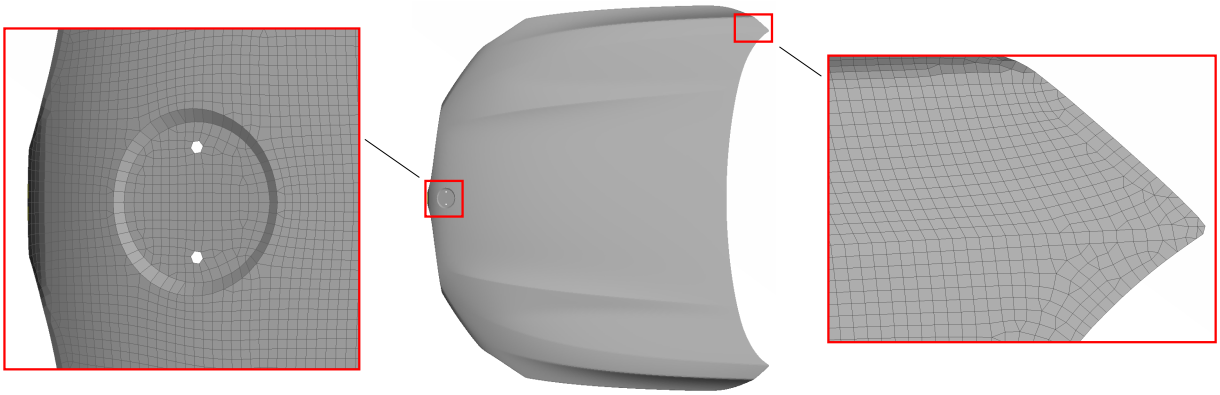

Figure 7.23: BMW engine bonnet exterior skin: Reference finite element model with a discretization of 95,784 linear elements (average element length around 4 mm). Figure taken from [54].

penalty-based boundary and coupling conditions via B-Rep edge elements reduced the critical time step size to 4.22×10^{-7} s; the minimum critical time step size of the individual shell elements would be 9.84×10^{-7} s. In Figure 7.25 the z-displacement response of the bonnet measured at the four points A–D shown in Figure 7.22a is plotted and compared with the FEA solution. Here, the goal is not to exactly reproduce the results obtained with the finely meshed FEA model, but to rather have an idea of whether the IGA results are reasonable or not. Despite the fact that the IGA model has a much coarser discretization and thus a stiffer behavior visible by the slightly faster response, the IGA and FEA solutions are in good agreement until around $t = 0.080$ s. Afterwards, the responses of both solutions drift apart noticeably. Still, this comparison shows that the results obtained through Explicit IBRA on the trimmed NURBS-based bonnet model are plausible. Figure 7.26 provides a comparison between the Explicit IBRA and the FEA results for the z-displacements at $t = 0.080$ s. For this comparison, the results of the NURBS-based IGA model are projected onto a background mesh with $p \times q$ finite elements per NURBS element and visualized in a standard postprocessing program.

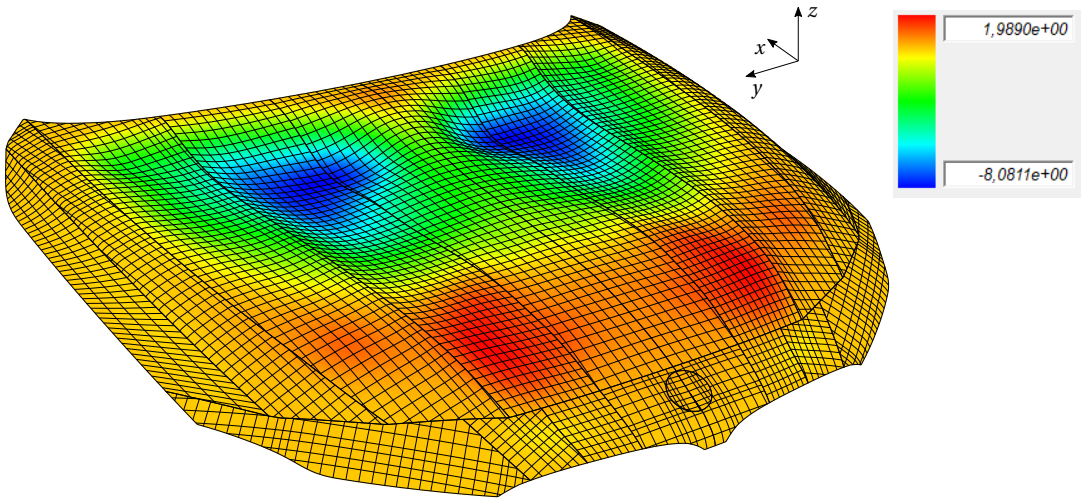

Figure 7.24: BMW engine bonnet exterior skin dynamically loaded by a uniform pressure: Scaled deformed shape of a configuration with $\alpha_r = 1$ (scale factor 10). The color plot indicates z-displacements in mm.

Compared to the problem presented in [54], the pressure load is doubled here. This leads to larger deformations, higher inertia effects, and hence requires a stabilization of light control points. Figure 7.27a depicts the deformed shape and the corresponding control points of an explicit analysis without light control point stabilization at $t = 0.026$ s, slightly before the entire simulation becomes unstable. Light control points with extremely high displacements are clearly visible. Figure 7.27b, on the other hand, shows the deformed shape and the corresponding control points of an explicit analysis solved with the penalty-based light control point stabilization scheme presented in this thesis. As

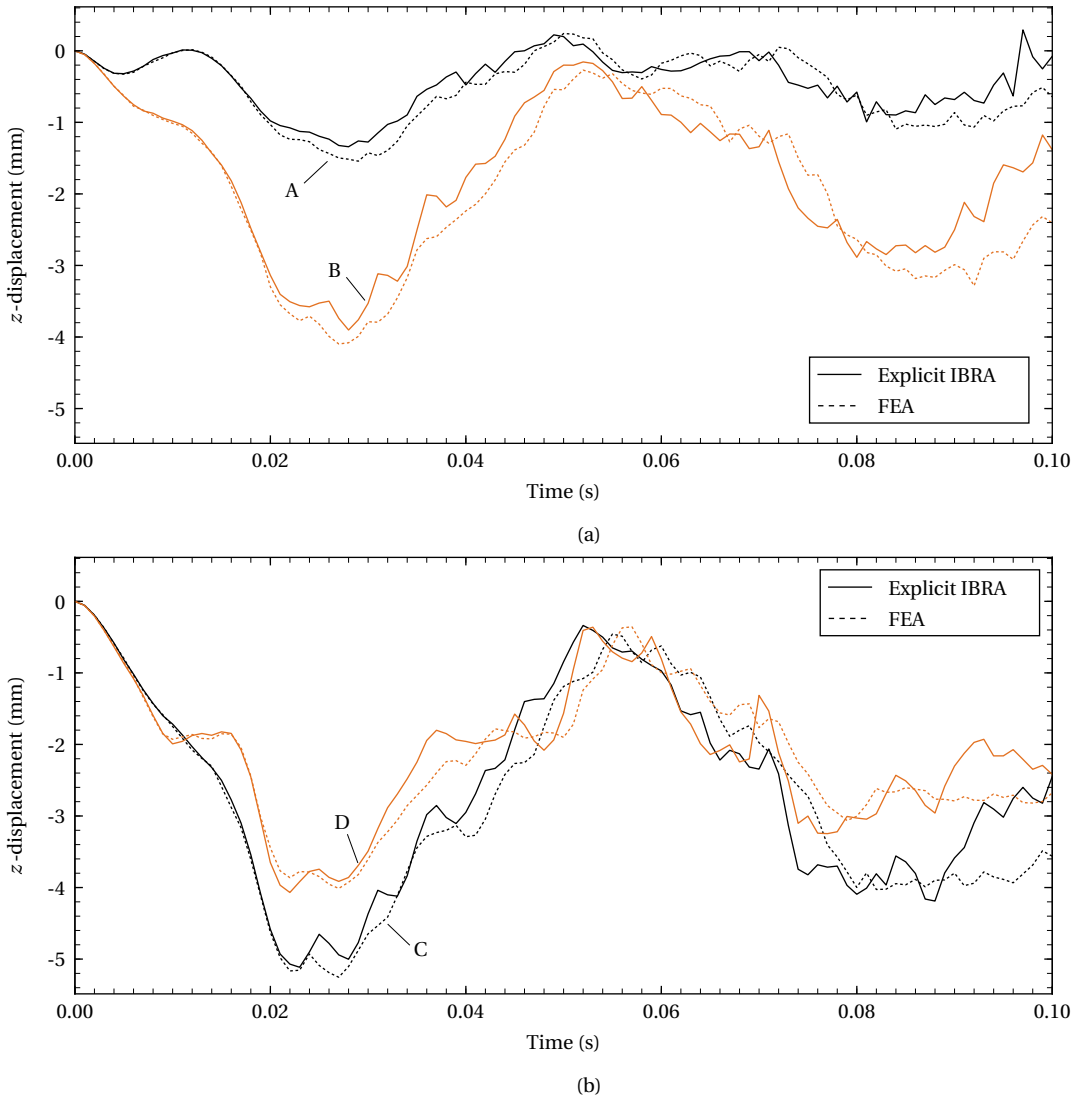

Figure 7.25: BMW engine bonnet exterior skin dynamically loaded by a uniform pressure: Comparison between Explicit IBRA ($\alpha_r = 1$) and FEA results for the z-displacement responses of points A–D depicted in Figure 7.22a.

can be seen, the stabilization approach ($\bar{\beta} = 0.01$, $f^s = 10$, $C_{\text{th}} = 0.01$) works as intended and the simulation finishes without instabilities. The corresponding displacement and rotation error measures for simulations with and without stabilization are provided in Figure 7.28. Without stabilization, the errors increase rapidly and tend towards infinity at around $t = 0.026$ s. With stabilization, the displacement and rotation errors remain small at levels of around 10^{-5} to 10^{-3}.

As mentioned before, a penalty factor of $\alpha_r = 1$ reduces the critical time step from 9.84×10^{-7} s (for shell elements only) to 4.22×10^{-7} s. For comparison, the critical time step size of the FEA model with 6.51×10^{-7} s is in the same range. Applying the local selective mass scaling approach proposed in this thesis allows recovering the critical time step of 9.84×10^{-7} s by specifically scaling control points according to the added penalty stiffness. This mass scaling achieves an increase in time step size by 133% with a total mass increase of $\Delta m = +9.9\%$. The specifically scaled control points are visualized in Figure 7.29. Herein, the control point volume is proportional to the control point mass and the color indicates the amount of added mass normalized by the maximum control point mass of the model m_{max}. In this example, the maximum mass added per control point is $0.55 m_{\text{max}}$.

The effect of this mass scaling on the z-displacement response of the four points A–D on the bonnet can be seen in Figure 7.30. Overall, the responses with and without the local selective mass scaling are in good agreement. The responses with mass scaling only lag slightly behind the responses without mass scaling. As already mentioned before, it depends on the specific application and intention of the analysis whether such a model modification is acceptable or not. Of course, also a smaller desired time step than the one without penalty (9.84×10^{-7} s) can be

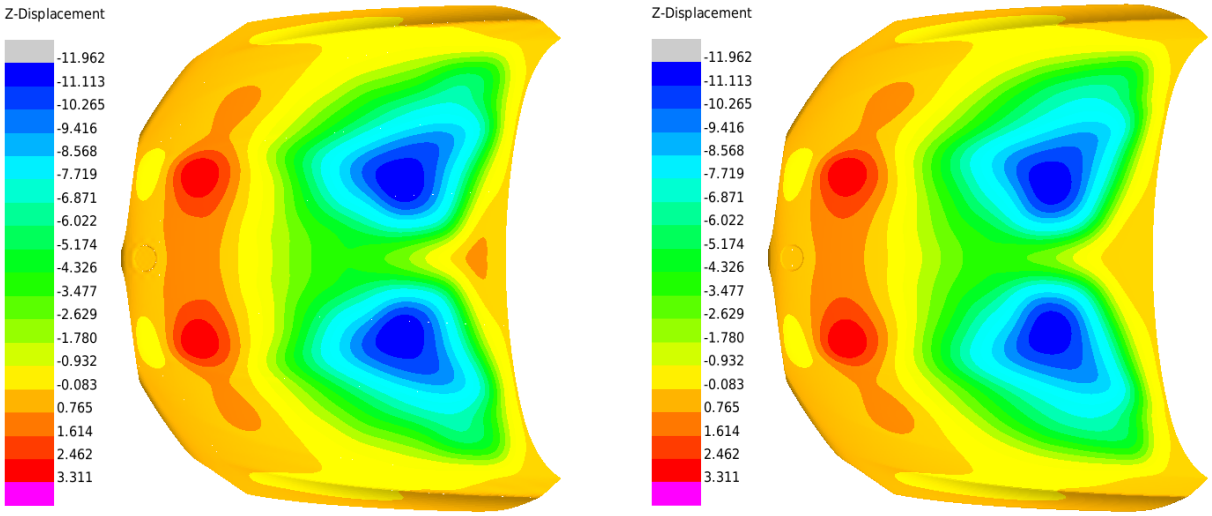

(a) Explicit IBRA.

(b) FEA.

Figure 7.26: BMW engine bonnet exterior skin dynamically loaded by a uniform pressure: Comparison of z-displacement results (in mm) for Explicit IBRA with $\alpha_r = 1$ and FEA at $t = 0.080\,\mathrm{s}$.

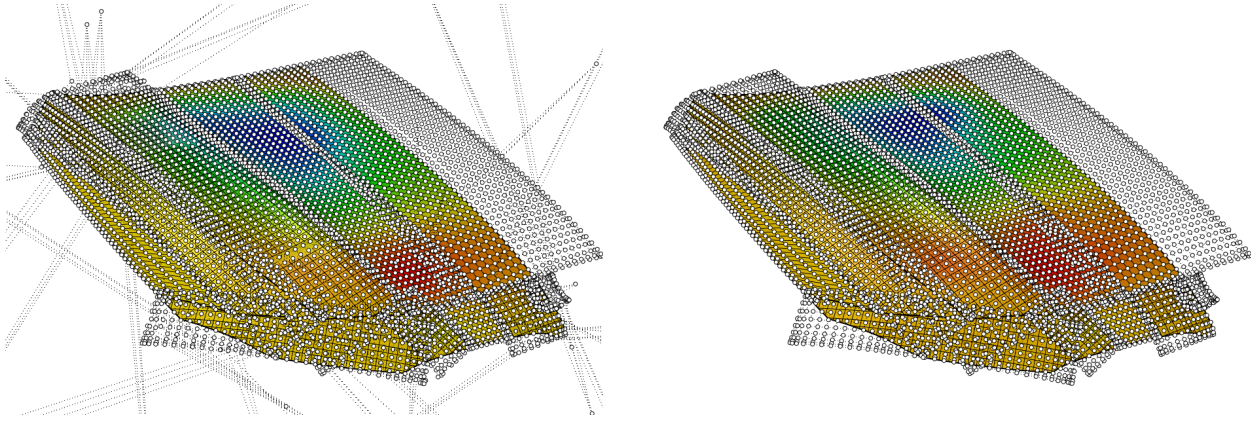

(a) Without light control point stabilization, $t = 0.026\,\mathrm{s}$.

(b) With light control point stabilization, $t = 0.10\,\mathrm{s}$.

Figure 7.27: BMW engine bonnet exterior skin dynamically loaded by a uniform pressure: Comparison of analysis results without and with light control point stabilization. Control points and control nets are visualized by black circles with white filling and dashed lines, respectively. The analysis without stabilization in (a) becomes unstable after $t = 0.026\,\mathrm{s}$, which can be seen from the extremely high displacements of light control points. The stabilized solution in (b) finishes and the stabilized light control points behave as intended ($\bar{\beta} = 0.01$, $f^{\mathrm{s}} = 10$, $C_{\mathrm{th}} = 0.01$).

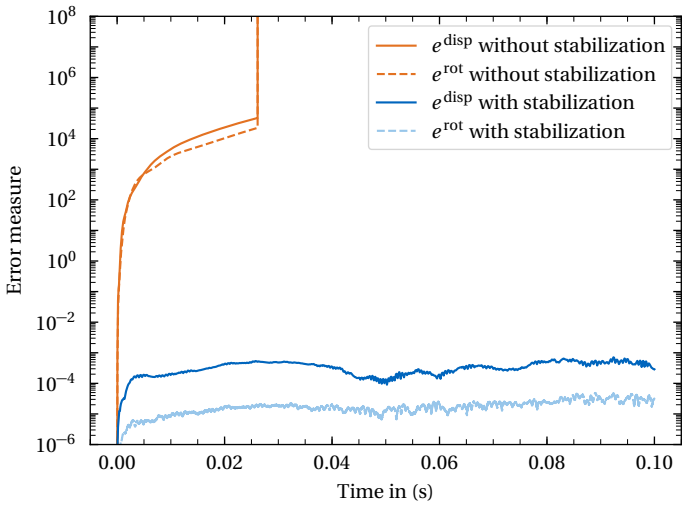

Figure 7.28: BMW engine bonnet exterior skin dynamically loaded by a uniform pressure: Comparison of displacement and rotation error measures for simulations without and with light control point stabilization ($\alpha_r = 1$, $\bar{\beta} = 0.01$, $f^{\text{s}} = 10$, $C_{\text{th}} = 0.01$).

specified for the local selective mass scaling (see Eq. (4.50) in Section 4.5), leading to a smaller amount of added mass and thus less impact on the solution.

In conclusion, this BMW engine bonnet example demonstrates the applicability of Explicit IBRA, the light control point stabilization scheme and the local selective mass scaling approach to large trimmed multi-patch NURBS models used in industrial CAD. Furthermore, it is shown that IGA models also need to conform with certain modeling guidelines. For a model following a number of suggested modeling guidelines, plausible results are obtained with a reasonable time step size.

7.3.3 Engine bonnet reinforcement structure

This example of a BMW bonnet reinforcement structure under dynamic loading is intended to demonstrate the applicability and robustness of the enhanced B-Rep element formulation and the developed stabilization scheme to even more complex models.

Figure 7.31 provides a comparison between the initial CAD model consisting of 5,888 (very small) trimmed surfaces and the guideline-conforming model consisting of 260 trimmed surface patches. For the guideline-conforming model small geometrically similar surfaces are merged and the polynomial degree is limited to $p = 4$. The problem description and an illustration of the refined model are provided in Figure 7.32. For the analysis of this symmetric problem, again only one half of the model is considered with appropriately applied symmetry boundary conditions. This half model consists of 130 trimmed patches and 14,912 active shell elements of a maximum polynomial degree of $p = 4$. Boundary and symmetry boundary conditions as well as internal coupling conditions are applied in a weak sense via 12,445 B-Rep edge elements in total. A uniform pressure load is applied in the form of a step function at $t = 0$ s. Here it should be noted that, within this thesis, a user-defined element interface not optimized for efficiency is used to implement B-Rep elements into LS-DYNA. Thus, one can imagine that such a (relatively) large model including 12,445 B-Rep edge elements almost reaches the limit of what is practically computable with this implementation.

Figure 7.33 depicts the scaled deformed shapes and z-displacements of the reinforcement structure obtained with a relative penalty factor of $\alpha_r = 1$ at $t = 0.01$ s and $t = 0.1$ s, visualized in the CAD program Rhinoceros with the postprocessing plug-in TeDA. As can be seen, reasonable deformations with smooth surfaces and without gaps are obtained, confirming the proper functioning of the enhanced B-Rep elements. In this example no restriction in time step size due to penalty-based boundary or coupling conditions is observed, that is, the critical time step is determined by the size of shell elements. During the analysis, 5601 light control points are successfully stabilized by the proposed penalty-based scheme with a parameter setting of $\bar{\beta} = 5 \times 10^{-4}$, $f^{\text{s}} = 10$, $C_{\text{th}} = 0.01$ and without a restriction in time step size. As in the previous examples, without stabilization, light control points show extremely large displacements and rotations, before the entire simulation becomes unstable at around $t = 3 \times 10^{-3}$ s.

Finally, it should be noted that also comparisons with results obtained from finite element analyses on a finely meshed model used in full vehicle crash simulations were made, but are omitted here. The results are in fact qualitatively

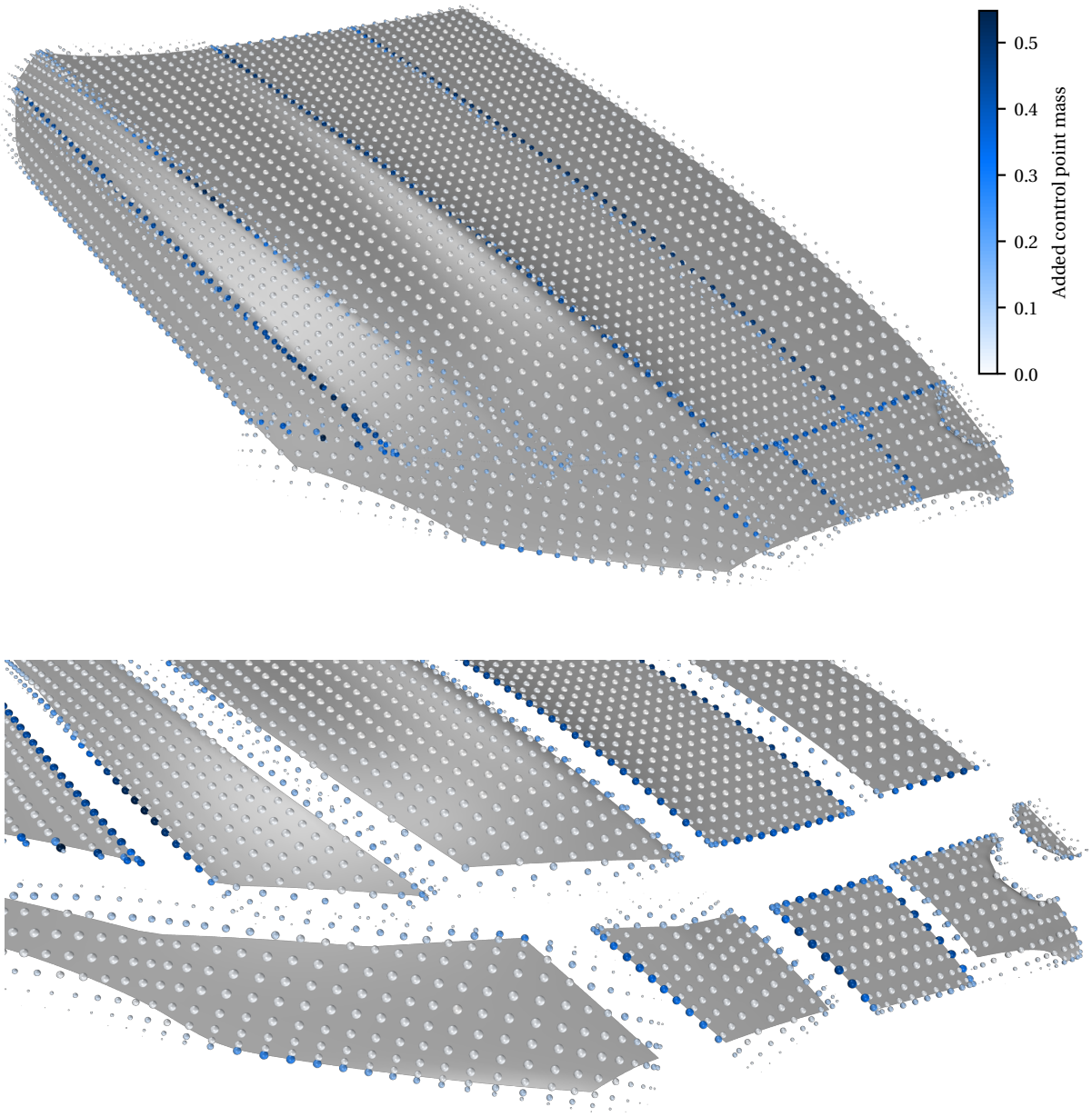

Figure 7.29: BMW engine bonnet exterior skin dynamically loaded by a uniform pressure: Results of the local selective mass scaling approach applied to a configuration with $\alpha_r = 1$, leading to an increase in critical time step size of +133% and a total mass increase of $\Delta m = +9.9\%$. The added mass per control point indicated by the colorbar is normalized with respect to the highest unscaled control point mass. The sphere volume of the control points represents the control point mass.

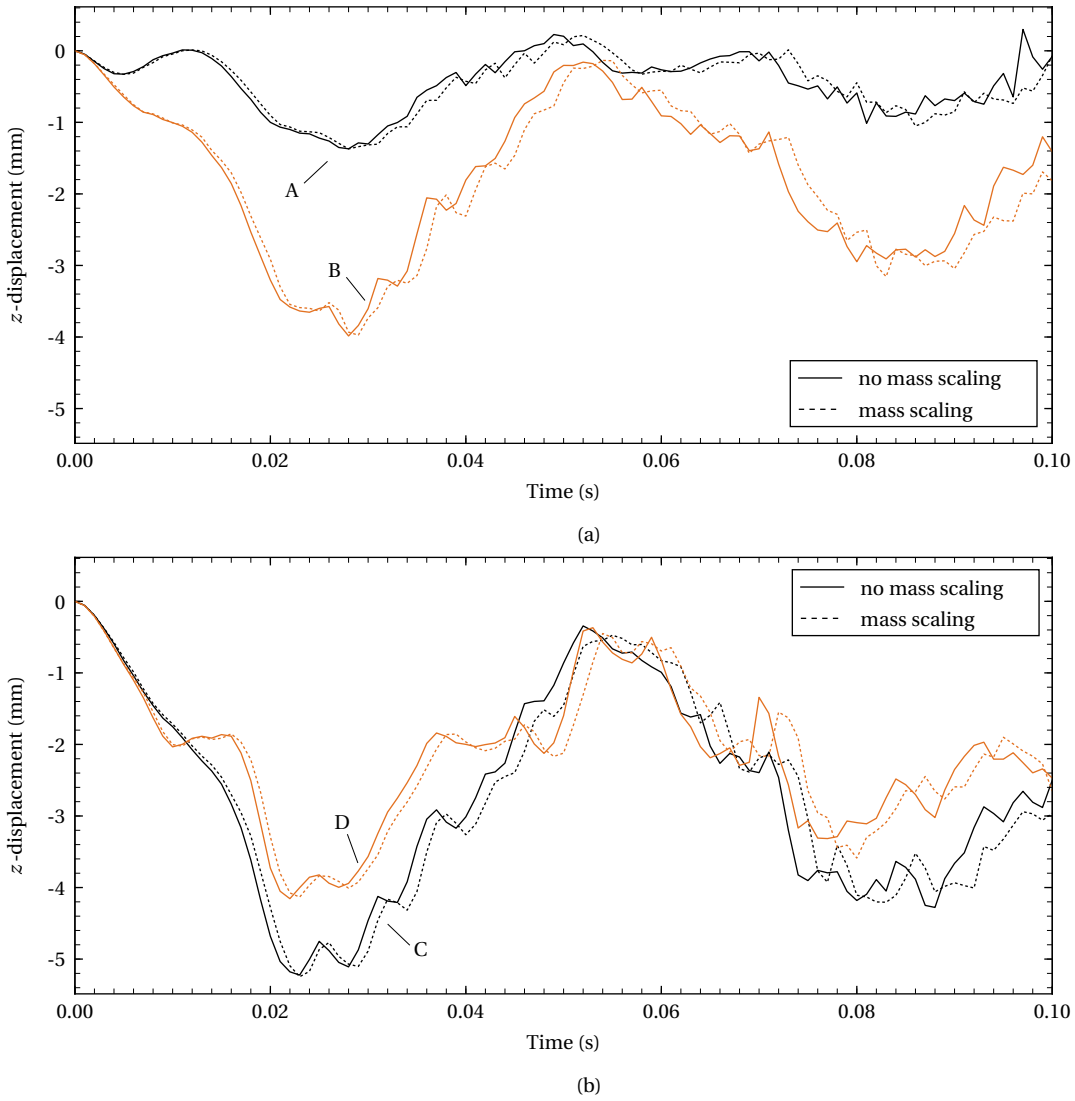

Figure 7.30: BMW engine bonnet exterior skin dynamically loaded by a uniform pressure: z-displacement responses of points A–D for simulations with and without local selective mass scaling of B-Rep elements.

similar, but a much finer discretization than the one shown in Figure 7.32a would be required to obtain good agreement in the dynamic response. Simulations with such a fine discretization, in turn, are not feasible with the current user-defined element implementation of Explicit IBRA in LS-DYNA. Nevertheless, this example clearly demonstrates the robustness of the Explicit IBRA framework and its applicability to large problems comprising hundreds of trimmed NURBS patches.

7.3.4 Head impact simulations for pedestrian safety

Finally, the two engine bonnet component models presented above shall be studied in a practically more relevant and more challenging scenario, namely a head impact test, commonly performed to assess the pedestrian safety of vehicles, for example in the Euro NCAP consumer test [164]. An actual engine bonnet of a car consists of multiple (partially bonded) components like the exterior skin and the reinforcement structure. Here, the exterior skin and the reinforcement structure are studied as separate components, which in fact does not correspond to the real case. Nevertheless, these problems still show the possibility to perform explicit dynamic impact simulations including material plasticity, large deformations and contact on trimmed multi-patch NURBS shell structures. Because the individual components have a lower stiffness, the problem setup is slightly adjusted compared to the actually conducted crash test [164]. Since the impactor is modeled by conventional solid and shell finite elements, these simulations furthermore demonstrate the capability of LS-DYNA to perform hybrid simulations comprising isogeometric and conventional finite element components – a feature that will strongly facilitate the introduction of IGA in industry.

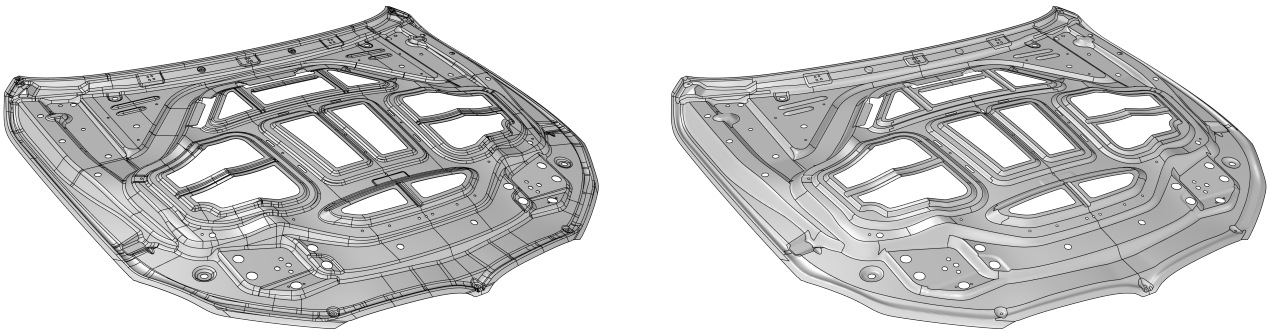

(a) (b)

Figure 7.31: BMW engine bonnet reinforcement structure: Initial CAD model (a) and guideline-conforming model (b). Surface patch boundaries are indicated by black lines.

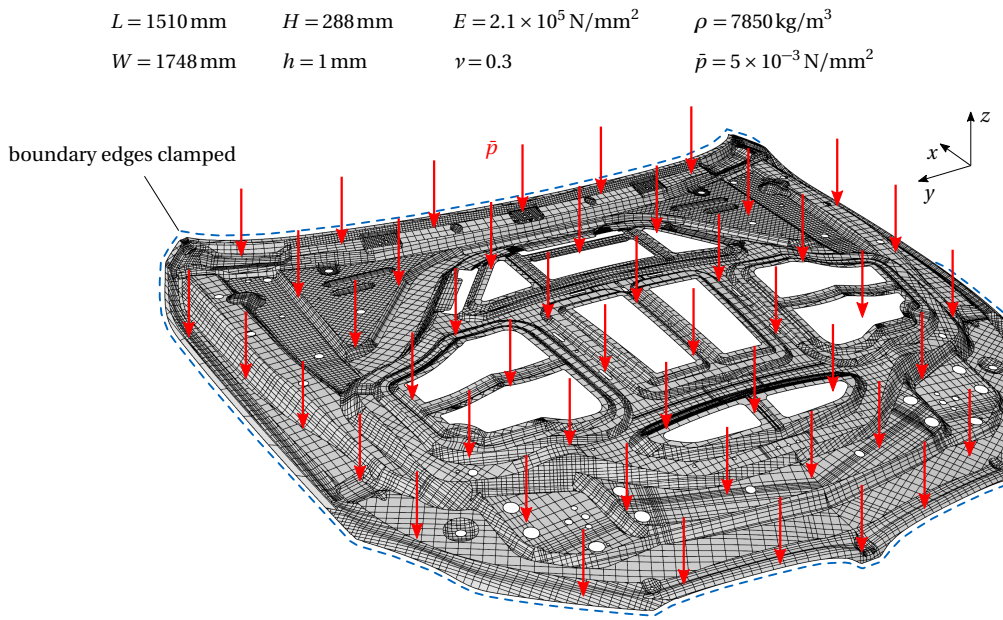

(a) Problem description and NURBS discretization: Clamped boundary edges are indicated by blue dashed curves.

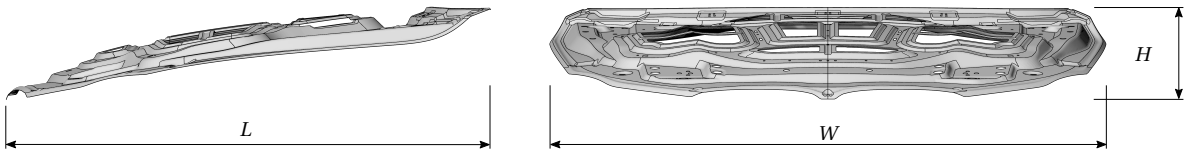

(b) CAD geometry and main model dimensions.

Figure 7.32: BMW engine bonnet reinforcement structures dynamically loaded by a uniform pressure: The guideline-conforming analysis model (half model) consists of 130 trimmed NURBS patches with 14,912 active shell elements of maximum degree $p = 4$. Weak penalty and coupling conditions are applied via 12,445 B-Rep edge elements.

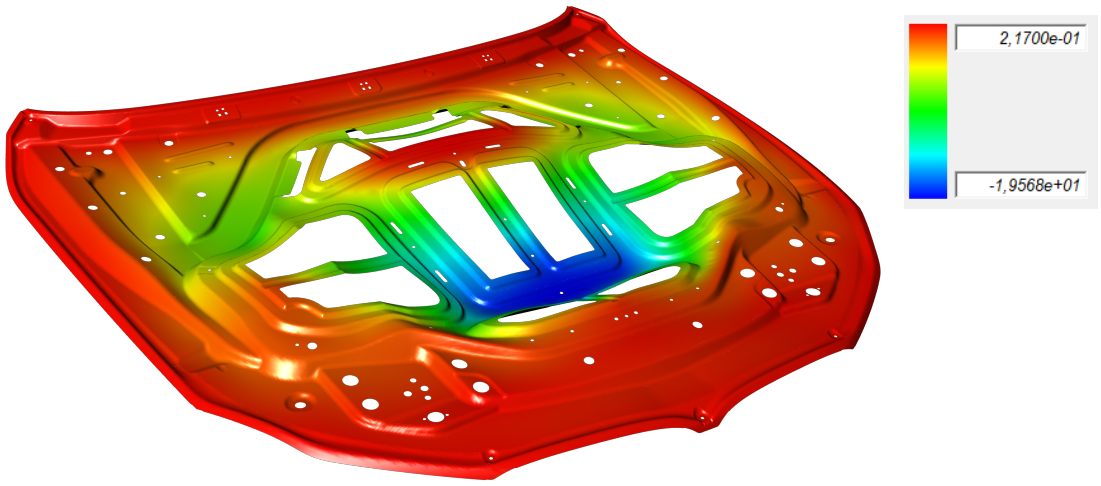

(a) Deformed shape at $t = 0.01\,\mathrm{s}$, scale factor 5.

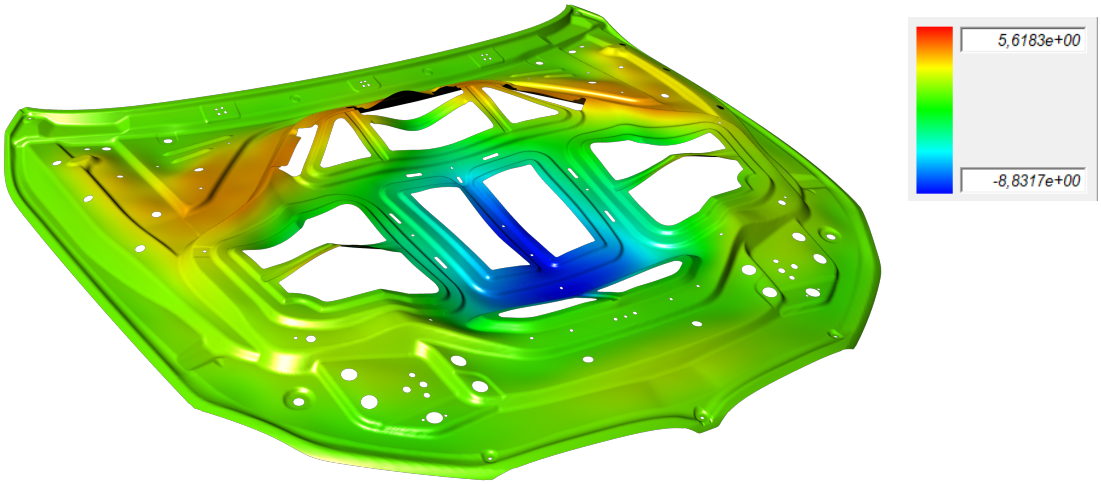

(b) Deformed shape at $t = 0.1\,\mathrm{s}$, scale factor 10.

Figure 7.33: BMW engine bonnet reinforcement structure dynamically loaded by uniform pressure: Deformed shapes obtained with a relative penalty factor $\alpha_r = 1$, visualized in the CAD program Rhinoceros with TeDA. The color plots indicate z-displacements in mm. Light control points are successfully stabilized with a parameter setting of ($\bar{\beta} = 5 \times 10^{-4}$, $f^{\mathrm{s}} = 10$, $C_{\mathrm{th}} = 0.01$).

The problem description is given in Figure 7.34. As can be seen, the impactor hits the bonnet models with $V_I = 35\,\mathrm{km/h}$ and at an angle of $\beta = 25°$ to the vertical. The boundary edges of the models, which are identical to the ones used in the previous sections, are clamped and again only half models are considered due to symmetry. Boundary conditions are again applied via B-Rep elements and for the coupling, in particular, enhanced B-Rep elements are employed. For all simulations a consistent penalty factor of $\alpha_r = 1$ is used. In contrast to the previous bonnet examples, the material behavior is considered as elasto-plastic with a stress-strain curve defined via the *MAT_PIECEWISE_LINEAR_PLASTICITY material model in LS-DYNA. A background finite element mesh on the NURBS-based components allows modeling the contact between the finite element impactor and the isogeometric bonnet models via the *CONTACT_AUTOMATIC_SURFACE_TO_SURFACE keyword in LS-DYNA.

Simulation results for both models visualized via TeDA in the CAD program Rhino are provided in Figures 7.35–7.38. A sequence of six deformed shapes of the half exterior skin model in side view is depicted in Figure 7.35, clearly showing the head impact event and relatively large deformations. The corresponding deformed shapes of the full model in perspective view with indicated total displacements are depicted in Figure 7.36. Figure 7.37 depicts the impact event for the reinforcement structure via six deformed shapes in side view. Due to the stiffer behavior, the resulting deformations are smaller than for the exterior skin, but with a maximum displacement of around 58 mm still significantly high. The deformed shapes of the full model in perspective view are give in Figure 7.38, in which the color plot again indicates total displacements.

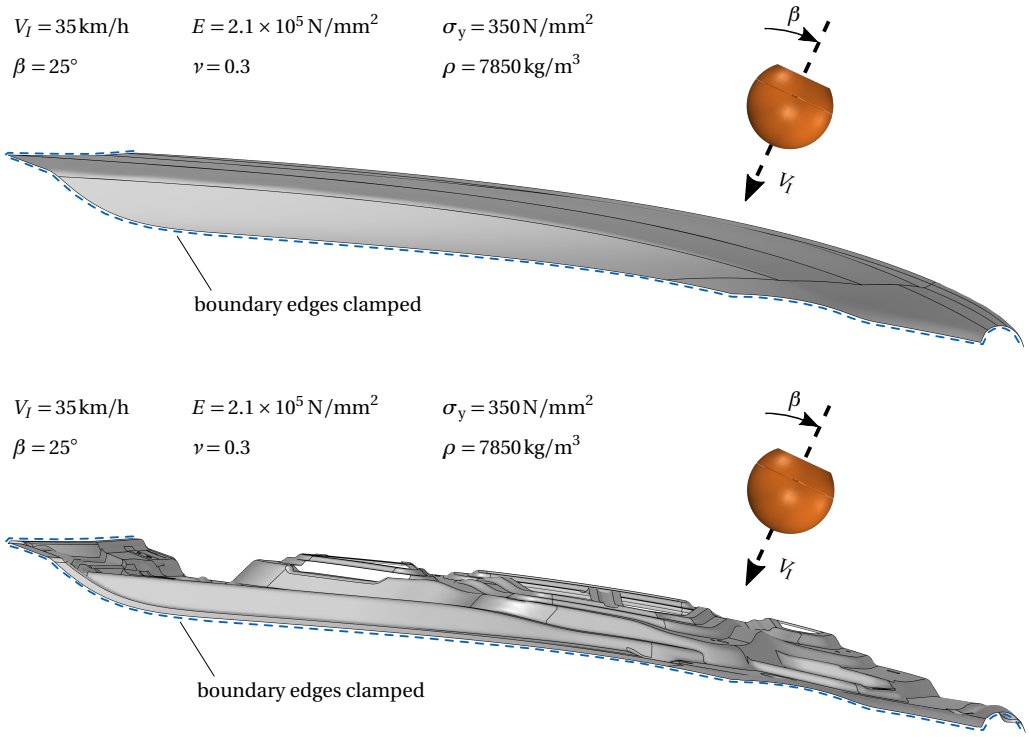

Figure 7.34: Head impact simulations for pedestrian safety: Problem description. The bonnet exterior skin and the reinforcement structure are modeled by trimmed multi-patch NURBS shells, see Figures 7.21a and 7.31b, respectively, while the impactor is modeled by shell and solid finite elements. Clamped boundary edges are indicated by blue dashed curves.

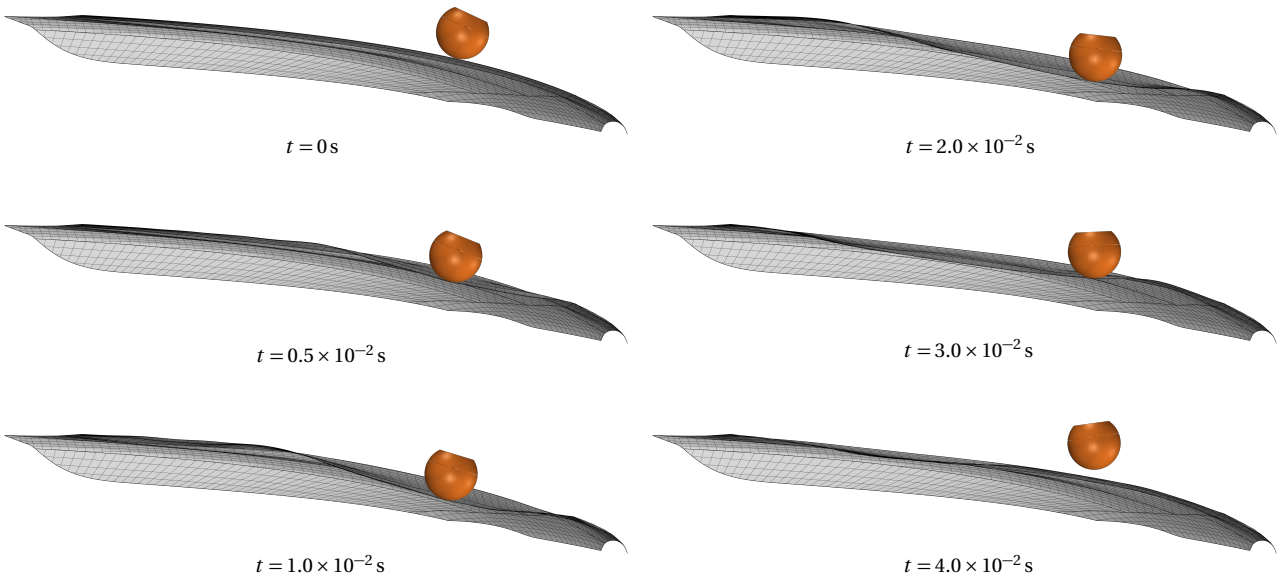

Figure 7.35: Head impact on the bonnet exterior skin: Sequence of six deformed shapes at different points in time in side view.

The smooth shapes visible in these figures show that the enhanced B-Rep element coupling works as intended, even in such highly dynamic impact scenarios including large deformations, plasticity and contact. Also the numerous light control points appearing in these relatively complex models are successfully stabilized in this impact scenario using the same parameter settings as in the previous sections (exterior skin: $\bar{\beta} = 0.01$, $f^{\mathrm{s}} = 10$, $C_{\mathrm{th}} = 0.01$, reinforcement structure: $\bar{\beta} = 5 \times 10^{-4}$, $f^{\mathrm{s}} = 10$, $C_{\mathrm{th}} = 0.01$). Furthermore, it is worth noting that the time step in these simulations is restricted by the finite elements of the impactor and not by the NURBS-based elements or the penalty-based B-Rep elements.

In conclusion, these head impact simulations clearly demonstrate the possibility to perform highly dynamic explicit isogeometric analysis including large deformations, material plasticity and contact on industrial NURBS-based models. The fact that these examples already involve most of the analysis features required for vehicle crash simulations enables first industrial applications of IGA in crash scenarios using hybrid vehicle models in LS-DYNA.

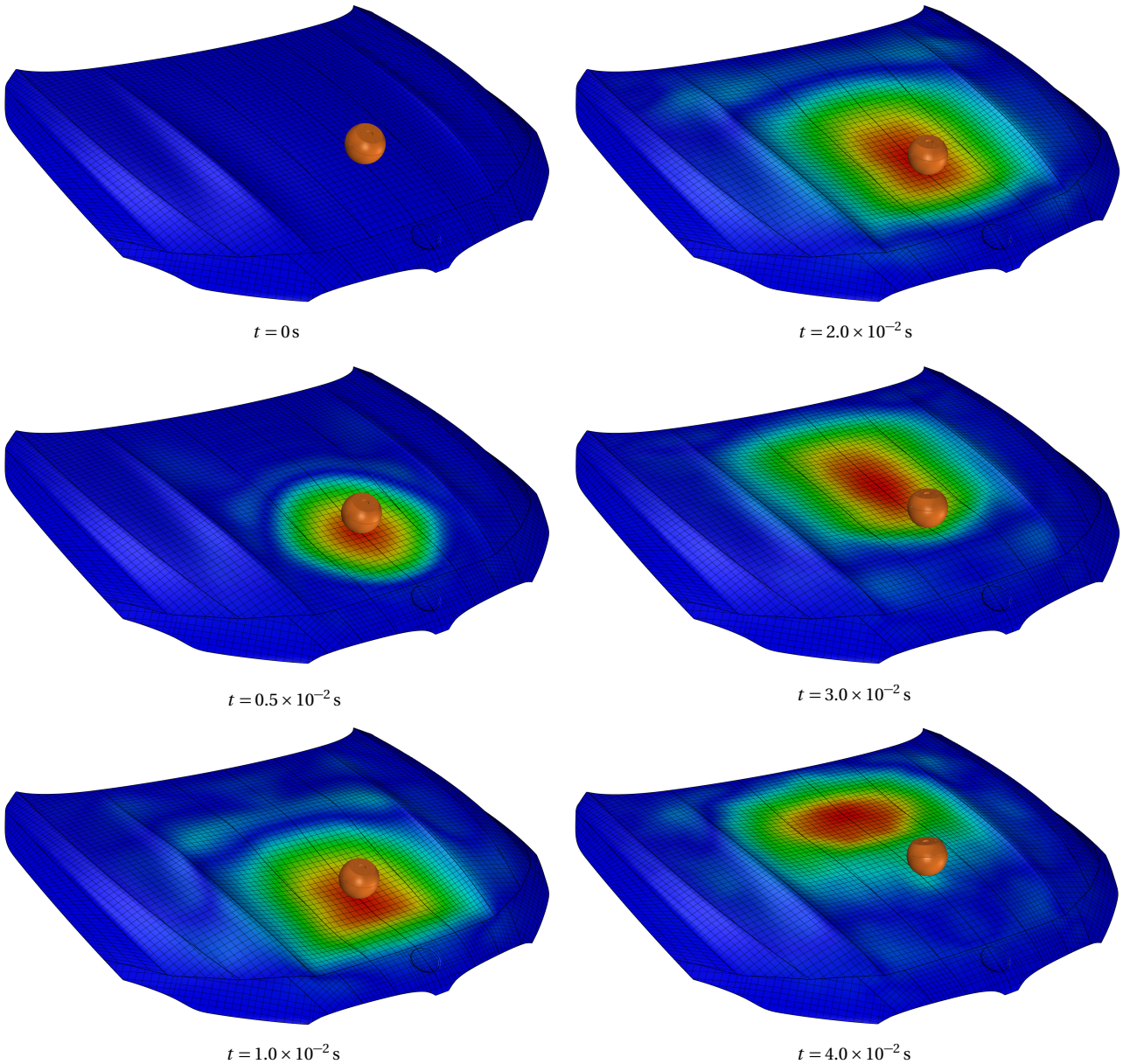

Figure 7.36: Head impact on the bonnet exterior skin: Sequence of six deformed shapes at different points in time. The color plot indicates total displacements (magnitude of the displacement vector).

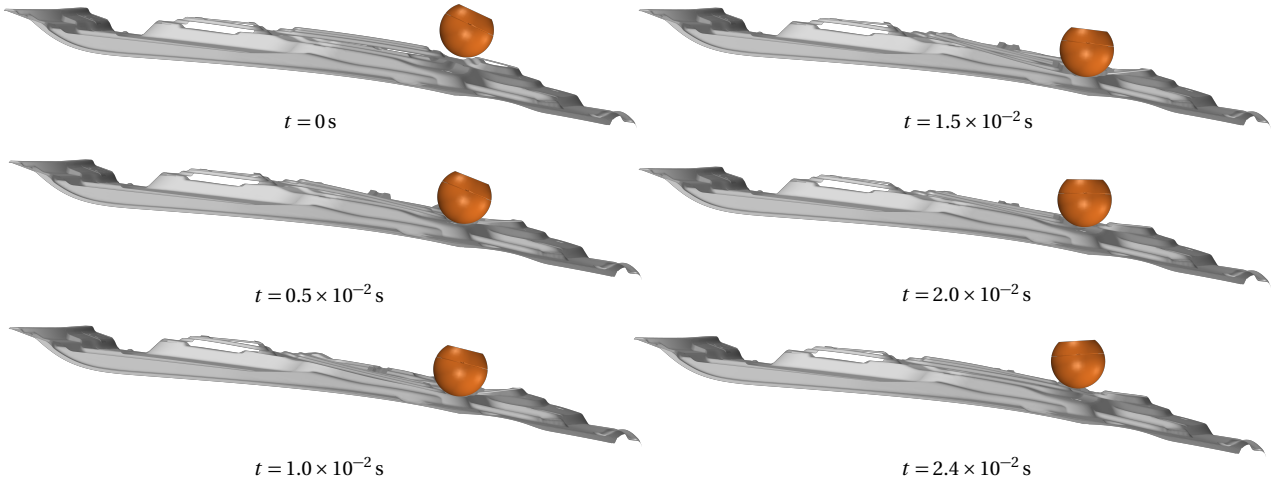

Figure 7.37: Head impact on the bonnet reinforcement structure: Sequence of six deformed shapes at different points in time in side view.

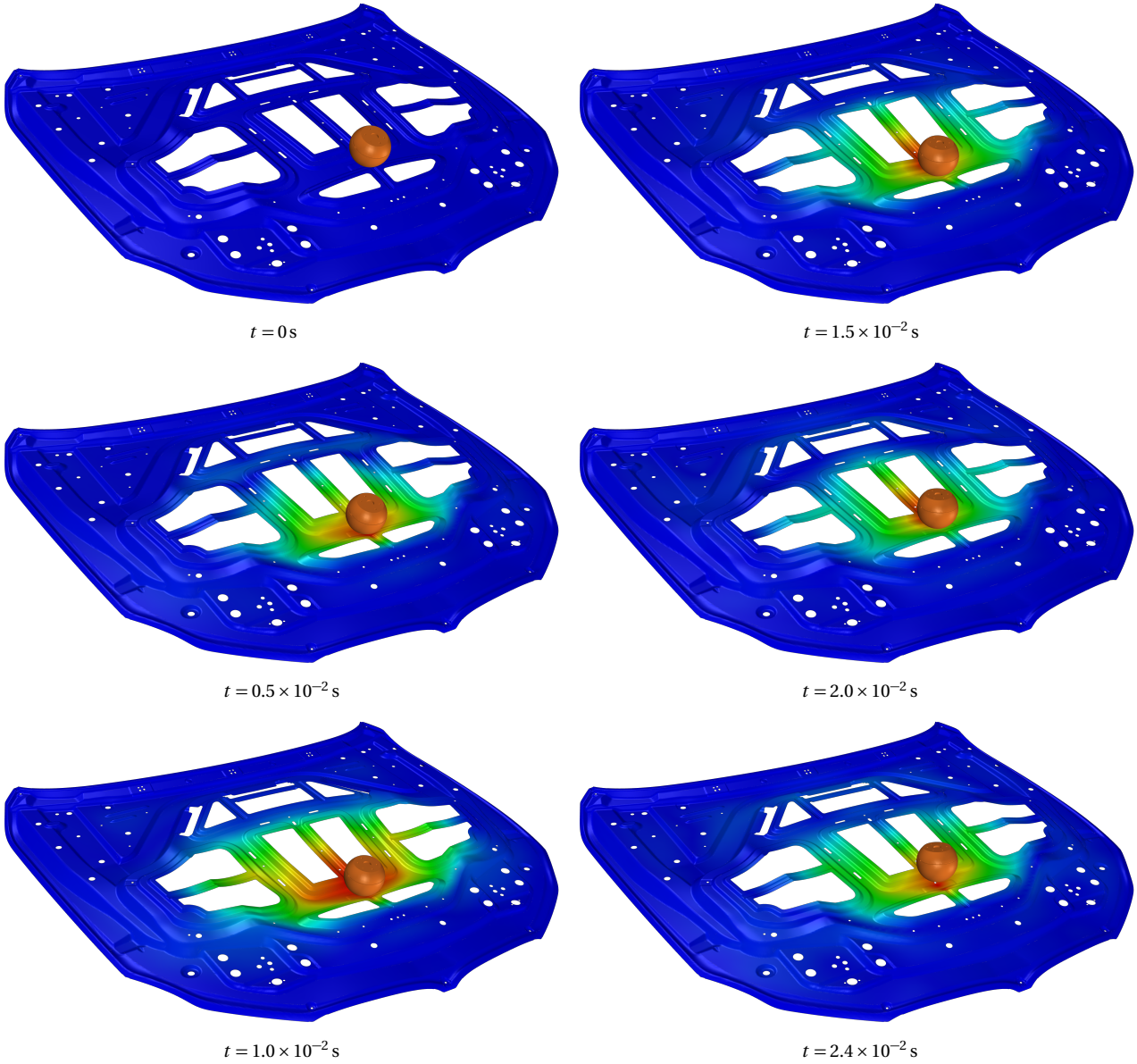

Figure 7.38: Head impact on the bonnet reinforcement structure: Sequence of six deformed shapes at different points in time. The color plot indicates total displacements (magnitude of the displacement vector).

7.4 Summary and conclusion of Chapter 7

In this chapter Explicit IBRA for trimmed multi-patch NURBS shells is validated by means of well-selected benchmark problems reaching from quasi-static linear elastic to highly dynamic nonlinear elasto-plastic cases including large deformations and contact. Furthermore, the applicability of Explicit IBRA and the related methods to dynamic (impact) problems on industrial trimmed multi-patch B-Rep models is demonstrated.

Weak penalty-based boundary and coupling conditions are applied via novel B-Rep element formulations for Reissner-Mindlin shells with rotational DOFs. The influence of B-Rep elements on the critical time step size is studied and accurate results are obtained with no or only a minor reduction in time step size.

It is shown that the enhanced B-Rep element formulation including coupled shell normals, as proposed in Section 3.4, is able to accurately couple trimmed NURBS shells even in extreme deformation scenarios. This is a significant improvement compared to the B-Rep element formulation only coupling translational and rotational DOFs as proposed in [54].

All problems suffering from instabilities caused by light control points are successfully stabilized through the proposed light control point stabilization scheme. Similar parameter settings are used for the considered examples and only slight adjustments are required depending on the problem type, e.g. for some problems including contact. Accurate results without a reduction in time step size are achieved through this penalty-based light control point stabilization scheme.

For problems in which B-Rep elements lead to a decrease in time step size, the proposed local selective mass scaling scheme for B-Rep elements is shown to be an effective measure to increase the critical time step size, while keeping the amount of added mass low. Figures visualizing the control point mass and the amount of added mass per control point, demonstrate the principle idea behind this mass scaling scheme, namely to specifically scale control point masses according to the introduced penalty stiffness.

Finally, it should be emphasized that solving the rather challenging problems presented in this chapter is now only possible because various difficulties associated with explicit dynamic analysis on trimmed multi-patch NURBS models were (i) identified, (ii) systematically studied, and (iii) effectively solved through specific methods within this thesis.

Chapter 8

Conclusion and Outlook

With the long-term goal of achieving a virtual vehicle development process of higher efficiency and predictive accuracy in mind, this thesis was devoted to Isogeometric Analysis (IGA) [12], a relatively young FEA technology that uses the NURBS-based geometry description from CAD also for the analysis. By using NURBS for describing the geometry and the solution field, IGA has not only the potential to connect design and analysis, but also to achieve a higher solution accuracy due to a precise geometry representation and the higher-order and higher-continuity nature of NURBS. Industrial CAD models typically consist of multiple trimmed surface patches, preventing a direct application of IGA in its original form. In order to perform analysis on such models, Isogeometric B-Rep Analysis (IBRA) [30] was chosen. IBRA uses so-called isogeometric B-Rep elements based on a penalty approach to apply coupling and boundary conditions along trimming edges of shell structures in a weak integral sense. The focus of this thesis was on explicit dynamic (crash) analysis. In the existing IBRA framework [30, 32], it was not possible to perform crash-type simulations, and in fact, the applicability of IBRA to explicit dynamics has never been assessed in the literature.

The aim of this thesis was to fill this gap by developing *Explicit IBRA*, the extension of IBRA to explicit dynamics. Explicit IBRA should achieve accurate, efficient and robust explicit dynamic analyses on penalty-coupled trimmed NURBS shells with the goal to enable an integrated design-analysis process for vehicular crashworthiness. This included (i) the extension of the IBRA theory to explicit dynamics and shear deformable Reissner-Mindlin shells, (ii) the development of novel B-Rep element formulations including rotational DOFs for coupling, Dirichlet and Neumann boundary conditions, (iii) systematic studies on the influence of boundary elements, trimming and penalty-based B-Rep elements on the critical time step size, (iv) the development of a local selective mass scaling scheme to eliminate potential time step restricting effects, (v) the development of a stabilization scheme for small trimmed elements applicable to explicit dynamic (crash) analysis on complex multi-patch shell structures, (vi) the implementation of the novel B-Rep element formulations and the developed methods into LS-DYNA via a user-defined interface, (vii) the set-up of an integrated design-analysis process between the CAD program Rhinoceros and the solver LS-DYNA and (viii) the assessment of the accuracy, efficiency and robustness of the developed methods by means of various benchmark examples and industry-type problems. The most important conclusions, developments and findings are concisely summarized below, following the structure of the thesis.

8.1 Explicit IBRA

As a first step, IBRA was theoretically extended to explicit dynamic analysis by considering B-Rep element forces and moments in the computations of accelerations within the explicit central difference scheme. Two novel types of penalty-based B-Rep element formulations, the *standard* and the *enhanced* formulation, were derived for shear-deformable RM shells with rotational DOFs defined in global coordinates. These B-Rep element formulations allow the application of coupling, Dirichlet and Neumann boundary conditions along trimmed shell edges in a weak sense. The standard B-Rep element formulation enforces the respective constraints directly on the three translational and three rotational DOFs. This was shown to be sufficient from a mechanical and shell theory point of view, and yielded accurate results for problems with small deformations. For large deformation and highly dynamic problems, on the contrary, the standard B-Rep element formulation was found to not achieve the desired rotational coupling accuracy. This was because rotational continuity was enforced solely based on rotational DOFs, whose inertias are

commonly scaled up in explicit analysis such that the rotational modes do not restrict the time step. This scaling and especially the loosened connection between trimmed control points and the material domain affect the accuracy of rotational DOFs. Although this has only little effect on the overall behavior of the shell, rotational DOFs were found to be not reliable enough for the imposition of rotational continuity between (trimmed) shells under large deformations. The enhanced B-Rep element formulation was developed to overcome this issue by *additionally* enforcing rotational continuity via constraints on the shell normals, uniquely defined by translational DOFs. It is worth noting that this additional constraint was inspired by Benson et al. [47], who used it to enforce rotational continuity between rotation-free Kirchhoff-Love shells. Thus, without the constraints on the rotational DOFs, the enhanced B-Rep element formulation is also expected to work well for the coupling of rotation-free KL shells. Control point forces and stiffness matrices were derived for both types of penalty-based B-Rep element formulations. These B-Rep element formulations are therefore not restricted to explicit analysis, but can also be used in static and implicit dynamic analysis. In fact, both B-Rep element formulations were implemented for explicit and implicit analysis into LS-DYNA via a user-defined interface.

Howsoever, the focus of this thesis was on explicit analyses, which are only conditionally stable. For the explicit central difference scheme, used within this thesis, the stability condition is only valid if the mass and stiffness matrices remain symmetric and positive semidefinite. It was shown that this holds for Explicit IBRA with penalty-based B-Rep elements as long as the penalty factor is positive. As a result, the well-known stability condition for the central difference scheme based on the maximum system eigenfrequency can also be used within Explicit IBRA. It is furthermore shown that those time step estimates that aim at directly estimating the maximum system eigenvalue also consider the effects of trimming and penalty coupling. This makes estimates like the power iteration method or the nodal time step estimate directly applicable to Explicit IBRA – a finding essential for efficient practical applications.

8.2 Stable time step size

To understand the influencing factors on the critical time step size within an Explicit IBRA setting of penalty-coupled trimmed NURBS patches, extensive analytical and numerical studies were conducted on one-dimensional bar and two-dimensional shell models.

First, trimming was shown to be an effective mean to remove the time step restricting effect of elements at the boundary of open knot vector patches. In this way, the critical time step of a quartic NURBS shell patch, for example, could be increased by 221%. For practical applications it was proposed to extend patches beyond their physical boundary and to subsequently trim off the problematic boundary elements.

Second, the effect of the trimmed element size on the critical time step size was studied both analytically and numerically. Through this, inter-element continuity was identified to be the decisive factor for the behavior of the critical time step. While for C^0 inter-element continuity the critical time step was observed to tend towards infinity as the trimmed element size decreased, for interior elements with an inter-element continuity of C^{p-1} and $p > 1$, trimming was found to have practically no influence on the time step. This fascinating result indicates that the concept of trimming (and similarly any type of immersed method) in combination with explicit analysis is only feasible with higher-order *and* higher-continuity basis functions such as NURBS. For FEA with C^0 continuous basis functions, arbitrarily small trimmed elements, which are unavoidable in practical applications, would require an arbitrarily small explicit time step. And as shown, increasing the order *without* increasing the inter-element continuity makes things even worse. This is another argument for the superiority of isogeometric elements with higher inter-element continuity over standard C^0 finite elements.

The third objective in this context was to study the behavior of the critical time step with respect to weak penalty-based coupling and boundary conditions. In fact, it was shown that if the introduced penalty stiffness dominates over the shell stiffness, which is the case for large penalty factors $\alpha > \alpha'$, the critical time step is determined by the penalty stiffness. It was furthermore shown that this penalty factor α' can be estimated by solving local eigenvalue problems for the shell and penalty contributions separately. This enables the a priori estimation of a penalty factor that does not lead to a reduction in time step size. For interior elements with $p > 1$, C^{p-1} and applied penalty-based boundary conditions, the critical time step was also found to be insensitive to the trimmed element size.

Finally, a local selective mass scaling approach was proposed to compensate for a possibly negative effect of penalty-based B-Rep elements on the time step. This approach specifically scales control points involved in B-Rep element formulations according to their nodal eigenfrequency, computed via a lumped stiffness matrix and the Gershgorin circle theorem. Through this approach the critical time step could be increased effectively by specifically adding the right amount of mass to the right control points.

8.3 Stabilization of small trimmed elements / light control points

Control points with low mass and stiffness caused by small trimmed elements, the so-called light control points, were found to cause instabilities in highly dynamic explicit analyses. It is worth noting that ill-conditioned system matrices are not the actual problem here, since no equation systems are solved in explicit analyses. The reasons for these instabilities were in fact found to be (i) the extremely large inverse masses amplifying inevitable inaccuracies in the forces when computing the accelerations within each of the probably hundreds of thousands time steps, and (ii) the low stiffness between light control points and the remaining material domain, allowing for nearly unrestricted movement. These instabilities were furthermore identified as closely related to weak instabilities, that is, steadily evolving during the simulation and not avoidable through smaller time steps. To solve this issue, a stabilization scheme appropriate for Explicit IBRA was developed, addressing the two aforementioned reasons for instabilities: (i) mass scaling of light control points to reduce the strong error amplifications and (ii) penalty-based stabilization constraints between light control points and stable adjacent control points to restrict the almost free movement of light control points. In this way, even the complex bonnet reinforcement structure consisting of 130 trimmed patches could be successfully stabilized. The proposed stabilization scheme is (a) compatible with weak coupling and boundary conditions, (b) does not restrict the time step and requires low numerical effort, (c) maintains the symmetry and positive semidefiniteness of the mass and stiffness matrices, and (d) is applicable to any type of shell and solid element formulation. Furthermore, this stabilization scheme can be easily implemented as a preprocessing add-on to existing solver environments, since it does neither require the deletion or modification of basis functions nor additional integration points. A disadvantage of the proposed stabilization scheme is, however, the necessary definition of a threshold value below which a control point is considered as a light control point, a penalty stabilization factor and a mass scaling parameter. Nevertheless the identification of problematic control points, nodes or elements as well as other stabilization parameters is required for almost all stabilization approaches proposed in the literature, see Section 1.2.4. To conclude, the proposed stabilization scheme enables highly dynamic explicit analyses of trimmed multi-patch shell structures that would not be possible otherwise.

8.4 Prototypical implementation of an integrated IBRA-based CAD/CAE process

The main motivation for this thesis was to achieve a more efficient virtual vehicle development process by connecting the currently rather separated fields of design and analysis. The feasibility of a fully integrated IBRA-based CAD/CAE process was demonstrated by a prototypical process between the commercial CAD program Rhinoceros [116] and the commercial solver LS-DYNA [45] based on the IBRA exchange format [52]. Through the pre- and postprocessing plug-in TeDA [74] for Rhinoceros, all design, pre- and postprocessing steps could be performed within the CAD environment. Using the IBRA exchange format, TeDA enabled to first extract all necessary information from CAD, and then to read analysis results for visualization in Rhinoceros. The integration of LS-DYNA into this process was achieved via user-defined LS-DYNA interfaces. A distinctive feature of this integrated design-analysis process is its consistent feature-based data structure containing geometry, topology and analysis information. Retaining the feature-based structure allows identifying holes, cut-outs, beadings or trimmed edges as actual features in both the design and the analysis model. This strongly facilitates a consistent assignment of material properties or boundary, coupling and loading conditions throughout the entire process, independent of the underlying discretization that may change frequently during the various design cycles.

8.5 Numerical examples

The validity and effectiveness of Explicit IBRA and the developed methods was assessed by means of several well-selected benchmark problems reaching from quasi-static linear elastic with small deformations to highly dynamic elasto-plastic with large deformations and contact. Furthermore, the practical applicability and robustness of the Explicit IBRA framework was demonstrated through dynamic (impact) analyses on two BMW vehicle components: the exterior skin and the reinforcement structure of an engine bonnet consisting of up to 130 trimmed NURBS surfaces. Especially worth noting are the promising results of head impact simulations on the bonnet models for pedestrian safety, which already include almost all relevant features for future vehicle crash simulations. The main conclusions from these numerical examples are:

- The developed penalty-based B-Rep elements are able to accurately couple trimmed NURBS-based RM shells with six DOFs. With the enhanced B-Rep element formulation even highly dynamic problems with large deformations were accurately solved.
- Accurate results were obtained with penalty factors that cause no or only a minor decrease in time step size.

- Local selective mass scaling of control points involved in B-Rep elements was found to be an effective mean to compensate for a possible decrease in time step size, while keeping the amount of added mass low.
- The developed stabilization scheme for light control points could successfully stabilize all numerical examples solved within this thesis, even the rather complex bonnet reinforcement structure consisting of 130 trimmed NURBS patches under dynamic (impact) loading. The considered examples were solved without a reduction in time step size and with similar parameter settings, requiring only small adjustments, e.g. for problems including contact.

Here, it should again be highlighted that the challenging problems presented within this thesis could only be solved because various difficulties associated with explicit dynamic analyses on trimmed multi-patch shell structures were (i) identified, (ii) systematically studied, and (iii) effectively solved through the aforementioned methods.

8.6 Analysis-suitable model discretization

Finite element models used in industrial applications have to fulfill various well-defined modeling criteria and high quality standards. In order to obtain accurate, efficient and robust (explicit) isogeometric analysis, similar criteria are also required for isogeometric models. In the course of this thesis, the following IGA-specific modeling criteria were identified:

- A prescribed minimum patch and element size to achieve reasonable time steps.
- A prescribed maximum polynomial degree in order to capture local effects accurately and to keep the cost of numerical integration low.
- Preferably a uniform element size as well as uniform and maximum inter-element continuity.

These criteria may seem simple or obvious, but are not at all fulfilled in current CAD models, because it was simply not necessary for geometric design so far. The BMW vehicle components studied within this thesis therefore had to be modified to fulfill these criteria. Some of these criteria like maximum polynomial degree, uniform element size and uniform continuity can be easily considered in CAD algorithms. Constructing future CAD models with a minimum patch size, on the other hand, could require some additional effort in the geometric design phase. Nevertheless, these criteria can result in CAD modeling guidelines for IGA, which the design engineer needs to follow in the future.

8.7 Practical aspects of an IGA/IBRA-based development process

Another often disregarded aspect is the need to generate a midsurface description from B-Rep volumes for shell analysis. In this respect it was proposed to construct the midsurface as an associated offset of either the exterior or the interior surface of the B-Rep volume model and to perform all boolean trim operations also directly on the midsurface. Ideally, the associated midsurface model would then be automatically updated in case the volume model is changed. Thus, the analysis model would be already provided as an output of the geometric design phase, permanently in sync with the design model.

Here one could argue that, as in FEA, again two different models for design and analysis are deployed and that this is not what IGA has originally promised. This is a good opportunity to qualify the often exaggerated expectations on IGA, namely to perform analyses directly on existing CAD models without further preparation effort. In fact, using only one model is theoretically possible, but as anyone familiar with numerical simulations knows, high quality results are only obtained through high quality input, no matter which numerical method is used. The crucial difference to FEA, however, is that these two models are in an active parametric relation, use the same consistent geometry description, the same consistent data structure and the same consistent feature-based modeling paradigm. In this way the efficiency of development processes is expected to be greatly improved, simply because “both worlds speak the same language”, hence avoiding unnecessary and cumbersome conversions whenever one of those two changes.

The realization of such an integrated IBRA-based development process in industry will certainly take time since this requires the involved individuals to rethink and adapt the current well-established processes, and to gain confidence in the new methods. What is still lacking is the dedication from CAD vendors to implement pre- and postprocessing capabilities for IGA. However, established preprocessing tools such as ANSA [120] already started to pave the way for first productive applications of IGA. In fact, (temporary) using the same toolchain as in the current FEA-based process without adaptations, will greatly facilitate the introduction of IGA. For example, nobody will set up a full IGA vehicle crash model including dummies and barriers from scratch with a completely new and unestablished tool. Using the familiar preprocessor environment with available IGA-features like ANSA in combination with the

FEA/IGA solver LS-DYNA, the engineer can simply replace certain FEA components within a full vehicle model with IGA components and perform tests without additional effort. Here it should again be emphasized that the key benefit of IGA/IBRA is the possibility to use one consistent and accurate model description throughout the entire process and not to just one tool.

8.8 Practical implications of this thesis

In conclusion, this thesis has shown that explicit dynamic (crash) analysis on trimmed multi-patch NURBS models are technically feasible, also for large models. The extension of IBRA to explicit dynamics and the gained knowledge provide another building block crucial for future applications in (automotive) industry and further implementations of IGA features into commercial codes. The main practical implications can be summarized as follows:

- Through the developed B-Rep element formulations, nonlinear explicit dynamic analysis can now be performed on trimmed multi-patch shell structures.
- The effects of trimming, and weak penalty-based coupling and boundary conditions on the critical time step size in explicit analysis are now understood.
- Possible time step restrictions caused by weak penalty-based coupling and boundary conditions can now be eliminated.
- Trimmed control points with low mass and stiffness can now be stabilized in explicit dynamic analysis.
- A fully-integrated IBRA-based CAD/CAE process was demonstrated to be technically feasible.
- First recommendations regarding analysis-aware CAD model structuring (e.g. integrated midsurface description) and criteria for an analysis-suitable model discretization are now available.

Some of these developments and findings have already found their way into commercial programs. This thesis has, for example, contributed to the fact that penalty-based B-Rep elements are now firmly implemented and available in the commercial solver LS-DYNA, see [143]. Such a professional implementation allows solving large problems on multiple processors efficiently. Furthermore, the suggestion to extend patches beyond their physical boundary and to subsequently trim off boundary elements in order to achieve a larger critical time step has been adopted in the preprocessor ANSA, see [120].

8.9 Outlook

Still, further steps remain to be taken towards a fully integrated CAD/CAE development process. Although many issues and features were already considered in the Explicit IBRA framework proposed in this work, several extensions and improvements are of course possible. First of all, only one, rather heuristically determined penalty factor for translations and rotations was used in the numerical examples, simply because no suitable criteria for the determination were available. Thus, methods for an a priori and objective determination of the penalty factor, for instance based on a predefined time step size or solution accuracy, are desired. Such methods would probably also allow for a further distinction between translational in-plane and out-of-plane penalty factors, as well as between rotational bending and twisting penalty factors. However, to enable this, the current B-Rep element formulation based on global coordinates needed to be adapted, i.e. a local coordinate system needed to be introduced along (trimmed) edges.

A possible improvement for the stabilization scheme would be to specifically scale the light control point masses according to the added stabilization penalty stiffness, based on the nodal eigenfrequency. This would, similarly to the local selective mass scaling approach for B-Rep elements, only add the amount of mass required to not restrict the time step.

Within this thesis, no systematic studies regarding the accuracy of stress evaluations in the vicinity of trimmed coupling edges were conducted. Thus, thorough investigations especially for problems including plasticity are suggested. In this context also the ability to consider material fracture and element deletion needs to be investigated.

The focus of thesis was on explicit dynamic analysis of shell structures. Similarly, the behavior of trimmed (or immersed) trivariate solid structures such as cut finite cells or V-Reps within explicit dynamic analysis needs to be studied. This would include the development of suitable (B-Rep) elements for the application of coupling and boundary conditions, an extension of the proposed stabilization scheme, modeling guidelines as well as the enhancement of the proposed design-analysis process. The combination of immersed shell and solid structures would provide a complete analysis methodology for vehicle safety design based on trimmed B-Rep models.

Another crucial aspect is the definition of further isogeometric analysis-suitable modeling guidelines, which are expected to only be discovered when using IGA in real industrial applications. Thus, pilot projects with actual productive use of NURBS-based components in full vehicle finite element simulations are suggested – as already mentioned, ANSA and LS-DYNA provide the necessary capabilities. The possibility to perform hybrid simulations on models with isogeometric and conventional finite element components enables first productive applications without additional effort. A predestined first application scenario with actual practical benefit would be the use of isogeometric models for critical, frequently modified components like the bumper system, as this would reduce model generation effort and thus speed up design cycles.

Appendix A

Linear stability analysis of the central difference method

For completeness, the linear stability condition (2.67) for the explicit central difference method is derived here, closely following [49] and similar to [54]. Starting point are the linearized semidiscrete equations of motion including damping:

$$\mathbf{M}\ddot{\mathbf{d}} + \mathbf{C}\dot{\mathbf{d}} + \mathbf{K}\mathbf{d} = \mathbf{f}^{\text{ext}}. \tag{A.1}$$

For the stability analysis it is convenient to decouple the actual problem into a single-degree-of-freedom problem by means of a modal (spectral) decomposition that exploits the orthogonality of the eigenvectors with respect to the undamped system, i.e. the eigenvectors $\mathbf{y}_I$ of the undamped eigenproblem

$$\mathbf{K}\mathbf{y}_I = \lambda_I \mathbf{M}\mathbf{y}_I. \tag{A.2}$$

Therefore, the damped equation system can only be decoupled if the damping matrix can be expressed in terms of $\mathbf{M}$ and $\mathbf{K}$. The Rayleigh damping matrix, for instance, is defined as a linear combination of mass and stiffness matrix as

$$\mathbf{C} = a_1 \mathbf{M} + a_2 \mathbf{K}. \tag{A.3}$$

For symmetric mass and stiffness matrices the eigenvectors $\mathbf{y}_I$ are orthogonal with respect to $\mathbf{M}$ and $\mathbf{K}$ and the corresponding eigenvalues λ_I are all real. In case the matrices are also positive semidefinite, all eigenvalues are positive. For standard FEA and IGA, this usually holds true because $\mathbf{M}$ is symmetric and positive definite, and $\mathbf{K}$ is symmetric and positive semidefinite. With eigenvectors orthonormalized with respect to $\mathbf{M}$ the following applies:

$$\mathbf{y}_J^T \mathbf{M}\mathbf{y}_I = \delta_{IJ} \quad \text{and} \quad \mathbf{y}_J^T \mathbf{K}\mathbf{y}_I = \lambda_I \delta_{IJ} \quad \text{(no sum on } I\text{)} \tag{A.4}$$

where δ_{IJ} denotes the Kronecker delta with $\delta_{IJ} = 1$ if $I = J$ and $\delta_{IJ} = 0$ if $I \neq J$. Since the eigenvectors $\mathbf{y}_J$ describe a basis in $\mathbb{R}^{n_{\text{DOF}}}$, one can express $\mathbf{d}$ as a linear combination of the eigenvectors $\mathbf{y}_J$:

$$\mathbf{d} = \sum_J \alpha_J(t)\mathbf{y}_J. \tag{A.5}$$

Inserting Eq. (A.5) into Eq. (A.1), pre-multiplying it with $\mathbf{y}_I$ and exploiting conditions (A.4) yields n_{DOF} decoupled equations

$$\ddot{\alpha}_I + (a_1 + a_2\omega_I^2)\dot{\alpha}_I + \omega_I^2 \alpha_I = 0 \quad \text{where} \quad \omega_I^2 = \lambda_I,\ I = 1, \ldots, n_{\text{DOF}}. \tag{A.6}$$

With the modal damping ratio ξ_I for Rayleigh damping

$$\xi_I = \frac{a_1}{2\omega_I} + \frac{a_2\omega_I}{2}, \tag{A.7}$$

one can write Eq. (A.6) as

$$\ddot{\alpha} + 2\xi\omega\dot{\alpha} + \omega^2\alpha = 0, \tag{A.8}$$

where the modal indices are omitted for brevity. Discretizing Eq. (A.8) in time and inserting the central difference formulas for the acceleration (2.58) and the velocity (2.57) one obtains

$$\frac{\alpha_{n+1}-2\alpha_n+\alpha_{n-1}}{\Delta t^2}+2\xi\omega\frac{\alpha_n-\alpha_{n-1}}{\Delta t}+\omega^2\alpha_n=0. \tag{A.9}$$

Here, it should be noted that the velocity term is evaluated at $t^{n-1/2}$ with a lag of a half time step, which is essential for the time integration procedure to be fully explicit [49]. Equation (A.9) allows performing the stability analysis of single-degree-of-freedom problems and carrying over the results to the actual problem (A.1). The validity of this approach is evident from (A.5): $\mathbf{d}$ remains bounded as long as all $\alpha_J(t)$ remain bounded. Applying an exponential ansatz function $\alpha_n=\mu^n$ to Eq. (A.9) and performing some algebraic operations then yields

$$\mu^2+\mu(g+h-2)+(1-g)=0 \quad \text{where} \quad g=2\xi\omega\Delta t, \quad h=\omega^2\Delta t^2. \tag{A.10}$$

As one can see, for $n\to\infty$ the coefficients $\alpha_n=\mu^n$ only remain bounded if $|\mu|\leq 1$. For a complex μ the stability condition $|\mu|\leq 1$ requires μ to be located in the unit circle in the complex plane, which can be difficult to show (for $|\mu|=1$ the multiplicity of the associated eigenvalue must not be greater than 1 for stability). Through the z-transform, one can simplify this problem by mapping the unit circle in the complex μ-plane to the left-hand side of the z-plane via

$$\mu=\frac{1+z}{1-z}. \tag{A.11}$$

This allows assessing an integration procedure as stable if the roots of the z-polynomial

$$\sum_{i=0}^{p} c_i z^{p-i}=0 \quad \text{with} \quad c_0>0 \tag{A.12}$$

have only negative real parts. This can be done by means of the Hurwitz matrix defined as

$$H_{ij}=\begin{cases} c_{2j-i} & \text{if } 0\leq 2j-i\leq p \\ 0 & \text{otherwise} \end{cases} \tag{A.13}$$

and a theorem that states that all roots of (A.12) are negative if and only if the leading principal minors of (A.13) are positive [165]. Applying the z-transform (A.11) to (A.10) then yields

$$z^2(4-2g-h)+z(2g)+h=0 \tag{A.14}$$

for which the Hurwitz matrix ($p=2$) is given as

$$\mathbf{H}=\begin{bmatrix} c_1 & 0 \\ c_0 & c_2 \end{bmatrix}. \tag{A.15}$$

The conditions on the leading principal minors Δ_1 and Δ_2 in combination with the condition $c_0>0$ then leads to

$$\Delta_1=c_1=2g=4\xi\omega\Delta t\geq 0, \tag{A.16}$$

$$\Delta_2=c_1c_2\geq 0\Rightarrow c_2=h=\omega^2\Delta t^2\geq 0, \tag{A.17}$$

$$c_0=4-2g-h=4-4\xi\omega\Delta t-\omega^2\Delta t^2>0. \tag{A.18}$$

Condition (A.16) is fulfilled for a positive damping ratio ($\xi\geq 0$), condition (A.17) is fulfilled because it is a product of c_1 and squares, whereas condition (A.18) yields a quadratic equation in $\omega\Delta t$ with the solution

$$\omega\Delta t=-2\xi\pm 2\sqrt{\xi^2+1}. \tag{A.19}$$

From this, the stability condition can be determined as a function of the time step. Since the negative root would imply negative time steps, only the positive root is relevant, leading to the desired stability condition in terms of a critical time step size as

$$\Delta t_{\text{crit}}=\min_I \frac{2}{\omega_I}\left(\sqrt{\xi_I^2+1}-\xi_I\right). \tag{A.20}$$

As one can see, within this derivation only two requirements are specified: (i) symmetric and positive semidefinite matrices $\mathbf{M}$ and $\mathbf{K}$ and (ii) the use of a Rayleigh damping matrix. Thus, the stability condition for the explicit central difference method (A.20) is applicable to any kind of problem of the form (A.1), for which these two requirements are fulfilled.

Bibliography

[1] European Commission, Directorate General for Transport. *European Commission, Vehicle Safety*. https://ec.europa.eu/transport/road_safety/sites/roadsafety/files/pdf/ersosynthesis2018-vehiclesafety.pdf. Accessed on March 05, 2020. 2018.

[2] *Euro NCAP web page*. https://www.euroncap.com/en/about-euro-ncap/. Accessed on February 28, 2020.

[3] Euro NCAP. *BMW 5-Series – Euro NCAP Results 2017*. https://euroncap.newsmarket.com/Find-a-car/all/bmw-5-series----euro-ncap-results-2017/s/5e2e2459-fa59-42e7-b5f7-a65e799bb813. Accessed on February 28, 2020. 2017.

[4] Dassault Systèmes, Simulia. *What is the next big thing in crashworthiness simulations?* https://www.3ds.com/fileadmin/PRODUCTS/SIMULIA/IMG/industry/transportation-and-mobility/SIMULIA-next-big-thing-in-crashworthiness-simulation.pdf. Accessed on February 25, 2020.

[5] *Dassault Systèmes 3DExperience platform*. https://www.3ds.com/products-services/simulia/solutions/transportation-mobility/crashworthiness/. Accessed on February 25, 2020.

[6] *Siemens Simcenter 3D*. https://www.plm.automation.siemens.com/global/de/products/simcenter/simcenter-3d.html. Accessed on February 25, 2020.

[7] *Altair SimSolid*. https://www.altair.com/simsolid/. Accessed on February 25, 2020.

[8] *Ansys Discovery Live*. https://www.ansys.com/products/3d-design/ansys-discovery-live. Accessed on February 25, 2020.

[9] I. Symington. ''Designer Oriented Software - Is It Accurate?'' In: *The international magazine for engineering designers & analysts from NAFEMS* January (2020).

[10] J. Parvizian, A. Düster, and E. Rank. ''Finite cell method.'' In: *Computational Mechanics* 41.1 (2007), pp. 121–133. DOI: 10.1007/s00466-007-0173-y.

[11] G.-R. Liu. *Meshfree Methods: Moving Beyond the Finite Element Method*. CRC press, 2009.

[12] T. J. R. Hughes, J. A. Cottrell, and Y. Bazilevs. ''Isogeometric analysis: CAD, finite elements, NURBS, exact geometry and mesh refinement.'' In: *Computer Methods in Applied Mechanics and Engineering* 194 (2005), pp. 4135–4195. DOI: 10.1016/j.cma.2004.10.008.

[13] J. A. Cottrell, T. J. R. Hughes, and A. Reali. ''Studies of refinement and continuity in isogeometric structural analysis.'' In: *Computer Methods in Applied Mechanics and Engineering* 196 (2007), pp. 4160–4183. DOI: 10.1016/j.cma.2007.04.007.

[14] S. Hartmann and D. J. Benson. ''Mass scaling and stable time step estimates for isogeometric analysis.'' In: *International Journal for Numerical Methods in Engineering* 102.3-4 (2015), pp. 671–687. DOI: 10.1002/nme.4719.

[15] I. Stroud. *Boundary Representation Modelling Techniques*. Springer-Verlag London, 2006. DOI: 10.1007/978-1-84628-616-2.

[16] B. Marussig and T. J. R. Hughes. ''A Review of Trimming in Isogeometric Analysis: Challenges, Data Exchange and Simulation Aspects.'' In: *Archives of Computational Methods in Engineering* 25.4 (2018), pp. 1059–1127. DOI: 10.1007/s11831-017-9220-9.

[17] E. Cohen, T. Martin, R. M. Kirby, T. Lyche, and R. F. Riesenfeld. ''Analysis-aware modeling: Understanding quality considerations in modeling for isogeometric analysis.'' In: *Computer Methods in Applied Mechanics and Engineering* 199.5-8 (2010), pp. 334–356. DOI: 10.1016/j.cma.2009.09.010.

[18] E. Catmull. *A subdivision algorithm for computer display of curved surfaces.* Tech. rep. University of Utah, 1974.

[19] F. Cirak and Q. Long. ''Subdivision shells with exact boundary control and non-manifold geometry.'' In: *International Journal for Numerical Methods in Engineering* 88 (2011), pp. 897–923. DOI: 10.1002/nme.3206.

[20] A. Riffnaller-Schiefer, U. H. Augsdörfer, and D. W. Fellner. ''Isogeometric shell analysis with NURBS compatible subdivision surfaces.'' In: *Applied Mathematics and Computation* 272 (2016), pp. 139–147. DOI: 10.1016/j.amc.2015.06.113.

[21] J. Shen, J. Kosinka, M. Sabin, and N. Dodgson. ''Converting a CAD model into a non-uniform subdivision surface.'' In: *Computer Aided Geometric Design* 48 (2016), pp. 17–35. DOI: 10.1016/j.cagd.2016.07.003.

[22] T. W. Sederberg, J. Zheng, A. Bakenov, and A. Nasri. ''T-splines and T-NURCCs.'' In: *ACM Trans. Graph.* 22.3 (2003), pp. 477–484. DOI: 10.1145/882262.882295.

[23] Y. Bazilevs, V. M. Calo, M. A. Scott, and T. W. Sederberg. ''Isogeometric analysis using T-splines.'' In: *Computer Methods in Applied Mechanics and Engineering* 199.5-8 (2010), pp. 229–263. DOI: 10.1016/j.cma.2009.02.036.

[24] M. A. Scott. ''T-splines as a Design-Through-Analysis Technology.'' PhD Thesis. University of Texas at Austin, USA, 2011.

[25] H.-J. Kim, Y.-D. Seo, and S.-K. Youn. ''Isogeometric analysis for trimmed CAD surfaces.'' In: *Computer Methods in Applied Mechanics and Engineering* 198.37-40 (2009), pp. 2982–2995. DOI: 10.1016/j.cma.2009.05.004.

[26] H.-J. Kim, Y.-D. Seo, and S.-K. Youn. ''Isogeometric analysis with trimming technique for problems of arbitrary complex topology.'' In: *Computer Methods in Applied Mechanics and Engineering* 199.45-48 (2010), pp. 2796–2812. DOI: 10.1016/j.cma.2010.04.015.

[27] Y. D. Seo, H. J. Kim, and S. K. Youn. ''Shape optimization and its extension to topological design based on isogeometric analysis.'' In: *International Journal of Solids and Structures* 47.11-12 (2010), pp. 1618–1640. DOI: 10.1016/j.ijsolstr.2010.03.004.

[28] Y. W. Wang, Z. D. Huang, Y. Zheng, and S. G. Zhang. ''Isogeometric analysis for compound B-spline surfaces.'' In: *Computer Methods in Applied Mechanics and Engineering* 261-262 (2013), pp. 1–15. DOI: 10.1016/j.cma.2013.04.001.

[29] P. Kang and S. K. Youn. ''Isogeometric analysis of topologically complex shell structures.'' In: *Finite Elements in Analysis and Design* 99 (2015), pp. 68–81. DOI: 10.1016/j.finel.2015.02.002.

[30] M. Breitenberger, A. Apostolatos, B. Philipp, R. Wüchner, and K.-U. Bletzinger. ''Analysis in computer aided design: Nonlinear isogeometric B-Rep analysis of shell structures.'' In: *Computer Methods in Applied Mechanics and Engineering* 284 (2015), pp. 401–457. DOI: 10.1016/j.cma.2014.09.033.

[31] B. Philipp, M. Breitenberger, I. D'Auria, R. Wüchner, and K.-U. Bletzinger. ''Integrated design and analysis of structural membranes using the Isogeometric B-Rep Analysis.'' In: *Computer Methods in Applied Mechanics and Engineering* 303 (2016), pp. 312–340. DOI: 10.1016/j.cma.2016.02.003.

[32] M. Breitenberger. ''CAD-integrated design and analysis of shell structures.'' PhD Thesis. Technical University of Munich, Germany, 2016. ISBN: 9783943683417.

[33] P. Kang and S. K. Youn. ''Isogeometric shape optimization of trimmed shell structures.'' In: *Structural and Multidisciplinary Optimization* 53.4 (2016), pp. 825–845. DOI: 10.1007/s00158-015-1361-6.

[34] B. Marussig, J. Zechner, G. Beer, and T.-P. Fries. ''Stable isogeometric analysis of trimmed geometries.'' In: *Computer Methods in Applied Mechanics and Engineering* 316 (2017), pp. 497–521. DOI: 10.1016/j.cma.2016.07.040.

[35] J. Xu, N. Sun, L. Shu, T. Rabczuk, and G. Xu. ''An Improved Integration for Trimmed Geometries in Isogeometric Analysis.'' In: *Computers, Materials & Continua* 60.2 (2019), pp. 615–632. DOI: 10.32604/cmc.2019.04464.

[36] R. Schmidt, R. Wüchner, and K.-U. Bletzinger. ''Isogeometric analysis of trimmed NURBS geometries.'' In: *Computer Methods in Applied Mechanics and Engineering* 241-244 (2012), pp. 93–111. DOI: 10.1016/j.cma.2012.05.021.

[37] Y. Guo, M. Ruess, and D. Schillinger. ''A parameter-free variational coupling approach for trimmed isogeometric thin shells.'' In: *Computational Mechanics* 59.4 (2017), pp. 693–715. DOI: 10.1007/s00466-016-1368-x.

[38] Y. Guo, J. Heller, T. J. R. Hughes, M. Ruess, and D. Schillinger. ''Variationally consistent isogeometric analysis of trimmed thin shells at finite deformations, based on the STEP exchange format.'' In: *Computer Methods in Applied Mechanics and Engineering* 336 (2017), pp. 39–79. DOI: 10.1016/j.cma.2018.02.027.

[39] E. Rank, M. Ruess, S. Kollmannsberger, D. Schillinger, and A. Düster. ''Geometric modeling, isogeometric analysis and the finite cell method.'' In: *Computer Methods in Applied Mechanics and Engineering* 249-252 (2012), pp. 104–115. DOI: 10.1016/j.cma.2012.05.022.

[40] M. Ruess, D. Schillinger, Y. Bazilevs, V. Varduhn, and E. Rank. ''Weakly enforced essential boundary conditions for NURBS-embedded and trimmed NURBS geometries on the basis of the finite cell method.'' In: *International Journal for Numerical Methods in Engineering* 95.10 (2013), pp. 811–846. DOI: 10.1002/nme.4522.

[41] M. Ruess, D. Schillinger, A. I. Özcan, and E. Rank. ''Weak coupling for isogeometric analysis of non-matching and trimmed multi-patch geometries.'' In: *Computer Methods in Applied Mechanics and Engineering* 269 (2014), pp. 46–71. DOI: 10.1016/j.cma.2013.10.009.

[42] D. Schillinger and M. Ruess. ''The Finite Cell Method: A Review in the Context of Higher-Order Structural Analysis of CAD and Image-Based Geometric Models.'' In: *Archives of Computational Methods in Engineering* 22.3 (2015), pp. 391–455. DOI: 10.1007/s11831-014-9115-y.

[43] A. P. Nagy and D. J. Benson. ''On the numerical integration of trimmed isogeometric elements.'' In: *Computer Methods in Applied Mechanics and Engineering* 284 (2015), pp. 165–185. DOI: 10.1016/j.cma.2014.08.002.

[44] D. J. Benson, S. Hartmann, Y. Bazilevs, M. Hsu, and T. J. R. Hughes. ''Blended isogeometric shells.'' In: *Computer Methods in Applied Mechanics and Engineering* 255 (2013), pp. 133–146. DOI: 10.1016/j.cma.2012.11.020.

[45] J. O. Hallquist. *LS-DYNA Theory Manual 04/27/17 (r:8339)*. Tech. rep. Livermore Software Technology Corporation, 2017.

[46] L. Coox, F. Greco, O. Atak, D. Vandepitte, and W. Desmet. ''A robust patch coupling method for NURBS-based isogeometric analysis of non-conforming multipatch surfaces.'' In: *Computer Methods in Applied Mechanics and Engineering* 316 (2017), pp. 235–260. DOI: 10.1016/j.cma.2016.06.022.

[47] D. J. Benson, A. P. Nagy, S. Hartmann, and I. Yeh. ''Tied Contact for Explicit Dynamics with Isogeometric Analysis.'' In: *13th U.S. National Congress on Computational Mechanics*. San Diego, USA, 2015.

[48] J. Nitsche. ''Über ein Variationsprinzip zur Lösung von Dirichlet-Problemen bei Verwendung von Teilräumen, die keinen Randbedingungen unterworfen sind.'' In: *Abhandlungen aus dem Mathematischen Seminar der Universität Hamburg* 36.1 (1971), pp. 9–15. DOI: 10.1007/BF02995904.

[49] T. Belytschko, W. K. Liu, B. Moran, and K. I. Elkhodary. *Nonlinear finite elements for continua and structures*. Second Edition. John Wiley & Sons, 2014.

[50] A. Apostolatos, R. Schmidt, R. Wüchner, and K.-U. Bletzinger. ''A Nitsche-type formulation and comparison of the most common domain decomposition methods in isogeometric analysis.'' In: *International Journal for Numerical Methods in Engineering* 97.7 (2014), pp. 473–504. DOI: 10.1002/nme.4568.

[51] Z. Lei, F. Gillot, and L. Jezequel. ''A C0/G1 multiple patches connection method in isogeometric analysis.'' In: *Applied Mathematical Modelling* 39.15 (2015), pp. 4405–4420. DOI: 10.1016/j.apm.2014.12.055.

[52] T. Teschemacher, A. M. Bauer, T. Oberbichler, M. Breitenberger, R. Rossi, R. Wüchner, and K.-U. Bletzinger. ''Realization of CAD-integrated Shell Simulation based on Isogeometric B-Rep Analysis.'' In: *Advanced Modeling and Simulation in Engineering Sciences* 5.19 (2018), pp. 1–54. DOI: 10.1186/s40323-018-0109-4.

[53] A. J. Herrema, E. L. Johnson, D. Proserpio, M. C. H. Wu, J. Kiendl, and M.-C. Hsu. ''Penalty coupling of non-matching isogeometric Kirchhoff-Love shell patches with application to composite wind turbine blades.'' In: *Comput. Methods Appl. Mech. Engrg.* 346 (2018), pp. 810–840. DOI: 10.1016/j.cma.2018.08.038.

[54] L. F. Leidinger, M. Breitenberger, A. M. Bauer, S. Hartmann, R. Wüchner, K.-U. Bletzinger, F. Duddeck, and L. Song. ''Explicit dynamic isogeometric B-Rep analysis of penalty-coupled trimmed NURBS shells.'' In: *Computer Methods in Applied Mechanics and Engineering* 351 (2019), pp. 891–927. DOI: 10.1016/j.cma.2019.04.016.

[55] C. Hesch and P. Betsch. ''Isogeometric analysis and domain decomposition methods.'' In: *Computer Methods in Applied Mechanics and Engineering* 213-216 (2012), pp. 104–112. DOI: 10.1016/j.cma.2011.12.003.

[56] E. Brivadis, A. Buffa, B. Wohlmuth, and L. Wunderlich. ''Isogeometric mortar methods.'' In: *Computer Methods in Applied Mechanics and Engineering* 284 (2015), pp. 292–319. DOI: 10.1016/j.cma.2014.09.012.

[57] R. Bouclier, J. C. Passieux, and M. Salaün. ''Development of a new, more regular, mortar method for the coupling of NURBS subdomains within a NURBS patch: Application to a non-intrusive local enrichment of NURBS patches.'' In: *Computer Methods in Applied Mechanics and Engineering* 316 (2017), pp. 123–150. DOI: 10.1016/j.cma.2016.05.037.

[58] W. Dornisch, G. Vitucci, and S. Klinkel. ''The weak substitution method – an application of the mortar method for patch coupling in NURBS-based isogeometric analysis.'' In: *International Journal for Numerical Methods in Engineering* 103.3 (2015), pp. 205–234. DOI: 10.1002/nme.4918.

[59] W. Dornisch, J. Stöckler, and R. Müller. ''Dual and approximate dual basis functions for B-splines and NURBS – Comparison and application for an efficient coupling of patches with the isogeometric mortar method.'' In: 316 (2017), pp. 449–496. DOI: 10.1016/j.cma.2016.07.038.

[60] K. Sommerwerk, M. Woidt, M. C. Haupt, and P. Horst. ''Reissner-Mindlin shell implementation and energy conserving isogeometric multi-patch coupling.'' In: *International Journal for Numerical Methods in Engineering* 109.7 (2017), pp. 982–1012. DOI: 10.1002/nme.5316.

[61] S. Schuß, M. Dittmann, B. Wohlmuth, S. Klinkel, and C. Hesch. ''Multi-patch isogeometric analysis for Kirchhoff-Love shell elements.'' In: *Computer Methods in Applied Mechanics and Engineering* 349 (2019), pp. 91–116. DOI: 10.1016/j.cma.2019.02.015.

[62] M. Dittmann, S. Schuß, B. Wohlmuth, and C. Hesch. ''Weak C^n coupling for multipatch isogeometric analysis in solid mechanics.'' In: *International Journal for Numerical Methods in Engineering* 118.11 (2019), pp. 678–699. DOI: 10.1002/nme.6032.

[63] V. P. Nguyen, P. Kerfriden, M. Brino, S. P. A. Bordas, and E. Bonisoli. ''Nitsche's method for two and three dimensional NURBS patch coupling.'' In: *Computational Mechanics* 53 (6 2014), pp. 1163–1182. DOI: 10.1007/s00466-013-0955-3.

[64] X. Du, G. Zhao, and W. Wang. ''Nitsche method for isogeometric analysis of Reissner–Mindlin plate with non-conforming multi-patches.'' In: *Computer Aided Geometric Design* 35-36 (2015), pp. 121–136. DOI: 10.1016/j.cagd.2015.03.005.

[65] Y. Guo and M. Ruess. ''Nitsche's method for a coupling of isogeometric thin shells and blended shell structures.'' In: *Computer Methods in Applied Mechanics and Engineering* 284 (2015), pp. 881–905. DOI: 10.1016/j.cma.2014.11.014.

[66] W. Jiang, C. Annavarapu, J. E. Dolbow, and I. Harari. ''A robust Nitsche's formulation for interface problems with spline-based finite elements.'' In: *International Journal for Numerical Methods in Engineering* 104.7 (2015), pp. 676–696. DOI: 10.1002/nme.4766.

[67] S. Kollmannsberger, A. I. Özcan, J. Baiges, M. Ruess, E. Rank, and A. Reali. ''Parameter-free, weak imposition of Dirichlet boundary conditions and coupling of trimmed patches.'' In: *International Journal for Numerical Methods in Engineering* 101.9 (2015), pp. 670–699. DOI: 10.1002/nme.4817.

[68] Y. Guo, J. Heller, T. J. R. Hughes, M. Ruess, and D. Schillinger. ''Variationally consistent isogeometric analysis of trimmed thin shells at finite deformations, based on the STEP exchange format.'' In: *Computer Methods in Applied Mechanics and Engineering* 336 (2018), pp. 39–79. DOI: 10.1016/j.cma.2018.02.027.

[69] X. Du, G. Zhao, W. Wang, and H. Fang. ''Nitsche's method for non-conforming multipatch coupling in hyperelastic isogeometric analysis.'' In: *Computational Mechanics* 65.3 (2020), pp. 687–710. DOI: 10.1007/s00466-019-01789-x.

[70] Y. Guo, H. Do, and M. Ruess. ''Isogeometric stability analysis of thin shells: From simple geometries to engineering models.'' In: *International Journal for Numerical Methods in Engineering* 118.8 (2019), pp. 433–458. DOI: 10.1002/nme.6020.

[71] A. Embar, J. Dolbow, and I. Harari. ''Imposing Dirichlet boundary conditions with Nitsche's method and spline-based finite elements.'' In: *International Journal for Numerical Methods in Engineering* 83.7 (2010), pp. 877–898. DOI: 10.1002/nme.2863.

[72] D. Elfverson, M. G. Larson, and K. Larsson. ''A new least squares stabilized Nitsche method for cut isogeometric analysis.'' In: *Computer Methods in Applied Mechanics and Engineering* 349 (2019), pp. 1–16. DOI: 10.1016/j.cma.2019.02.011.

[73] D. J. Benson, Y. Bazilevs, M. C. Hsu, and T. J. R. Hughes. ''Isogeometric shell analysis: The Reissner–Mindlin shell.'' In: *Computer Methods in Applied Mechanics and Engineering* 199.5-8 (2010), pp. 276–289. DOI: 10.1016/j.cma.2009.05.011.

[74] *TeDA*. https://www.bgu.tum.de/st/software2/forschung/teda/. Accessed on January 3, 2020.

[75] M. J. Pratt. ''Introduction to ISO 10303 - The STEP standard for product data exchange.'' In: *Journal of Computing and Information Science in Engineering* 1.1 (2001), pp. 102–103.

[76] K.-J. Bathe. *Finite Element Procedures*. Second edition: fourth printing 2016. Bathe, Klaus-Jürgen, 2016.

[77] D. J. Benson, Y. Bazilevs, M.-C. Hsu, and T. J. R. Hughes. ''A large deformation, rotation-free, isogeometric shell.'' In: *Computer Methods in Applied Mechanics and Engineering* 200.13-16 (2011), pp. 1367–1378. DOI: 10.1016/j.cma.2010.12.003.

[78] S. Hartmann, D. J. Benson, L. Li, and A. P. Nagy. ''Sheet Metal Forming Simulation with IGA in LS-DYNA.'' In: *Proceedings of the 15th International LS-DYNA Users Conference*. Detroit, Michigan, USA, 2018.

[79] D. J. Benson, A. P. Nagy, L. Li, and S. Hartmann. ''Recent developments in isogeometric analysis for LS-DYNA.'' In: *Proceedings of the 15th International LS-DYNA Users Conference*. Detroit, Michigan, USA, 2018.

[80] L. Li and S. Hartmann. ''Recent Developments in Isogeometric Analysis with Solid Elements in LS-DYNA.'' In: *Proceedings of the 15th International LS-DYNA Users Conference*. Detroit, Michigan, USA, 2018.

[81] C. Adam, S. Bouabdallah, M. Zarroug, and H. Maitournam. ''Stable time step estimates for NURBS-based explicit dynamics.'' In: *Computer Methods in Applied Mechanics and Engineering* 295 (2015), pp. 581–605. DOI: 10.1016/j.cma.2015.03.017.

[82] J. Chan and J. A. Evans. ''Multi-patch discontinuous Galerkin isogeometric analysis for wave propagation: Explicit time-stepping and efficient mass matrix inversion.'' In: *Computer Methods in Applied Mechanics and Engineering* 333 (2018), pp. 22–54. DOI: 10.1016/j.cma.2018.01.022.

[83] L. Chen, N. Nguyen-Thanh, H. Nguyen-Xuan, T. Rabczuk, S. Bordas, and G. Limbert. ''Explicit finite deformation analysis of isogeometric membranes.'' In: 277 (2014), pp. 104–130. DOI: 10.1016/j.cma.2014.04.015.

[84] M. Occelli. ''Explicit dynamics isogeometric analysis: lr b-splines implementation in the radioss solver.'' PhD Thesis. Université de Lyon, France, 2018.

[85] *Radioss*. https://altairhyperworks.com/product/RADIOSS. Accessed on January 31, 2020.

[86] A. K. Schaeuble, A. Tkachuk, and M. Bischoff. ''Variationally consistent inertia templates for B-spline- and NURBS-based FEM: Inertia scaling and customization.'' In: *Computer Methods in Applied Mechanics and Engineering* 326 (2017), pp. 596–621. DOI: 10.1016/j.cma.2017.08.035.

[87] J. A. González, J. Kopačka, R. Kolman, S. S. Cho, and K. C. Park. ''Inverse mass matrix for isogeometric explicit transient analysis via the method of localized Lagrange multipliers.'' In: *International Journal for Numerical Methods in Engineering* 117.9 (2019), pp. 939–966. DOI: 10.1002/nme.5986.

[88] C. Anitescu, C. Nguyen, T. Rabczuk, and X. Zhuang. ''Isogeometric analysis for explicit elastodynamics using a dual-basis diagonal mass formulation.'' In: *Computer Methods in Applied Mechanics and Engineering* 346 (2019), pp. 574–591. DOI: 10.1016/j.cma.2018.12.002.

[89] F. Auricchio, L. Beirão da Veiga, T. J. R. Hughes, A. Reali, and G. Sangalli. ''Isogeometric collocation for elastostatics and explicit dynamics.'' In: *Computer Methods in Applied Mechanics and Engineering* 249-252 (2012), pp. 2–14. DOI: 10.1016/j.cma.2012.03.026.

[90] J. A. Evans, R. R. Hiemstra, T. J. R. Hughes, and A. Reali. ''Explicit higher-order accurate isogeometric collocation methods for structural dynamics.'' In: *Computer Methods in Applied Mechanics and Engineering* 338 (2018), pp. 208–240. DOI: 10.1016/j.cma.2018.04.008.

[91] E. Marino, J. Kiendl, and L. De Lorenzis. ''Explicit isogeometric collocation for the dynamics of three-dimensional beams undergoing finite motions.'' In: *Computer Methods in Applied Mechanics and Engineering* 343 (2019), pp. 530–549. DOI: 10.1016/j.cma.2018.09.005.

[92] D. Schillinger, J. A. Evans, A. Reali, M. A. Scott, and T. J. R. Hughes. ''Isogeometric collocation: Cost comparison with Galerkin methods and extension to adaptive hierarchical NURBS discretizations.'' In: *Computer Methods in Applied Mechanics and Engineering* 267 (2013), pp. 170–232. DOI: 10.1016/j.cma.2013.07.017.

[93] R. A. K. Sanches, P. B. Bornemann, and F. Cirak. ''Immersed b-spline (i-spline) finite element method for geometrically complex domains.'' In: *Computer Methods in Applied Mechanics and Engineering* 200.13-16 (2011), pp. 1432–1445. DOI: 10.1016/j.cma.2010.12.008.

[94] C. V. Verhoosel, G. J. van Zwieten, B. van Rietbergen, and R. de Borst. ''Image-based goal-oriented adaptive isogeometric analysis with application to the micro-mechanical modeling of trabecular bone.'' In: *Computer Methods in Applied Mechanics and Engineering* 284 (2015), pp. 138–164. DOI: 10.1016/j.cma.2014.07.009.

[95] D. Elfverson, M. G. Larson, and K. Larsson. ''CutIGA with basis function removal.'' In: *Advanced Modeling and Simulation in Engineering Sciences* 5.1 (2018), pp. 1–19. DOI: 10.1186/s40323-018-0099-2.

[96] M. Dauge, A. Düster, and E. Rank. ''Theoretical and Numerical Investigation of the Finite Cell Method.'' In: *Journal of Scientific Computing* 65.3 (2015), pp. 1039–1064. DOI: 10.1007/s10915-015-9997-3.

[97] F. de Prenter, C. V. Verhoosel, G. J. van Zwieten, and E. H. van Brummelen. ''Condition number analysis and preconditioning of the finite cell method.'' In: *Computer Methods in Applied Mechanics and Engineering* 316 (2017), pp. 297–327. DOI: 10.1016/j.cma.2016.07.006.

[98] F. de Prenter, C. V. Verhoosel, and E. H. van Brummelen. ''Preconditioning immersed isogeometric finite element methods with application to flow problems.'' In: *Computer Methods in Applied Mechanics and Engineering* 348 (2019), pp. 604–631. DOI: 10.1016/j.cma.2019.01.030.

[99] B. Mößner and U. Reif. ''Stability of tensor product B-splines on domains.'' In: *Journal of Approximation Theory* 154.1 (2008), pp. 1–19. DOI: 10.1016/j.jat.2008.02.001.

[100] A. Buffa, R. Puppi, and R. Vázquez. *A minimal stabilization procedure for Isogeometric methods on trimmed geometries*. 2019. arXiv: 1902.04937 [math.NA].

[101] K. Höllig, U. Reif, and J. Wipper. ''Weighted Extended B-Spline Approximation of Dirichlet Problems.'' In: *Society for Industrial and Applied Mathematics* 39.2 (2001), pp. 442–462. DOI: 10.1137/S0036142900373208.

[102] K. Höllig and U. Reif. ''Nonuniform web-splines.'' In: *Computer Aided Geometric Design* 20.5 (2003), pp. 277–294. DOI: 10.1016/S0167-8396(03)00045-1.

[103] K. Höllig. *Finite Element Methods with B-Splines*. Frontiers in applied mathematics. Philadelphia, USA: Society for Industrial and Applied Mathematics, 2003. DOI: 10.1137/1.9780898717532.

[104] K. Höllig, J. Hörner, and A. Hoffacker. ''Finite Element Analysis with B-Splines: Weighted and Isogeometric Methods.'' In: *Curves and Surfaces*. Ed. by J.-D. Boissonnat, P. Chenin, A. Cohen, C. Gout, T. Lyche, M.-L. Mazure, and L. Schumaker. Lecture Notes in Computer Science. Springer, Berlin, Heidelberg, 2012, pp. 330–350. ISBN: 978-3-642-27413-8. DOI: 10.1007/978-3-642-27413-8_21.

[105] T. Rüberg and F. Cirak. ''Subdivision-stabilised immersed b-spline finite elements for moving boundary flows.'' In: *Computer Methods in Applied Mechanics and Engineering* 209-212 (2012), pp. 266–283. DOI: 10.1016/j.cma.2011.10.007.

[106] T. Rüberg and F. Cirak. ''A fixed-grid b-spline finite element technique for fluid-structure interaction.'' In: *International Journal for Numerical Methods in Fluids* 74.9 (2014), pp. 623–660. DOI: 10.1002/fld.3864.

[107] B. Marussig, R. Hiemstra, and T. J. R. Hughes. ''Improved conditioning of isogeometric analysis matrices for trimmed geometries.'' In: *Computer Methods in Applied Mechanics and Engineering* 334 (2018), pp. 79–110. DOI: 10.1016/j.cma.2018.01.052.

[108] S. Badia, F. Verdugo, and A. F. Martín. ''The aggregated unfitted finite element method for elliptic problems.'' In: *Computer Methods in Applied Mechanics and Engineering* 336 (2018), pp. 533–553. DOI: 10.1016/j.cma.2018.03.022. eprint: 1709.09122.

[109] E. Burman. ''Ghost penalty.'' In: *Comptes Rendus Mathematique* 348.21-22 (2010), pp. 1217–1220. DOI: 10.1016/j.crma.2010.10.006.

[110] E. Burman, S. Claus, P. Hansbo, M. G. Larson, and A. Massing. ''CutFEM: Discretizing geometry and partial differential equations.'' In: *International Journal for Numerical Methods in Engineering* 104.7 (2015), pp. 472–501. DOI: 10.1002/nme.4823.

[111] R. Schmidt, J. Kiendl, K.-U. Bletzinger, and R. Wüchner. ''Realization of an integrated structural design process: Analysis-suitable geometric modelling and isogeometric analysis.'' In: *Computing and Visualization in Science* 13.7 (2010), pp. 315–330. DOI: 10.1007/s00791-010-0147-z.

[112] M.-C. Hsu, C. Wang, A. J. Herrema, D. Schillinger, A. Ghoshal, and Y. Bazilevs. ''An interactive geometry modeling and parametric design platform for isogeometric analysis.'' In: *Computers & Mathematics with Applications* 70.7 (2015), pp. 1481–1500. DOI: 10.1016/j.camwa.2015.04.002.

[113] J. Benzaken, A. J. Herrema, M.-C. Hsu, and J. A. Evans. ''A rapid and efficient isogeometric design space exploration framework with application to structural mechanics.'' In: *Computer Methods in Applied Mechanics and Engineering* 316 (2017), pp. 1215–1256. DOI: 10.1016/j.cma.2016.12.026.

[114] T. Elguedj, A. Duval, F. Maurin, and H. Al-Akhras. ''Abaqus user element implementation of NURBS based isogeometric analysis.'' In: *6th European Congress on Computational Methods in Applied Science and Engineering*. Vienna, Austria, 2012.

[115] Y. Lai, Y. J. Zhang, L. Liu, X. Wei, E. Fang, and J. Lua. ''Integrating CAD with Abaqus: A practical isogeometric analysis software platform for industrial applications.'' In: *Computers & Mathematics with Applications* 74.7 (2017), pp. 1648–1660. DOI: 10.1016/j.camwa.2017.03.032.

[116] *Rhinoceros*. https://www.rhino3d.com/. Accessed on January 3, 2020.

[117] *Siemens NX*. https://www.plm.automation.siemens.com/global/de/products/nx/. Accessed on January 3, 2020.

[118] C. Whetten, M. Sederberg, and M. Scott. ''Isogeometric analysis using the *IGA _ INCLUDE _ BEZIER keyword in LS-DYNA.'' In: *Proceedings of the 12th European LS-DYNA Conference 2019*. Koblenz, Germany, 2019.

[119] *Abaqus*. https://www.3ds.com/de/produkte-und-services/simulia/produkte/abaqus/. Accessed on February 13, 2020.

[120] L. Rorris, A. Nagy, S. Hartmann, I. Chalkidis, and A. Vafeidis. ''The ANSA / LS-DYNA approach for IGA Simulations.'' In: *Proceedings of the 12th European LS-DYNA Conference 2019*. Koblenz, Germany, 2019.

[121] J. A. Cottrell, T. J. R. Hughes, and Y. Bazilevs. *Isogeometric Analysis: Toward Integration of CAD and FEA*. John Wiley & Sons, Ltd, 2009.

[122] L. Piegl and W. Tiller. *The NURBS book*. Second Edition. Springer-Verlag Berlin Heidelberg New York, 1997.

[123] D. F. Rogers. *An Introduction to NURBS: With Historical Perspective*. Morgan Kaufmann Publishers, 2001.

[124] G. Brunnett. ''Geometric Design with Trimmed Surfaces.'' In: *H. Hagen, G. Farin, H. Noltemeier (eds.), Geometric Modelling, Computing Supplement 10*. Dagstuhl, Germany: Springer-Verlag Wien New York, 1995, pp. 101–115.

[125] L. A. Piegl and W. Tiller. ''Geometry-based triangulation of trimmed NURBS surfaces.'' In: *CAD Computer Aided Design* 30.1 (1998), pp. 11–18. DOI: 10.1016/S0010-4485(97)00047-X.

[126] T. W. Sederberg, D. C. Anderson, and R. N. Goldman. ''Implicit representation of parametric curves and surfaces.'' In: *Computer Vision, Graphics and Image Processing* 28.1 (1984), pp. 72–84. DOI: 10.1016/0734-189X(84)90140-3.

[127] Y. Basar and W. B. Krätzig. *Mechanik der Flächentragwerke. Theorie, Berechnungsmethoden, Anwendungsbeispiele*. Wiesbaden: Springer Fachmedien, 1985. ISBN: 978-3-322-93984-5.

[128] J. M. Kiendl. ''Isogeometric Analysis and Shape Optimal Design of Shell Structures.'' PhD Thesis. Technical University of Munich, Germany, 2011.

[129] M. Bischoff, K.-U. Bletzinger, W. A. Wall, and E. Ramm. ''Models and Finite Elements for Thin-Walled Structures.'' In: *Encyclopedia of Computational Mechanics*. Ed. by E. Stein, R. de Borst, and T. J. R. Hughes. Vol. 2. John Wiley & Sons, Ltd., 2004. Chap. 3. DOI: 10.1002/0470091355.ecm026.

[130] T. J. R. Hughes and W. K. Liu. ''Nonlinear finite element analysis of shells: Part I. three-dimensional shells.'' In: *Computer Methods in Applied Mechanics and Engineering* 26.3 (1981), pp. 331–362. DOI: 10.1016/0045-7825(81)90121-3.

[131] S. Key and Z. E. Beisinger. ''The transient dynamic analysis of thin shells by the finite element method.'' In: *Proceedings of the 3rd Conference on Matrix Methods in Structural Mechanics*. Wright-Patterson Air Force Base, Ohio, USA, 1971.

[132] T. J. R. Hughes, W. K. Liu, and I. Levit. ''Nonlinear Dynamic Finite Element Analysis of Shells.'' In: *Nonlinear Finite Element Analysis in Structural Mechanics*. Ed. by W. Wunderlich, E. Stein, and K.-J. Bathe. Berlin, Heidelberg: Springer Berlin Heidelberg, 1981, pp. 151–168. ISBN: 978-3-642-81589-8.

[133] J. Kiendl, K.-U. Bletzinger, J. Linhard, and R. Wüchner. ''Isogeometric shell analysis with Kirchhoff-Love elements.'' In: *Computer Methods in Applied Mechanics and Engineering* 198.49-52 (2009), pp. 3902–3914. DOI: 10.1016/j.cma.2009.08.013.

[134] T. J. R. Hughes. *The Finite Element Method: Linear Static and Dynamic Finite Element Analysis*. Dover Publications, 2000.

[135] T. J. R. Hughes, K. S. Pister, and R. L. Taylor. ''Implicit-explicit finite elements in nonlinear transient analysis.'' In: *Computer Methods in Applied Mechanics and Engineering* 17-18.PART 1 (1979), pp. 159–182. DOI: 10.1016/0045-7825(79)90086-0.

[136] T. Belytschko, P. Smolinski, and W. K. Liu. ''Stability of multi-time step partitioned integrators for first-order finite element systems.'' In: *Computer Methods in Applied Mechanics and Engineering* 49.3 (1985), pp. 281–297. DOI: 10.1016/0045-7825(85)90126-4.

[137] R. Courant, K. Friedrichs, and H. Lewy. ''Über die partiellen Differenzengleiehungen der mathematischen Physik.'' In: *Mathematische Annalen* 100 (1928), pp. 32–74.

[138] D. P. Flanagan and T. Belytschko. ''Eigenvalues and stable time steps for the uniform strain hexahedron and quadrilateral.'' In: *Journal of Applied Mechanics* 51.1 (1984), pp. 35–40. DOI: 10.1115/1.3167594.

[139] S. Gerschgorin. ''Über die Abgrenzung der Eigenwerte einer Matrix.'' In: *Bulletin de l'Académie des Sciences de l'URSS. Classe des sciences mathématiques et naturelles* 6 (1931), pp. 749–754.

[140] E. Isaacson and H. B. Keller. *Analysis of Numerical Methods*. Dover Publications, Inc., New York, 1994. DOI: 10.2307/2003280.

[141] D. J. Benson. ''Stable time step estimation for multi-material Eulerian hydrocodes.'' In: *Computer Methods in Applied Mechanics and Engineering* 167.1-2 (1998), pp. 191–205. DOI: 10.1016/S0045-7825(98)00119-4.

[142] K. Y. Sze, X. H. Liu, and S. H. Lo. ''Popular Benchmark Problems for Geometric Nonlinear Analysis of Shells.'' In: *Finite Elements in Analysis and Design* 40.11 (2004), pp. 1551–1569. DOI: 10.1016/j.finel.2003.11.001.

[143] S. Hartmann, L. F. Leidinger, D. J. Benson, L. Li, A. P. Nagy, and M. Pigazzini. ''Enabling the Analysis of Topologically Connected Multi-Patch Trimmed NURBS Shells in LS-DYNA.'' In: *12th European LS-DYNA Conference 2019*. Koblenz, Germany, 2019.

[144] R. K. Murugan. ''Investigation and Estimation of Time Step Size in Explicit Isogeometric B-Rep Analysis.'' Master's Thesis. Technical University of Munich, Germany, 2018.

[145] T. Pasch. ''A priori estimation of the penalty factor w.r.t. accuracy and explicit time step size for weak coupling and boundary conditions on trimmed NURBS-based shell structures.'' Master's Thesis. Technical University of Munich, Germany, 2020.

[146] Z. Lian. *Explicit Isogeometric B-Rep Analysis - Critical time step size, stress evaluation and plasticity*. RWTH Aachen University, Germany. 2019.

[147] T. Pasch. *Mass scaling for explicit isogeometric B-Rep analysis*. Technical University of Munich, Germany. 2019.

[148] J.-h. Kwon. ''A Penalty-based Stabilization Method for Trimmed Multi-Patch NURBS Shells in Explicit Isogeometric B-Rep Analysis.'' Master's Thesis. Technical University of Munich, Germany, 2019.

[149] J. R. Bunch. ''The Weak and Strong Stability of Algorithms in Numerical Linear Algebra.'' In: *Linear Algebra and its Applications* 88-89 (1987), pp. 49–66. DOI: 10.1016/0024-3795(87)90102-9.

[150] G. Noh and K.-J. Bathe. ''An explicit time integration scheme for the analysis of wave propagations.'' In: *Computers and Structures* 129 (2013), pp. 178–193. DOI: 10.1016/j.compstruc.2013.06.007.

[151] P. Deuflhard and F. Bornemann. *Numerische Mathematik 2: Gewöhnliche Differentialgleichungen*. 3. Auflage. Berlin, New York: Walter de Gruyter, 2008. ISBN: 978-3-11-020356-1.

[152] D. P. Mok. ''Partitionierte Lösungsansätze in der Strukturdynamik und der Fluid-Struktur-Interaktion.'' PhD Thesis. Universität Stuttgart, Germany, 2001.

[153] D. Schillinger. ''The p- and B-spline versions of the geometrically nonlinear finite cell method and hierarchical refinement strategies for adaptive isogeometric and embedded domain analysis.'' PhD Thesis. Technical University of Munich, Germany, 2012.

[154] *Carat++*. https://www.bgu.tum.de/en/st/software2/research/carat/. Accessed on January 20, 2020.

[155] *Python*. https://www.python.org/. Accessed on March 13, 2020.

[156] F. Massarwi and G. Elber. ''A B-spline based framework for volumetric object modeling.'' In: *Computer-Aided Design* 78.September 2016 (2016), pp. 36–47. DOI: 10.1016/j.cad.2016.05.003.

[157] Y. Zhang, W. Wang, and T. J. R. Hughes. ''Solid T-spline construction from boundary representations for genus-zero geometry.'' In: *Computer Methods in Applied Mechanics and Engineering* 249-252 (2012), pp. 185–197. DOI: 10.1016/j.cma.2012.01.014.

[158] *Animator*. https://gns-mbh.com/products/animator/. Accessed on April 05, 2020.

[159] T. Belytschko, H. Stolarski, W. K. Liu, N. Carpenter, and J. S. J. Ong. ‘‘Stress projection for membrane and shear locking in shell finite elements.’’ In: *Computer Methods in Applied Mechanics and Engineering* 51 (1985), pp. 221–258. DOI: 10.1016/0045-7825(85)90035-0.

[160] T. Belytschko, J. I. Lin, and C.-S. Tsay. ‘‘Explicit algorithms for the nonlinear dynamics of shells.’’ In: *Computer Methods in Applied Mechanics and Engineering* 42 (1984), pp. 225–251. DOI: 10.1016/0045-7825(84)90026-4.

[161] D. J. Benson and J. O. Hallquist. ‘‘A single surface contact algorithm for the post-buckling analysis of shell structures.’’ In: *Computer Methods in Applied Mechanics and Engineering* 78.2 (1990), pp. 141–163. DOI: 10.1016/0045-7825(90)90098-7.

[162] *ANSA*. https://www.beta-cae.com/ansa.htm. Accessed on January 28, 2020.

[163] L. F. Leidinger, S. Hartmann, L. Rorris, M. Breitenberger, A. M. Bauer, R. Wüchner, K.-U. Bletzinger, F. Duddeck, and L. Song. ‘‘Connecting design and analysis: Explicit Isogeometric Analysis using ANSA and LS-DYNA.’’ In: *8th Before Reality Conference*. Munich, Germany, 2019.

[164] *Euro NCAP Head Impact*. https://www.euroncap.com/en/vehicle-safety/the-ratings-explained/vulnerable-road-user-vru-protection/head-impact/. Accessed on March 29, 2020.

[165] A. Hurwitz. ‘‘Ueber die Bedingungen, unter welchen eine Gleichung nur Wurzeln mit negativen reellen Theilen besitzt.’’ In: *Mathematische Annalen* 46.2 (1895), pp. 273–284.